N72-18677

NASA CONTRACTOR REPORT

NASA CR-111565

NASA CR-111565

CASE FILE COPY

NUCLEAR BRAYTON TURBOALTERNATOR-COMPRESSOR (TAC) CONCEPTUAL DESIGN STUDY

by E. A. Mock and J. E. Davis

Prepared by
AIRESEARCH MANUFACTURING COMPANY OF ARIZONA
Phoenix, Ariz.
for Lewis Research Center

NATIONAL AERONAUTICS AND SPACE ADMINISTRATION • WASHINGTON, D. C. • JANUARY 1972

1. Report No.	2. Government Accession No.	3. Recipient's Catalog No.
NASA CR-111565		

4. Title and Subtitle	5. Report Date
NUCLEAR BRAYTON TURBOALTERNATOR-COMPRESSOR (TAC) CONCEPTUAL DESIGN STUDY	January 1972
	6. Performing Organization Code
7. Author(s)	8. Performing Organization Report No.
E. A. Mock and J. E. Davis	APS-5355-R
	10. Work Unit No.
9. Performing Organization Name and Address	11. Contract or Grant No.
AiResearch Manufacturing Company of Arizona Phoenix, Arizona	NAS 3-13448
	13. Type of Report and Period Covered
12. Sponsoring Agency Name and Address	Contractor Report
National Aeronautics and Space Administration Washington, D. C. 20546	14. Sponsoring Agency Code

15. Supplementary Notes

16. Abstract

The NASA is engaged in a research and technology investigation of nuclear powered Brayton cycle space electric power systems. The turboalternator-compressor (TAC) component of the system is one of the most critical. As part of this program, AiResearch Manufacturing Company has performed a comprehensive analysis and conceptual design study of the turboalternator-compressor components using HeXe as the working fluid. The study was conducted in three phases: general configuration analysis (Phase I), design variations (Phase II), and conceptual design study (Phase III). During the Phase I analysis, individual turbine, alternator, compressor, and bearing and seal designs were evaluated. Six turboalternator-compressor (TAC) configurations were completed. Phase II consisted of evaluating one selected Phase I TAC configuration to calculate its performance when operating under new cycle conditions, namely, one higher and one lower turbine inlet temperature and one case with krypton as the working fluid. Based on the Phase I and II results, a TAC configuration that incorporated a radial compressor, a radial turbine, a Lundell alternator, and gas bearings was selected. During Phase III a new layout of the TAC was prepared that reflects the cycle state points necessary to accommodate a zirconium hydride moderated reactor and a 400 Hz alternator. The final TAC design rotates at 24,000 rpm and produces 160 kWe, 480V, 3-phase, 400 hertz power.

17. Key Words (Suggested by Author(s))	18. Distribution Statement
Turboalternator compressor design Brayton cycle Space electric power	Unclassified - unlimited

19. Security Classif. (of this report)	20. Security Classif. (of this page)	21. No. of Pages	22. Price*
Unclassified	Unclassified	321	$3.00

*For sale by the National Technical Information Service, Springfield, Virginia 22151

FOREWORD

The research described in this report was conducted by the AiResearch Manufacturing Company of Arizona under NASA contract NAS 3-13448. Mr. E. E. Kempke of the Lewis Research Center Space Power Systems Division was the NASA Project Manager.

The study was performed in three phases, a component performance and conceptual design analysis (Phase I), a design variation analysis (Phase II), and a conceptual design study (Phase III). AiResearch was assisted by two subcontractors: Westinghouse Aerospace Electrical Division, which was responsible for the alternator design, and the Franklin Institute Research Laboratories, which performed portions of the bearing analyses.

The report was originally issued as AiResearch Report APS-5355-R.

TABLE OF CONTENTS

		Page
1.	INTRODUCTION	1
2.	PHASE I CONFIGURATION SUMMARY	3
2.1	TAC-A - 24,000 rpm - Radial Compressor - Gas Bearings	7
2.2	TAC-B - 24,000 rpm - Axial Compressor - Gas Bearings	10
2.3	TAC-C - 36,000 rpm - Radial Compressor - Rolling Element Bearings	10
2.4	TAC-D - 36,000 rpm - Axial Compressor - Rolling Element Bearings	15
2.5	TAC-E - 36,000 rpm - Radial Compressor - Oil Film Bearings	18
2.6	TAC-F - 36,000 rpm - Axial Compressor - Oil Film Bearings	18
2.7	Part Load Performance	23
2.8	TAC Configuration Comparisons	28
3.	TAC PHASE II SUMMARY	33
3.1	Design Variation Discussion	35
3.2	Operation of TAC-A at 2560°R	49
4.	PHASE III SUMMARY	55
5.	TAC PHASE I COMPONENT STUDIES	63
5.1	Preliminary Reference Cycles	63
5.2	TAC Compressor Preliminary Design	66
5.2.1	Centrifugal Compressor Optimization	66
5.2.2	Axial Compressor Preliminary Design	78
5.2.3	Recommendations	85
5.2.4	References for Section 5.2	85
5.3	Turbine Studies	88
5.3.1	Turbine Design Procedure	89
5.3.2	Final Loss Distribution and Efficiency Predictions	107
5.3.3	Turbine Stress Analysis	109
5.3.4	References for Section 5.3	120
5.4	TAC Alternator Studies	121
5.4.1	Preliminary Screening Studies	121
5.4.2	Final Alternator Summary	126
5.4.3	Alternator Rotor Stress and Fabrication Considerations	146
5.4.4	Corona Considerations for Voltage Selection	149
5.4.5	Alternator Thermal Analysis	156
5.4.6	Alternator Overall Conclusions and Recommendations	165
5.4.7	References for Section 5.4	166
5.5	Rotor Dynamics	167
5.6	TAC Bearing Configurations	177
5.6.1	Gas Lubricated Bearing System	177
5.6.2	Oil/Mist Lubrication with Rolling Element Bearings	192
5.6.3	Oil Film Bearings	204

TABLE OF CONTENTS (Contd)

		Page
5.7	Alternator Windage Loss Summary	212
5.7.1	Windage Loss Analysis	212
5.7.2	Isolation Seals	215
5.7.3	Alternator Cavity Pressure Reduction	220
5.7.4	TAC Loss Summary	220
5.7.5	References for Section 5.7	223
6.	PHASE III COMPONENT SUMMARY	225
6.1	Compressor Design	225
6.2	Turbine Phase III Design Point	230
6.2.1	Preliminary Design Optimization	231
6.2.2	Turbine Design Results	232
6.3	Phase III Alternator Study	234
6.3.1	Alternator Requirements	234
6.3.2	Electrical Design	237
6.3.3	Thermal Analysis	254
6.3.4	Mechanical Design Considerations	272
6.3.5	Alternator Conclusions and Recommendations	283
6.4	Rotor Dynamics	286
6.5	Bearing Design	291
6.5.1	Journal Bearing Design	291
6.5.2	Thrust Bearing	299
6.5.3	Combined Bearing System Losses	302
6.6	Labyrinth Seal Leakage	303
7.	TAC FAILURE MODE AND EFFECTS ANALYSIS	308

LIST OF FIGURES

		Page
1.	TAC Reference Schematic	4
2.	TAC-A Layout	8
3.	TAC-B Layout	11
4.	TAC-C Layout	13
5.	TAC-D Layout	16
6.	TAC-E Layout	19
7.	TAC-F Layout	21
8.	24,000 rpm TAC Part Load Performance	26
9.	36,000 rpm TAC Part Load Performance	27
10.	2060°R (1144°K) TAC Off-Design Performance	40
11.	1610°R (894°K) TAC Off-Design Performance	41
12.	2560°R (1422°K) TAC Off-Design Performance	42
13.	Performance of 2060°R (1144°K) TAC at SNAP-8 Reactor Conditions (600 KW_t Input)	44
14.	Low Temperature Cycles	45
15.	2060°R (1144°K) Cycles	46
16.	High Temperature Cycles	47
17.	Performance of 2060°R (1144°K) TAC with Krypton Working Fluid (MW = 83.8) as a Function of Shaft Speed	48
18.	24,000 RPM High Temperature Turbine at Overspeed and Overtemperature	50
19.	24,000 RPM High Temperature Turbine at Overspeed and Overtemperature	51
20.	Equivalent Stress Distributions vs Radial Dimension, TAC Radial Turbine	52
21.	Critical Speeds for TAC-A with TZM Turbine	54
22.	TAC Reference Schematic	56
23.	Phase III TAC Layout with 400 Hz Alternator	59
24.	36,000 RPM TAC - Compressor Inlet Pressure Selection	65
25.	TAC Radial Compressor Station Definition	67
26.	Slip Factor vs Number of Blades	68
27.	TAC Radial Compressor Efficiency (24,000 rpm)	71
28.	TAC Radial Compressor Performance (36,000 rpm)	72
29.	TAC Radial Compressor Vaned Diffuser Optimization (24,000 rpm)	74

LIST OF FIGURES (Contd)

		Page
30.	TAC Radial Compressor Vaned Diffuser Optimization (36,000 rpm)	75
31.	24,000 RPM TAC Axial Compressor Preliminary Optimized Hub-Tip Radius Ratio	80
32.	24,000 RPM TAC Axial Compressor Study	81
33.	36,000 RPM TAC Axial Compressor Study	82
34.	TAC 5-Stage Axial Compressor	84
35.	TAC Radial Inflow Turbine Reference Stations	91
36.	Optimum Slip Factor vs Number of Blades TAC Radial Turbine	94
37.	Normal Thickness Distribution - TAC 36,000 RPM Turbine	97
38.	Normal Thickness Distribution - TAC 24,000 RPM Turbine	98
39.	Blade Loss and Diffuser Loss as a Function of Rotor Reaction Ratio	101
40.	Typical Velocity Distribution - Hub Line - 24,000 RPM	102
41.	Typical Velocity Distribution - 50 Percent Streamline - 24,000 RPM	103
42.	Typical Velocity Distribution - Shroud Line - 24,000 RPM	104
43.	Vector Diagrams for 24,000 RPM TAC	105
44.	Vector Diagrams for 36,000 RPM TAC	106
45.	Overall Turbine to Diffuser Exit Total-to-Total Efficiency and Diffuser Length as Functions of Diffuser Exit Mach No.	110
46.	BRU Turbine Efficiency vs Turbine Reynolds Number	111
47.	Equivalent Stress Definition	113
48.	24,000 RPM TAC Turbine at Overspeed and Overtemperature	115
49.	24,000 RPM TAC Turbine at Overspeed and Overtemperature	116
50.	36,000 RPM TAC Turbine at Overspeed and Overtemperature	117
51.	Equivalent Stress Distribution vs Radial Dimension (24,000 rpm)	118
52.	Equivalent Stress Distribution vs Radial Dimension (36,000 rpm)	119
53.	Lundell Alternator, 24,000 RPM	129
54.	Lundell Alternator, 24,000 RPM	130
55.	Lundell Alternator 24,000 RPM Saturation Curves	131
56.	Lundell Alternator 24,000 RPM Efficiency	132
57.	Lundell Alternator, 36,000 RPM	134
58.	Lundell Alternator, 36,000 RPM	135

LIST OF FIGURES (Contd)

		Page
59.	Lundell Alternator, 36,000 RPM Saturation Curves	136
60.	Lundell Alternator, 36,000 RPM Efficiency	137
61.	Inductor Alternator, 36,000 RPM	139
62.	Inductor Alternator, 36,000 RPM	140
63.	Inductor Alternator, 36,000 RPM Saturation Curves	141
64.	24,000 RPM Lundell Stresses	147
65.	36,000 RPM Lundell Rotor	148
66.	Conductor Configurations	150
67.	Conductor Configurations	150
68.	Helium Voltage vs Gap Length	153
69.	Minimum Pressure vs Gap Length	153
70.	Conductor to Stack Configuration	154
71.	Ionization of Helium in TAC Alternator	155
72.	Representative Thermal Map 24,000 RPM Lundell Cooled End Bell, No Gas Flow	157
73.	Representative Thermal Map 24,000 RPM Lundell Cooled End Bell, Gas Flow in Gap	158
74.	Representative Thermal Map 24,000 RPM Lundell Cooled End Bell, Gas Flow in Gap	159
75.	Representative Thermal Map 24,000 RPM Lundell, Gas Flow in Gap	161
76.	Representative Thermal Map 24,000 RPM Lundell Gas Flow in Gap, Gas Flow in Conical and Main Gaps	162
77.	Representative Thermal Map SNAP-8 Coolant 24,000 RPM Cooled End Bell Gas Flow in Gap	163
78.	Mass and Stiffness Model	168
79.	TAC-A Critical Speed Analysis	171
80.	TAC-B Critical Speed Analysis	172
81.	TAC-C Critical Speed Analysis	173
82.	TAC-D Critical Speed Analysis	174
83.	TAC-E Critical Speed Analysis	175
84.	TAC-F Critical Speed Analysis	176
85.	TAC Gas Journal Bearing Load Capacity vs Clearance Ratio	180

LIST OF FIGURES (Contd)

		Page
86.	TAC Gas Journal Bearing Load Capacity vs Clearance Ratio	181
87.	TAC Gas Journal Bearing Pad Load Capacity vs Pivotal Film Thickness	182
88.	TAC Gas Journal Bearing Pad Load Capacity vs Pivotal Film Thickness	183
89.	Reduced Test Data Gas Bearing Stability Study	184
90.	Tilting Pad Gas Journal Bearing Performance	186
91.	Tilting Pad Gas Journal Bearing Performance	187
92.	Performance of Gas-Lubricated Double-Acting Step Thrust Bearing	189
93.	Performance of Gas-Lubricated Double-Acting Step Thrust Bearing	190
94.	Ball Bearing B_1 Fatigue Life Comparison	193
95.	Roller Bearing B_1 Fatigue Life Comparison	194
96.	Compressor End Bearing Compartment	196
97.	Turbine End Bearing Compartment	197
98.	Performance of Oil Lubricated Journal Bearing	205
99.	Performance of Oil Lubricated Journal Bearing	206
100.	Performance of Oil Lubricated Double-Acting Tapered Load 8-Pad Thrust Bearing	208
101.	Performance of Oil Lubricated Double-Acting Tapered Load 8-Pad Thrust Bearing	209
102.	Windage Loss Friction Coefficients	214
103.	TAC Alternator Windage Loss vs Cavity Pressure	216
104.	TAC Labyrinth Seal Leakage	217
105.	Hydrodynamic Lift-Off Seal Leakage	221
106.	Two-Stage Ejector Performance	222
107.	TAC Phase III Compressor	227
108.	TAC Phase III Compressor	228
109.	Radial Gap Study	239
110.	TAC Phase III Alternator Layout	242
111.	Saturation Curves	250
112.	Saturation Curves	251
113.	Cooling Gas Flow Rate	258

LIST OF FIGURES (Contd)

		Page
114.	Alternator Windage Losses	259
115.	Alternator Windage Losses	260
116.	Alternator Thermal Map	263
117.	Alternator Thermal Map	263
118.	Alternator Thermal Map	264
119.	Alternator Thermal Map	264
120.	Alternator Thermal Map	265
121.	Alternator Thermal Map	265
122.	Alternator Thermal Map	266
123.	Alternator Thermal Map	266
124.	Alternator Thermal Map	267
125.	Alternator Thermal Map	267
126.	Alternator Thermal Map	268
127.	Stub Shaft Thermal Integration	270
128.	TAC Phase III Alternator Rotor Details	278
129.	Mass and Stiffness Model	288
130.	Shaft Mode Shape at Critical Speeds	289
131.	Bearing Load and Critical Speed Analysis	290
132.	TAC Gas Journal Bearing Pad Load Capacity vs Pivotal Film Thickness	293
133.	TAC Gas Journal Bearing Pad Load Capacity vs Pivotal Film Thickness	294
134.	Tilting Pad Gas Journal Bearing Performance	295
135.	Tilting Pad Gas Journal Bearing Performance	297
136.	Thrust Bearing Hydrodynamic Performance	301
137.	Coefficient of Discharge for Contractions	304
138.	Alternator Seal Leakage	305
139.	Turbine Seal Leakage	306

LIST OF TABLES

		Page
1.	TAC Specifications	5
2.	TAC Configurations	6
3.	TAC-A Performance Summary	9
4.	TAC-B Performance Summary	12
5.	TAC-C Performance Summary	14
6.	TAC-D Performance Summary	17
7.	TAC-E Performance Summary	20
8.	TAC-F Performance Summary	22
9.	TAC Weight and Efficiency Summary	29
10.	Potential Development Problem Areas for Various TAC Configurations	30
11.	Summary of Design Variations	34
12.	TAC Design for T_6 = 2060°R (1144°K)	36
13.	TAC Design for T_6 = 1610°R (894°K)	37
14.	TAC Design for T_6 = 2560°R (1422°K)	38
15.	TAC Design for Krypton - T_6 = 2060°R (1144°K)	39
16.	Phase III TAC Specifications	57
17.	Phase III TAC Performance Summary	60
18.	Comparison of 2-Pole and 6-Pole Alternators at Phase III Operating Conditions	61
19.	TAC Component Performance	66
20.	Centrifugal Compressor Summary	77
21.	Axial Compressor Summary	86
22.	Comparison of Axial Flow and Radial Flow Compressors for TAC Application	87
23.	Parameters Governing the Vector Diagrams of a Radial Turbine	90
24.	Turbine Phase I Parametric Design	99
25.	Estimated Distribution of Losses: TAC Turbines	108
26.	TAC Alternator Summary Specifications	121
27.	Alternator Configurations	122
28.	214 KVA Lundell Generator Design Summary	123
29.	214 KVA Lundell Generator Design Summary	124

LIST OF TABLES (Contd)

		Page
30.	214 KVA Inductor Alternator Design Summary	125
31.	Internal Design Details Summary	127
32.	TAC Alternator Materials List	142
33.	Summary of Bearing and Rotating Group Characteristics Used in Critical Speed Analysis	169
34.	TAC-A Seal Leakages	191
35.	TAC-B Seal Leakages	191
36.	Bearing Compartment Seal Summary	200
37.	TAC Loss Summary	224
38.	Compressor Design Comparison	225
39.	Phase III Compressor Design	229
40.	Turbine Design Comparison	230
41.	Phase III Turbine Design	233
42.	TAC Phase III Alternator Design Summary	243
43.	Alternator Loss Summary	245
44.	Alternator Loss Summary	246
45.	Alternator Loss Summary	247
46.	Alternator Loss Summary	248
47.	Minimum Allowable Pressures Based on Corona Considerations	252
48.	Listing of Thermal Maps	262
49.	Journal and Thrust Bearing Performance	300
50.	TAC Failure Mode Analysis	309

TURBOALTERNATOR-COMPRESSOR (TAC) STUDY - FINAL REPORT

1. INTRODUCTION

This report, submitted by The AiResearch Manufacuring Company of Arizona, A Division of The Garrett Corporation, presents the analysis and final results of a program conducted under NASA-Lewis Research Center Contract NAS 3-13449, "Conceptual Design Study of a Nuclear Brayton Turboalternator-Compressor". The program was conducted in three phases: general configuration analyses (Phase I), design variations (Phase II) and conceptual design study (Phase III). The objective of the study was to define and study a 160-kw Brayton rotating assembly.

During the Phase I analyses, individual turbine, alternator, compressor, and bearing and seal designs were evaluated and six Turboalternator-Compressor (TAC) configurations submitted to NASA for their review and approval. Phase II consisted of evaluating one selected Phase I TAC configuration to determine its performance when operating under new cycle conditions with both higher and lower turbine inlet temperatures and one case with Krypton (vs Argon) as the working fluid.

Based on the Phase I and II results, NASA selected a TAC configuration that incorporated a radial compressor, a radial turbine, a Lundell alternator, and gas bearings. Prior to the initiation of Phase III, NASA redirected the TAC study to utilize a zirconium hydride moderated SNAP-8 type reactor as the heat source. A turbine inlet temperature of 1610°R (894°K) was specified in lieu of the 2060°R (1144°K) specified in Phase I. NASA also specified that a 2-pole, 400-Hz alternator be evaluated for feasibility in the TAC in lieu of the 1200-Hz alternator design selected during Phase I.

During Phase III a new layout of the TAC was prepared that reflects the new cycle state points and a 400-Hz alternator. It was concluded that the Phase III TAC unit is a feasible and practical design. Comparison of the 1200- and 400-Hz designs is included in Section 4 of this report.

Assisting AiResearch in the performance of the study were two subcontractors. Westinghouse Aerospace Division was responsible for the alternator electromechanical design. The Franklin Institute Research Laboratories performed portions of the bearing and seal analyses.

This report is divided into five main sections that include a summary of the Phase I, II, and III configuration analyses (Sections 2, 3, and 4, respectively) and summaries of the Phase I and III component evaluations (Sections 5 and 6).

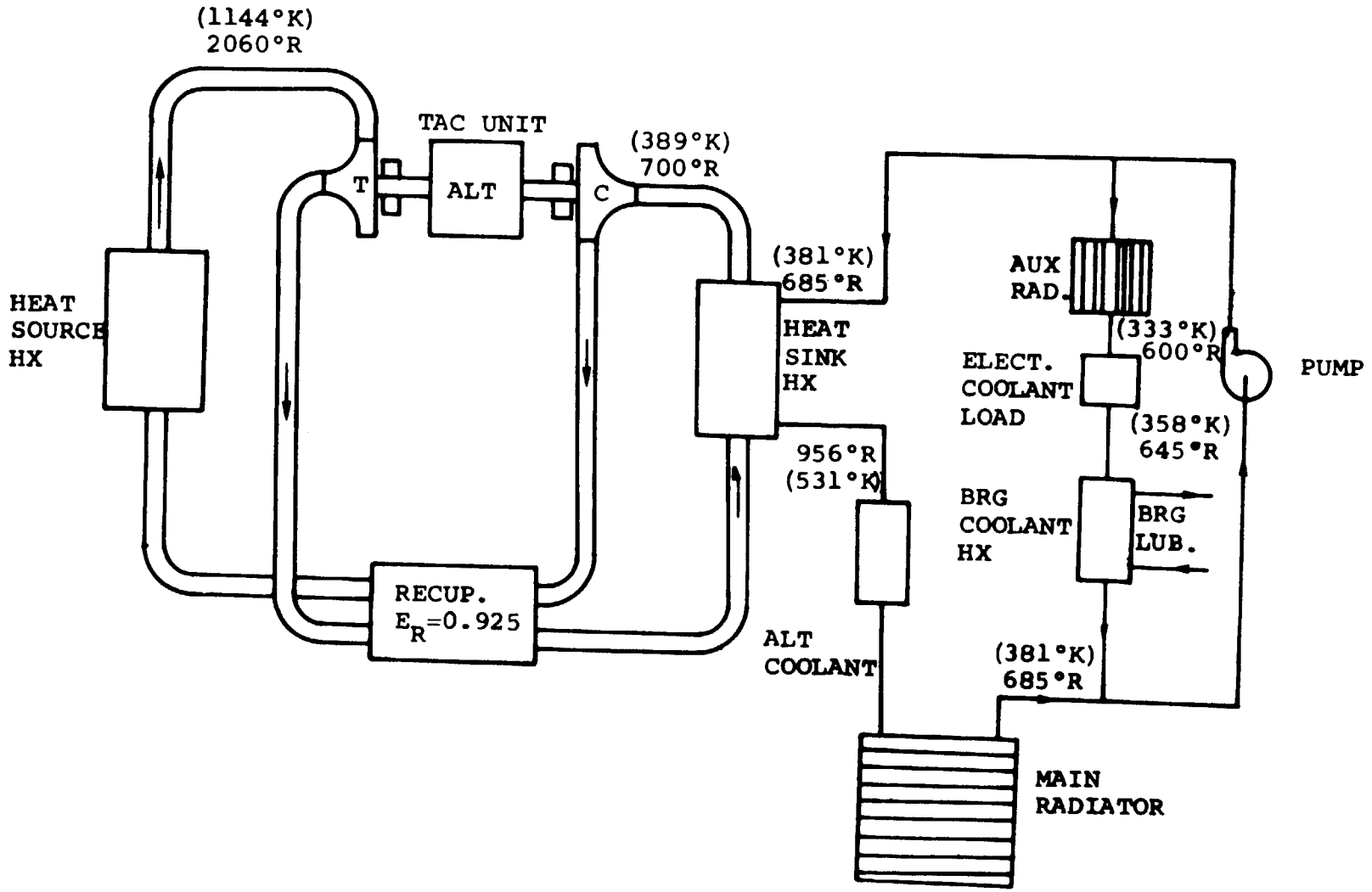
2. PHASE I CONFIGURATION SUMMARY

The objective of the Phase I study was to evaluate component design and define six configurations of a Brayton-cycle Turboalternator-Compressor (TAC) with a design electrical output power range of 40 to 160 kw_e. Each configuration was to be suitable for use in the closed Brayton power system schematically shown in Figure 1. General specifications of the TAC unit are shown in Table 1.

Preliminary feasible arrangement drawings were prepared for each of the six TAC configurations listed in Table 2. Each arrangement is the result of parametric analysis of the major components making up the particular TAC unit. The six TAC units were subjected to critical speed analysis and the rotating assembly dimensions modified as necessary to place the normal operating speed range (100 to 120 percent design speed) in a region safely removed from either rigid body or flexible shaft mode critical speeds.

The overall efficiency of the six TAC units was calculated assuming fixed values of turbine and compressor inlet temperature and a fixed value of recuperative effectiveness as defined by Figure 1. This value of overall cycle efficiency for each TAC unit includes the effects of compressor, turbine and alternator efficiency and losses due to seal leakage, bearing power loss and alternator windage loss. The 36,000 rpm units all require ejectors to reduce the alternator cavity pressure and thus windage to acceptable levels. The cycle penalties due to this compressor bleed flow are included in the determination of cycle efficiency.

The six TAC units are described below. Drawings of the units and a summary performance table for each unit follow the discussion. Each of the six configurations utilize a Lundell-type alternator with 1200 Hz output frequency.



TAC REFERENCE SCHEMATIC

FIGURE 1

TABLE 1

TAC SPECIFICATIONS

DESIGN POWER, kw_e	160
POWER RANGE, kw_e	40 to 160
SPEED, rpm	24,000 and 36,000
WORKING FLUID, mol wt	39.94
COMPRESSOR PRESSURE RATIO	1.9
COMPRESSOR INLET PRESSURE, psia (KN/m^2 abs)	55 (379) at 24,000 rpm 120 (827) to 360 (2482) at 36,000 rpm
COMPRESSOR INLET TEMPERATURE, °R (°K)	700 (389)
TURBINE INLET PRESSURE	0.97 P_2
TURBINE INLET TEMPERATURE, °R (°K)	2060 (1144)

TABLE 2

TAC CONFIGURATIONS			
TAC-A	24,000 RPM	Radial Compressor	Gas Bearings
TAC-B	24,000 RPM	Axial Compressor	Gas Bearings
TAC-C	36,000 RPM	Radial Compressor	Rolling Element Bearings
TAC-D	36,000 RPM	Axial Compressor	Rolling Element Bearings
TAC-E	36,000 RPM	Radial Compressor	Oil Film Bearings
TAC-F	36,000 RPM	Axial Compressor	Oil Film Bearings

2.1 TAC-A 24,000 rpm - Radial Compressor - Gas Bearings

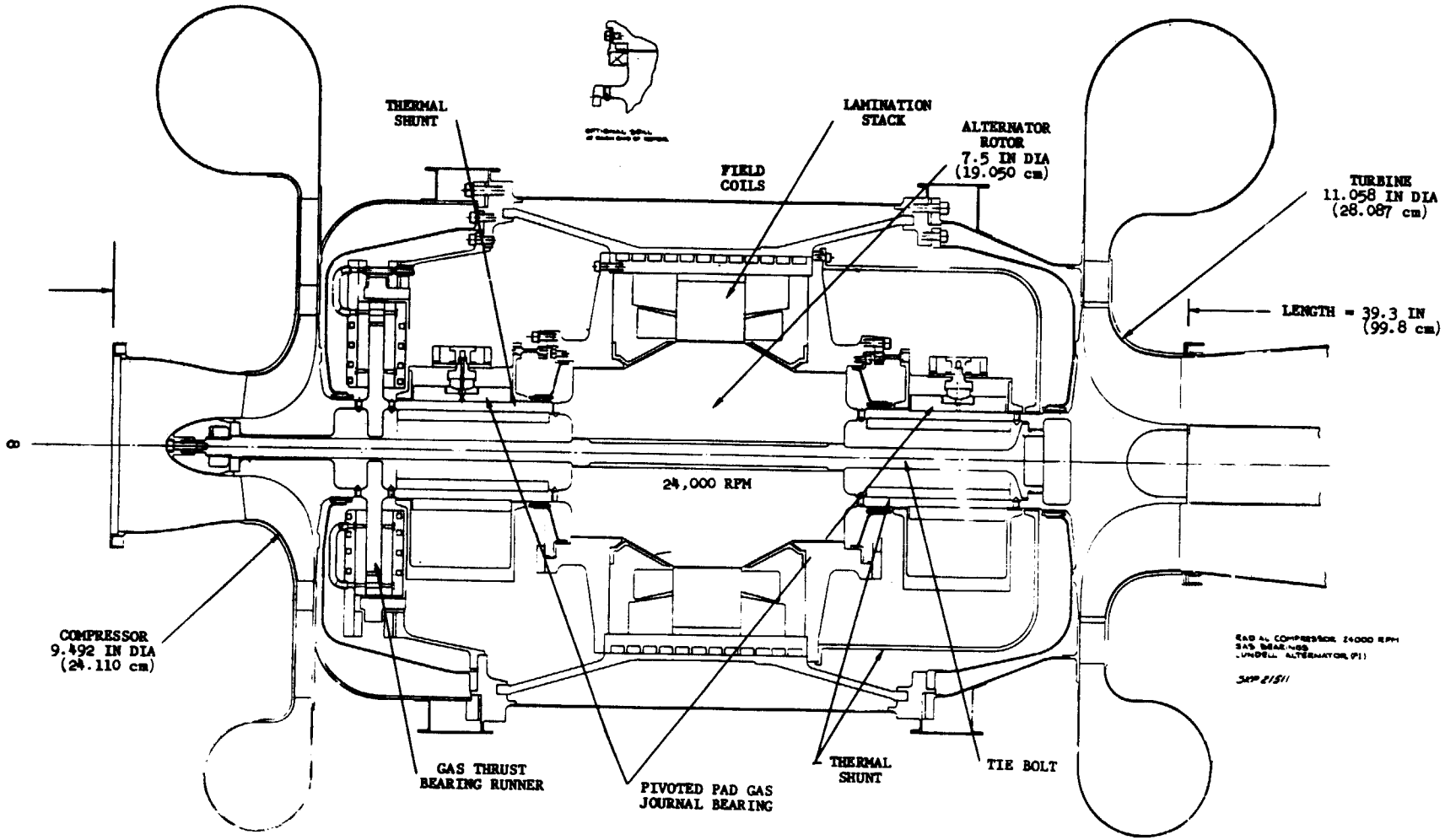
Figure 2 shows the arrangement drawing of TAC-A and Table 3 shows the major component performance factors and overall cycle efficiency of the unit when used in the system defined by Figure 1. Mechanically this unit is very similar to the NASA Brayton Rotating Unit (BRU) which is now under test at NASA Lewis Research Center.

The high predicted aerodynamic performance of this unit is due to the large physical size of the flow passages which minimize clearance losses. The unit will operate at a compressor specific speed that results in nearly maximum obtainable compressor efficiency.

It should be noted that the aerodynamic component efficiency estimates were based on flow rates determined by preliminary cycle analyses as discussed in Section 5.1. Final component efficiencies will vary due to the differences in flow rate in the final configuration.

Three pad pivoted-pad gas journal bearings [3.5 in. (8.89 cm) diameter] are used with one flexibily mounted pivot for preload application. Hydrostatic gas for lift-off at start up is supplied through the conforming pivot sockets. A gimbal mounted Rayleigh step sector thrust bearing is shown with cooling provisions in the thrust bearing stator.

Labyrinth seals are used surrounding each bearing compartment. The bearing compartments are pressurized to compressor discharge pressure to maximize bearing load capacity. The alternator rotor cavity is vented to the compressor inlet which results in acceptable windage loss values without the complication of an ejector.



TAC-A LAYOUT

FIGURE 2

TABLE 3

TAC-A PERFORMANCE SUMMARY		
EFFICIENCIES:		
Cycle efficiency at 160 kw_e	0.309	
Turbine efficiency	0.916	
Compressor efficiency	0.870	
Alternator efficiency	0.942	
SHAFT POWER LOSSES, KW:		
Alternator windage*	3.55	
Alternator cavity seals	0.0	
Bearings		
Thrust	1.93	
Journal	0.77	
Bearing compartment (Seals, churning losses)	0.0	
TOTAL LOSSES	6.25	
MASS FLOWS:	lb/sec	kg/sec
Compressor inlet	8.9769	4.0710
Compressor bleed		
Seal leakage	0.131	0.059
Ejector flow	0.0	0.0
Total bleed	0.131	0.059
MASS	lb	kg
Rotating group	200	90.7
Total TAC mass	800	362.8

*Cavity pressure = 55 psia (379 kN/m^2 abs)

This unit has the highest predicted efficiency of any of the six TAC configurations, due to the good aerodynamic performance and lack of parasitic losses.

2.2 TAC-B - 24,000 rpm - Axial Compressor - Gas Bearings

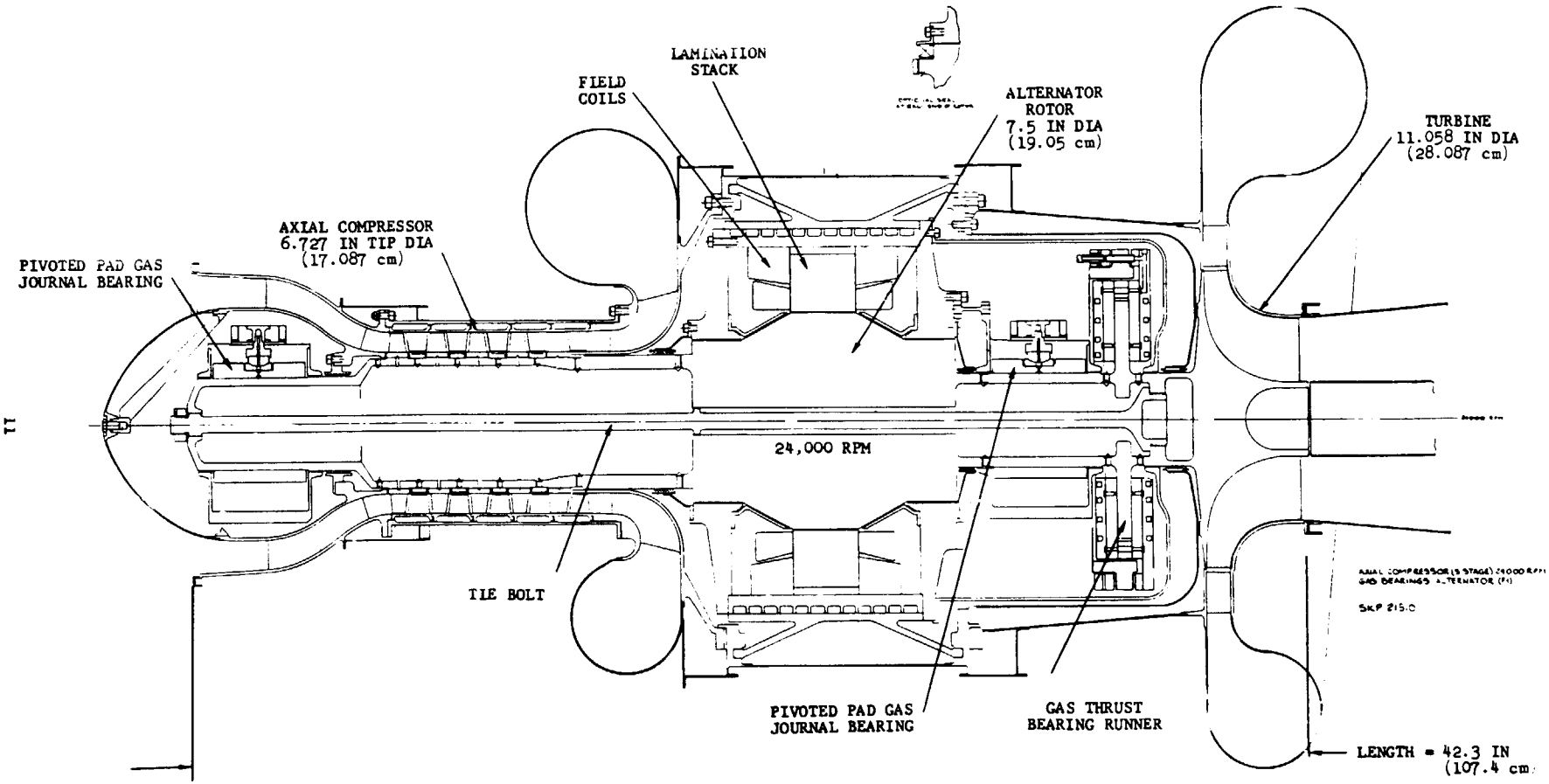
The unit utilizes the same turbine, alternator, and bearing system as TAC-A but a five stage axial compressor is used instead of the single radial compressor. Figure 3 shows the arrangement drawing and Table 4 summarizes the estimated performance. The compressor end bearing is located outboard of the compressor to minimize shaft bending problems. Critical speed considerations will limit the number of compressor stages which can be used in the TAC. A five stage unit was selected over a shortened six stage design to assure reasonable chord length in each stage with adequate axial length for a diffuser after the last compressor stage.

The predicted aerodynamic efficiency of this compressor is essentially the same as the radial compressor in TAC-A and therefore this unit has essentially the same overall cycle efficiency as TAC-A.

2.3 TAC-C - 36,000 rpm - Radial Compressor - Rolling Element Bearings

The aerodynamic components in this unit are similar to, but smaller than, those of TAC-A due to higher shaft speed and higher pressure as shown in Figure 4. The compressor and turbine efficiencies (Table 5) are lower primarily due to clearance losses and size effect.

The bearing support system for this unit utilizes, as required by contract, the techniques described in NASA CR 1229 and UAC report PWA 3349.



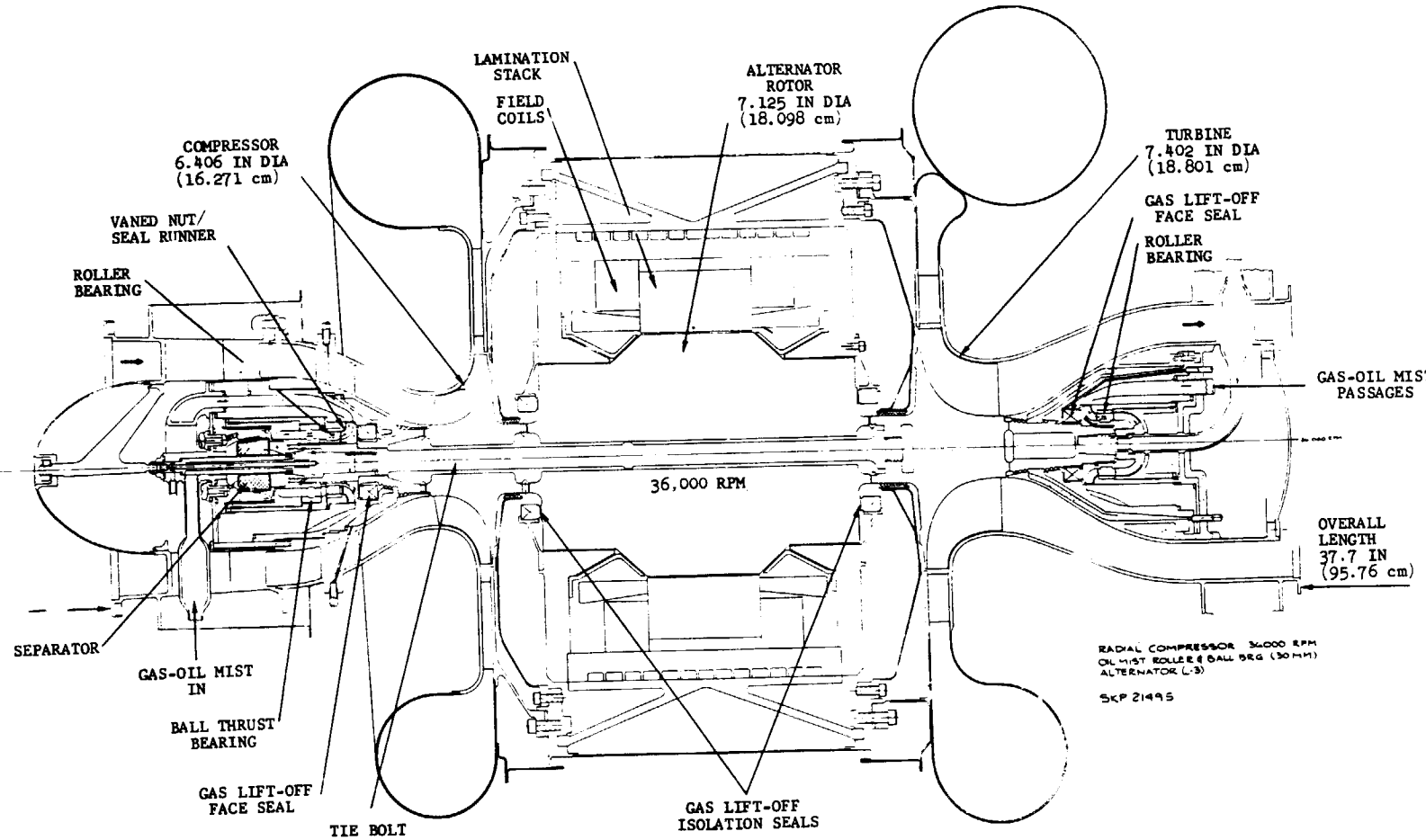
TAC-B LAYOUT

FIGURE 3

TABLE 4

TAC-B PERFORMANCE SUMMARY		
EFFICIENCIES:		
Cycle efficiency at 160 kw_e	0.308	
Turbine efficiency	0.916	
Compressor efficiency	0.869	
Alternator efficiency	0.942	
SHAFT POWER LOSSES, KW:		
Alternator windage*	3.55	
Alternator cavity seals	0.0	
Bearings		
Thrust	1.93	
Journal	0.77	
Bearing compartment (Seals, churning losses)	0.0	
TOTAL LOSSES	6.25	
MASS FLOWS:	lb/sec	kg/sec
Compressor inlet	9.0392	4.0993
Compressor bleed		
Seal leakage	0.1495	0.068
Ejector flow	0.0	0.0
Total bleed	0.1495	0.068
MASS	lb	kg
Rotating group	207	93.9
Total TAC mass	850	385.5

*Cavity pressure = 55 psia (379 kN/m^2 abs)



TAC-C LAYOUT

FIGURE 4

TABLE 5

TAC-C PERFORMANCE SUMMARY		
EFFICIENCIES:		
Cycle efficiency at 160 kw_e	0.292	
Turbine efficiency	0.908	
Compressor efficiency	0.863	
Alternator efficiency	0.942	
SHAFT POWER LOSSES, KW:		
Alternator windage*	6.00	
Alternator cavity seals	1.31	
Bearings		
Ball bearings	0.35	
Roller bearings	0.45	
Bearing compartment (Seals, churning losses)	1.06	
TOTAL LOSSES	9.17	
MASS FLOWS:	lb/sec	kg/sec
Compressor inlet	9.6469	4.3748
Compressor bleed		
Seal leakage	0.0938	0.043
Ejector flow	0.1168	0.053
Total bleed	0.2106	0.096
MASS	lb	kg
Rotating group	124	56.2
Total TAC mass	560	254.0

*Cavity pressure = 40 psia (276 kN/m^2 abs)

Gas-oil mist lubrication and cooling is utilized with 30-mm bore bearings selected because they yield the maximum bearing life in this application. A roller bearing is used at each end of the machine to carry all the radial loads. A single ball bearing is used at the compressor end of the unit to carry only thrust load.

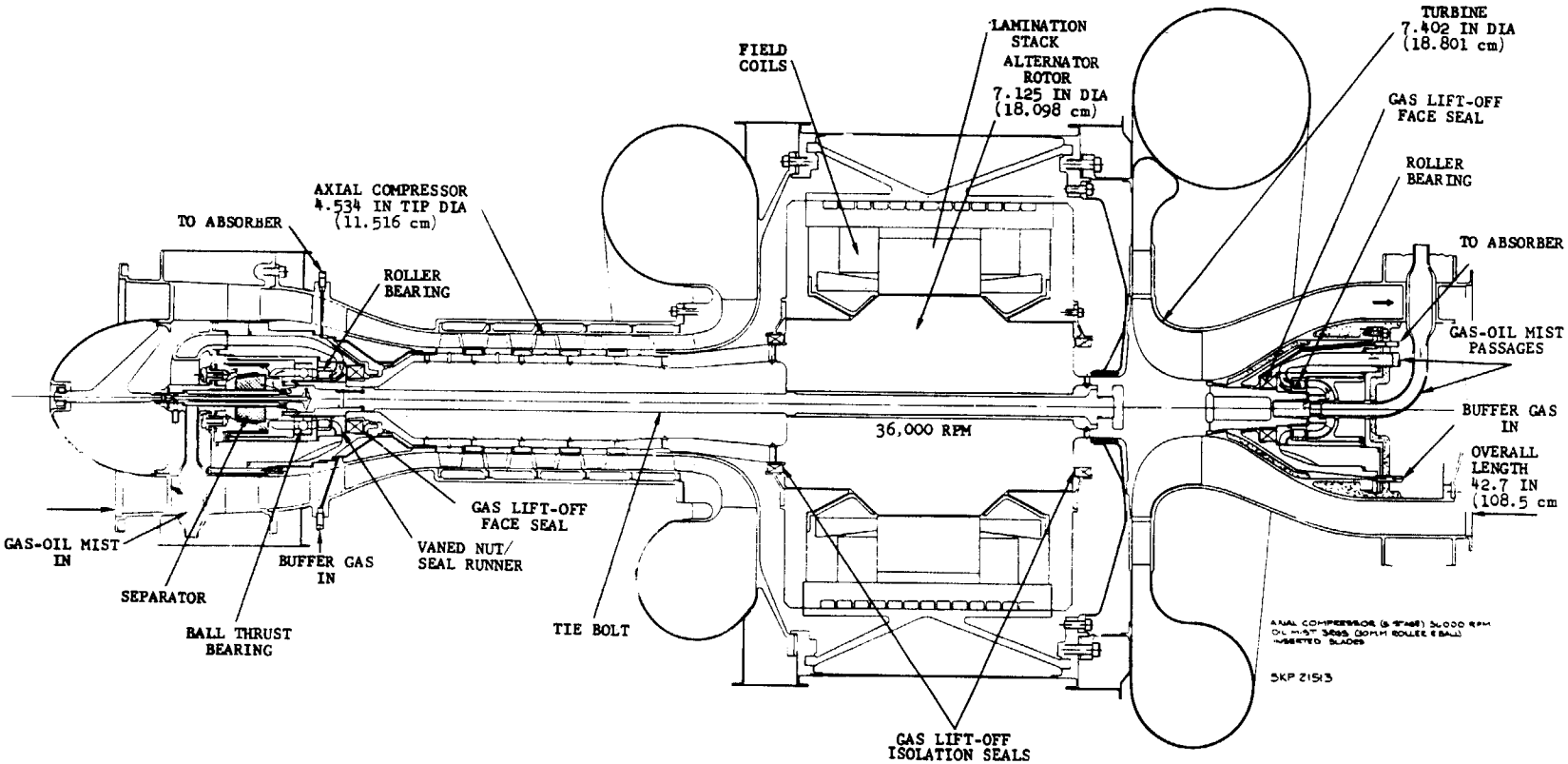
Sealing of the bearing compartment is achieved with buffered gas lift-off seals similar to those developed for NASA-LeRC by AiResearch for the BRU-R (rolling element bearing version of the BRU).

The alternator cavity operates at a reduced pressure achieved by pumping with a two stage ejector powered with compressor bleed and pumping to the compressor inlet pressure. Gas lift-off seals similar to those used in the bearing compartment are used to isolate the alternator cavity and to limit the gas leakage into the cavity to a small value.

The alternator rotor in all the 36,000 rpm TAC machines operates at a tip speed higher than the 24,000 rpm units. Late in the Phase I studies it was found that the tie-bolt hole should be eliminated from the alternator. One approach to solving this problem was to pierce the turbine wheel and mount it on a small diameter stub shaft extending from the alternator. Analysis showed that this approach would increase stresses in the turbine wheel to the point that some creep would occur. An alternative approach is recommended that retains the curvic couplings and eliminates the hole from both turbine and alternator. An outside nut is used to hold the curvic coupling together. This assembly technique would be recommended in all of the 36,000 rpm designs.

2.4 TAC-D - 36,000 rpm - Axial Compressor - Rolling Element Bearings

This unit is identical to TAC-C except for the substitution of a five stage axial compressor (Figure 5). Alternator cavity isolation



TAC-D LAYOUT

FIGURE 5

TABLE 6

TAC-D PERFORMANCE SUMMARY		
EFFICIENCIES:		
Cycle efficiency at 160 kw_e	0.271	
Turbine efficiency	0.908	
Compressor efficiency	0.860	
Alternator efficiency	0.942	
SHAFT POWER LOSSES, KW:		
Alternator windage*	7.71	
Alternator cavity seals	1.89	
Bearings		
Ball Bearing	0.35	
Roller Bearings	0.45	
Bearing compartment (Seals, churning losses)	1.06	
TOTAL LOSSES	11.46	
MASS FLOWS:	lb/sec	kg/sec
Compressor inlet	10.6763	4.8417
Compressor bleed		
Seal leakage	0.167	0.076
Ejector flow	0.374	0.170
Total bleed	0.541	0.246
MASS	lb	kg
Rotating group	133	60.3
Total TAC mass	580	263.0

*Cavity pressure = 56 psia (386 kN/m^2 abs)

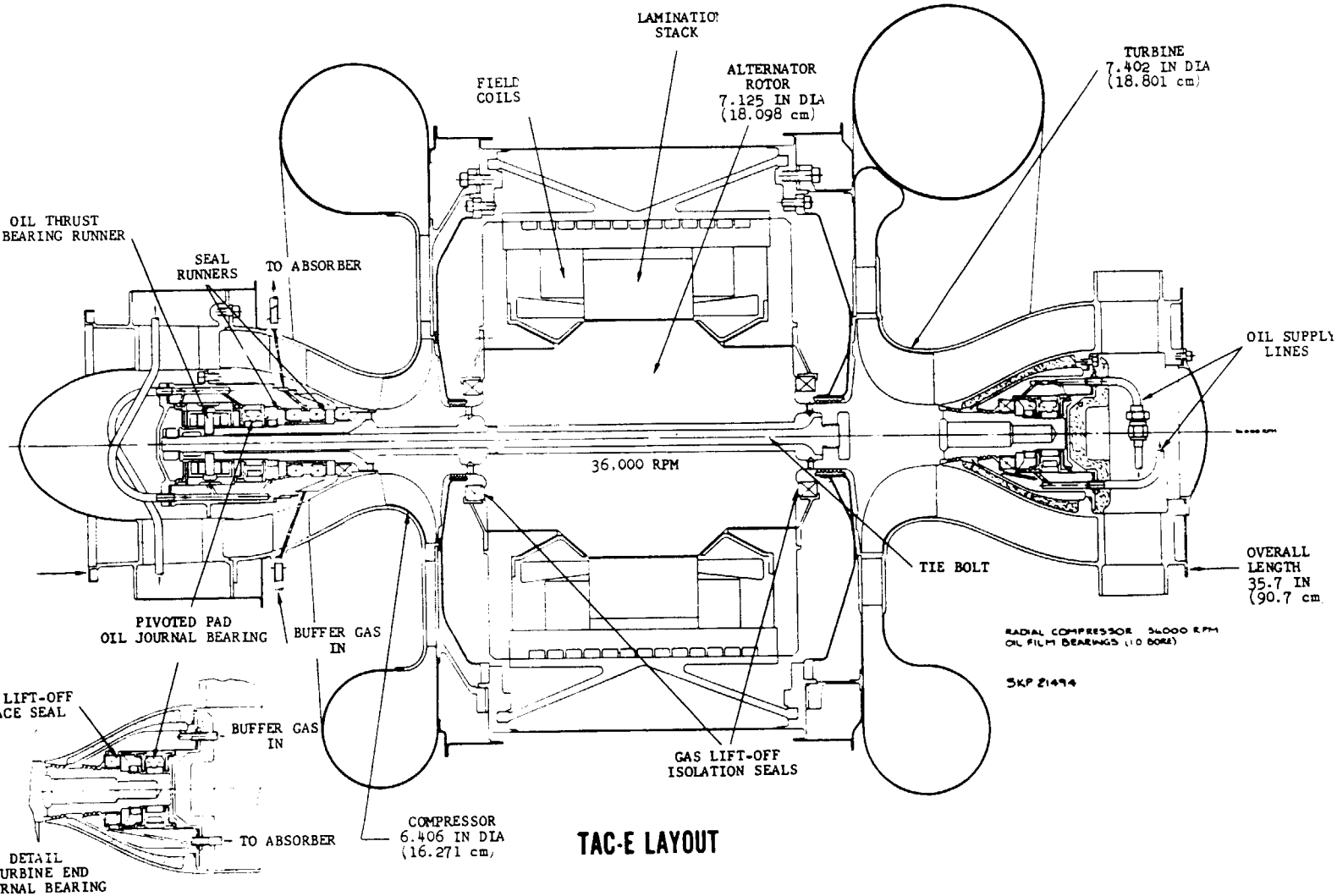
seals are at a larger diameter than in TAC-C and result in larger leakage flows and larger power losses as shown in Table 6. Cycle efficiency is lower than TAC-C, reflecting lower compressor efficiency and more parasite losses to seals and increased ejector flow.

2.5 TAC-E - 36,000 rpm - Radial Compressor - Oil Film Bearings

This unit is similar to TAC-C except for the substitution of flooded compartment oil film bearings (Figure 6). The bearing compartments are located outboard to minimize bearing losses. A preliminary version of this machine with inboard bearings required a shaft diameter of 2.8 to 3.0 inches (7.11 to 7.62 cm) to provide adequate shaft stiffness. The bearing losses and compartment churning losses were found to be excessively high. Moving the bearing compartments outboard allowed the minimization of these losses by selecting a small 1.0 inch (2.54 cm) diameter journal bearings. The number of oil-to-gas seals was also reduced to one per compartment. Churning losses still contribute a large fraction of the losses in this machine as shown in Table 7. Seals for this machine include oil pumping lift-off seals similar to those being developed for SNAP-8. These seals are buffered by either labyrinth seals (as shown on the turbine end) or by a pair of gas lift-off seals as shown on the compressor end.

2.6 TAC-F - 36,000 rpm - Axial Compressor - Oil Film Bearings

This unit is identical to TAC-E except for the substitution of a five stage axial compressor as shown in Figure 7. This unit has the lowest overall cycle efficiency of the six TAC units due largely to parasitic losses in bearings and in ejector bleed flow losses as shown on Table 8.



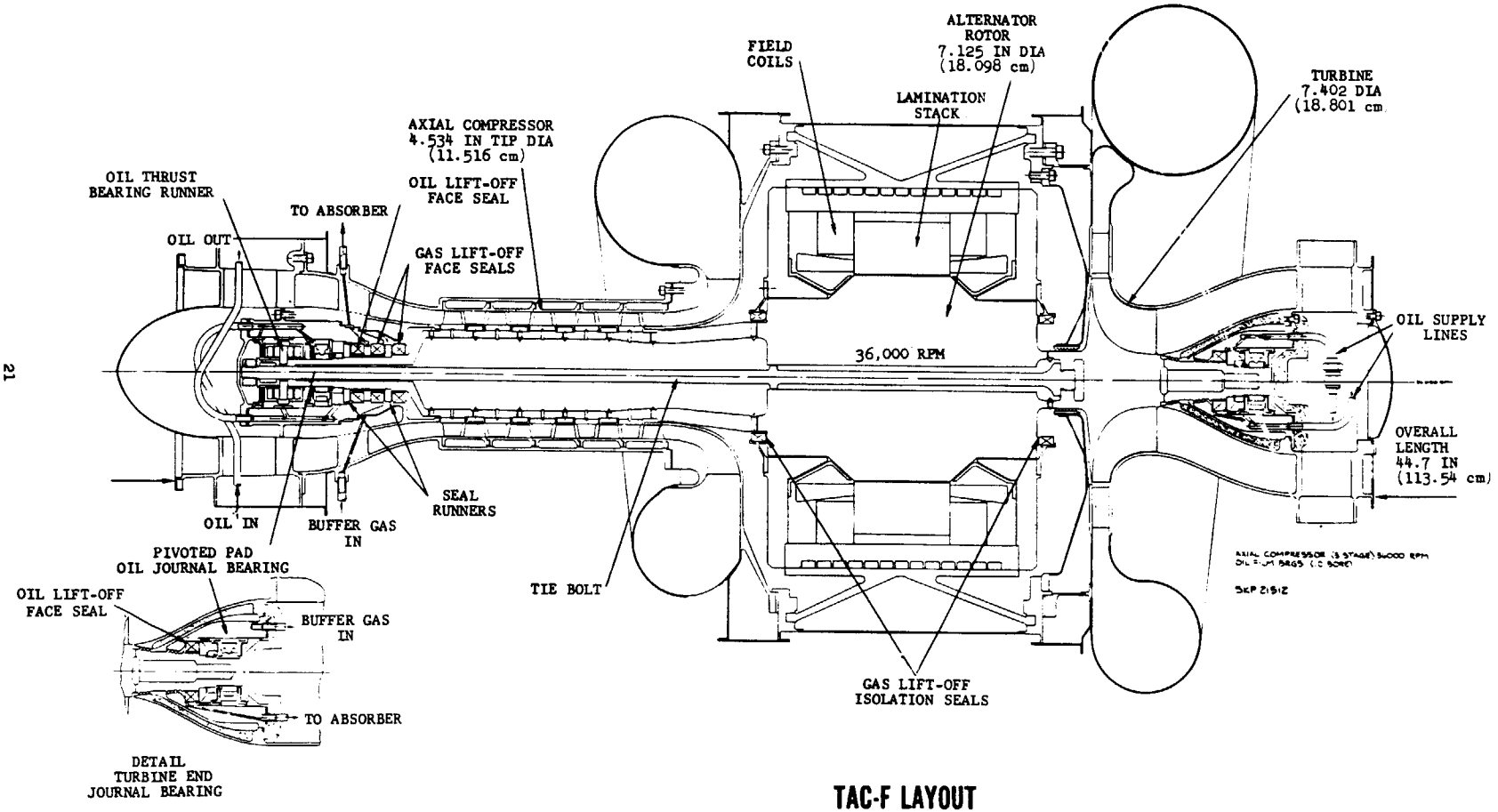
TAC-E LAYOUT

FIGURE 6

TABLE 7

TAC-E PERFORMANCE SUMMARY		
EFFICIENCIES:		
Cycle efficiency at 160 kw_e	0.283	
Turbine efficiency	0.908	
Compressor efficiency	0.863	
Alternator efficiency	0.942	
SHAFT POWER LOSSES, KW:		
Alternator windage*	6.00	
Alternator cavity seals	1.31	
Bearings		
Thrust	1.86	
Journal	0.78	
Bearing compartment (Seals, churning losses)	6.63	
TOTAL LOSSES	16.58	
MASS FLOWS:	lb/sec	kg/sec
Compressor inlet	9.9343	4.5052
Compressor bleed		
Seal leakage	0.059	0.027
Ejector flow	0.117	0.053
Total bleed	0.176	0.080
MASS	lb	kg
Rotating group	126	57.1
Total TAC mass	550	249.4

*Cavity pressure = 40 psia (276 kN/m^2 abs)



TAC-F LAYOUT

FIGURE 7

TABLE 8

TAC-F PERFORMANCE SUMMARY		
EFFICIENCIES:		
Cycle efficiency at 160 kw_e	0.266	
Turbine efficiency	0.908	
Compressor efficiency	0.860	
Alternator efficiency	0.942	
SHAFT POWER LOSSES, KW:		
Alternator windage*	7.71	
Alternator cavity seals	1.89	
Bearings		
Thrust	1.86	
Journal	0.78	
Bearing compartment (Seals, churning losses)	6.63	
TOTAL LOSSES	18.87	
MASS FLOWS:	lb/sec	kg/sec
Compressor inlet	10.9642	4.9723
Compressor bleed		
Seal leakage	0.132	0.060
Ejector flow	0.374	0.170
Total bleed	0.506	0.230
MASS	lb	kg
Rotating group	132	59.9
Total TAC mass	570	258.5

*Cavity pressure = 56 psia (386 kN/m^2 abs)

2.7 Part Power Performance

TAC hardware designed in Phase I was analyzed at part load conditions ranging from 40 kw_e output to the design value of 160 kw_e. The analysis was performed using the computer capability described below:

An existing computer program is used to perform detailed off-design performance calculations. The off-design program was written to permit investigation of the performance of fixed hardware in a power system subjected to conditions differing from those prescribed by the reference cycle. Any of the key cycle design parameters may be varied. In the present form of the program, the aerodynamic and thermodynamic design values are input along with the geometry of the turbomachinery and heat exchangers. The general method of solution is iterative convergence of aerodynamic component matching, system heat transfer, system pressure drop and alternator performance.

The options presently available for treatment of the heat sink heat exchanger include:

(a) Assume constant compressor inlet temperature (i.e., assume heat rejection loop controls are designed to modulate coolant flow or temperature so as to hold compressor inlet temperature constant).

(b) Compressor inlet temperature can be arbitrarily varied.

(c) Assume coolant flow rate and inlet temperature are constant. This results in calculation of the heat sink, heat-exchanger off-design performance.

(d) Assume coolant flow rate constant and constant radiator area.

Likewise there are several options for treatment of the heat source heat exchanger. These are:

(a) Assume constant turbine inlet temperature

(b) Assume constant thermal heat flux

(c) Assume constant liquid inlet temperature

(d) Assume constant liquid flow rate

The calculation for the recuperator allows either fixed performance or a calculated off-design effectiveness and pressure drop.

The compressor performance is handled using a generalized map for radial compressors which is scaled to meet the compressor design conditions. A Reynolds number correlation is included to adjust efficiency at off-design conditions.

The turbine performance is predicted using the analytical technique of Jansen and Quale.[1] The turbine performance is then adjusted to meet the design conditions and corrected for Reynolds number effects.

The performance of the heat exchangers (operating in an off-design condition) is computed using the input geometries of each in conjunction with empirical data for heat transfer and pressure drop (f and j curves) for the core configurations involved.

The effect of variations in alternator performance in an off-design power condition may also be considered.

[1]Jansen, W. and E.B. Quale, "A Rapid Method for Predicting the Off-Design Performance of Radial-Inflow Turbines", ASME 67-WA/GT-3.

The program allows individual variation of the following parameters:

Rotating Speed

Compressor Inlet Temperature

Compressor Inlet Pressure

System Working Fluid

Turbine Inlet Temperature

Alternator Performance

Performance of All Heat Exchangers

Compressor Bleed Flow

Parasitic Losses

System Pressure Drop

Thermal Input Power

Radiator Area

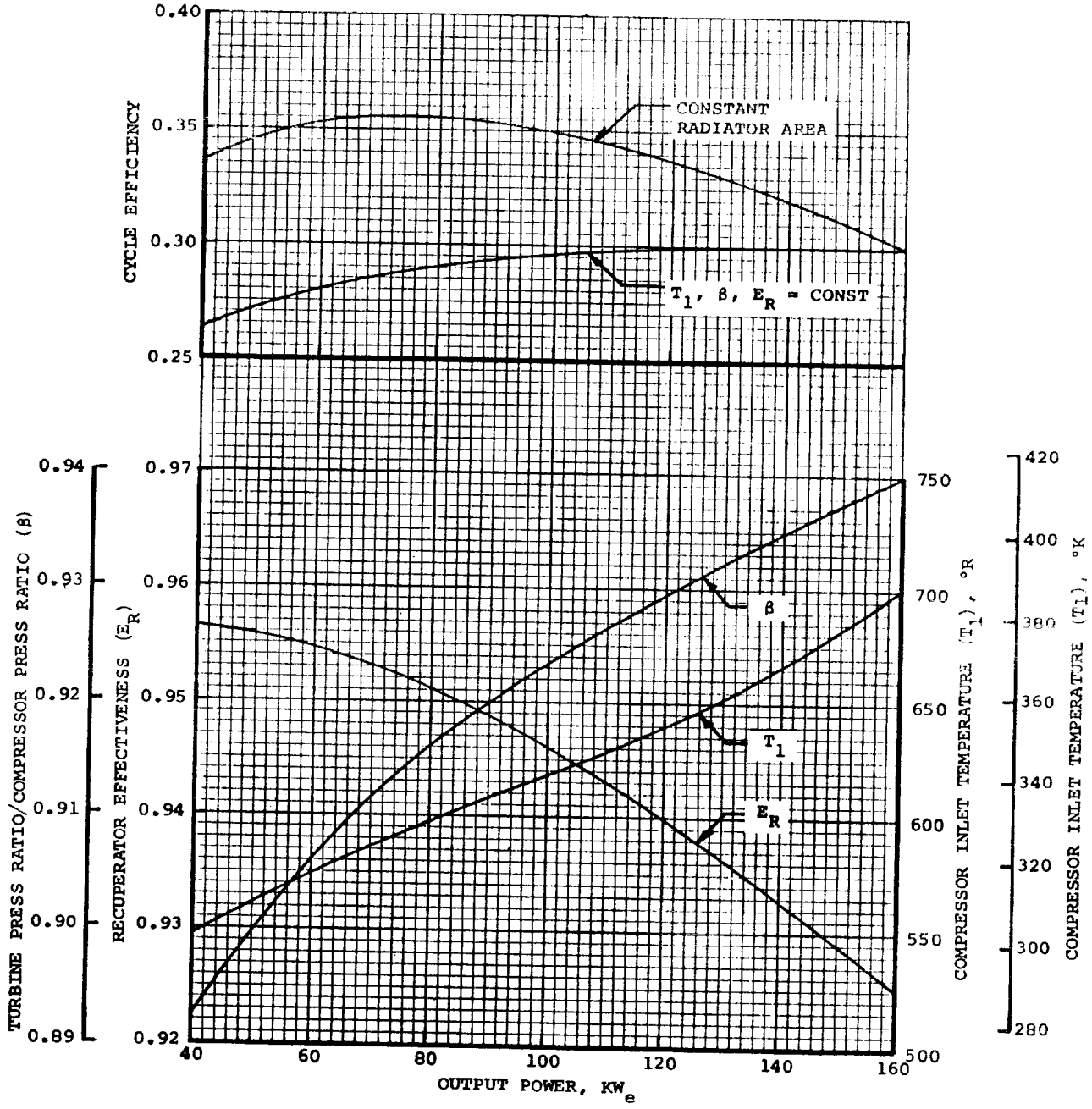
Heat Sink Coolant Flow and Temperature

Heat Source Coolant Flow and Temperature

Output Power Level

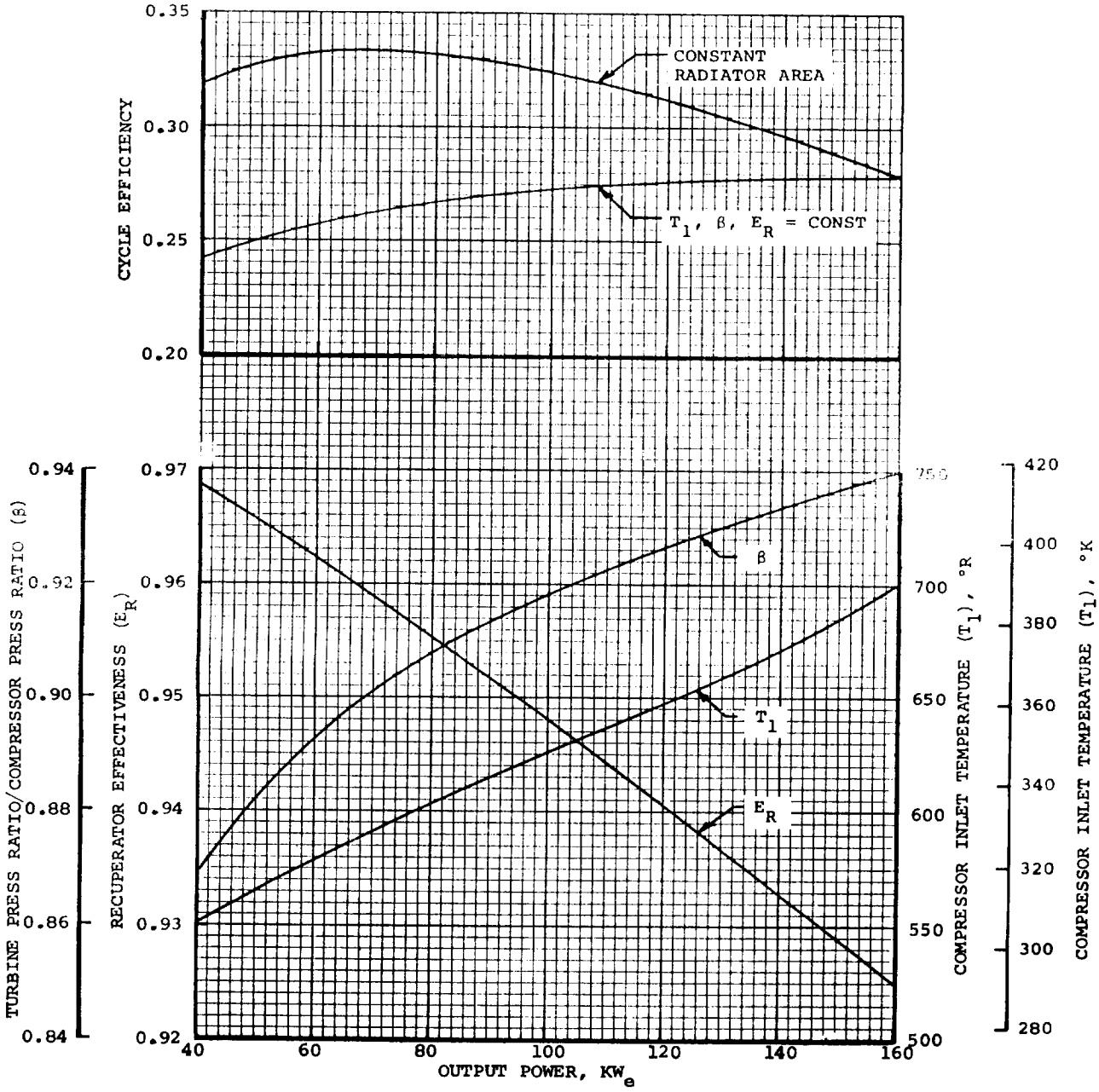
Having completed calculation of the performance of an off-design system, the program presents a comprehensive summary of the cycle performance at this condition. This summary includes the cycle efficiency, all system pressures and temperatures, parasitic losses and component efficiencies and effectivenesses.

The TAC Phase I hardware performance at part load conditions is depicted in Figures 8 and 9. These results are typical and do not necessarily represent any one of the final TAC configurations. Two conditions were considered for both the 24,000 and 36,000 rpm designs.



24,000 RPM TAC PART LOAD PERFORMANCE

FIGURE 8



36,000 RPM TAC PART LOAD PERFORMANCE

FIGURE 9

One calculation considers the case of fixed compressor inlet temperature, fixed recuperator effectiveness, and fixed system pressure loss. This case is intended to show the independent effect of the prediced turbomachinery efficiencies, alternator efficiency and the system parasitic losses. This condition is summarized by the one line in the upper portion of the two figures. The second case represents the performance of the system with a constant radiator geometry matched to the design point. All system parameters are computed for this case. As can be seen in Figures 8 and 9, the cycle efficiency at all part load conditions is higher than design. This effect is due, primarily, to the increase in Carnot efficiency associated within the declining compressor inlet temperature. Since the specific radiator area increases by a factor of four as the power is reduced to 40 kw_e, the tendency for cycle efficiency to increase is understandable. Also shown in Figures 8 and 9 is the off-design variation of compressor inlet temperature (T_1), system pressure loss (β), and recuperator effectiveness (E_R). The decrease of T_1 and increase of E_R combine to provide the initial rise in cycle efficiency as power is reduced. The increasing influence of system parasitic losses, increasing system pressure loss and decreasing turbomachinery and alternator efficiencies cause the cycle efficiency to peak and decline at low power levels.

2.8 TAC Configuration Comparisons

Table 9 shows the overall cycle efficiency and weight associated with each TAC configuration. Ranking in the table is in order of decreasing cycle efficiency. Both of the 24,000 rpm TAC units are clearly more efficient than any of the 36,000 rpm units, largely due to higher aerodynamic efficiency and to low parasite losses in the bearings. The major advantage of the 36,000 rpm units is lower weight.

Table 10 lists the potential development problems to be expected in the various TAC units. The gas bearing 24,000 rpm units appear to offer the fewest development problem areas. The alternator rotor

TABLE 9

TAC WEIGHT AND EFFICIENCY SUMMARY*

Configuration	Weight		Overall Cycle Efficiency	
	lb	kg		
24,000 rpm Radial Compressor Gas Bearing	800	363	0.309	TAC - A
24,000 rpm Axial Compressor Gas Bearing	850	386	0.308	TAC - B
36,000 rpm Radial Compressor Rolling Element Bearing	560	254	0.292	TAC - C
36,000 rpm Radial Compressor Fluid Film Bearing	550	250	0.283	TAC - E
36,000 rpm Axial Compressor Rolling Element Bearing	580	263	0.271	TAC - D
36,000 rpm Axial Compressor Fluid Film Bearing	570	259	0.266	TAC - F

*Ranked by cycle efficiency

TABLE 10

POTENTIAL DEVELOPMENT PROBLEM AREAS VARIOUS TAC CONFIGURATIONS

24,000 RPM GAS BEARING TAC UNITS

1. ALTERNATOR ROTOR FABRICATION
2. GAS BEARING/ROTOR SUSPENSION SYSTEM
   - A. Aerodynamic Thrust Load Balancing*
   - B. Thrust Bearing/Gimbal Stability (Dampers, Inertial Properties, Spring Rates)*
   - C. Shock and Vibration (Rub Tolerance)

*Denotes Critical Problem Areas

36,000 RPM TAC UNITS ON OIL/MIST BEARINGS AND OIL FILM BEARINGS

1. ALTERNATOR ROTOR MATERIAL PROPERTIES AND FABRICATION TECHNIQUES*
2. BEARING/ROTOR SUSPENSION SYSTEM
   - A. Aerodynamic Thrust Load Balancing (Critical for Life of Oil/Mist Bearings)
   - B. Life Improvement Required for Rolling Elements
3. LUBRICATION SYSTEMS
   - A. Compartment Seals (Gas Lift-Off, Pumping Oil Lift-Off)*
   - B. Absorber (Oil Film Bearings, Oil/Mist Bearing System)*
   - C. Oil/Gas Separator (Oil Film Bearings)*
   - D. Lubricant
   - E. Lubricant Contamination in Refractory Systems (Future)*
   - F. Transient Operation, Startup, Shutdown*
4. ALTERNATOR CAVITY WINDAGE REDUCTION DEVICE (EJECTOR)
5. ALTERNATOR CAVITY ISOLATION SEALS (GAS LIFT-OFF)

fabrication problems to be expected with the 24,000 rpm units are much less severe than with the 36,000 rpm units. The tie-bolt hole would have to be eliminated in the 36,000 rpm design. Additional background technology development would be required on the 36,000 rpm rotor before embarking on actual alternator fabrication.

The gas bearing/rotor suspension system appears as the only major development area for the 24,000 rpm TAC units. Aerodynamic thrust load balancing will be required to assure that the gas thrust bearing will not be overloaded. The techniques and methods needed to achieve good thrust balance are known and understood but some hardware modifications may well be required before this goal is adequately met.

The gas thrust bearing and gimbal will be more critical than the journal bearings. The large size [approximately 8.0 inches (20.3 cm)] of the thrust runner will present problems in controlling runout and distortion. It is probable that damping and liquid cooling will be required in the thrust bearing. Designing the bearings to be tolerant of momentary rubs due to shock or vibration loading will probably require coating of the bearing surfaces.

The major problems in the 36,000 rpm rotor suspension and lubrication systems involve several items as shown in Table 10. The most formidable of these problems involve sealing of oil from the gas loop. Both types of seals, gas lift-off and oil lift-off seals, have been demonstrated for short times but more development may be required for the long operating life required for TAC. Transient operation, start-up, and shutdown will also complicate the requirements of zero oil leakage in these systems. By contrast, the 24,000 rpm gas bearing units require only simple labyrinth seals and leakage causes only small system performance penalties.

Cavity pressure reduction systems are required for the 36,000 rpm machines. Ejectors will be used and do not appear to offer serious development problems.

Gas lift-off seals are required to isolate the alternator cavity in the 36,000 rpm units. These seals would be developed along with those used for bearing compartment sealing. The only significant difference in these seals is a larger diameter and probable higher operating temperature.

Conclusion

TAC-A with radial compressor and gas bearings and operating at 24,000 rpm appears to have the fewest development problems and offers the highest cycle efficiency of any of the TAC units. It is therefore recommended as the first choice as the final TAC configuration. NASA selected the TAC-A configuration.

3. TAC PHASE II SUMMARY

During Phase II the performance of one selected Phase I TAC configuration was analysed to determine its performance when operated under new cycle conditions with both higher and lower turbine inlet temperature conditions and one case with Krypton (molecular weight = 83.8) as the working fluid.

The performance of the Phase I hardware operating "off design" at these new conditions was compared with new TAC hardware specifically designed for each of the new cycle conditions. The Phase I TAC unit selected by AiResearch for study at these off design conditions was the 24,000-rpm radial compressor gas bearing unit, TAC-A. The NASA project manager approved the selection of TAC-A for this study.

In summary, the Phase I TAC hardware (i.e. TAC-A) would operate with good efficiency at both the SNAP-8 reactor temperatures and the high temperature conditions. For SNAP-8 conditions, the Phase I hardware would result in about 2 percent lower (0.254 vs 0.274) cycle efficiency than a TAC unit specifically designed for that application. The Phase I hardware (with a TZM turbine wheel and T111 turbine housing) would also perform well at 2560°R (1422°K) turbine inlet temperature. In this case cycle efficiency was slightly higher (0.387 vs 0.382) than the NASA selected high temperature design point system.

Table 11 summarizes the results of this design variation study. In this table each horizontal line of data is all for a fixed hardware TAC unit designed for the conditions marked (__ __ __ __ __). Hardware designed for either the original TAC conditions, or the new SNAP-8 conditions will perform well over the entire range of turbine inlet conditions shown.

TABLE 11

SUMMARY OF DESIGN VARIATIONS

Design Turbine Inlet Temp		Turbine Tip Speed		Snap 8 Reactor Conditions (600 kw_t) T_6 = 1610°R (894°K) T_1 = 580°R (322°K)					Original TAC Conditions (160 kw_e) T_6 = 2060°R (1144°K) T_1 = 700°R (389°K)				High Temperature Conditions (160 kw_e) T_6 = 2560°R (1422°K) T_1 = 691°R (384°K)			
°R	°K	ft/sec	m/sec	Power, kw_e	η_c, %	SRA, ft^2/kw_e	SRA, m^2/kw_e	r_c	η_c, %	SRA, ft^2/kw_e	SRA, m^2/kw_e	r_c	η_c, %	SRA, ft^2/kw_e	SRA, m^2/kw_e	r_c
1610	894	1019	311	164.3	27.4	53.93	5.01	1.9	29.9	19.70	1.83	1.73	37.6	13.63	1.27	1.75
2060	1144	1152	351	152.3	25.4	56.43	5.24	2.11	30.1	18.48	1.72	1.9	38.7	12.24	1.14	1.93
2560	1422	1418	432	89.5	14.9	102.2	9.49	2.42	24.9	22.67	2.11	2.15	38.2	11.90	1.11	2.2

NOTE: Design conditions marked ⌊— — —⌋

η_{gen} = 0.926 Cooler, E_c = 0.95 Thermal capacity ratio (liquid/gas) = 1.15

T_{sink} = 450°R (250°K) Recuperator E_R = 0.925 Prime to actual radiator area ratio = 0.746

ϵ_{rad} = 0.9 r_t r_c = 0.94

3.1 Design Variation Discussion

Tables 12, 13, 14 and 15 are computer printouts from the AiResearch Brayton cycle system design program and represent the four design points of interest for this Phase II study. These are:

Table 12 - Original TAC-A system, T_6 = 2060°R (114°K), 160 kw_e

Table 13 - SNAP-8 TAC system, T_6 = 1610°R (894°K), 600 kw_t input

Table 14 - High temperature system, T_6 = 2560°R (1422°K), 160 kw_e

Table 15 - Krypton system, T_6 = 2060°R (1144°K), 160 kw_e

For all these cases bearing losses were held constant at 3.5 kw and the 7.5 in. (19.05 cm) TAC-A Lundell alternator was assumed for windage loss calculations. An alternator electrical efficiency of 0.926 was used throughout. The TAC-A performance at its design point is not precisely identical to that shown in the Phase I summary since this study was conducted in parallel with Phase I in order to present Phase I and II results at the same time as requested by NASA.

The design point TAC hardware defined in Tables 12, 13, and 14 were subsequently analyzed individually to determine how each set of TAC hardware would operate under different turbine inlet temperature conditions. Figures 10, 11, and 12 represent the 2060°R (1144°K) TAC hardware, 1610°R (894°K) TAC hardware, and the 2560°R (1422°K) TAC hardware operating at turbine inlet conditions ranging from 1610 to 2560°R (894 to 1422°K) with three different cycle temperature ratios (0.36, 0.34, and 0.27). Cycle efficiency, compressor pressure ratio, and compressor inlet pressure are all shown in the figures with the system output power held constant at 160 kw_e. These calculations presume that heat exchangers are provided to hold the temperatures indicated and to hold recuperator effectiveness constant at 0.925. The system pressure losses are held constant at 6 percent. Both 1610°R (894°K) hardware and 2060°R (1144°K) hardware (original TAC)

TABLE 12

TAC DESIGN FOR T_6 = 2060°R (1144°K)

03/31/70
12:35:38

GENERATOR OUTPUT (KW) 1.60000+002	GEN.ROTOR DIAMETER (IN.) 7.50000+000	GROSS SHAFT POW.OUT. (KW) 1.79129+002	GEN. WINDAGE LOSS (KW) 2.64233+000	CYCLE EFFICIENCY (----) 3.01013-001
RECUPERATOR EFFECT. (----) 9.25000-001	CRU ROTATION. SPEED (RPM) 2.40000+004	BLEED FLOW FRACTION (----) 2.00000-002	COMP.TOT.TEMP.RATIO (----) 1.33525+000	PRESS. LOSS FACTOR (PRT/PRC) 9.39997-001
COMP. ADIAB. EFF. (----) 8.70011-001	COMPR. ROTOR DIAM. (IN.) 9.42983+000	COMPR. PRESS. RATIO (----) 1.90000+000	REQD. SURFACE FINISH (MICRO IN.) 2.44733+001	COMPR. SPEC. SPEED (----) 1.04200-001
TURB. ADIAB. EFF. (----) 9.15382-001	TURB. ROTOR DIAM. (IN.) 1.10055+001	TURB. PRESS.RATIO (----) 1.78599+000	TURB. ROTOR TIP SPEED (FPS) 1.15250+003	TURB. SPEC. SPEED (----) 9.09121-002
COMPR. + TURB. WEIGHT (LB.) 6.27944+001	GEN. PER. REV. NO. (----) 2.32902+004	COMPR. MEAN SPEC.SP. (----) 7.01830+001	COMPR. EXPAN.EFF. (----) 8.87578-001	GEN. DISK REV. NO. (----) 1.24769+006
RADIATOR AREA (SQ FEET) 2.95639+003	RAD CLNT TEMP IN (DEGREES RANKINE) 6.84747+002	RAD CLNT TEMP OUT (DEGREES RANKINE) 9.36885+002	SINK TEMP (DEGREES RANKINE) 4.50000+002	COOLER EFF (----) 9.50000-001
SPEC RAD AREA (SQ FT/KW) 1.84775+001	BEARING LOSS = 3.5 KW			

COMPONENT	FLOW (LB/SEC)	INLET TEMP. (R)	INLET PRESS. (PSIA)	OUTLET TEMP. (R)	OUTLET PRESS. (PSIA)
COMPRESSOR	9.28244+000	7.03000+002	4.99884+001	9.34676+002	9.49779+001
RECUPERATOR	9.09679+000	9.34676+002	9.46930+001	1.61472+003	9.44089+001
HEATER	9.09679+000	1.61472+003	9.44089+001	2.06000+003	9.22932+001
TURBINE	9.09679+000	2.06000+003	9.22932+001	1.66986+003	5.16761+001
RECUPERATOR	9.09679+000	1.66986+003	5.16761+001	9.99815+002	5.09009+001
COOLER	9.28244+000	9.88712+002	5.09009+001	7.00000+002	5.02901+001

TABLE 13

TAC DESIGN FOR T_6 = 1610°R (894°K)

04/20/70
19:23:06

GENERATOR OUTPUT (KW) 1.64422+002	GEN.ROTOR DIAMETER (IN.) 7.50000+000	GROSS SHAFT POW.OUT. (KW) 1.84741+002	GEN. WINDAGE LOSS (KW) 3.67941+000	CYCLE EFFICIENCY (----) 2.74043-001
RECUPERATOR EFFECT. (----) 9.25000-001	CRU ROTATION. SPEED (RPM) 2.40000+004	BLEED FLOW FRACTION (----) 2.00000-002	COMP.TCT.TEMP.RATIO (----) 1.33645+000	PRESS. LOSS FACTOR (PRT/PRC) 9.39997-001
COMP. ADIAB. EFF. (----) 8.70000-001	COMPR. ROTOR DIAM. (IN.) 8.59891+000	COMPR. PRESS. RATIO (----) 1.90000+000	REQD. SURFACE FINISH (MICRO IN.) 1.36184+001	COMPR. SPEC. SPEED (----) 1.11178-001
TURB. ADIAB. EFF. (----) 9.16000-001	TURB. ROTOR DIAM. (IN.) 9.72949+000	TURB. PRESS.RATIO (----) 1.78599+000	TURB. ROTOR TIP SPEED (FPS) 1.01887+003	TURB. SPEC. SPEED (----) 9.79393-002
COMPR. + TURB. WEIGHT (LB.) 4.58143+001	GEN. PER. REY. NO. (----) 3.30794+004	COMPR. MEAN SPEC.SP. (----) 7.43351+001	COMPR. EXPAN.EFF. (----) 8.87433-001	GEN. DISK REY. NO. (----) 1.77211+006
RADIATOR AREA (SQ FEET) 8.87417+003	RAD CLNT TEMP IN (DEGREES RANKINE) 5.67638+002	RAD CLNT TEMP OUT (DEGREES RANKINE) 7.71976+002	SINK TEMP (DEGREES RANKINE) 4.50000+002	COOLER EFF (----) 9.50000-001
SPEC RAD AREA (SQ FT/KW) 5.39719+001	BEARING LOSS = 3.5 KW			

COMPONENT	FLOW (LB/SEC)	INLET TEMP. (R)	INLET PRESS. (PSIA)	OUTLET TEMP. (R)	OUTLET PRESS. (PSIA)
COMPRESSOR	1.35291+001	5.80000+002	7.10000+001	7.75141+002	1.34900+002
RECUPERATOR	1.32585+001	7.75141+002	1.34495+002	1.26515+003	1.34092+002
HEATER	1.32585+001	1.26515+003	1.34092+002	1.61000+003	1.31087+002
TURBINE	1.32585+001	1.61000+003	1.31087+002	1.30488+003	7.33971+001
RECUPERATOR	1.32585+001	1.30488+003	7.33971+001	8.14871+002	7.22961+001
COOLER	1.35291+001	8.14076+002	7.22961+001	5.80000+002	7.14286+001

TABLE 14

TAC DESIGN FOR T_6 = 2560°R (1422°K)

03/31/70
12:36:26

GENERATOR OUTPUT (KW) 1.60000+002	GEN.ROTOR DIAMETER (IN.) 7.50000+000	GROSS SHAFT POW.OUT (KW) 1.77697+002	GEN. WINDAGE LOSS (KW) 1.41040+000	CYCLE EFFICIENCY (----) 3.82284-001
RECUPERATOR EFFECT. (----) 9.25000-001	CRU ROTATION. SPEED (RPM) 2.40000+004	BLEED FLOW FRACTION (----) 2.00000-002	COMP.TOT.TEMP.RATIO (----) 1.42911+000	PRESS. LOSS FACTOR (PRT/PRC) 9.39997-001
COMP. ADIAB. EFF. (----) 8.61210-001	COMPR. ROTOR DIAM. (IN.) 1.05997+001	COMPR. PRESS. RATIO (----) 2.20000+000	REQD. SURFACE FINISH (MICRO IN.) 5.48587+001	COMPR. SPEC. SPEED (----) 1.04200-001
TURB. ADIAB. EFF. (----) 9.01793-001	TURB. ROTOR DIAM. (IN.) 1.35409+001	TURB. PRESS.RATIO (----) 2.06799+000	TURB. ROTOR TIP SPEED (FPS) 1.41801+003	TURB. SPEC. SPEED (----) 8.63049-002
COMPR. + TURB. WEIGHT (LB.) 1.06852+002	GEN. PER. REY. NO. (----) 8.78370+003	COMPR. MEAN SPEC.SP. (----) 6.82926+001	COMPR. EXPAN.EFF. (----) 8.87554-001	GEN. DISK REY. NO. (----) 4.70555+005
RADIATOR AREA (SQ FEET) 1.90374+003	RAD CLNT TEMP IN (DEGREES RANKINE) 6.71483+002	RAD CLNT TEMP OUT (DEGREES RANKINE) 9.94093+002	SINK TEMP (DEGREES RANKINE) 4.50000+002	COOLER EFF (----) 9.50000-001
SPEC RAD AREA (SQ FT/KW) 1.18984+001	BEARING LOSS = 3.5 KW			

COMPONENT	FLOW (LB/SEC)	INLET TEMP. (R)	INLET PRESS. (PSIA)	OUTLET TEMP. (R)	OUTLET PRESS. (PSIA)
COMPRESSOR	4.96016+000	6.91000+002	1.88513+001	9.87518+002	4.14729+001
RECUPERATOR	4.86095+000	9.87518+002	4.13485+001	1.90385+003	4.12245+001
HEATER	4.86095+000	1.90385+003	4.12245+001	2.56000+003	4.03006+001
TURBINE	4.86095+000	2.56000+003	4.03006+001	1.97815+003	1.94878+001
RECUPERATOR	4.86095+000	1.97815+003	1.94878+001	1.06182+003	1.91955+001
COOLER	4.96016+000	1.06033+003	1.91955+001	6.91000+002	1.89651+001

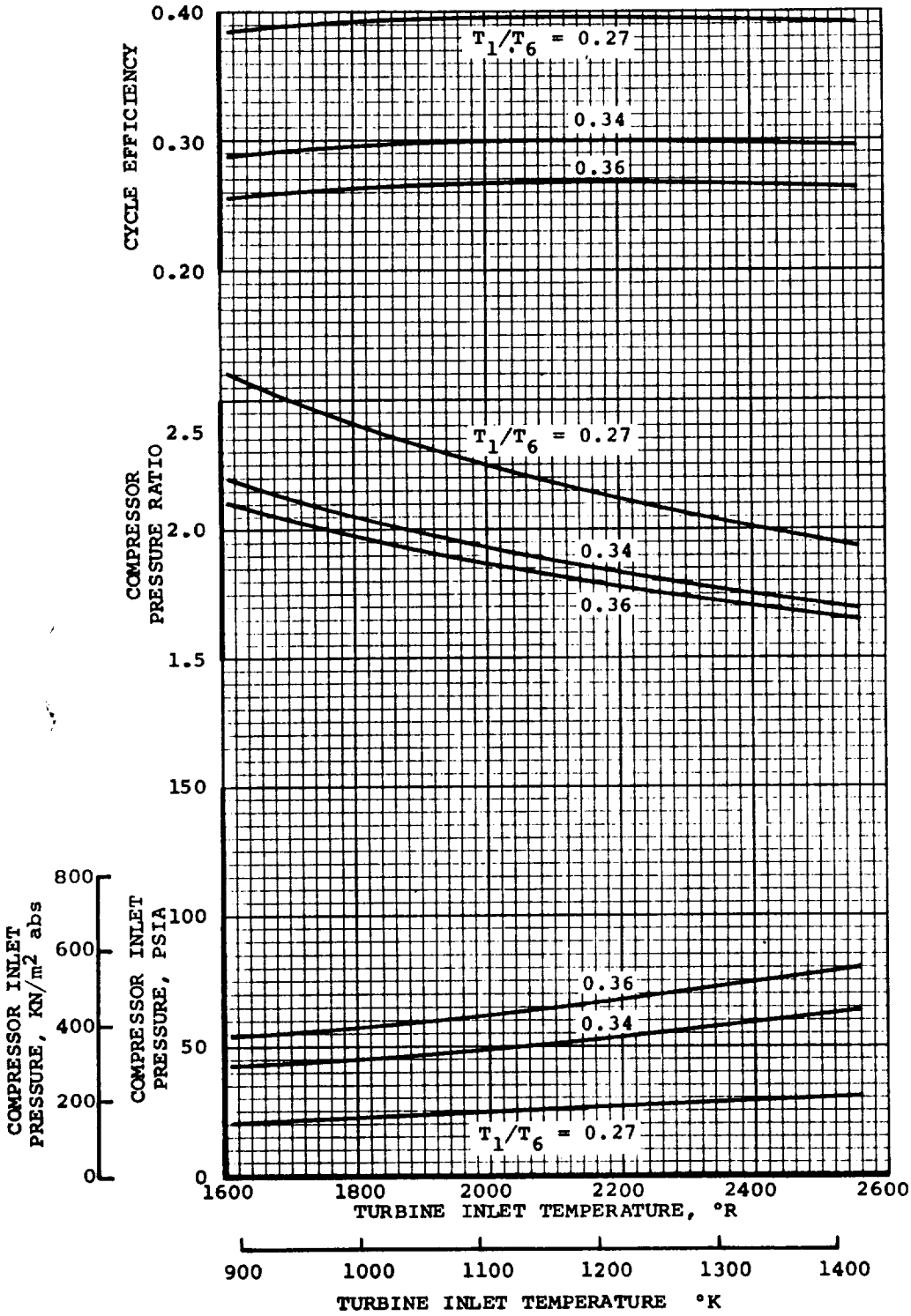
TABLE 15

TAC DESIGN FOR KRYPTON - T_6 = 2060°R (1144°K)

04/02/70
17:09:24

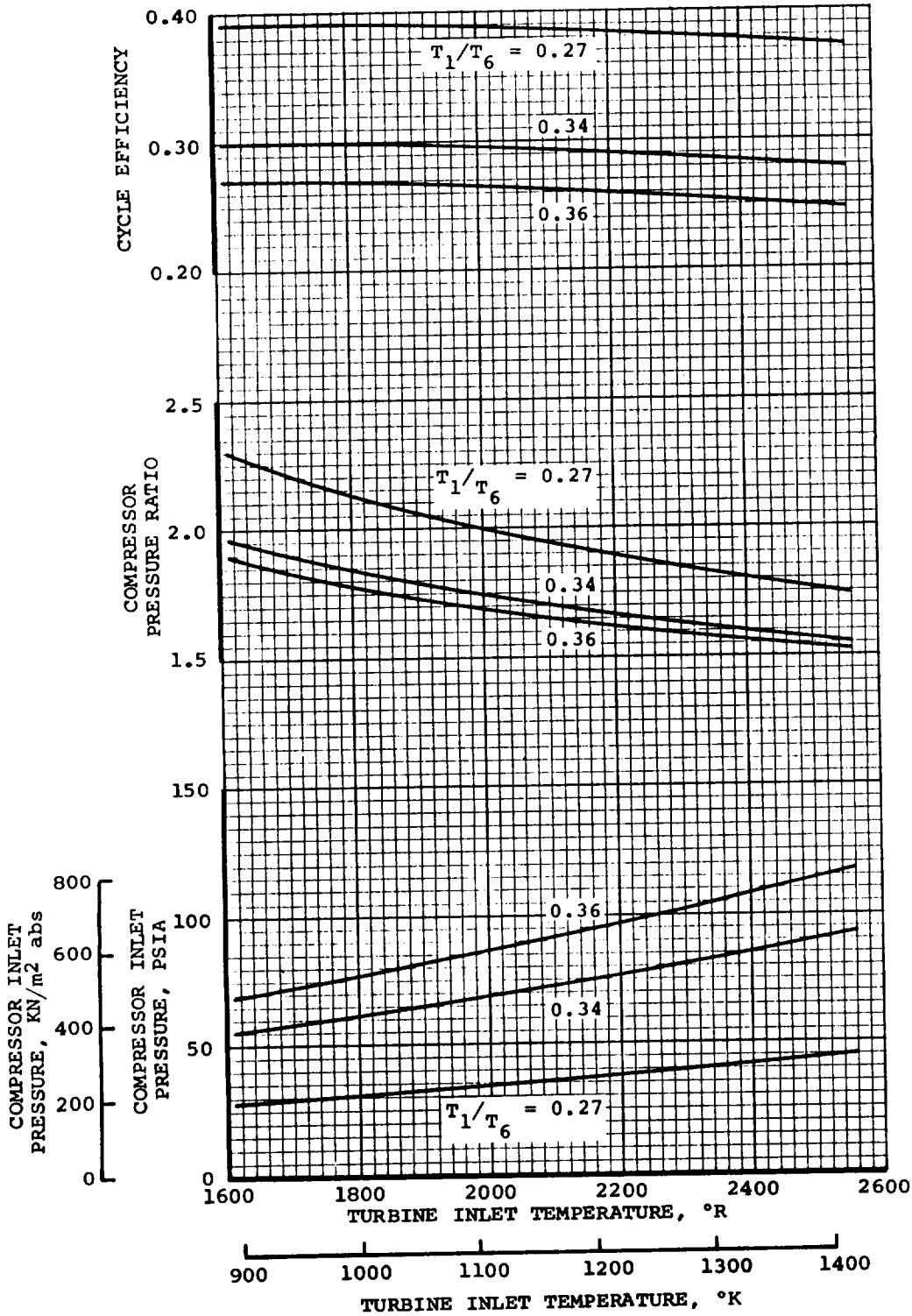
GENERATOR OUTPUT (KW) 1.60000+002	GEN.ROTOR DIAMETER (IN.) 7.50000+000	GROSS SHAFT POW.OUT. (KW) 1.87949+002	GEN. WINDAGE LOSS (KW) 1.16632+001	CYCLE EFFICIENCY (----) 2.81020-001
RECUPERATOR EFFECT. (----) 9.25000-001	CRU ROTATION. SPEED (RPM) 2.40000+004	BLEED FLOW FRACTION (----) 2.00000-002	COMP.TOT.TEMP.RATIO (----) 1.34031+000	PRESS. LOSS FACTOR (PRT/PRC) 9.39997-001
COMP. ADIAB. EFF. (----) 8.57920-001	COMPR. ROTOR DIAM. (IN.) 6.55958+000	COMPR. PRESS. RATIO (----) 1.90000+000	REQD. SURFACE FINISH (MICRO IN.) 5.08503+000	COMPR. SPEC. SPEED (----) 1.04200+001
TURB. ADIAB. EFF. (----) 9.16113-001	TURB. ROTOR DIAM. (IN.) 7.59829+000	TURB. PRESS.RATIO (----) 1.78599+000	TURB. ROTOR TIP SPEED (FPS) 7.95693+002	TURB. SPEC. SPEED (----) 9.10151-002
COMPR. + TURB. WEIGHT (LB.) 2.41180+001	GEN. PER. REY. NO. (----) 1.60525+005	COMPR. MEAN SPEC.SP. (----) 6.95459+001	COMPR. EXPAN.EFF. (----) 8.87576+001	GEN. DISK REY. NO. (----) 8.59957+006
RADIATOR AREA (SQ FEET) 3.18695+003	RAD CLNT TEMP IN (DEGREES RANKINE) 6.84575+002	RAD CLNT TEMP OUT (DEGREES RANKINE) 9.39547+002	SINK TEMP (DEGREES RANKINE) 4.50000+002	COOLER EFF (----) 9.50000-001
SPEC RAD AREA (SQ FT/KW) 1.99185+001	BEARING LOSS = 3.5 KW			

COMPONENT	FLOW (LB/SEC)	INLET TEMP. (R)	INLET PRESS. (PSIA)	OUTLET TEMP. (R)	OUTLET PRESS. (PSIA)
COMPRESSOR	2.08581+001	7.00000+002	1.62299+002	9.38220+002	3.08367+002
RECUPERATOR	2.04409+001	9.38220+002	3.07442+002	1.61472+003	3.06520+002
HEATER	2.04409+001	1.61472+003	3.06520+002	2.06000+003	2.99651+002
TURBINE	2.04409+001	2.06000+003	2.99651+002	1.66957+003	1.67778+002
RECUPERATOR	2.04409+001	1.66957+003	1.67778+002	9.93071+002	1.65261+002
COOLER	2.08581+001	9.91974+002	1.65261+002	7.00000+002	1.63278+002



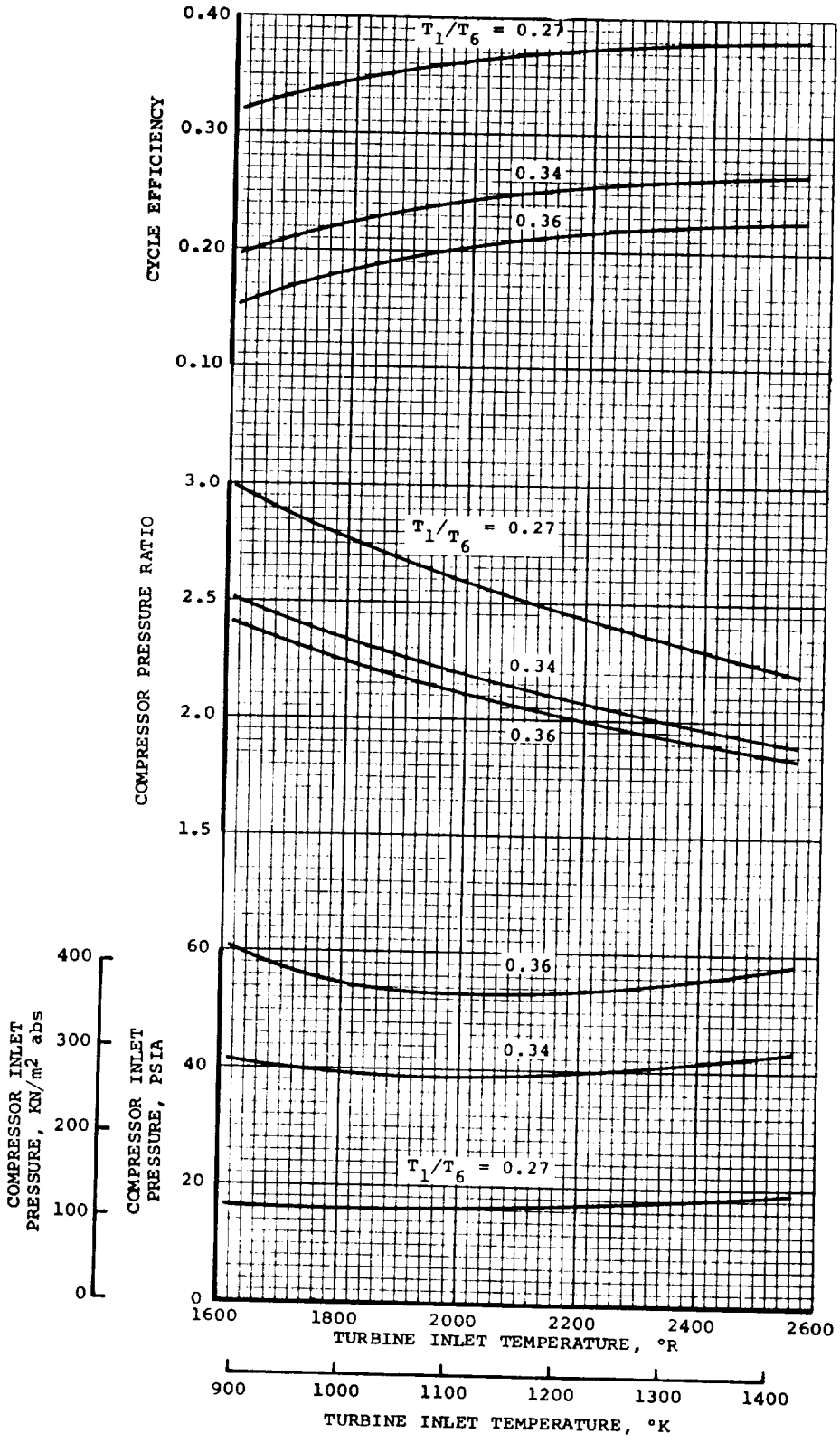
2060°R (1144°K) TAC OFF-DESIGN PERFORMANCE

FIGURE 10



1610°R (894°R) TAC OFF-DESIGN PERFORMANCE

FIGURE 11



2560°R (1422°K) TAC OFF-DESIGN PERFORMANCE

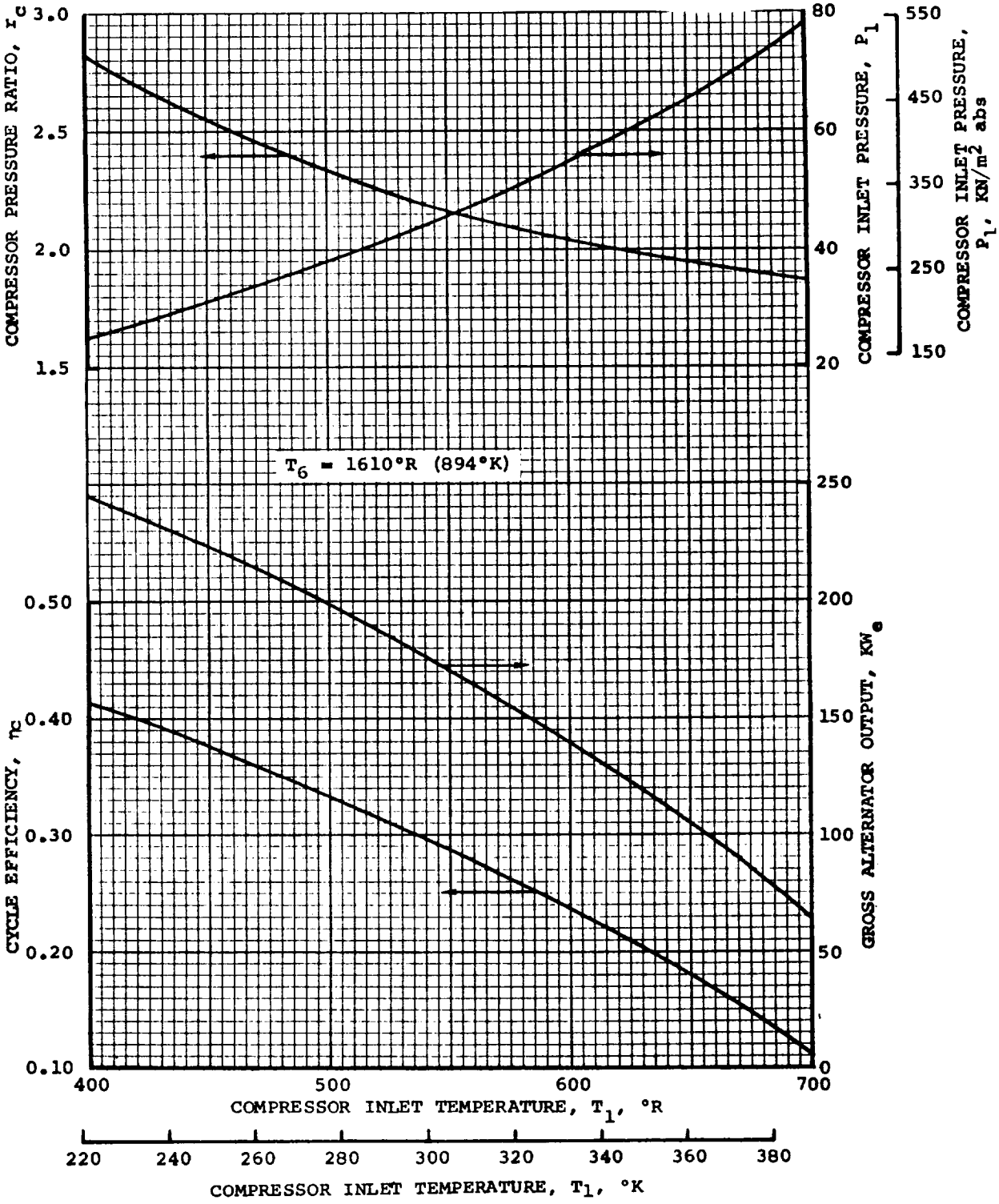
FIGURE 12

show only small variations in efficiency over the entire turbine inlet temperature range. The 2560°R (1422°K) system efficiency decreased at lower turbine inlet conditions due largely to a decrease in compressor efficiency caused by the high pressure ratios which result at off-design operation.

Figure 13 illustrates the performance of the 2060°R (1144°K) TAC-A operating at a SNAP-8 turbine inlet temperature of 1610°R (894°K) and the reactor limited to 600 kw_t output power.

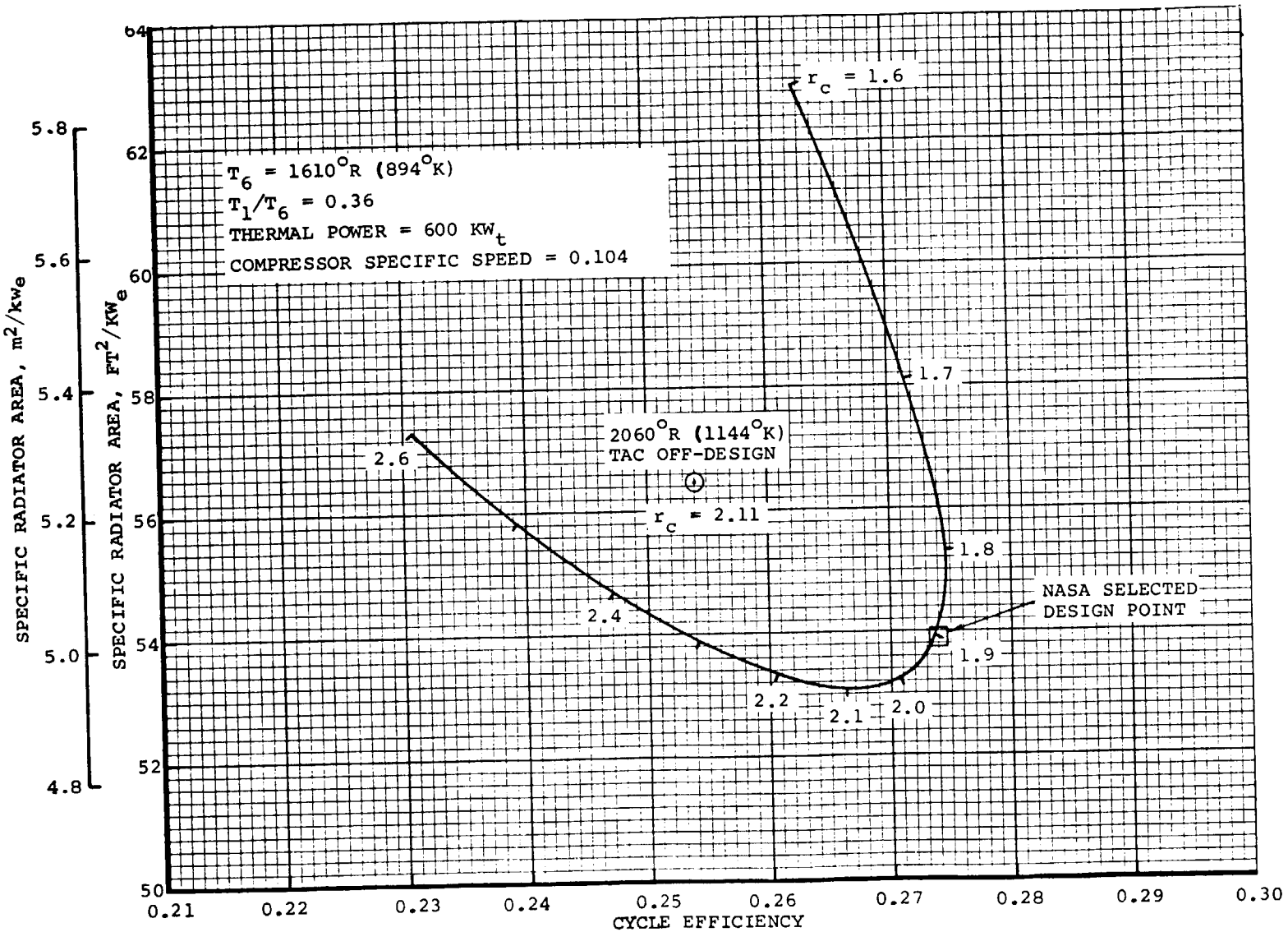
Figures 14, 15, and 16 are representative of the possible cycle efficiency-specific radiator area variations as a function of the selected compressor pressure ratio. These figures are presented for each of the cycles of interest. Also shown on each figure is the design value of pressure ratio selected and the off-design operating points of the two remaining alternative systems. Performance of the 2560°R (1422°K) TAC is not shown at 1610°R (894°K) since it is outside the scale.

Figure 17 shows the cycle efficiency of the 24,000 rpm TAC-A hardware when Krypton (MW = 83.8) is used as the working fluid. This data is presented as a function of shaft rotational speed to show why the cycle performance is so harshly degraded at design speed. At 16,600 rpm the system passes through its aerodynamic design match point speed and provides a cycle efficiency of about 30 percent (assuming the alternator performance can be maintained). As the rotor speed is increased toward the 24,000 rpm design value, the turbomachinery becomes badly mismatched and cycle efficiency degrades rapidly. As speed is increased to 24,000 rpm, Figure 17 shows the compressor pressure ratio is approaching 3.0 and the compressor is at 145 percent of the aerodynamic match point design speed. The TAC-A unit as designed appears incapable of delivering acceptable performance with this variation in working fluid molecular weight. If operation with Krypton is desired at 24,000 rpm the new aerodynamic components defined in Table 15 should be used.



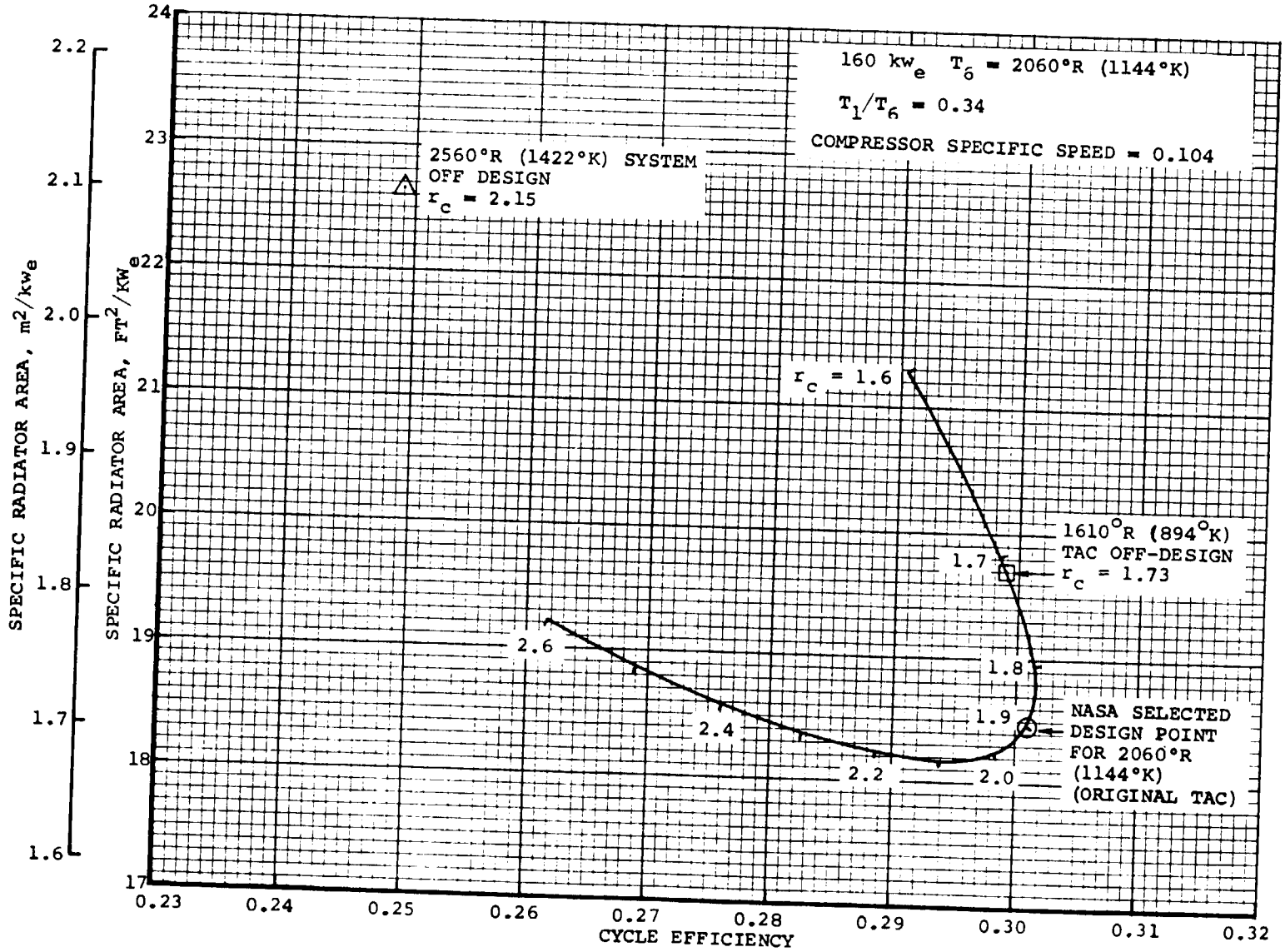
PERFORMANCE OF 2060°R (1144°K) TAC AT SNAP-8 REACTOR CONDITIONS (600 KW_t INPUT)

FIGURE 13



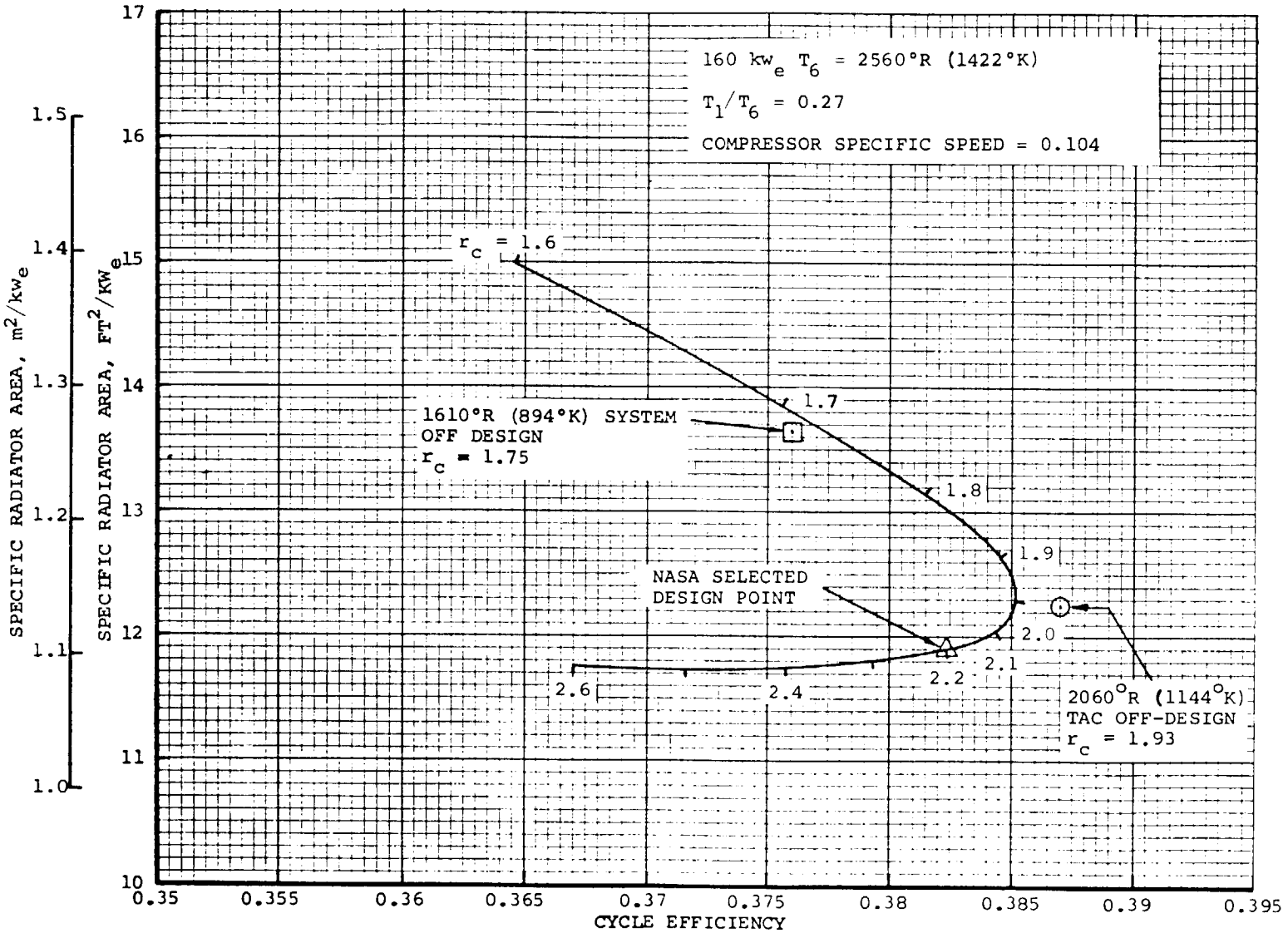
LOW TEMPERATURE CYCLES

FIGURE 14



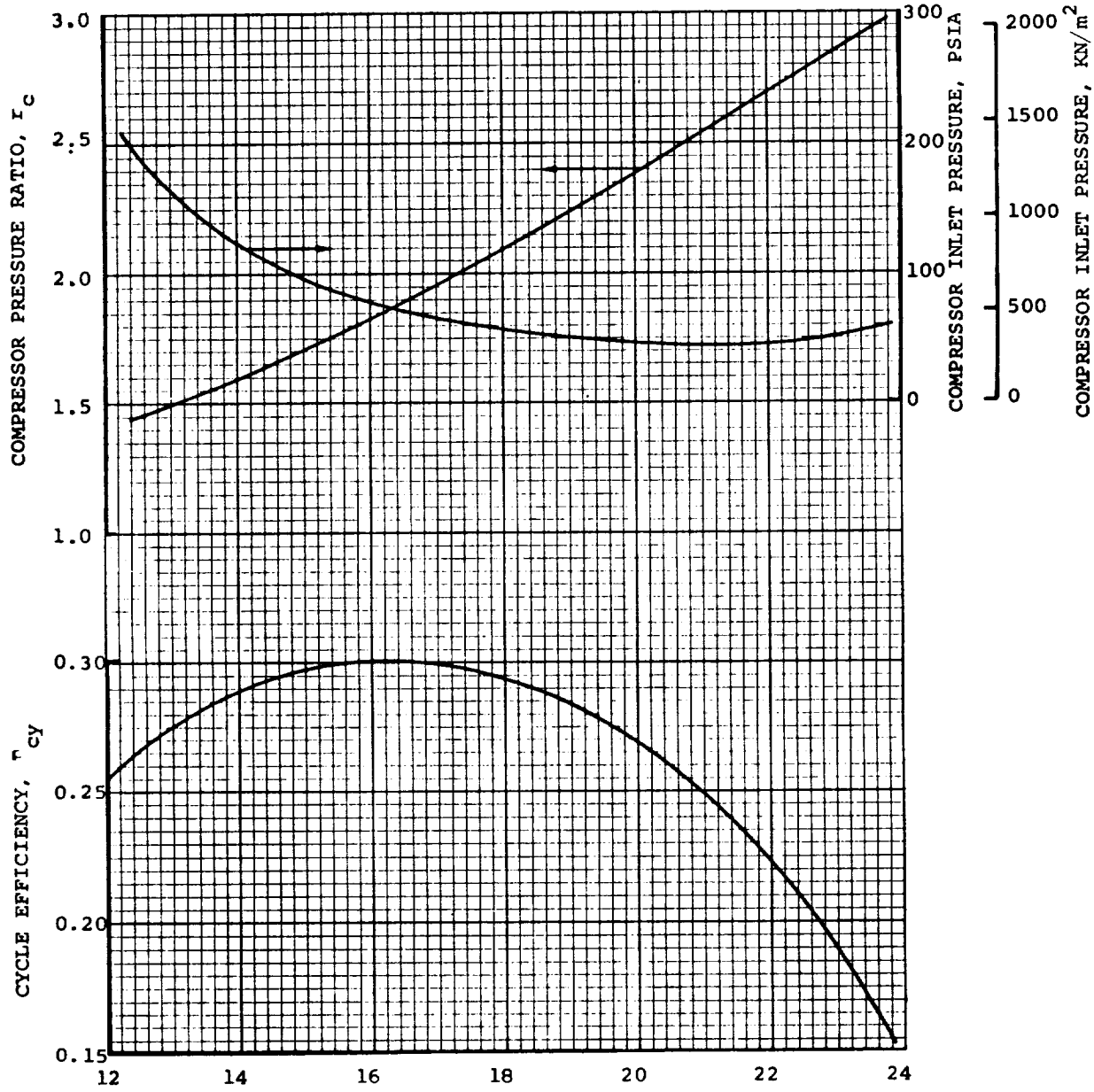
2060°R (1144°K) CYCLES

FIGURE 15



HIGH TEMPERATURE CYCLES

FIGURE 16



PERFORMANCE OF 2060°R (1144°K) TAC WITH KRYPTON WORKING FLUID (MW = 83.8) AS A FUNCTION OF SHAFT SPEED

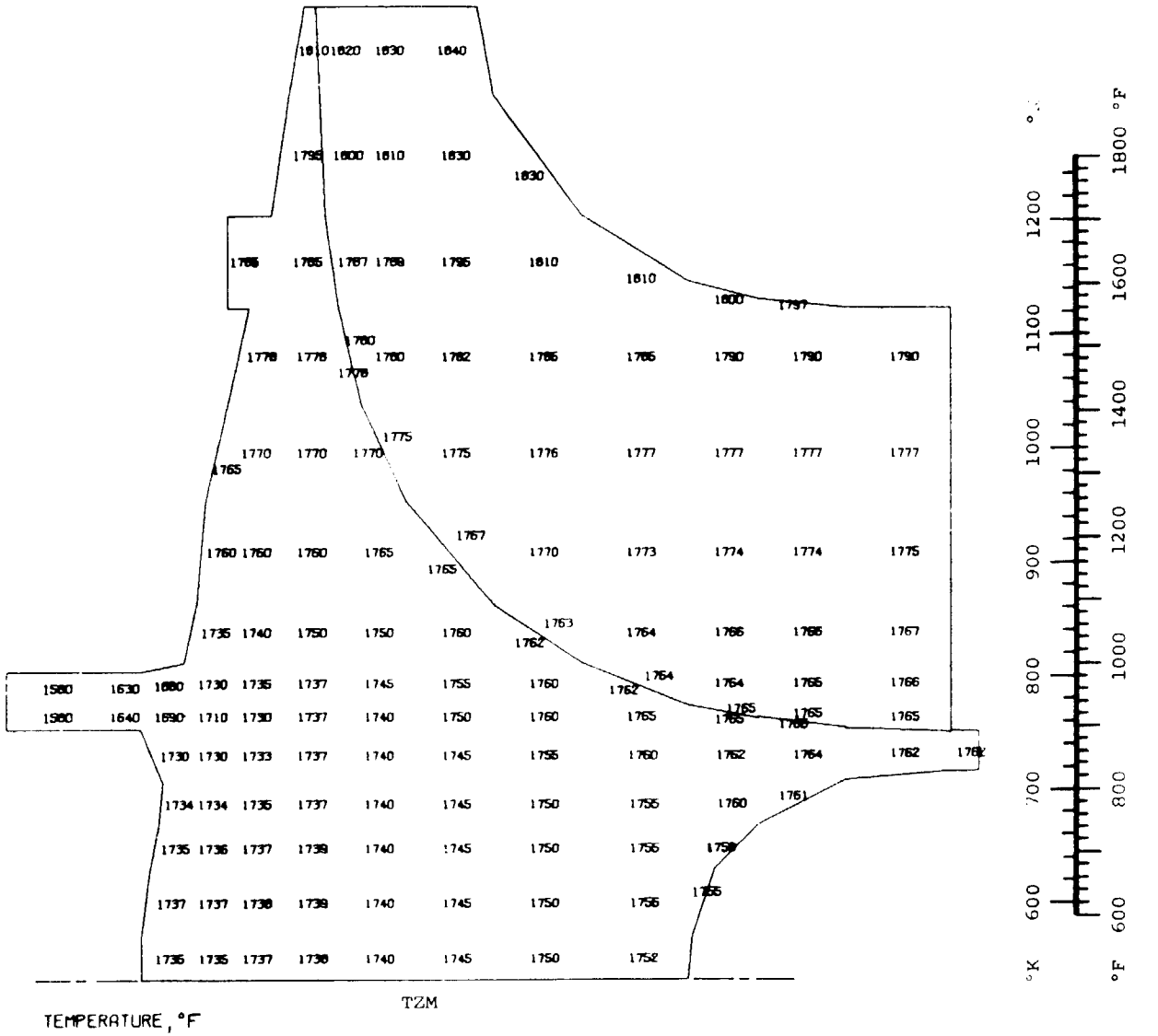
FIGURE 17

3.2 Operation of TAC-A at 2560°R

The original TAC-A-unit will use an INCO-713 cast turbine wheel for operation at 2060°R (1144°K) turbine inlet conditions. If operation at 2560°R (1422°K) turbine inlet is required, a refactory metal turbine wheel and turbine scroll would be necessary. A brief consultation with metallurgical specialists disclosed no obvious questions regarding the feasibility of direct substitution of refractory materials for the turbine scroll/nozzle assembly and the turbine wheel. T-111 should be readily fabricable into the configuration required for the scroll/nozzle assembly. Attachment of the T-111 scroll to the conventional material of the rear alternator support flange by the presently defined mechanical fasteners appears feasible but would obviously require analysis to determine the effects of differential thermal expansion. A bimetallic transition in the final weld seal closure (see Drawing of TAC-A, Figure 2) would be required.

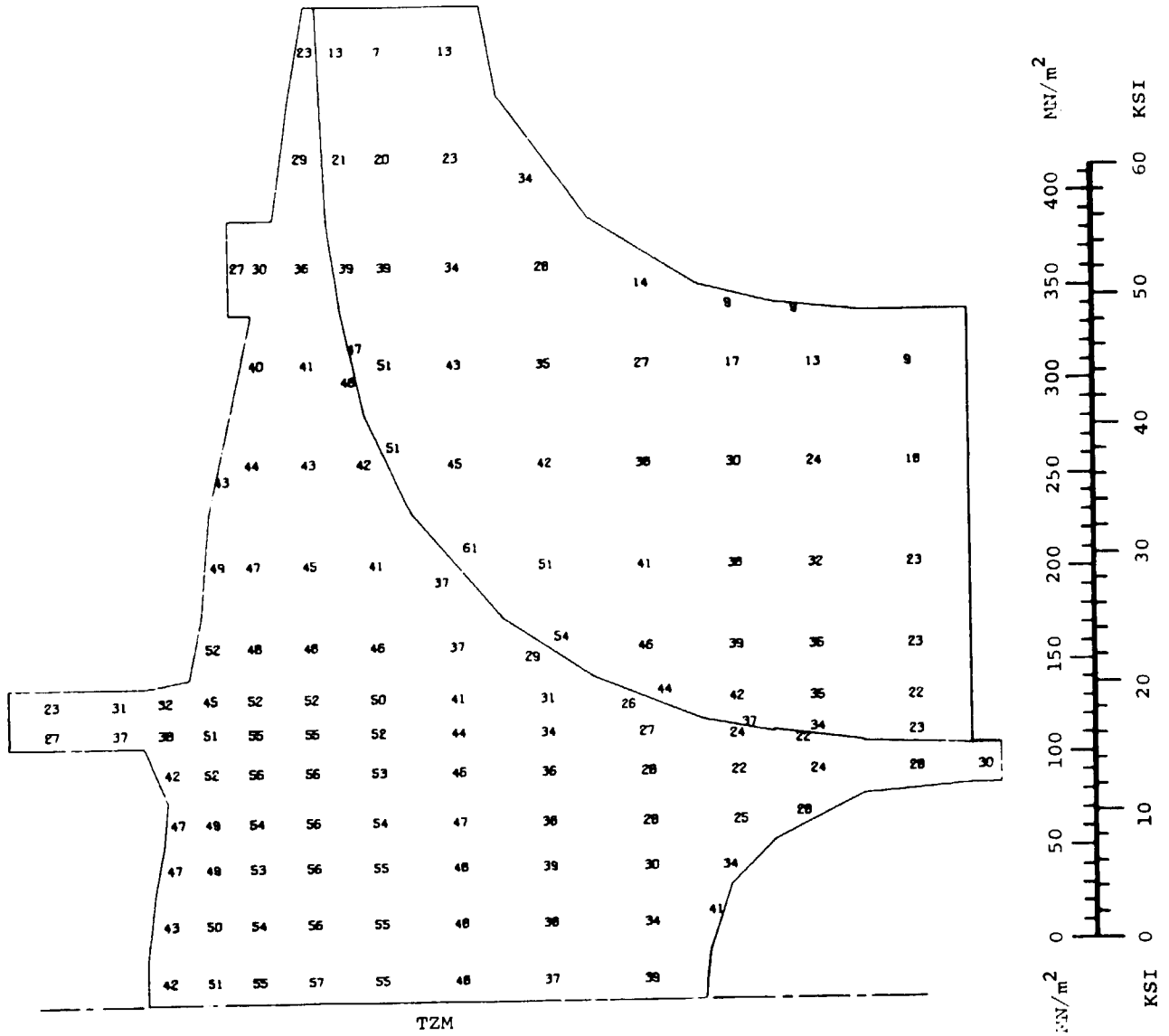
A complete thermal analysis of the TAC would be required to determine the temperatures and heat flows associated with 2560°R (1422°K) operation. In order to obtain some indication of the suitability of TZM to this turbine wheel application, a preliminary stress analysis was performed using the TAC-A wheel design. A finite element stress analysis was performed on the wheel at 24,000 rpm and at 29,000 rpm (120 percent speed). Temperatures were approximated using temperature scaling factors from previous designs. Figures 18 and 19 show the temperature and equivalent stress as computed for the wheel at 20 percent overspeed conditions.

Figure 20 compares the maximum stresses at each radial location in the wheel with 0.5 percent creep strength of KDTZM-1175 at the local metal temperature. A preliminary calculation indicated no measurable creep would occur at design speed for 50,000 hours. The wheel is also quite safe from a burst standpoint at 120 percent speed for short time operation. It appears that KTDZM is suitable for application

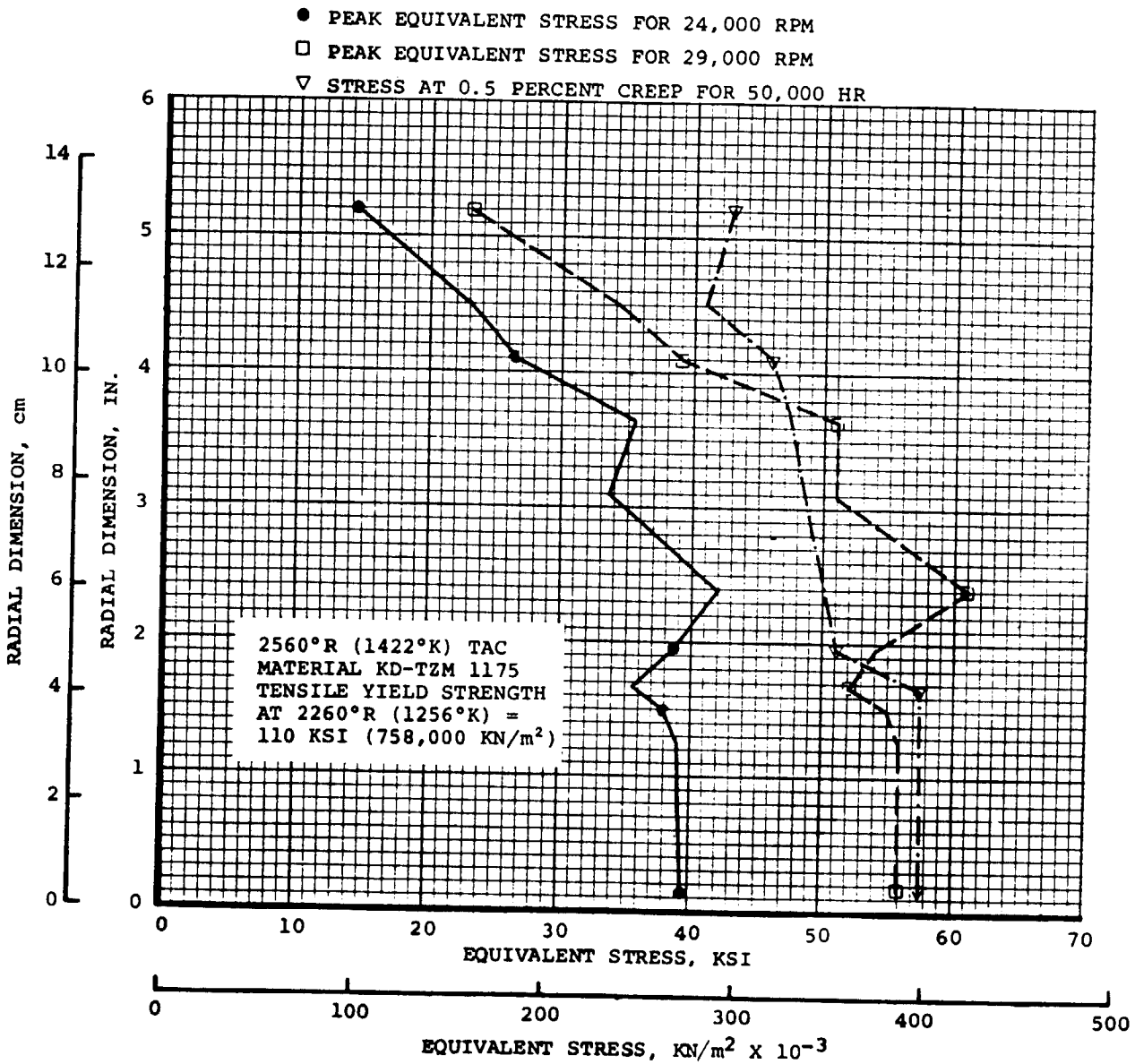


24,000 RPM HIGH TEMPERATURE TURBINE AT OVERSPEED AND OVERTEMPERATURE

FIGURE 18



24,000 RPM HIGH TEMPERATURE TURBINE AT OVERSPEED AND OVERTEMPERATURE

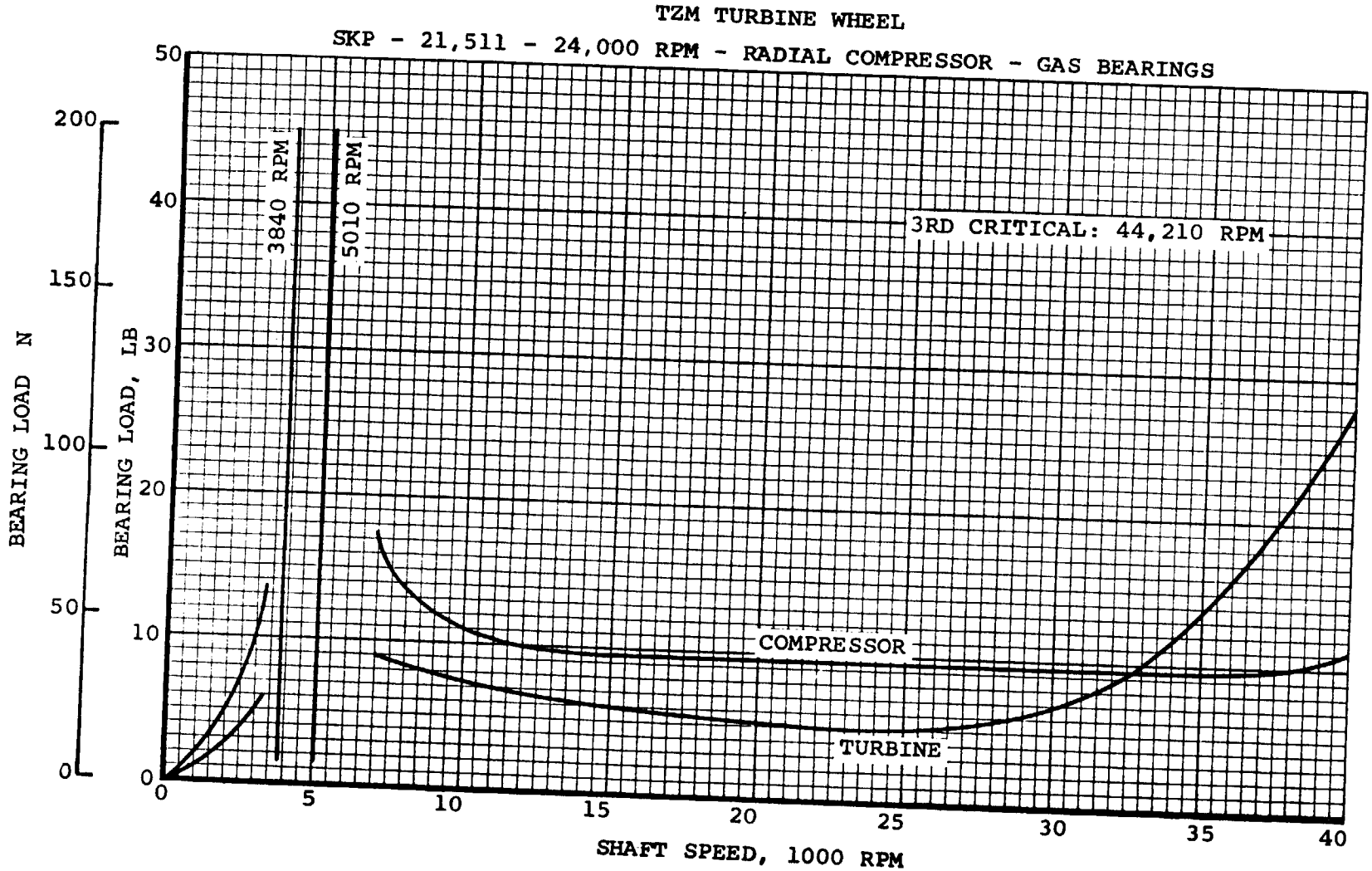


EQUIVALENT STRESS DISTRIBUTION VS RADIAL DIMENSION
TAC RADIAL TURBINE

FIGURE 20

ɔ a 2560°R (1422°K) TAC system with TAC-A hardware. It should be ɔted, however, that the NASA selected system for the 2560°R (1422°K) ase has a much higher turbine tip speed than does TAC-A (see Table 11) nd would present more difficult stress problems.

A substitution of TZM instead of INCO-713 was made in the critical peed analysis of the TAC-A rotating group. Figure 21 shows the esults of that analysis and indicates that the greater density of TZM ould not markedly increase shaft bending problems in TAC-A. Rotor ynamic performance with TZM turbine wheel appears satisfactory. esults of the rotor dynamics analysis of all the Phase I TAC machines s discussed in more detail in Section 5.5.



CRITICAL SPEEDS FOR TAC-A WITH TZM TURBINE

FIGURE 21

4. PHASE III SUMMARY

At the completion of Phases I and II NASA selected the TAC-A configuration, (i.e., 24000 rpm, radial compressor, gas bearings) for further evaluation during Phase III. Between Phase II and III NASA changed the TAC cycle state points to reflect a lower 1610°R (894°K) turbine inlet temperature consistant with the capabilities of the zirconium-hydride moderated SNAP-8 reactor. Figure 22 shows the cycle state points used in the Phase III studies.

During Phase I, 1200 Hz alternators were selected for all TAC configurations. NASA redirected the Phase III effort to evaluate the feasibility of a 400 Hz alternator. Table 16 shows a summary of the phase III specifications.

The major objectives of the abbreviated (2 month) Phase III TAC study were:

(a) Determine feasibility of a 400 Hz alternator version of TAC.

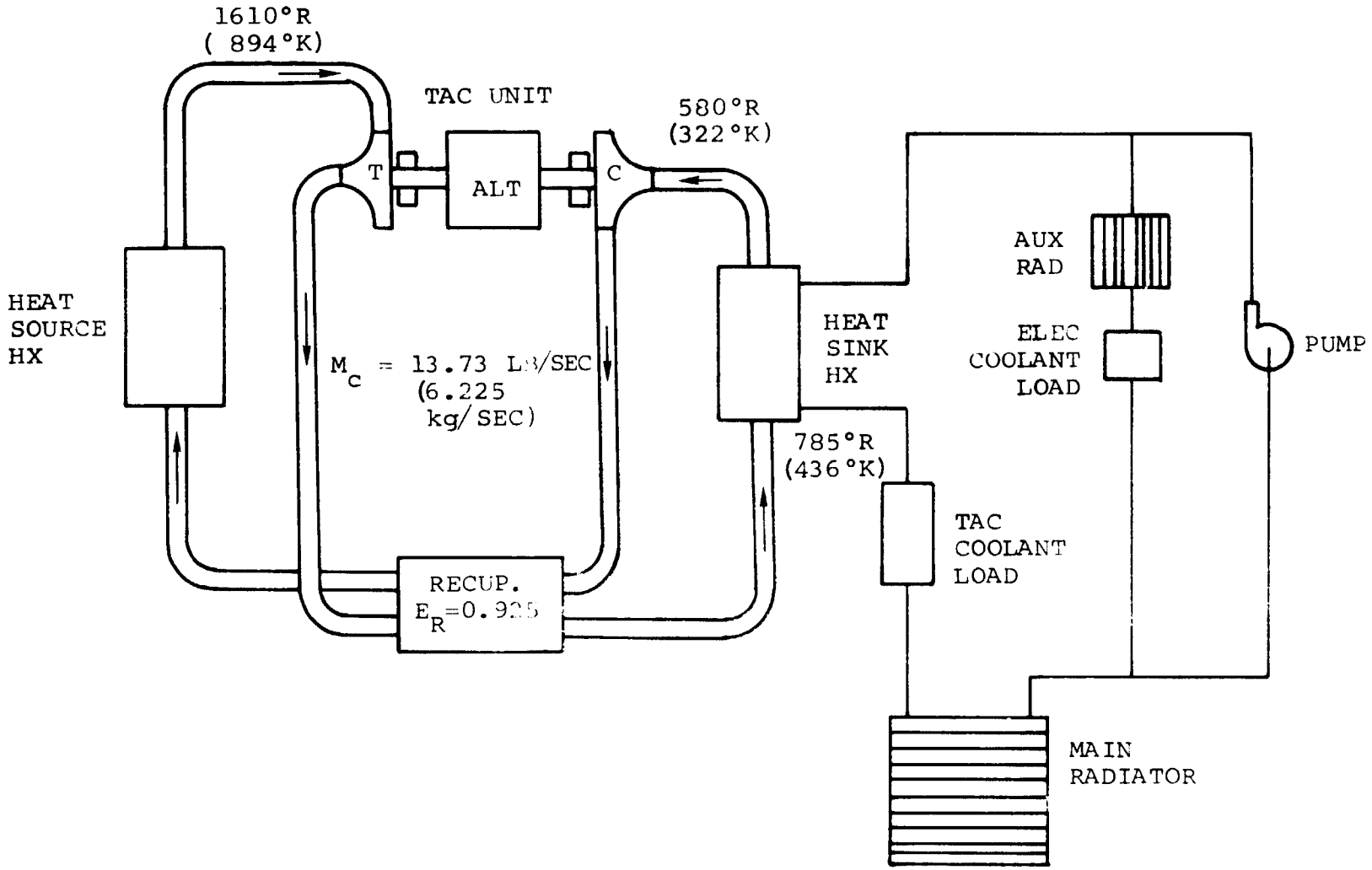
(b) Examine the effects of the new cycle conditions on compressor and turbine aerodynamic performance.

(c) Determine rotor dynamics and new bearing and seal dimensions consistant with the heavier rotating assembly.

(d) Prepare a new TAC layout with a 400 Hz alternator.

(e) Present comparative data for evaluating the 400 Hz TAC versus a 1200 Hz TAC.

These objectives have been met and the following paragraphs briefly summarize the results. Supporting detail regarding component design is given in Section 6.0 "Phase III Components".



TAC REFERENCE SCHEMATIC

FIGURE 22

TABLE 16

PHASE III TAC SPECIFICATIONS

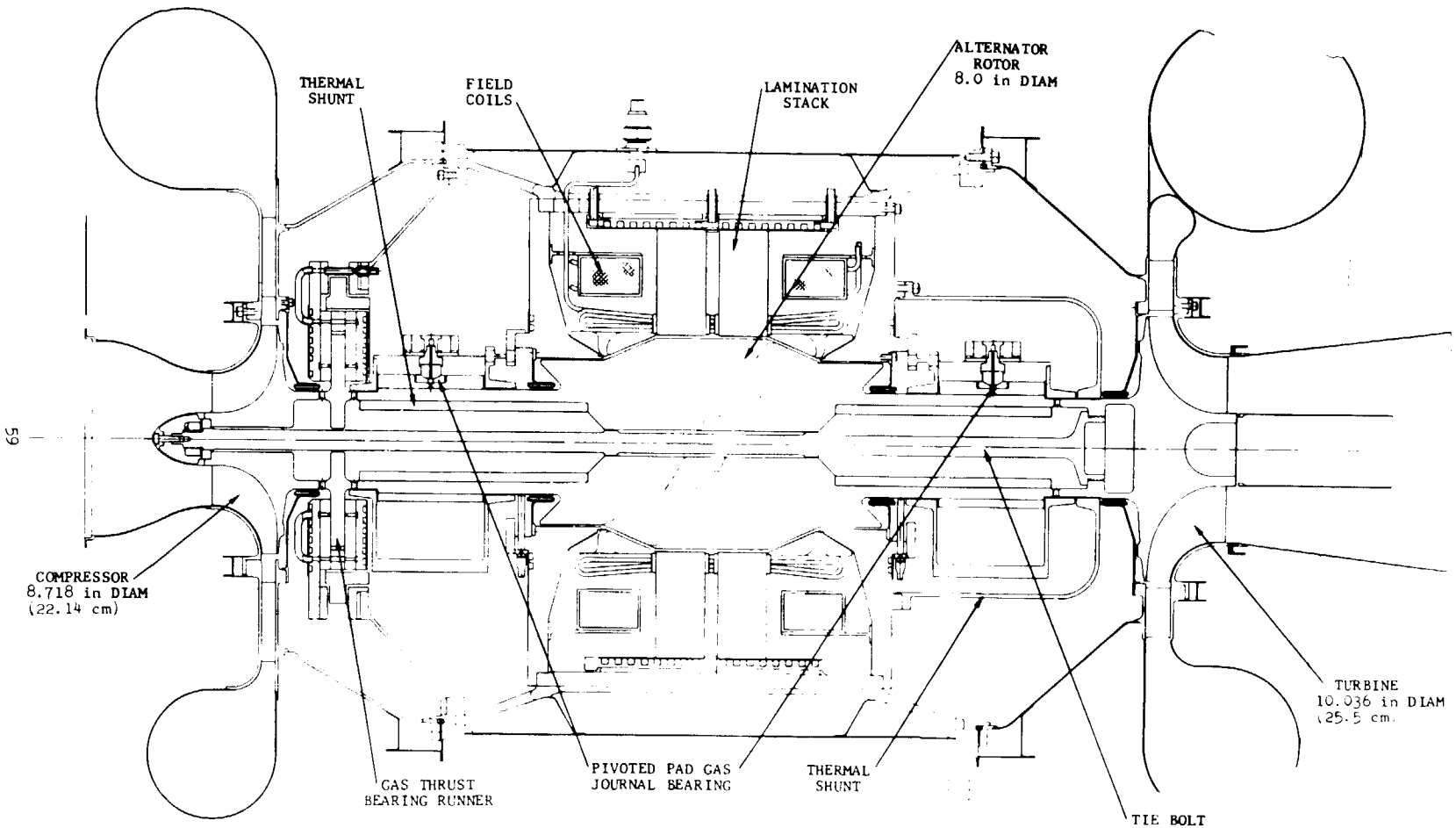
Alternator design power, kw_e	160
Shaft speed, rpm	24,000
Working fluid mol wt (XeHe)	39.944
Compressor inlet flow, lb/sec (kg/sec)	13.73 (6.225)
Compressor inlet pressure, psia (kN/m^2 abs)	70 (483)
Compressor pressure ratio	1.9
Compressor inlet temperature, °R (°K)	580 (322)
Turbine inlet pressure, psia (kN/m^2 abs)	130 (895)
Turbine pressure ratio	1.824
Turbine inlet temperature, °R (°K)	1610 (894)
Component configurations	
Compressor type-radial	
Turbine type-radial	
Alternator type-Lundell	
Bearings - gas	

Figure 23 presents the layout of the TAC machine with a 400 Hz alternator. Table 17 shows the performance factors for the Phase III TAC machine with a 400 and a 1200 Hz alternator. Conceptually, the unit is identical with the Phase I TAC-A unit, which in turn is very similar to the NASA Brayton Rotating Unit now under test at NASA Lewis Research Center. The rotating unit consists of a radial compressor and turbine directly coupled to the rotor of the 2 pole Lundell alternator. The entire rotating assembly operates at 24,000 rpm and is supported by gas bearings. Journal bearings [4.0 in (10.16 cm) dia] are the pivoted pad type with 3 pads; 2 rigid (constrained against radial deflection) and one flexibly mounted. Hydrostatic gas for lift-off at start is supplied through the conforming pad pivot sockets. A gimbal mounted Rayleigh step sector thrust bearing is shown with cooling passages in the stators.

Labyrinth seals are used surrounding each bearing compartment. The bearing compartments are pressurized to compressor discharge pressure to maximize bearing load capacity over the operating pressure range. The alternator cavity is vented to the compressor inlet pressure to reduce windage losses.

Cooling of the alternator is accomplished by recirculating some of the working fluid gas inside the alternator cavity. The conical regions of the alternator rotor serve as pumps to circulate gas through the main gap. At the center of the stator stack the recirculating gas flows radially outward through in axial space between halves of the lamination stack. At the stator stack O.D. the gas flow splits longitudinally in both directions through fins in an oil cooled heat exchange which cools the gas. The gas then flows downward on both ends of the alternator, cooling the end turns and re-enters the rotor gap at the base of the rotor cones, completing the recirculating loop.

Table 18 shows the major factors of comparison between the 400 and 1200 Hz alternators.



PHASE III TAC LAYOUT WITH 400 HZ ALTERNATOR

FIGURE 23

TABLE 17

PHASE III TAC PERFORMANCE SUMMARY				
ALTERNATOR FREQUENCY; Hz	400		1200	
EFFICIENCIES:				
Cycle efficiency at design*	0.284		0.292	
Turbine	0.918		0.918	
Compressor	0.865		0.865	
Alternator	0.933		0.942	
POWER OUTPUT, kw	178.1		182.8	
SHAFT POWER LOSSES, kw				
Alternator windage**	9.15		5.97	
Bearings ***				
Thrust	1.47		1.47	
Journals	1.28		1.28	
Total losses	11.90		8.72	
LENGTHS:	IN.	CM	IN	CM
Bearing span	21.45	54.48	17.05	43.31
Overall length	44.0	111.8	39.6	100.6
MASS FLOWS	LB/SEC	KG/SEC	LB/SEC	KG/SEC
Compressor inlet	13.73	6.225	13.73	6.225
Compressor bleed	0.308	0.140	0.308	0.140
MASS	LB	KG	LB	KG
Rotating group	225	102	175	79.4
Total TAC mass	1100	498	800	363

*Recuperator effectiveness = 0.925

**Cavity pressure = 70 psia (483 kN/m^2 abs)

***Bearing losses are for zero g operation

TABLE 18

COMPARISON OF 2-POLE AND 6-POLE ALTERNATORS
AT PHASE III OPERATING CONDITIONS

ITEM	6-POLE	2-POLE
ELECTROMAGNETIC WEIGHT	279 lbs (126 kg)	571 lbs (259 kg)
	Further optimization may reduce the 2-pole weight significantly. The rotor for the 2-pole alternator presented is about 50 percent heavier than the 6-pole rotor.	
ELECTROMAGNETIC EFFICIENCY	94.2% @ full load 89.3% @ 1/4 load	93.3% @ full load 85.8% @ 1/4 load
OVERALL ALTERNATOR EFFICIENCY	91.0% @ full load (approx.) 86.3% @ 1/4 load (approx.)	88.6% @ full load 79.9% @ 1/4 load
	Based on 70 psia (483 kN/m^2) cavity and estimate using Phase III windage calculation methods. The stator iron losses do not decrease significantly with load, and they are the predominate loss at part load; they are nearly twice as high in the 2-pole. Less efficient use is made of the back-iron since flux enters and leaves in only two places on the 2-pole. Also, the 2-pole requires greater field power. The 2-pole armature losses are relatively higher for equal wire sizes and currents due to the relatively large amount of wire in the end turns not performing useful work.	
ROTOR FABRICATION	No basic differences between bonding a 6-pole and a 2-pole rotor. This applies for both brazing and diffusion pressure bonding.	
	Adequate design obtainable with two materials for 120 volt design.	May require a 3rd material on the pole faces for a 120 volt design.
	The addition of the 3rd material to the rotor does not present significant additional problems with proper development. The possible requirement of a 3rd material for the 2-pole should not be considered detrimental.	
STATOR STACK FABRICATION	DBS = 1.25 in. (3.18 cm)	DBS = 3.21 in. (8.15 cm)
	The greater height of the depth-behind-slot (DBS) on the 2-pole is of concern since this enhances the possibility of stack flare and folding. While the 6-pole requires special mechanical structure to retain the stack, the 2-pole requires even more.	
ARMATURE COIL FABRICATION	40° THROW	120° THROW
	Both have five turns per coil set but the 2-pole is pulled over a greater arc. The expanse of this arc makes handling more difficult and enhances the likelihood of handling damage to the wire insulation.	
ARMATURE ASSEMBLY	4.55 in. end-turn length (11.6 cm)	12.23 in. end-turn (31.1 cm)
	The very large end-turn length of the 2-pole is of concern, especially over the life of the machine as the insulation falls off and/or the coils shift or sag (closing the spacing between phases). Special end-turn supports or potting encapsulation will be required for the 2-pole. Also, the longer span will have a significantly lower natural frequency and greater amplitude which may be of concern for vibration integrity. Standard, 8-pole aircraft alternator end-turn designs have a measured natural frequency of 700 Hz (typical).	
MASS UNBALANCES	Symmetrical	Nonsymmetrical. Requires removal of about a cubic inch of Inconel from each cone section of the rotor.
THERMAL DISTORTION OF SHAFT	Thermal distortion is symmetrical	The rotor has a nonsymmetrical distortion pattern due to 2-pole configuration; may cause problems such as warping of the shaft.
MAGNETIC UNBALANCES	Has unbalance in auxiliary gap and in main gap; no unbalanced moments due to pole fringing flux.	Has unbalance in auxiliary gap and a small moment due to unsymmetrical fringing flux about pole ends.
OVERALL SIZE	9.5 in. long x 13.6 in. dia (0.24 x 0.35 m)	13.9 in. long x 18.5 in. dia (0.35 x 0.47 m)
	Volumetric space for the field coil is limited and may dictate restrictions to end bell stator mounting structure.	Ample room for field coil and for changing the end bell configuration to accommodate stator mounting.
	The greater dimensions of the 2-pole adds structural weight to the unit and increases the bearing span. However, more space is available for design innovations as pointed out above.	
VRE AND FIELD POWER REQUIREMENTS	F.L. field power = 1.16 kW	F.L. field power = 1.16 kW
	The 2-pole requires a VRE with about twice the rating; however, because the field coil space is crowded on the 6-pole, the ampere rating of the 6-pole alternator VRE may be 2 to 3 times greater; e.g., 80 to 90 amperes typical, to obtain the necessary ampere turns. The number of turns is limited by the minimum practical wire or strap size which will still yield a design that is capable of being easily cooled. On the 2-pole, because of the extra volume available, the necessary ampere turns can be obtained by a greater number of the same size turns.	
DEVELOPMENT REQUIREMENTS	Will require special rotor development, etc. common to the 6-pole and 2-pole, but it has no distinctive development requirements particular to the 6-pole alone.	According to the previous items, will probably require some stator fabrication development on the first unit. Unbalances and nonsymmetrical rotor deformation problems at high temperatures will require experimental development.

The conclusions reached during the Phase III studies are:

(a) The 400 Hz TAC unit is both feasible and practical, although heavier and less efficient than the 1200 Hz TAC unit of Phase I.

(b) Only one significant development uncertainty difference exists between the 1200 and 400 Hz units. The non-symmetry of the 2-pole alternator rotor may result in shaft distortions which could cause bearing problems.

The symmetry inherent in the 6 pole rotor eliminates any possibility of this problem.

(c) The likelihood of the high temperature Anadur wire insulation eventually flaking off the end turns and entering the gas circuit as an abrasive dust precludes the use of Anadur in the TAC alternator. Some alternate high temperature insulation systems can be recommended but these will require materials development to reduce laboratory techniques to practical hardware. The other alternative insulation system is a conventional organic insulation which is suitable for this application with the use of low temperature 107°F (315°K) alternator coolant.

(d) The TAC will operate efficiently at the SNAP-8 reactor temperature levels specified for Phase III. The capability for efficient operation at 2060°R (1144°K) turbine inlet temperature has been maintained.

5. TAC PHASE I COMPONENT STUDIES

5.1 Preliminary Reference Cycles

The TAC Phase I system schematic supplied in the contract (Figure 1, Page 4) was subjected to analysis by the AiResearch Brayton Cycle system analysis program. The temperatures shown indicated a recuperator effectiveness of 0.925 for the TAC system. This value was assumed in all subsequent complete cycle analyses. Arbitrary assumptions were made for several variables in the system:

Alternator electrical efficiency = 90%

Combined windage, bearing and seal losses = 9.6 kw
= 6% of output

$$\frac{\text{Compressor flow - Turbine flow}}{\text{Compressor flow}} = \text{Bleed} = 2\%$$

Turbine diffuser efficiency = 60%

Several other cycle parameters were defined in the contract statement of work:

Working fluid molecular weight	39.944
Turbine inlet temperature	2060°R (1144°K)
Compressor inlet temperature	700°R (389°K)
Compressor pressure ratio	1.90
Turbine pressure ratio	1.786
Compressor inlet pressure at 24,000 rpm	55 psia ($379\ kN/m^2$ abs)

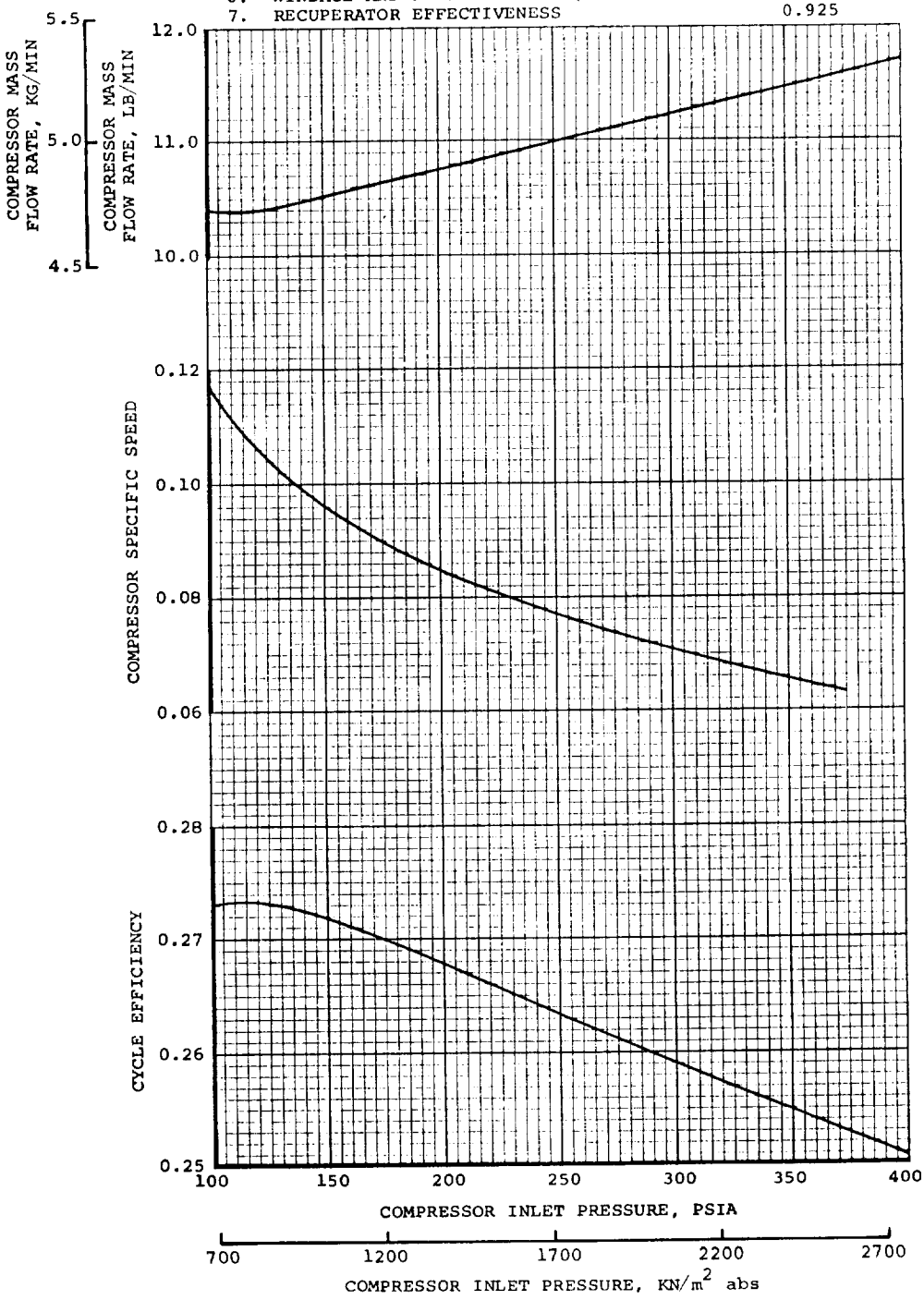
Compressor inlet pressure at 36,000 rpm	120 to 360 psia (827 to 2480 kN/m^2 abs)
Turbine inlet pressure (% compressor discharge)	0.974

Using the above values as input, Figure 24 was generated to show compressor specific speed, compressor mass flow rate, and cycle efficiency as a function of compressor inlet pressure for a 36,000-rpm unit. From this data, it is apparent that the lowest permissible compressor inlet pressure yields the highest cycle efficiency; therefore, 120 psia (827 kN/m^2 abs) was selected as the design-point for the 36,000-rpm TAC unit at an output power of 160 kw_e. The cycle analysis conducted at 24,000 rpm used the prescribed compressor inlet pressure of 55 psia (379 kN/m^2 abs). The specific speed of the turbomachinery was nearly identical for the 24,000- and 36,000-rpm machines. Further, the value of specific speed, approximately 0.1, assures that high aerodynamic efficiency can be achieved in either the 24,000- or 36,000-rpm TAC unit.

Table 19 shows the initial predicted efficiencies of the turbines and compressors for the TAC at the two required shaft speeds. Flow rates and overall cycle efficiencies are also shown. The efficiency values were predicted by empirical specific speed/efficiency correlations for radial flow turbomachinery. The aerodynamic component parametric analyses were based on the mass flow estimates shown below; final component flow rates were determined (Section 2) after a detailed estimate of the losses had been made.

NOTES:

1.	COMPRESSOR INLET TEMPERATURE, °R (°K)	700 (389)
2.	TURBINE INLET TEMPERATURE, °R (°K)	2,060 (1144)
3.	SHAFT SPEED, RPM	36,000
4.	OUTPUT POWER, KW	160.0
5.	ALTERNATOR EFFICIENCY	0.90
6.	WINDAGE AND BEARING LOSSES, KW	9.60
7.	RECUPERATOR EFFECTIVENESS	0.925



36,000 RPM TAC - COMPRESSOR INLET PRESSURE SELECTION
FIGURE 24

TABLE 19

TAC COMPONENT PERFORMANCE

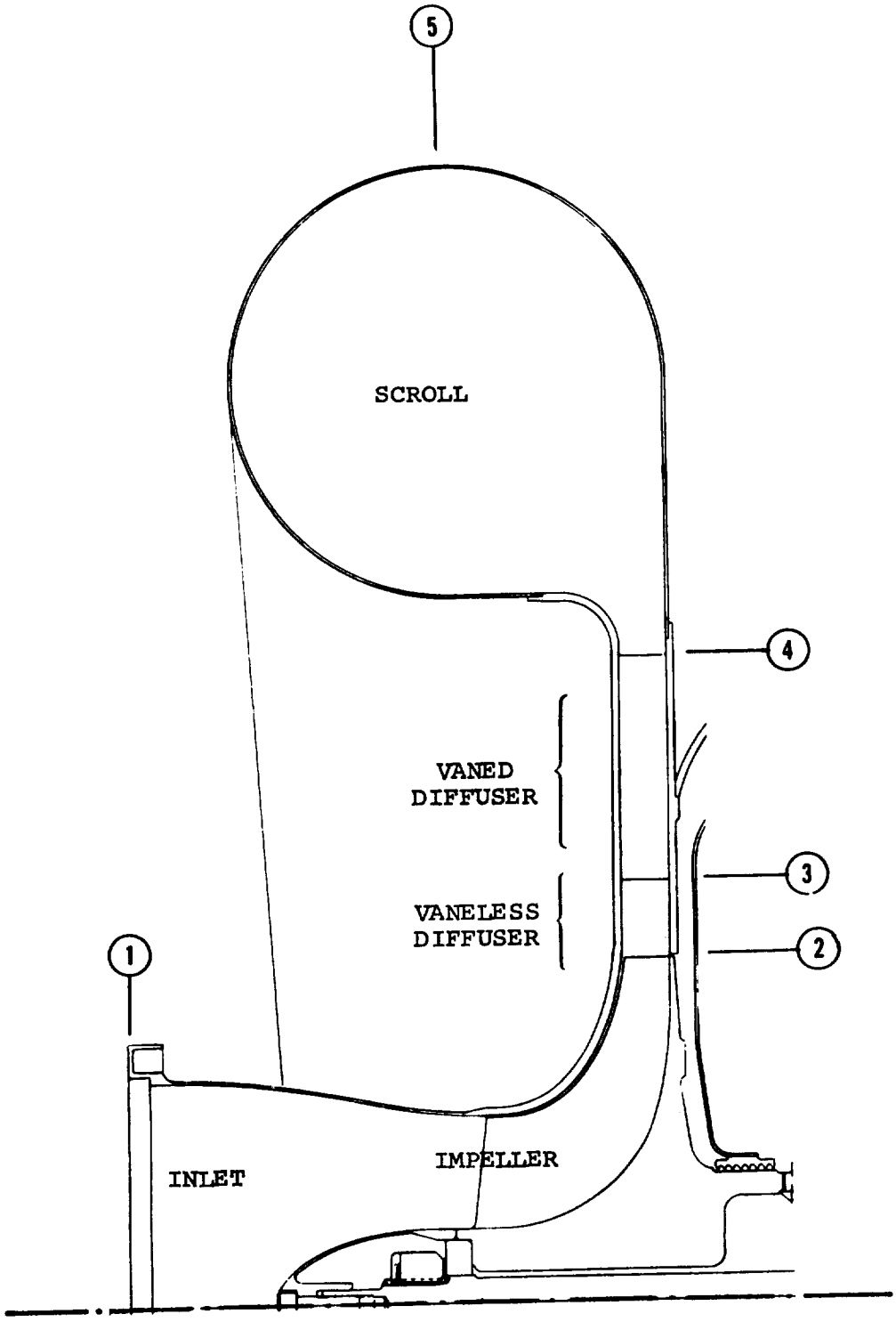
Shaft speed, rpm	24,000	36,000
Compressor inlet pressure, psia (kN/m^2 abs)	55.0 (379.0)	120.0 (827.0)
Compressor inlet flow, lbs/sec (kg/sec)	10.133 (4.596)	10.398 (4.716)
Compressor efficiency	0.854	0.841
Turbine efficiency	0.911	0.911
Cycle efficiency	0.281	0.274

5.2 TAC Compressor Preliminary Design

5.2.1 Centrifugal Compressor Optimization

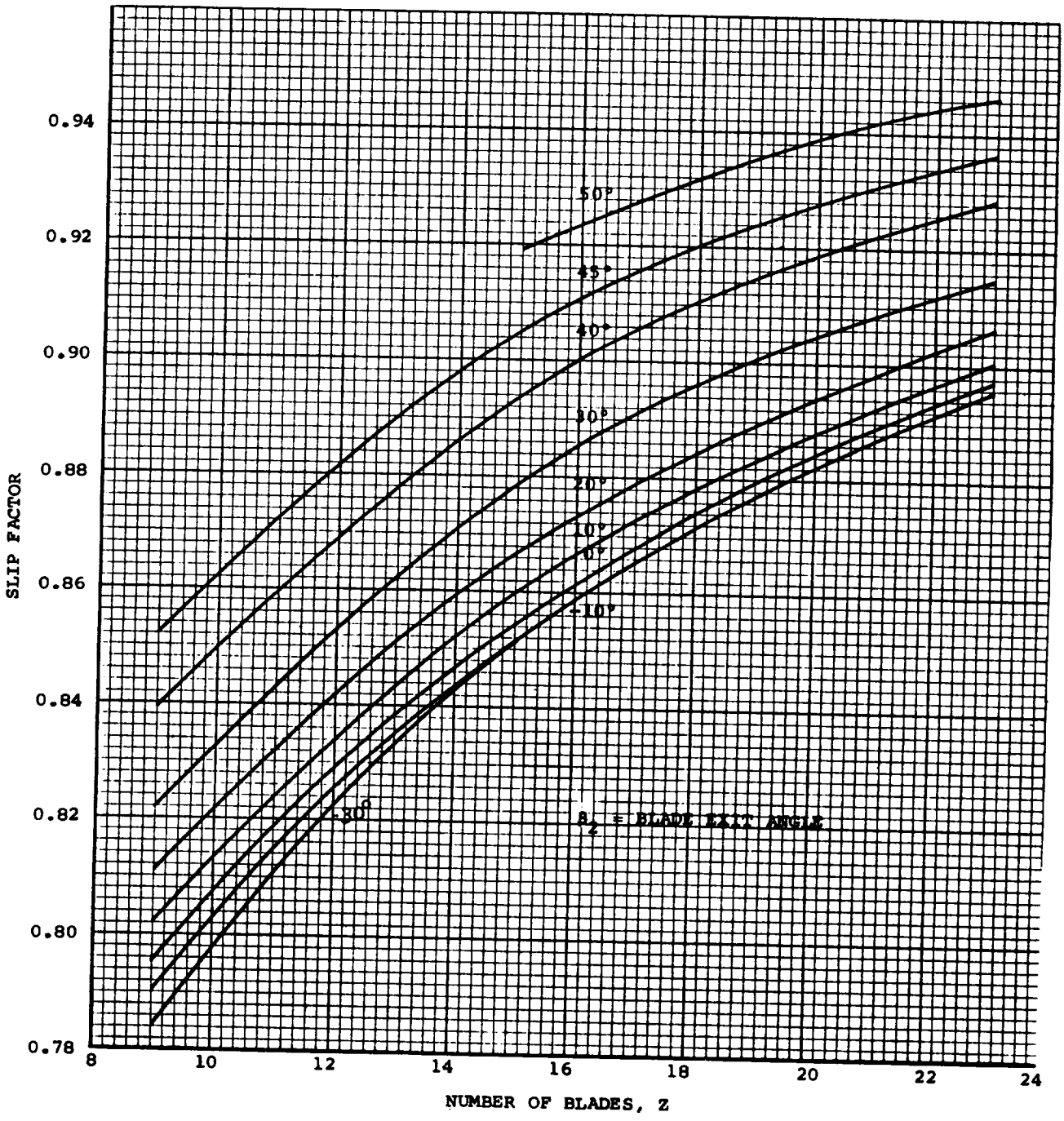
In order to establish a reference efficiency level for the centrifugal compressor stages shown in Figure 25, an AiResearch correlation of stage efficiency versus specific speed was employed. This correlation is based on hundreds of tests on all types of centrifugal compressors. The correlation indicated that if good axial clearances and Reynolds numbers (based on tip diameter and tip speed) higher than 0.5×10^6 could be maintained, that an efficiency of approximately 0.870 could be obtained at either speed. With this estimate the required compressor work ($\frac{\Delta T}{T}$) could be computed and used in the parametric study that followed.

The primary variables considered during the parametric analysis were inducer hub diameter and impeller exit blade angle. The slip factor was selected to be compatible with the blade number and exit blade angle in accordance with Figure 26 which is based on a slip factor estimation program that has proven to be reliable on several designs. Blade thicknesses were obtained from stress considerations and were based on previous AiResearch experience.



TAC RADIAL COMPRESSOR
STATION DEFINITION

FIGURE 25



SLIP FACTOR VERSUS NUMBER OF BLADES

FIGURE 26

A relative velocity ratio of 0.6 (shroud exit relative velocity over shroud inlet relative velocity) was selected for this study. This value has been shown to be near optimum for centrifugal impellers.

For purposes of the preliminary calculations the blade number was selected to be 13. This is lower than is generally used for centrifugal impellers but noting the low pressure ratio and relatively light blade loadings this value is not unreasonable and should result in reduced blade friction losses. Of course, in the detailed design of the final selected configuration the blade loadings will be investigated in great detail and any required adjustments in blade number can be made at that time.

The optimization procedure consists of calculating the sum of the various losses for a particular combination of the variables and repeating until a minimum loss sum is obtained. The losses considered in this study were:

(a) Aerodynamic losses - blade friction and turbulence losses

(b) Axial clearance losses

(c) Impeller mixing losses

(d) Backface disc friction losses

(e) Vaneless space loss

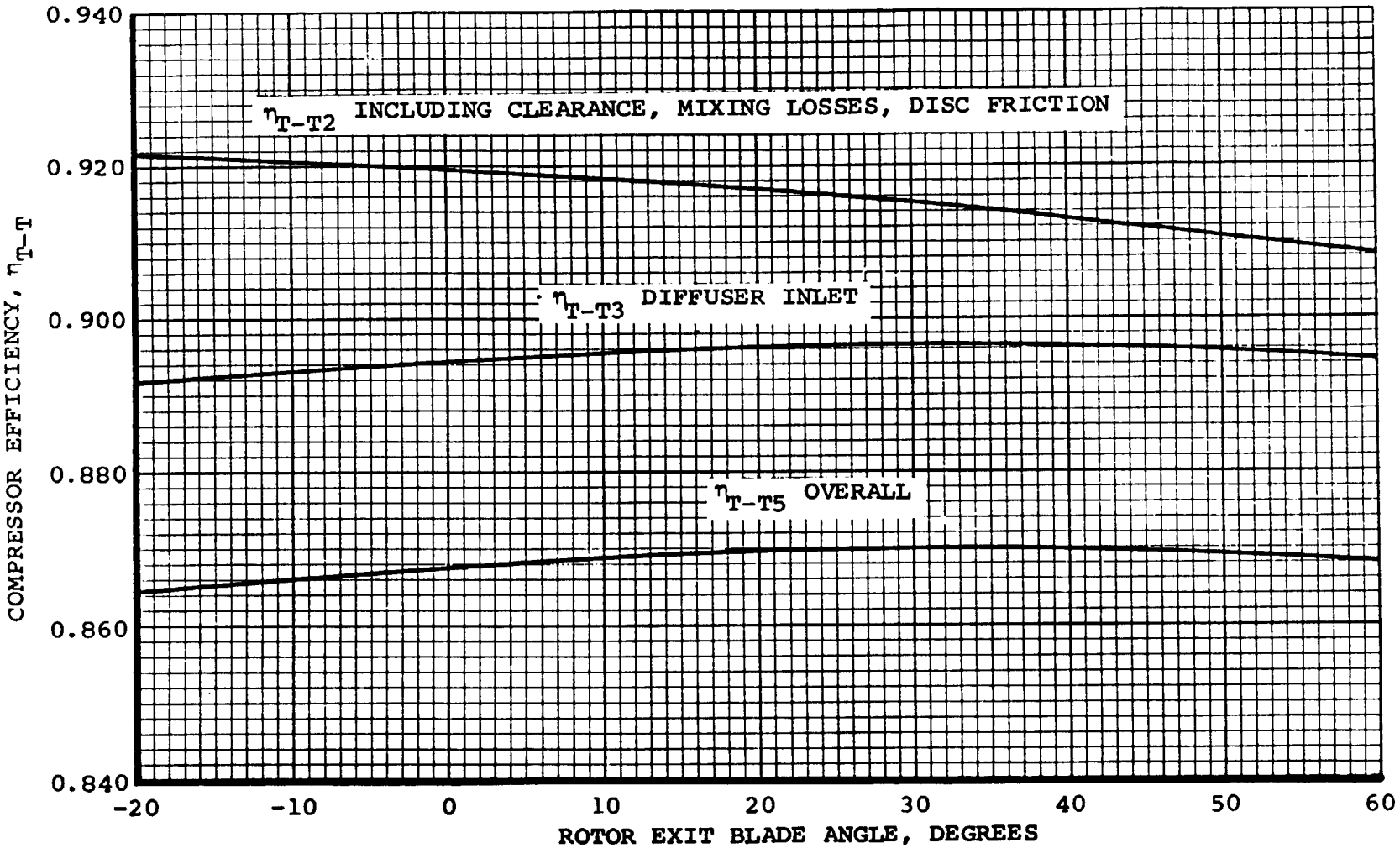
(f) Vaned diffuser losses

(g) Scroll losses

While the inducer hub diameter was initially considered to be a variable, from mechanical and critical speed considerations it was determined that the minimum practical inducer hub diameter was 2.0 in (5.08 cm) for both operating speeds and this value was maintained in all subsequent calculations. Preliminary loss calculations up to Station 2 (just downstream of the impeller) indicated that very little compromise in efficiency was involved in using this hub diameter compared to 1.5 in (3.81 cm). The remaining major variable left undefine was impeller exit blade angle. For a range of impeller exit blade angles from -20° (forward curved) to +60° the efficiency, including aerodynamic and clearance losses, disk friction, and dumping losses up to Station 2 (see Figure 25 for station definition) was calculated. The results are presented in the top curve of Figure 27 for the 24,000 rpm configuration and Figure 28 for the 36,000 rpm configuration. From this curve it appears that at least up to Station 2 the optimum impell exit angle is more than -20° (forward curved).

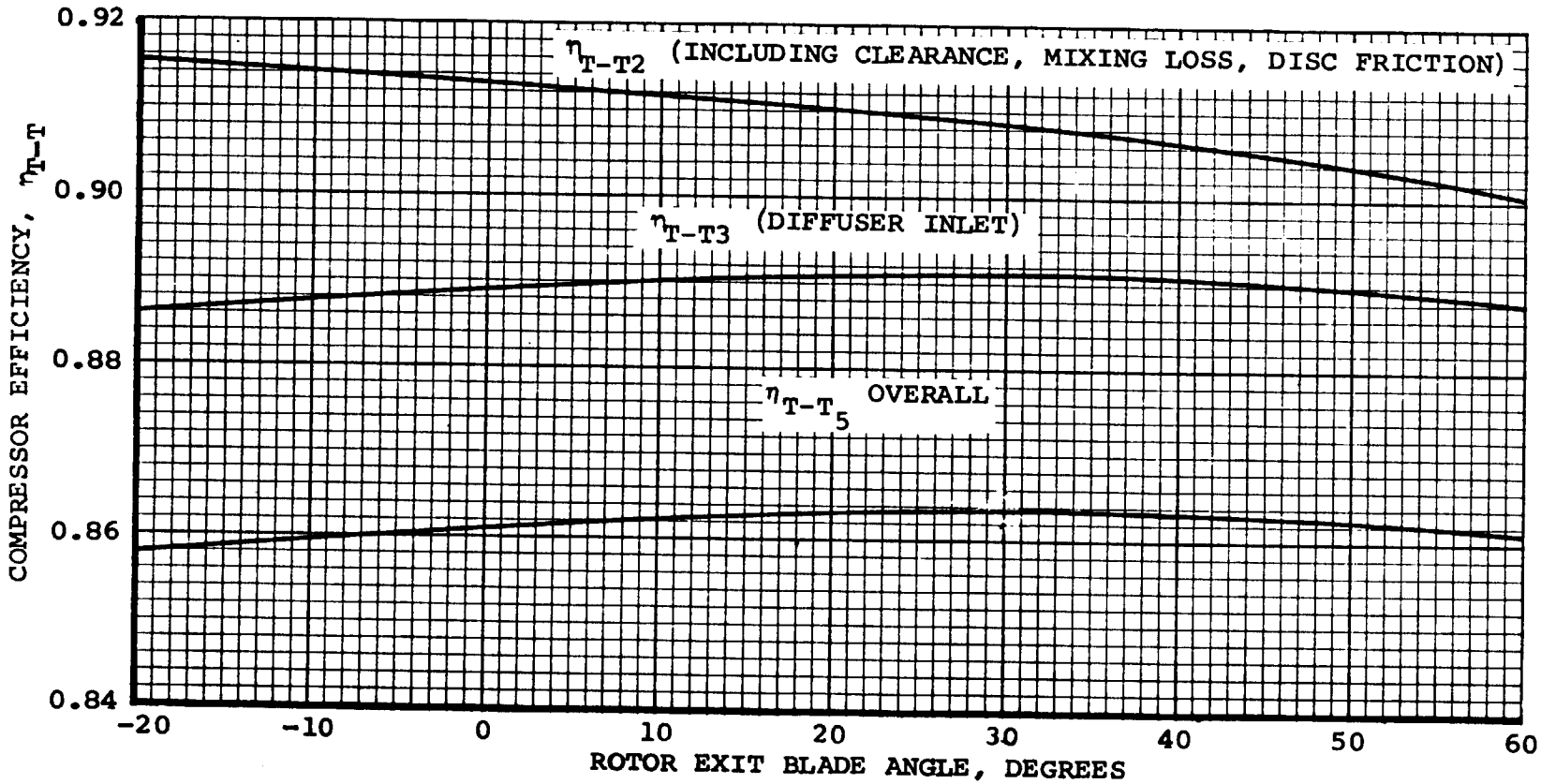
The next step was to include the vaneless space and vaned diffuse losses in the efficiency calculations.

Normally, in higher pressure ratio designs, the impeller exit Mac Number is sonic or higher and the vaneless space is employed to mainly reduce the Mach Number to about 0.85 (since vaned diffuser losses increase markedly at inlet Mach Numbers higher than 0.85). In the prese case, the impeller exit absolute Mach Number is subsonic and lower tha 0.8 for all blade exit angles considered. It was therefore of interes to determine whether an optimum diffusion split between the vaneless space and vaned diffuser existed. For this investigation the vaned diffuser exit radius at Station 4 was fixed at 8.9 and 6.5 in (22.6 and 16.5 cm) for the 24,000 rpm and 36,000 rpm configurations, respectively. This yields diffuser exit to impeller tip radius ratios in the order of 2.0 which is consistant with good design practice.



TAC RADIAL COMPRESSOR EFFICIENCY
(24,000 RPM)

FIGURE 27



TAC RADIAL COMPRESSOR PERFORMANCE
(36,000 RPM)

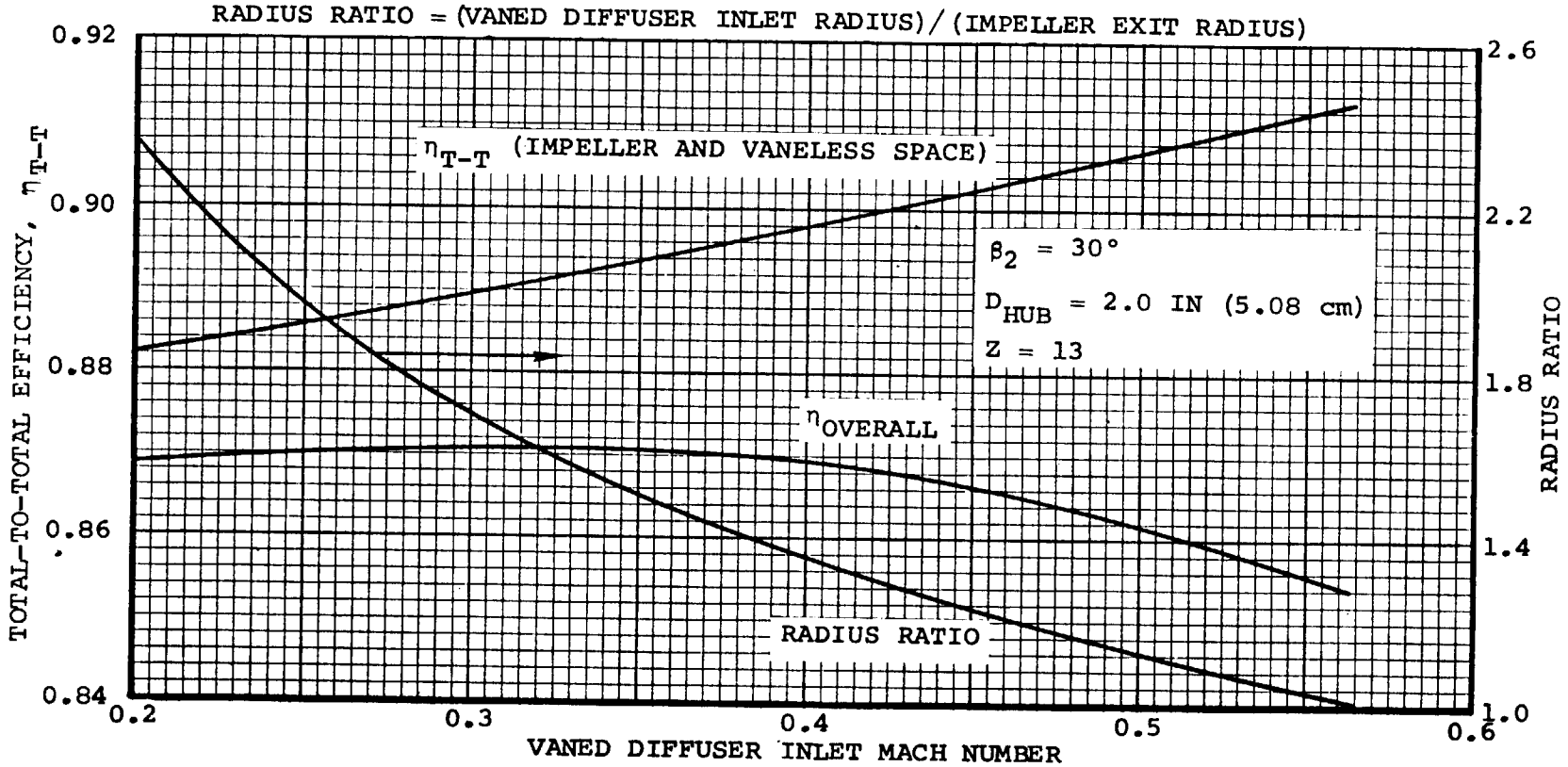
FIGURE 28

For a "first solution" a vaned diffuser inlet Mach Number of about 0.4 was selected. Using a vaneless diffuser program, the radius at which this Mach Number was obtained in the vaneless space was calculated along with the total pressure loss to that radius. An optimum vaned diffuser based on the data of Reference 1 was then defined based on the vaneless space exit conditions. The loss in the vaned diffuser was also calculated by assuming boundary layer conditions at the vaned diffuser inlet and again using data from Reference 1. From the resultant vaned diffuser exit conditions, the scroll loss was estimated.

In the center curves of Figures 27 and 28 the efficiency to the vaneless space exit are presented as a function of impeller exit blade angle. In the lower curves of the same two figures the total-to-total efficiency to the scroll exit is presented. Note that the efficiency peaks for both speeds at about 30° (backward curved).

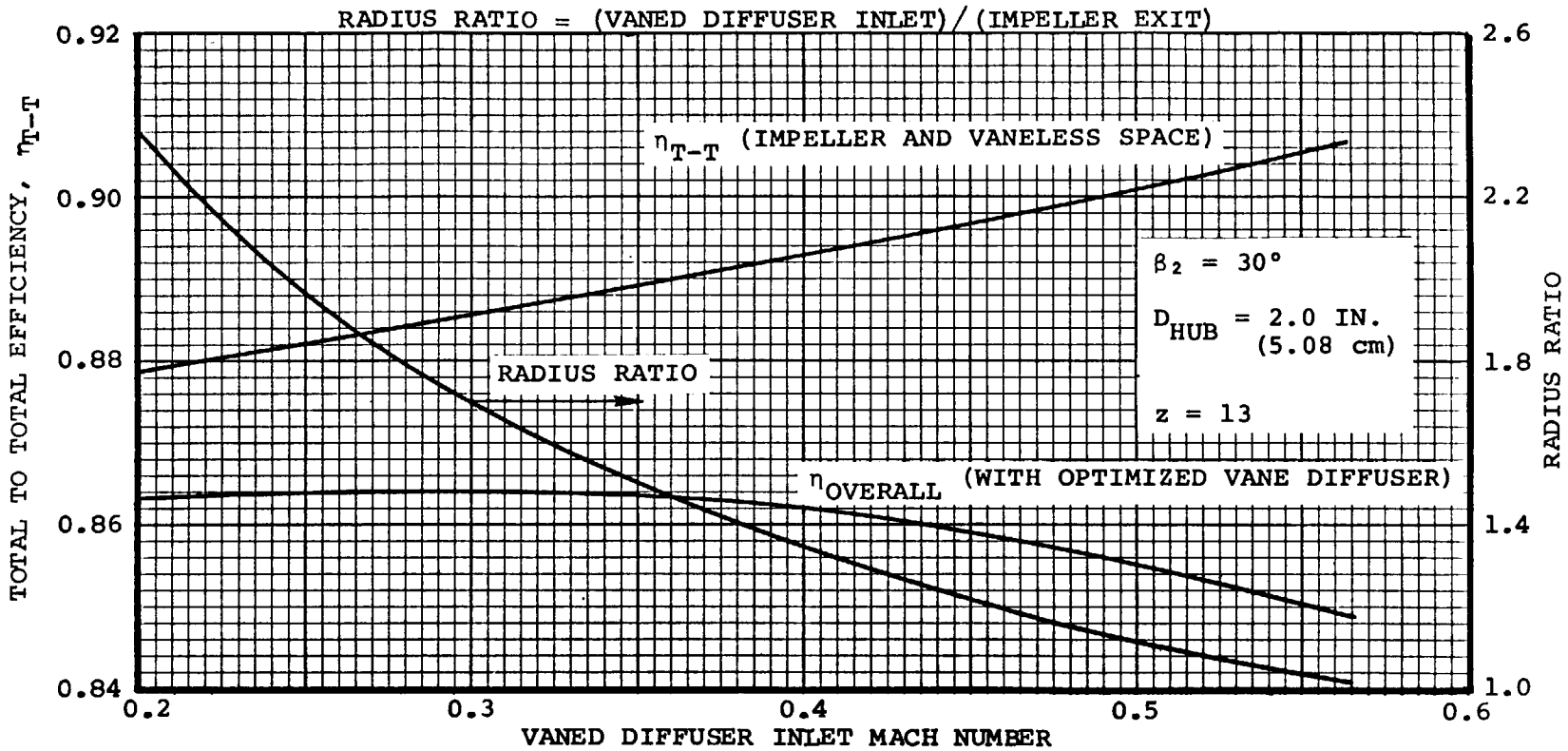
In order to investigate the effect of vaned diffuser inlet Mach Numbers other than 0.4, (i.e., different diffusion splits between the vaneless space and vaned diffuser) it was assumed that a blade exit angle of 30° would continue to be optimum for all reasonable diffusion splits. With this angle fixed, the losses and efficiency to the end of the vaneless space and to the scroll exit were calculated (Figures 29 and 30) for a range of vaned diffuser inlet Mach Numbers from about 0.2 to 0.56.

The overall efficiency (inlet total-to-scroll exit total) appears to peak for both speeds at a vaned diffuser inlet Mach Number of about 0.3. This would require a very large vaneless space. In these calculations it was assumed, for purposes of loss calculation in the vaned diffuser, that the boundary layer condition at the vaned diffuser inlet was constant. In a large vaneless space considerable diffusion occurs accompanied by deterioration of the side wall boundary layer. Therefore, the loss estimate for the vaned diffusers following large vaneless spaces is probably underestimated and it was decided to select a vaned diffuser inlet Mach number of 0.4.



TAC RADIAL COMPRESSOR VANED DIFFUSER OPTIMIZATION
(24,000 RPM)

FIGURE 29



TAC RADIAL COMPRESSOR VANED DIFFUSER OPTIMIZATION
(36,000 RPM)

FIGURE 30

In the detailed design of the final selected TAC configuration a much more careful investigation of the diffusion split must be made along with detailed boundary layer calculations in the vaneless space.

A summary of the preliminary design data for the radial compressors is given in Table 20.

It may be argued that the estimated overall efficiencies of 0.870 and 0.864 seem high compared to values being obtained on similar low pressure Brayton cycle compressor hardware. Four reasons for this potential improvement are:

(a) This design will be tailored from the beginning for this application and will not be a scale of another unit operating off design.

(b) The number of blades will be reduced consistant with the moderate blade loadings allowed by the low pressure ratio.

(c) The Reynolds numbers are extremely high due to the high cycle pressure levels.

(d) The relative axial clearance (clearance to blade exit height ratio) is small because of the larger size impellers, especially for the 24,000 rpm configuration.

TABLE 20

CENTRIFUGAL COMPRESSOR SUMMARY

SPEED, rpm	24,000	36,000
INLET TOTAL PRESS, psia (KN/m^2 abs)	55.0 (379)	120.0 (827)
INLET TOTAL TEMPERATURE, °R (°K)	700 (389)	700. (389)
PRESSURE RATIO	1.9	1.9
FLOW, lb/sec (kg/sec)	10.13 (4.60)	10.39 (4.72)
SPECIFIC SPEED, $\frac{N\sqrt{Q}_{in.}}{g^{3/4}H_{ad}^{3/4}}$;	0.1044	0.1074
NUMBER BLADES	13	13
$\Delta T/T$ OVERALL	0.3364	0.3390
$\eta_{OVERALL}$	0.870	0.864
EXIT TOTAL TEMP, °R (°K)	935.5 (519.7)	937.3 (520.7)
IMPELLER TIP DIA, in. (cm)	9.493 (24.11)	6.406 (16.27)
VANED DIFFUSER INLET DIA, in. (cm)	13.40 (34.04)	9.08 (23.06)
VANED DIFFUSER EXIT DIA, in. (cm)	17.80 (45.21)	13.0 (33.02)
IMPELLER TIP SPEED, ft/sec (m/sec)	994.0 (303)	1006.4 (306.8)
IMPELLER EXIT BLADE HEIGHT, in. (cm)	0.595 (1.511)	0.379 (0.963)
IMPELLER EXIT BLADE ANGLE, deg	30.0	30.0
INDUCER TIP DIA, in. (cm)	5.145 (13.07)	3.798 (9.65)
INDUCER HUB DIA, in. (cm)	2.000 (5.08)	2.000 (5.08)
AXIAL CLEARANCE, in. (cm)	0.010 (0.0254)	0.010 (0.0254)
REY NO., $\frac{\rho U_{tip} D_{tip}}{\mu}$	10.453 x 10^6	15.584 x 10^6

5.2.2 Axial Compressor Preliminary Design

During the preliminary design of the axial compressor, the fundamental tool was an AiResearch program which combines NASA cascade loss data with the radial equilibrium equations. For an assumed meridional flow path, and the required flow, pressure ratio, and rotating speed, the program selects optimum blading and calculates total-to-total efficiencies for any selected number of stages. Due to the low overall pressure ratio required for TAC and the probability that 3 or more stages would be required in order to keep the annular diffuser losses down, it was felt certain that subsonic blading would be satisfactory. Accordingly, the loss characteristics of the NASA 65 Series Cascades were selected for use in the computer program.

To provide initial estimates of the meridional flow paths preliminary calculations were made to identify hub-tip ratios which would yield minimum relative velocity levels along with acceptable rotor and stator diffusion factors. For this study the maximum allowable diffusion factor was set at 0.4.

The following simplifying assumptions were made:

(a) The flow is turned to the axial direction after each stage

(b) The axial velocity is constant

(c) The work input is constant for each stage

With these assumptions it was possible to develop equations relating diffusion factor and hub/tip ratio resulting in minimum relative velocity for various numbers of stages.

The object in using these equations was to find the lowest axial Mach Number required for a given number of stages while maintaining rotor and stator diffusion factors less than 0.4 with an optimum hub/tip ratio. A plot of the resulting exit Mach Number, diffusion factors, and hub/tip ratios as a function of stage number is presented in Figure 31.

With the "optimum" inlet hub/tip ratios defined for each number of stages it was now possible to define initial meridional flow paths. For each number of stages several simple meridional shapes were tried to obtain maximum estimated total-to-total efficiency. Note that this procedure is similar to that carried out in much greater detail during a final design.

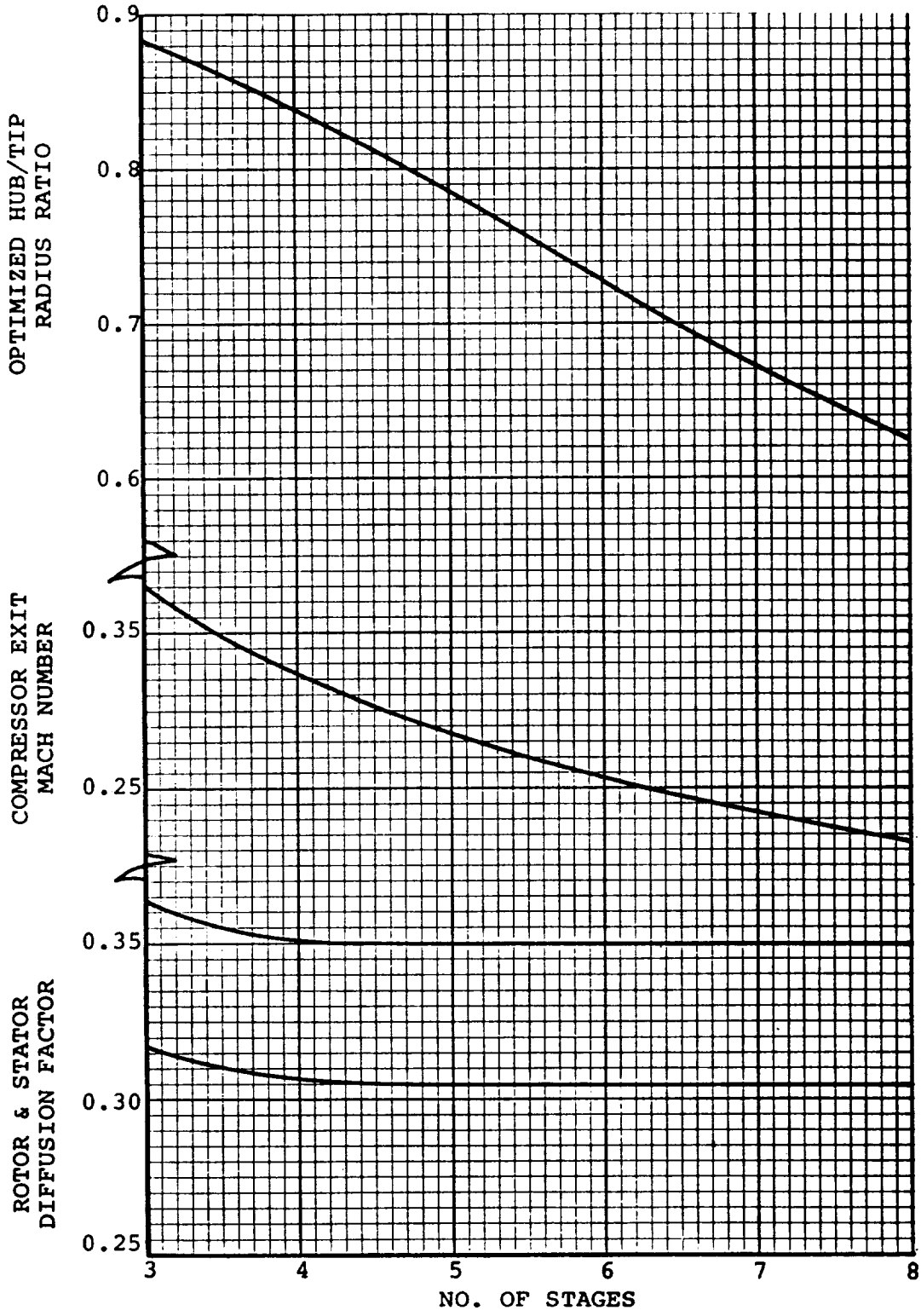
The resulting total-to-total efficiencies and exit absolute Mach Numbers are plotted as a function of stage number in Figures 32 and 33.

The next step was to estimate clearance and annular diffusion losses for each case.

A radial clearance of 0.005 in. was selected as being physically realistic for this design. The efficiency losses corresponding to this clearance were estimated using the method of B. Lakshminarayana in Reference 2.

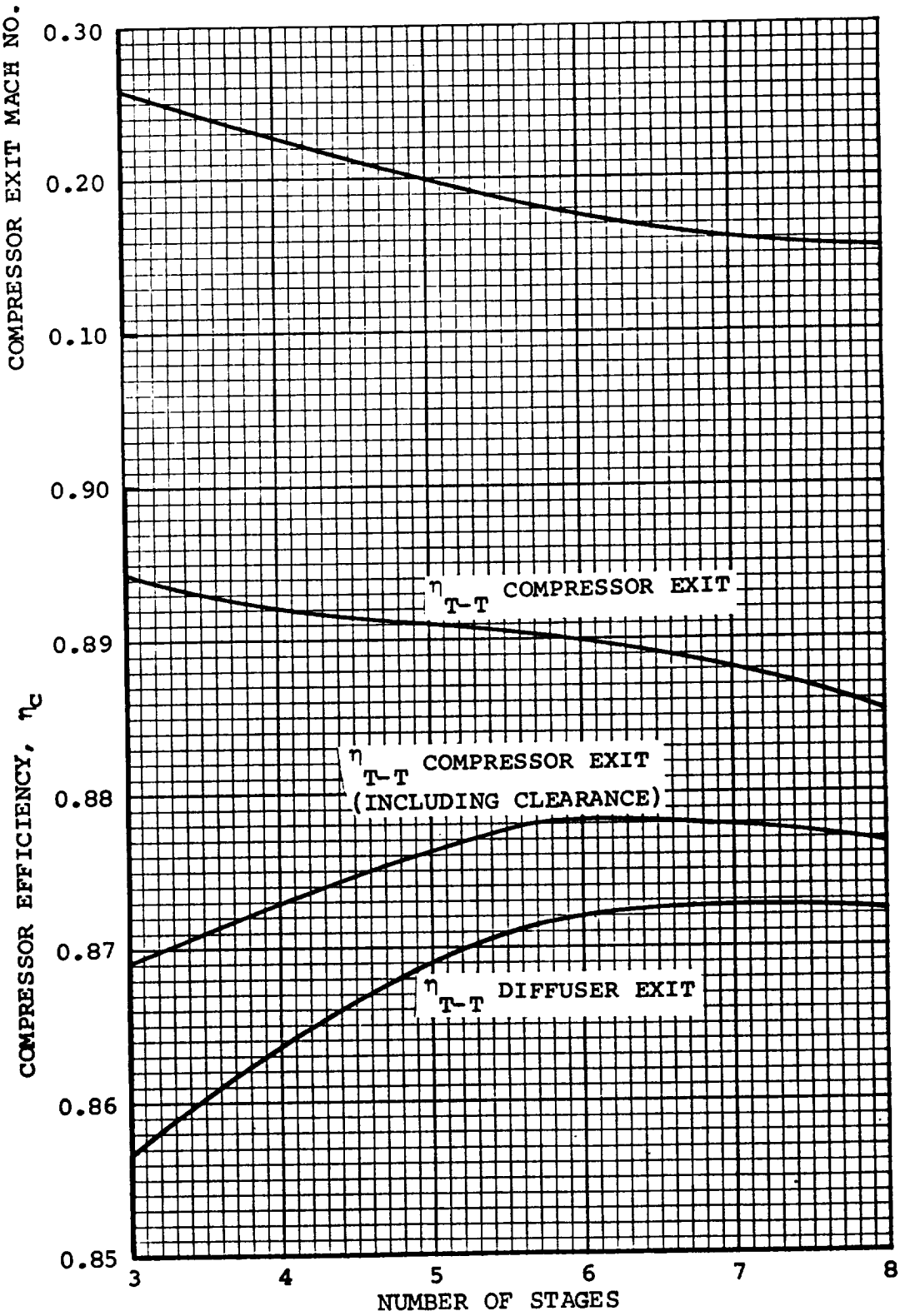
Total-to-total efficiency curves revised to account for clearance loss are also shown in Figures 32 and 33.

In order to estimate the total pressure loss in the diffuser it was assumed that a 0.60 pressure recovery factor could be obtained in the diffuser-scroll combination. This is felt to be readily achievable at the Mach Numbers being considered assuming sufficient axial



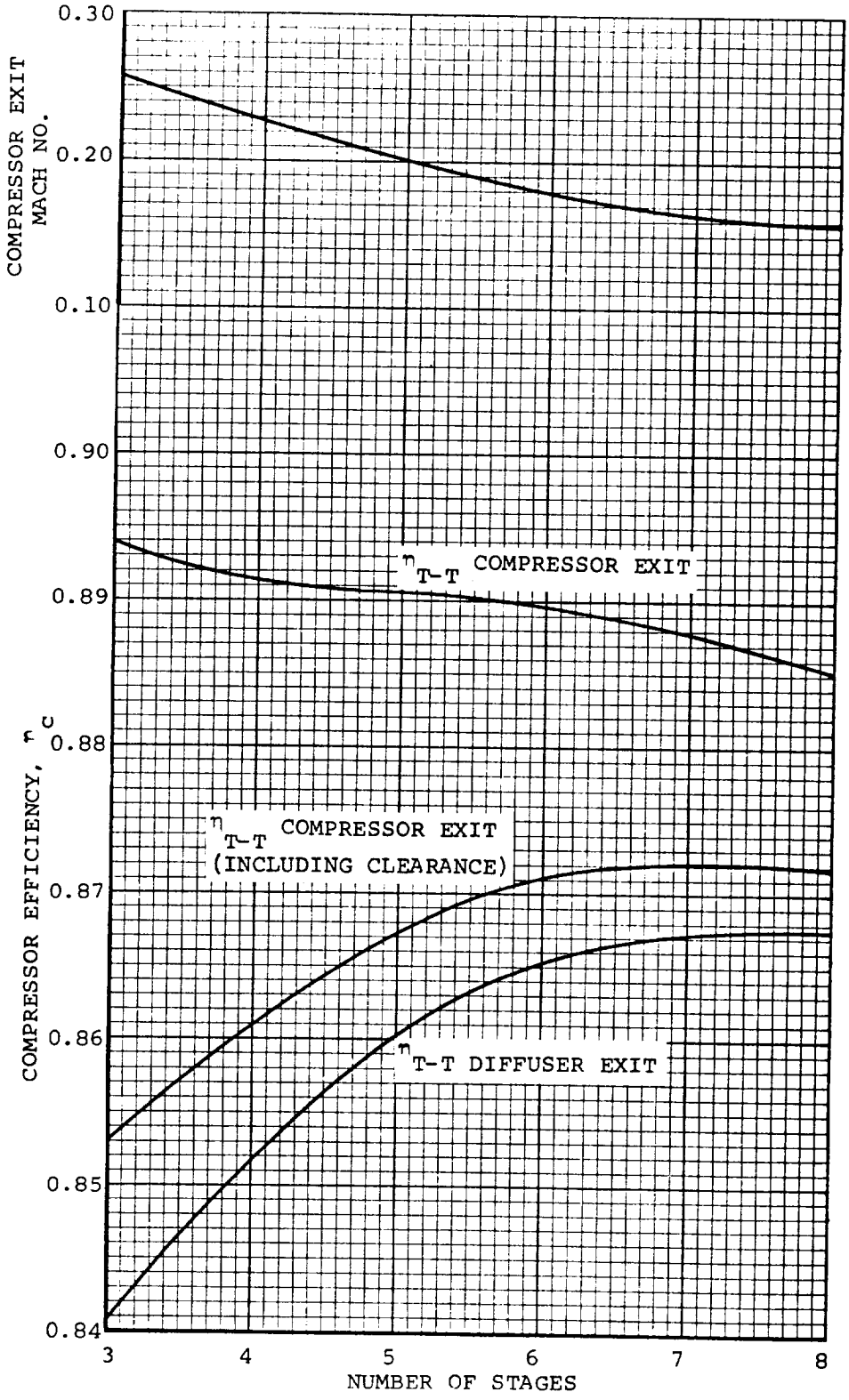
24,000 RPM TAC AXIAL COMPRESSOR
PRELIMINARY OPTIMIZED HUB-TIP RADIUS RATIO

FIGURE 31



24,000 RPM TAC AXIAL COMPRESSOR STUDY

FIGURE 32



36,000 RPM TAC AXIAL COMPRESSOR STUDY

FIGURE 33

length is available for optimum annular diffuser geometry. The resulting overall efficiency to the diffuser scroll exit is also shown in Figures 32 and 33. It is evident that with respect to efficiency the optimum number of stages is about six for the 24,000-rpm case and seven for the 36,000-rpm case.

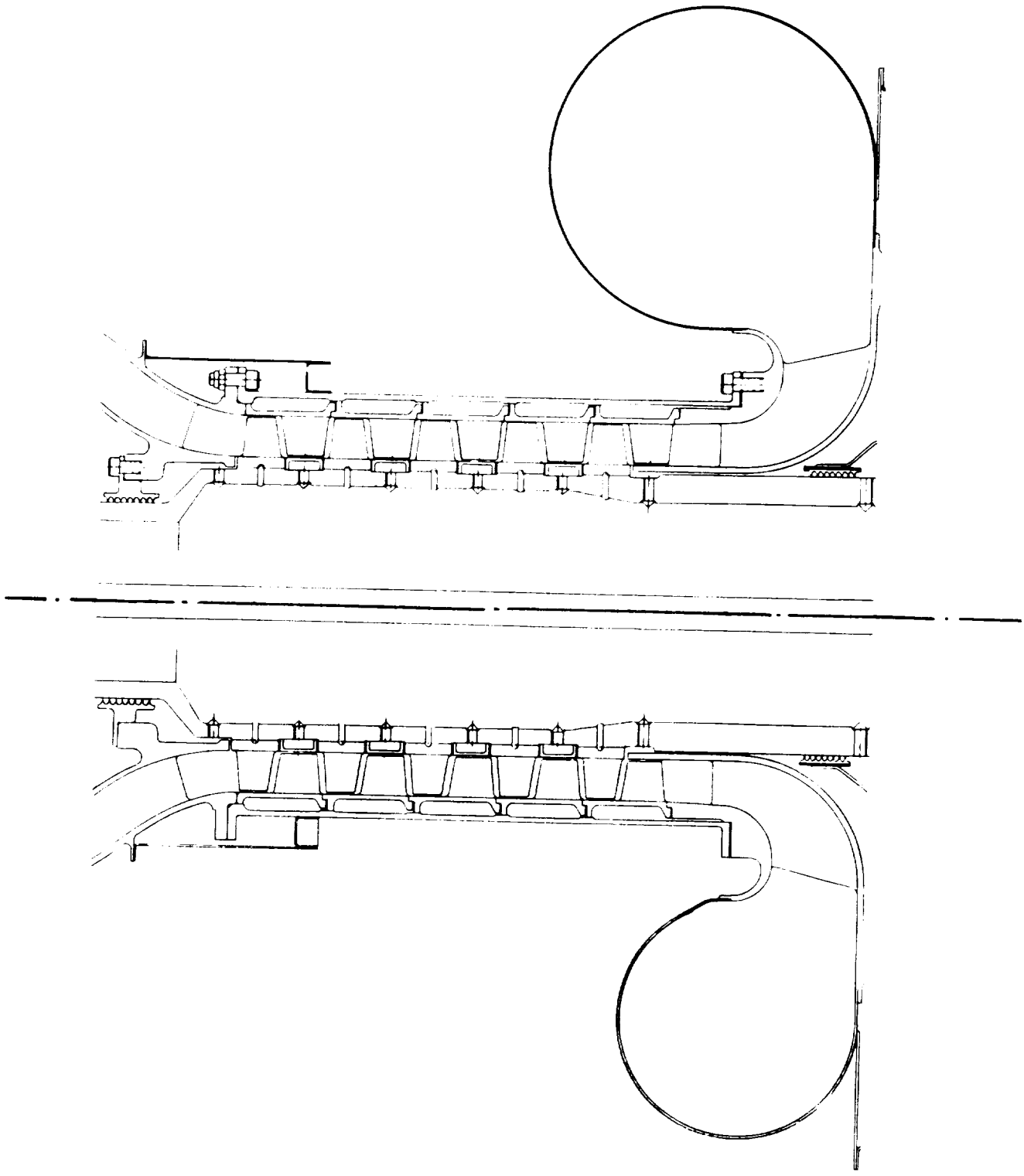
The final number of stages selected for both speeds was five as shown in Figure 34. The selection is justified by the following considerations:

(a) Critical speed analyses for both the 24,000 and 36,000 rpm designs indicated that in order to prevent severe problems the length of the axial compressor should be limited and the hub diameter as large as practical.

(b) In order to obtain the efficiencies predicted above, good blade contour control is required. Departure from ideal blade contour of less than 0.1 percent of the blade chord is considered the maximum permissible. Present manufacturing techniques will yield contour variations of about 0.001 in. (0.0254 mm). Therefore, minimum chord lengths for good efficiency should be approximately 1.0 in. (2.54 cm).

(c) Providing sufficient axial length for an adequate diffuser while observing minimum blade chord length implies no more than five stages could fit in the available axial space.

While the selection of five stages appears to result in a decrease in attainable efficiency of about 0.004 for the 24,000 rpm design and about 0.0075 for the 36,000 rpm design--it is more than justified by the easing of stage matching development problems.



TAC 5-STAGE AXIAL COMPRESSOR

FIGURE 34

The development problems inherent in axial designs with a large number of small chorded stages are exemplified by recent data taken on a small six-stage axial compressor designed for a NASA BRU application. While very high efficiencies were recorded on an off design portion of the performance map, the design pressure ratio, efficiency and work input were in error by a wide margin.

A summary of the preliminary design data for the selected axial compressors is presented in Table 21.

5.2.3 Recommendations

(a) 24,000 rpm vs 36,000 rpm - From a standpoint of maximum attainable efficiency it is clear that the 24,000 rpm designs, either radial or axial appear more promising. This is largely due to the greater significance of clearance effect in the smaller bladed 36,000 rpm design.

(b) Radial vs Axial - While the projected efficiency levels of both the radial and axial compressors are comparable, it is felt that other factors may be important to consider when making the final decision. These factors are summarized in Table 22.

5.2.4 References for Section 5.2

[1]Rundstadler, P.W. and Dean, R.C.; "Straight Channel Diffuser Performance at High Inlet Mach No., ASME Paper No. 68-WA/FE-19.

[2]Lakshminarayana, B., "Methods of Predicting the Tip Clearance Effects in Axial Flow Machining", ASME Paper No. 69-WA/FE-26.

TABLE 21

AXIAL COMPRESSOR SUMMARY

SPEED, rpm	24,000	36,000
INLET TOTAL PRESSURE, psia (KN/m^2 abs)	55.0 (379)	120.0 (827)
INLET TOTAL TEMPERATURE, °R (°K)	700. (389)	700. (389)
PRESSURE RATIO	1.9	1.9
FLOW, lb/sec (kg/sec)	10.13 (4.60)	10.39 (4.72)
SPECIFIC SPEED $\frac{N/Q_{in.}}{g^{3/4}\ H_{ad}{}^{3/4}}$;	0.1044	0.1074
$\Delta T/T$ OVERALL	0.3368	0.3404
$\eta_{OVERALL}$	0.869	0.860
EXIT TOTAL TEMPERATURE, °R (°K)	935.8 (519.9)	938.3 (521.3)
TIP SPEED, ft/sec (m/sec)	704.47 (214.72)	712.22 (217.08)
TIP DIA, in. (cm)	6.727 (17.09)	4.534 (11.52)
HUB DIA, in. (cm)	5.301 (13.46)	3.543 (9.00)
RADIAL CLEARANCE, in. (cm)	0.005 (0.0127)	0.005 (0.0127)
REYNOLDS NO., $\frac{\rho U_m\ C}{u}$	6.279×10^6	9.201×10^6

TABLE 22

COMPARISON OF AXIAL FLOW AND RADIAL FLOW COMPRESSORS FOR TAC APPLICATION

Factor	Radial	Axial
Fabrication	Technique well developed No problems	Techniques "State of Art" - but requires tighter tolerances, and/or special fabrication processes because of sensitifity to small deviations from design geometry
Stress/Vibration Problems	None	Potential blade flutter problems lead to insertable blade construction
Adaptability to TAC Application	Leads to least complicated TAC Configuration	Complicates TAC configuration, adds additional weight
Cost	Modest cost	High cost due to increased complexity Adds to rotating group balancing problems

5.3 Turbine Studies

In order to arrive at efficiency estimates for the 24,000- and 36,000-rpm TAC turbines, the designs were subjected to an optimizatic procedure and detailed three-dimensional analysis. An in-depth analysis was considered necessary to predict the expected efficiency values for the two radial turbine designs specified by the contract work statement. While empirical and analytical correlations are avai able based on bulk flow parameters such as specific speed, their predictions fall with a somewhat wide tolerance band. The predictions given here are based on a detailed study of the boundary layers inte nal to the turbine vanes and rotors.

Design point data pertinent to the TAC turbine designs are summarized below:

TURBINE DESIGN POINT SUMMARY

Shaft speed, rpm	24,000	36,000
Turbine inlet temperature, °R (°K)	2060 (1144)	2060 (1144)
Turbine inlet pressure, psia (kN/m^2 abs)	101.4 (699)	221.2 (1525)
Turbine pressure ratio	1.786	1.786
Mass flow rate, lb/sec (kg/sec)	9.930 (4.504)	10.190 (4.622)
Corrected mass flow rate, lb/sec (kg/sec)	2.869 (1.301)	1.3495 (0.612)
Specific speed	74.3	76.5

The turbine inlet temperature, pressure, and pressure ratio wer specified by the contract work statement. The turbine flow rates we established as shown in Section 5.1.

5.3.1 Turbine Design Procedure

To begin the turbine design procedure an initial set of vector diagrams were generated. The vector diagrams of a radial turbine are defined when the set of parameters listed in Table 23 have values assigned to them. The AiResearch vector diagram calculation procedure for radial turbines is the simultaneous solution of the energy, continuity and free vortex flow equations for a nonviscous, compressible fluid. The procedure was as follows:

(a) Initially, the parameters $\frac{\Delta S_{stator}}{\Delta S_{stage}}$ and $\frac{\Delta P'_{3-4}}{P'_4}$ (diffuser loss) are estimates based on AiResearch experience and are later verified by boundary layer calculations performed on the geometry that results from the particular turbine designs.

(b) The stator inlet swirl ($V_u/a_{cr'}$) was set at 45 deg to give the same inlet swirl angle as the BRU turbine developed under Contract NAS 3-9427 (Brayton Rotating Unit).

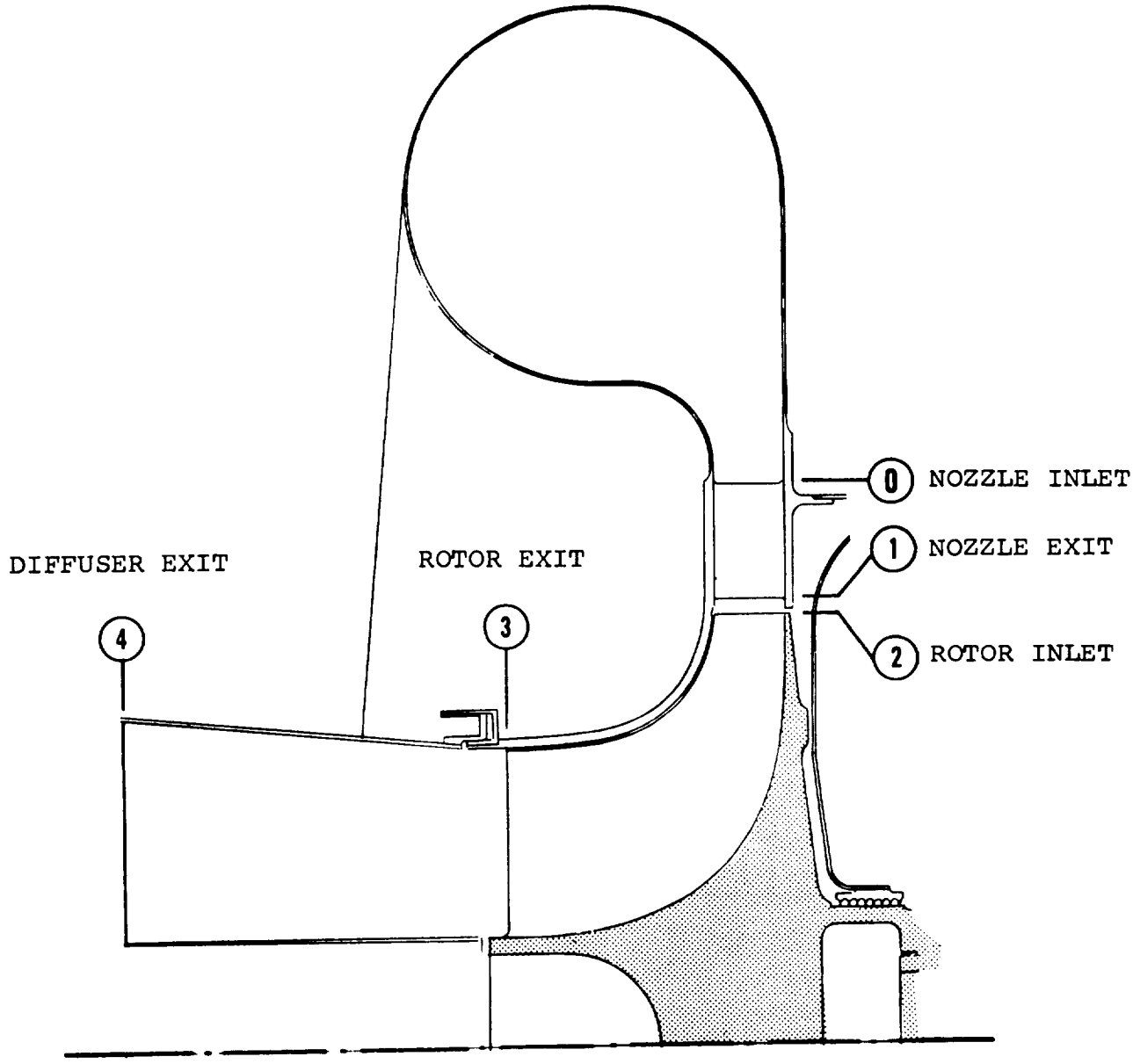
(c) Wheel exit swirl was eliminated for both TAC turbines by setting $\left(\frac{V_u}{u}\right)_{3,H} = 0$. The relative flow angle at the hub at wheel exit, $\beta_{3,H'}$ and the hub radius at the wheel exit, $R_{3,H'}$ were varied to satisfy the constraints of shaft diameter. The optimum exducer tip radius to wheel tip radius ratio was given by Rohlik[1] as 0.70 based on the specific speeds of the two TAC turbines.

(d) The radius and passage width ratios R_1/R_2, R_0/R_1 and B_2/B_1 were chosen to be identical to the BRU turbine values. The vaneless space pressure drop ratio was set at 0.1 based on experience.

TABLE 23

PARAMETERS GOVERNING THE VECTOR DIAGRAMS OF A RADIAL TURBINE*
*(Station Nomenclature Given in Figure 35)

T'_0	- Inlet total temperature
T'_4	- Outlet total temperature
H'_0	- Inlet total enthalpy
H'_4	- Outlet total enthalpy
P'_0/P'_4	- Turbine-diffuser total-to-total pressure ratio
$\Delta P/P'_4$	- Diffuser total pressure loss ratio
$\left(\frac{w\sqrt{\theta}}{\delta}\right)_{in}$	- Equivalent inlet mass flow
R	- Gas constant
$\Delta S_{stator}/\Delta S_{stage}$	- Stator-to-stage entropy increase ratio
w_3/w_2	- Rotor reaction ratio
$\left(\frac{V_u}{u}\right)_{3,H}$	- Rotor exit hub work coefficient
$r_{3,H}$	- Rotor exit hub radius
$\beta_{3,H}$	- Rotor exit hub relative velocity angle, deg.
u_T	- Tip speed
Ω	- Rotational speed, rpm
$\left(\frac{V_u}{a_{cr'}}\right)_0$	- Stator inlet swirl
r_1/r_2	- Stator-rotor clearance ratio
r_0/r_1	- Stator radius ratio
b_2/b_1	- Rotor-to-stator meridional plane b-width ratio
$\frac{\Delta P_{1-2}}{\Delta P_{0-2}}$	- Vaneless space pressure drop ratio
$F_v = \frac{U_T}{\sqrt{gJ\Delta H'_{ideal}}}$	- Velocity factor



TAC RADIAL INFLOW TURBINE REFERENCE STATIONS

FIGURE 35

(e) Initial estimates of efficiency for the turbines were those shown in Table 19 (0.911 for both turbines). This efficiency estimate is necessary in order to establish the downstream temperature and enthalpy for preliminary vector diagrams.

The AiResearch vector diagram program requires two remaining parameters to calculate the vector diagrams--the rotor tip speed and the rotor reaction ratio.

5.3.1.1 Rotor Tip Speed Study

Highly stressed radial turbine designs normally limit the tip speed to some maximum value which then requires a tradeoff between wheel inlet incidence losses and wheel exit swirl losses depending on the required pressure ratio. For much lower stressed Brayton cycle radial turbines, tip speed is normally not as important a parameter as wheel inlet slip factor. Thus, the procedure for calculating Brayton cycle vector diagrams is to vary tip speed to achieve proper values of F_v (velocity factor) and wheel inlet slip factor.

Values of rotor reaction ratio and rotor tip speed for the TAC turbines are not arbitrary but must satisfy the following constraints:

(a) The stator exit flow angle is 74° based on AiResearch experience and the correlation of Rohlik[1] for the specific speeds of the two designs.

(b) The velocity factor, F_v, should be very close to a value of 1.0 with zero exit swirl and a reasonable blade number based on the Rohlik correlation and AiResearch experience.

(c) The exducer tip blade angle was limited to a maximum value of 70° from the axial direction. Rotor inlet slip factor (V_u/U) should be that which permits a reasonable number of blades.

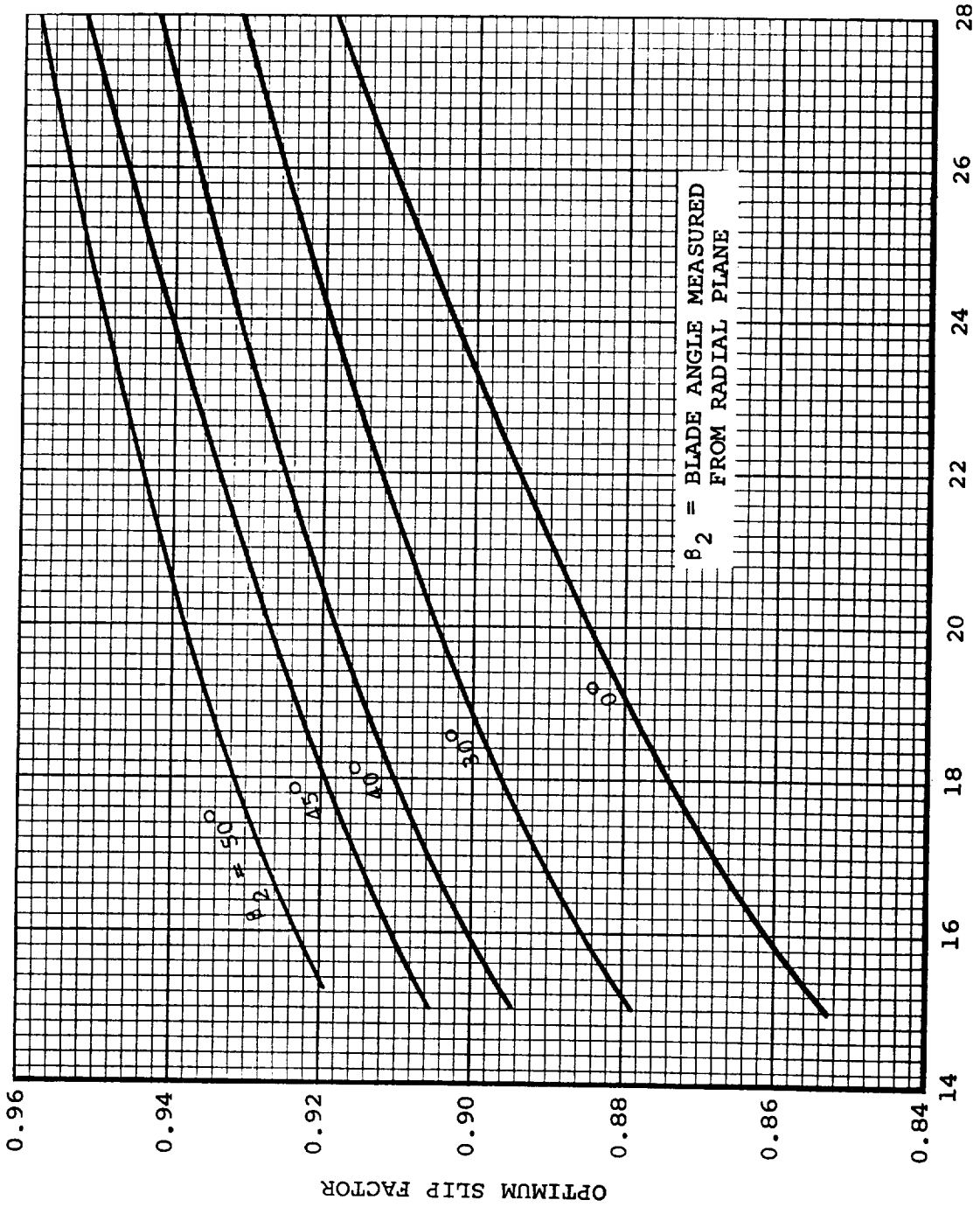
Preliminary vector diagrams were generated for both turbines by initially choosing the rotor reaction ratio to be the same value as the BRU design and varying the rotor tip speed values until F_v values close to 1.0 were obtained. These preliminary vector diagrams, together with resultant reasonable stress distributions for both designs, indicated that the optimum value of F_v could be met without compromise.

5.3.1.2 Rotor Reaction Ratio Study

A detailed tradeoff study was conducted to establish a rotor reaction ratio that would produce a minimum combination of rotor and diffuser dump losses. High reaction ratios favor rotor efficiency while low reaction ratios reduce diffuser losses.

The tradeoff study required velocity distributions within the nozzle vanes and rotors. Therefore, for each reaction ratio investigated, it was necessary to generate complete turbine geometry and the resultant velocity distributions followed by a boundary layer analysis calculation.

The number of rotor blades for the two turbine designs was selected from the shockless entry slip factor criterion of Senoo[2] with due regard for the physical size of the wheels. Figure 36 is a plot of optimum slip factor as a function of blade number and wheel tip blade angle. Experience with the 20-blade BRU design combined with the data of Figure 36 indicates that the reasonable blade number range for the TAC turbines is 16 to 24. A blade number on the high side of



OPTIMUM SLIP FACTOR VS NUMBER OF BLADES
TAC RADIAL TURBINE

FIGURE 36

this range improves the blade-to-blade loadings of the wheels but increases the wetted surface area. The establishment of optimum blade number requires detailed calculations of blade surface velocities and boundary layer momentum thickness. Blade numbers of 24 (12 full blade and 12 splitter blades) for the 24,000-rpm design and 22 (11 full blade and 11 splitter blades) for the 36,000-rpm design were tentatively selected based on the assumption that blade-to-blade loadings were more critical than the penalty associated with the increased surface area. This assumption will be verified by detailed loss calculations that will be made during the final design calculations. This blade number for the final design may be different than that given here.

All of the factors discussed to this point produce turbine wheel geometries that exist as two annulii unrelated by an axial dimension. The axial lengths for the two rotor designs were determined by using the pitch previously obtained and the Zweiful[3] blade loading criterion for the wheel exducer sections. It was assumed that axial turning occurs from an axial location corresponding to the rotor inlet passage b width to the exducer trailing edge. A Zweiful loading coefficient value slightly lower than that used in the BRU design produced reasonable wheel axial lengths.

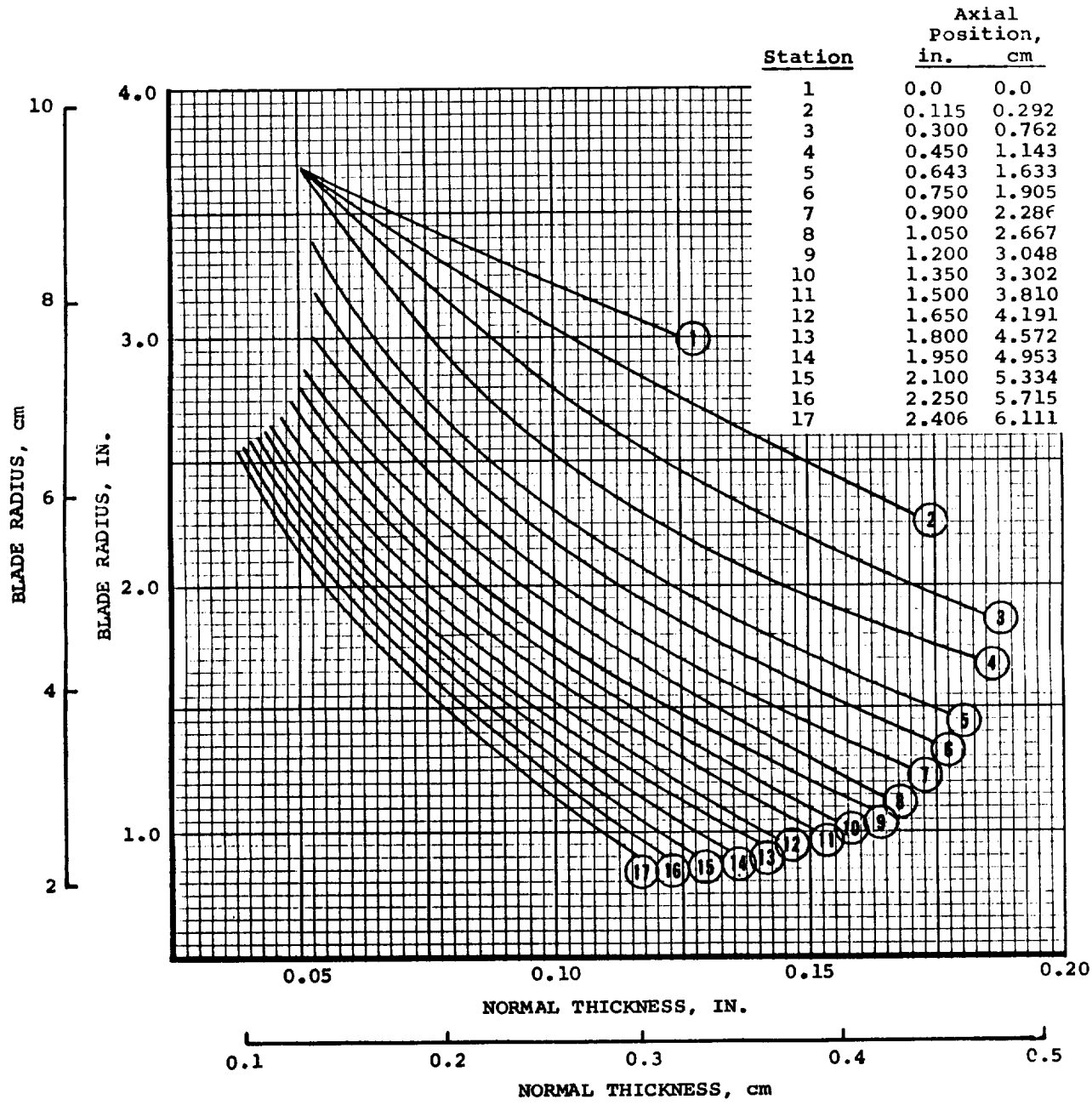
The shroud contours were calculated to have smooth first and second derivatives. The blade theta distribution was generated as a first order involute using the suction surface along the shroud streamline. Because the wheels were designed having radial blades, the shroud contour and theta distribution completely defines the blade beta distribution.

The blade normal thickness distributions were scaled from two current AiResearch designs as a compromise between a highly stressed advance APU design and the lightly stressed BRU design. The normal thickness distributions used for the TAC wheels are shown in Figures 37 and 38. This thickness distribution is intended to provide blade stress levels consistent with design-life criterion.

Using the geometry shown on Table 24, a detailed flow analysis was made considering the effects of rotor blade blockage and blade loading (both axi-symmetric and blade-to-blade). The potential flow analysis includes velocity distributions along the blade as well as the axi-symmetric flow solution.

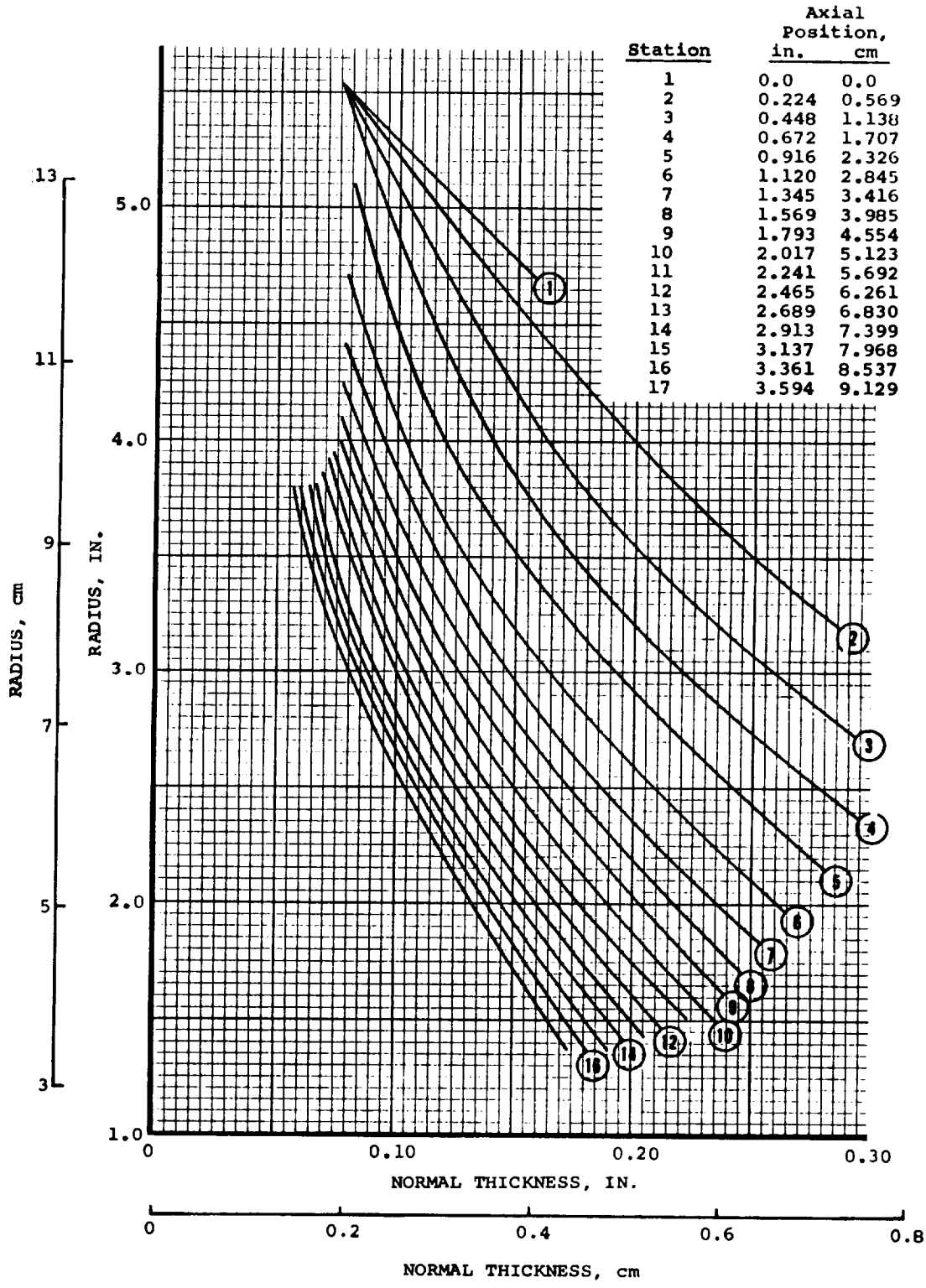
In addition, to calculate stator losses, a boundary layer analysis must be made of the velocity distribution along the blade surface. Thus, at least a "first pass" stator design must be available. As mentioned previously, the nozzle inlet angle from the scroll was assumed to be the same as the BRU nozzle angle of 45°. The nozzle profiles were generated to satisfy the nozzle vector diagrams including the effect of trailing edge blockage. The design procedure actually designs the blade profiles in an axial plane and transforms the resulting shape and velocity distribution to the radial plane using a log-spiral transformation resulting from a sink-vortex flow.

A boundary layer analysis was then made of the calculated stator vane velocity distribution in order to compute fractional total pressure loss. Because the vane end walls are subjected to the same boundary layer experienced by the vanes, a simple area ratio correction gave the loss of the entire vane from the boundary layer calculated along the blade surfaces. The resulting predicted total fractional pressure losses for the scroll, nozzle, end walls, and vaneless space are 0.01868 for the 24,000-rpm turbine and 0.01719 for the 36,000 rpm turbine.



NORMAL THICKNESS DISTRIBUTION - TAC 36,000 RPM TURBINE

FIGURE 37



NORMAL BLADE THICKNESS DISTRIBUTION FOR 24,000 RPM TAC TURBINE

FIGURE 38

TABLE 24

TURBINE PHASE I PARAMETRIC DESIGN

	24,000 rpm	36,000 rpm
Inlet temperature, °R (°K)	2060. (1144)	2060. (1144)
Overall pressure ratio	1.786	1.786
Corrected flow, lb/sec (kg/sec)	2.869 (1.301)	1.350 (0.612)
Tip speed, ft/sec (m/sec)	1157.9 (352.9)	1162.6 (354.4)
Inducer tip radius, in. (cm)	5.529 (14.044)	3.701 (9.401)
Exducer tip radius, in. (cm)	3.790 (9.627)	2.590 (6.579)
Exducer hub radius, in. (cm)	1.3871 (4.752)	0.9247 (2.349)
Inducer blade width, in. (cm)	0.9157 (2.326)	0.6426 (1.632)
Wheel axial length, in. (cm)	3.594 (9.129)	2.406 (6.111)
Exit swirl angle, deg.	0.	0.
Nozzle angle, deg.	74.	74.
Diffuser pressure recovery factor	0.60	0.60
Exducer exit Mach number	0.157	0.157
Number of blades	24	22
Velocity factor	1.012	1.016

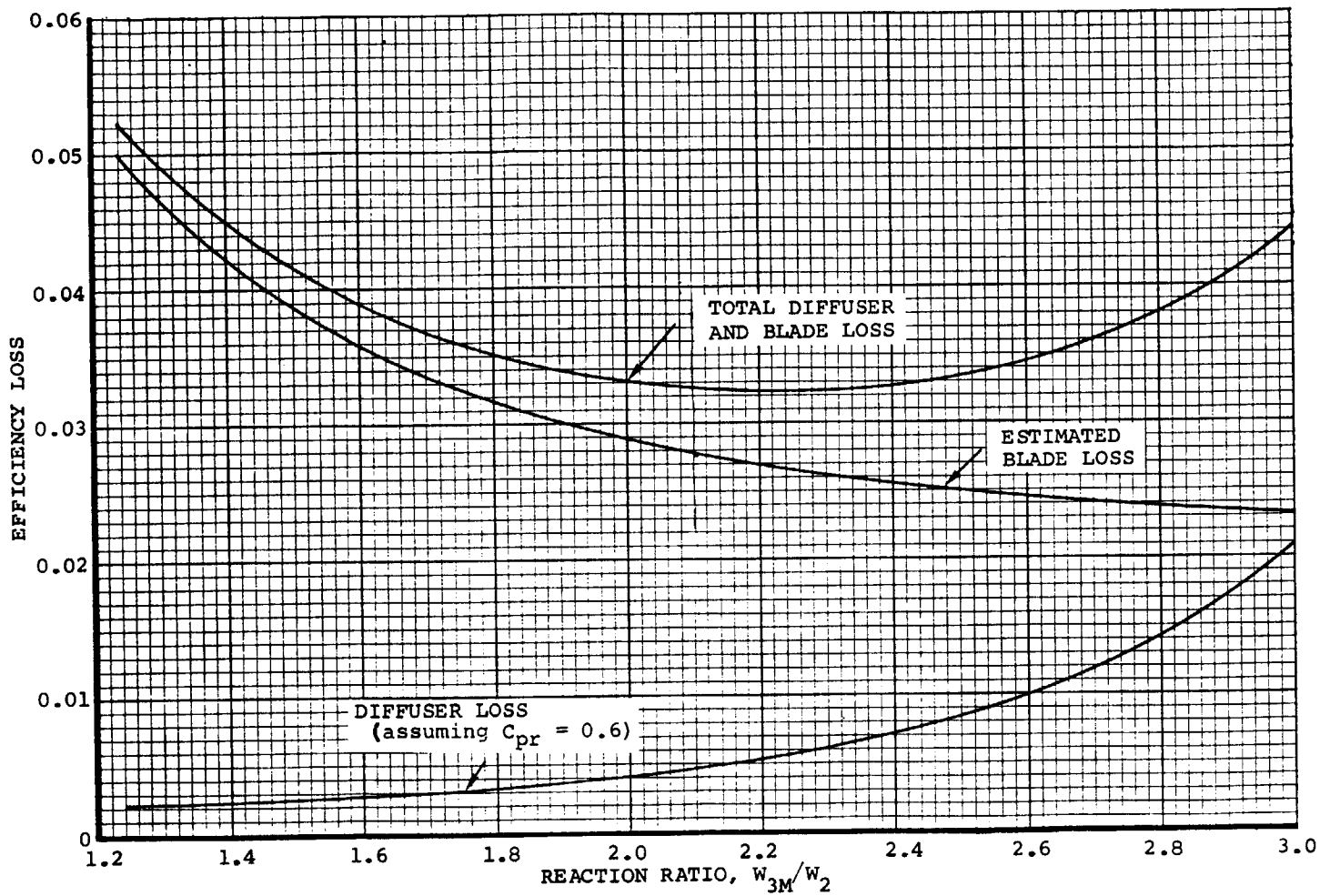
The effect of rotor reaction on turbine efficiency was estimated by utilizing the tentative geometry and vector diagrams obtained from the first solution. For each value of reaction ratio examined (from 1.2 to 3.0), a blade surface boundary layer calculation was performed for both the TAC turbines.

Using efficiency data from the BRU turbine, the blade surface boundary losses were estimated. These losses were applied to the TAC turbines by assuming that the TAC losses would vary as the ratio of the TAC calculated boundary layer momentum thickness to the BRU calculated boundary layer momentum thickness at the pitch line.

The BRU wheel surface loss was estimated to be 2.8 efficiency points based on published pitch-line efficiency[7] after subtracting estimated nozzle and scroll losses. TAC blade surface losses and the diffuser loss (based on 60-percent recovery) are shown on Figure 39 as a function of reaction ratio (w_{3m}/w_2). The optimum reaction ratio appears to lie within the range of 2.00 to 2.40 with respect to minimized losses.

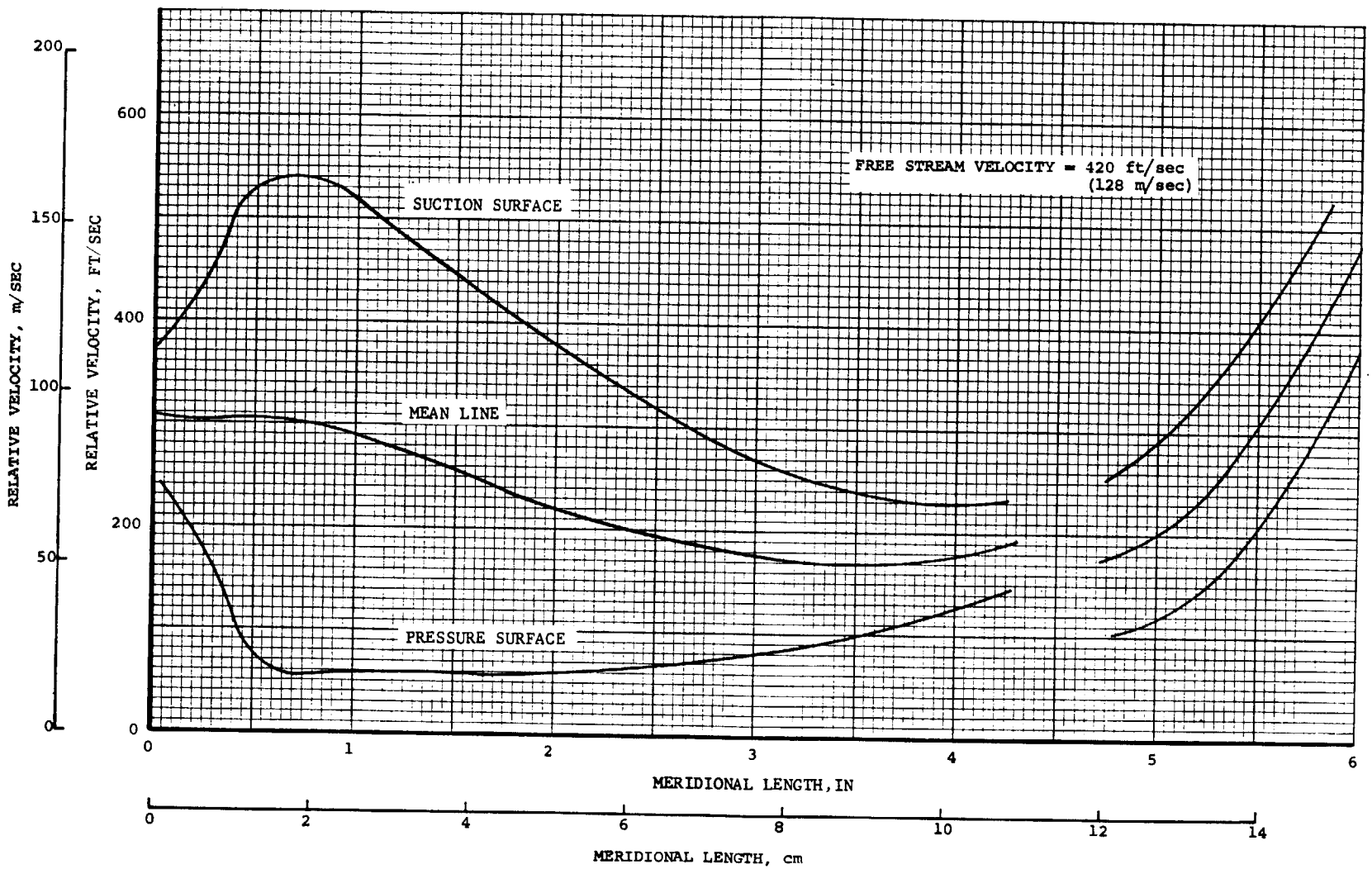
Selection of an optimum reaction ratio for the two turbines permitted final solution of the detailed valocity distribution and boundary layer analysis.

Figures 40, 41, and 42 present the relative velocity profiles generated by the computer program for the 24,000-rpm design. Only the hub, mean, and tip stream tubes are plotted although both turbines were analyzed using 15 stream tubes. Figures 43 and 44 present the final vector diagrams for the turbines, including the effects of blockage and tangential velocity gradient.



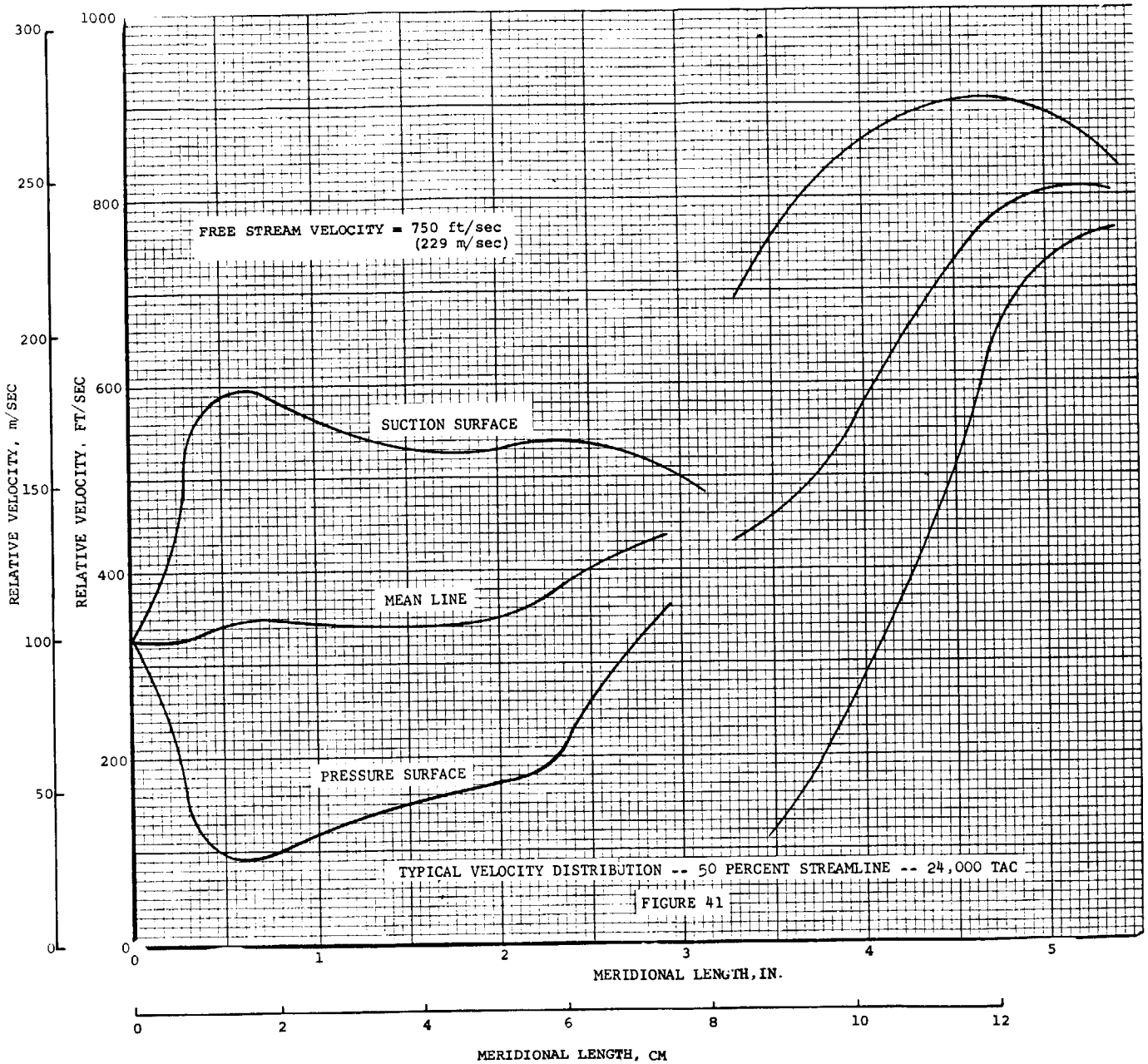
BLADE LOSS AND DIFFUSER LOSS AS A FUNCTION OF ROTOR REACTION RATIO

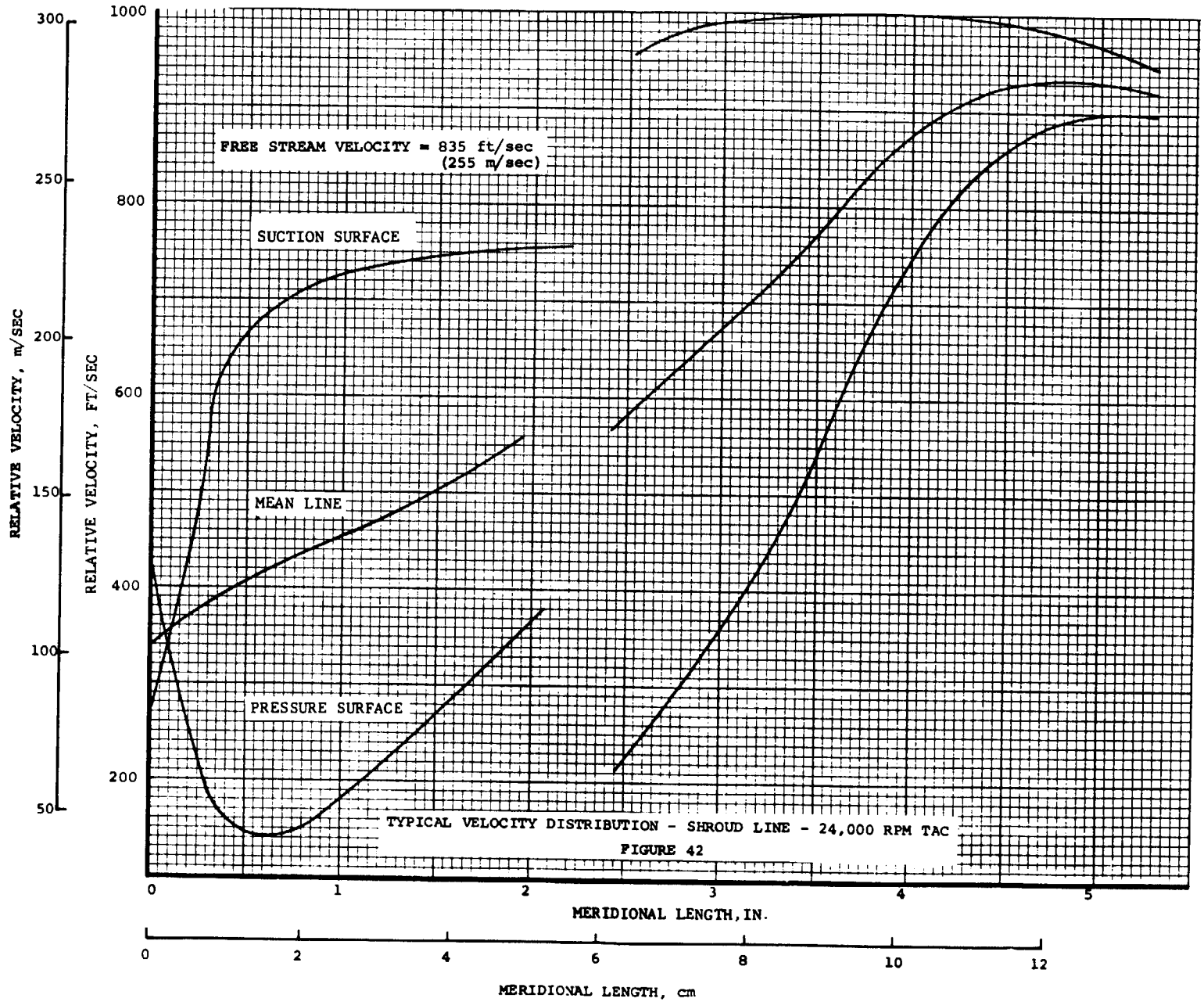
FIGURE 39



TYPICAL VELOCITY DISTRIBUTION--HUB LINE--24,000 TAC

FIGURE 40


FREE STREAM VELOCITY = 750 ft/sec
(229 m/sec)
SUCTION SURFACE
MEAN LINE
PRESSURE SURFACE
RELATIVE VELOCITY, m/SEC
RELATIVE VELOCITY, FT/SEC
MERIDIONAL LENGTH, IN.
MERIDIONAL LENGTH, CM
TYPICAL VELOCITY DISTRIBUTION -- 50 PERCENT STREAMLINE -- 24,000 TAC
FIGURE 41



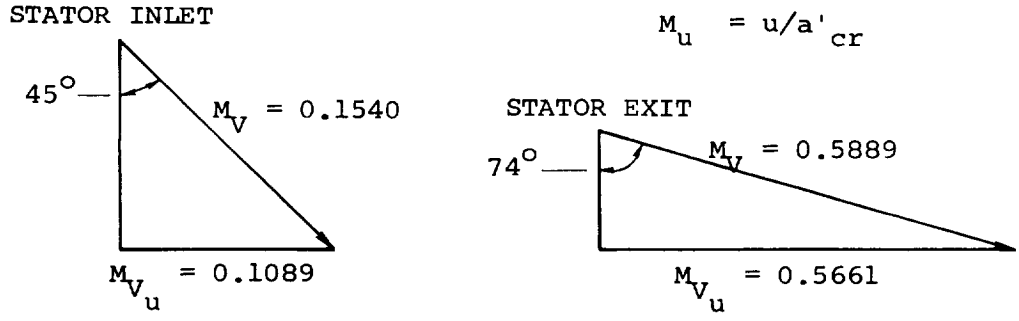
TYPICAL VELOCITY DISTRIBUTION - SHROUD LINE - 24,000 RPM TAC

FIGURE 42

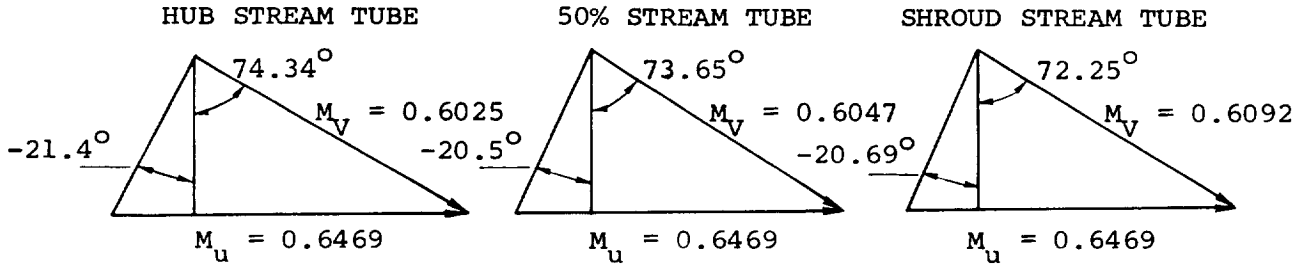
NOMENCLATURE: $M_V = V/a'_{cr}$

$M_{V_u} = V_u/a'_{cr}$

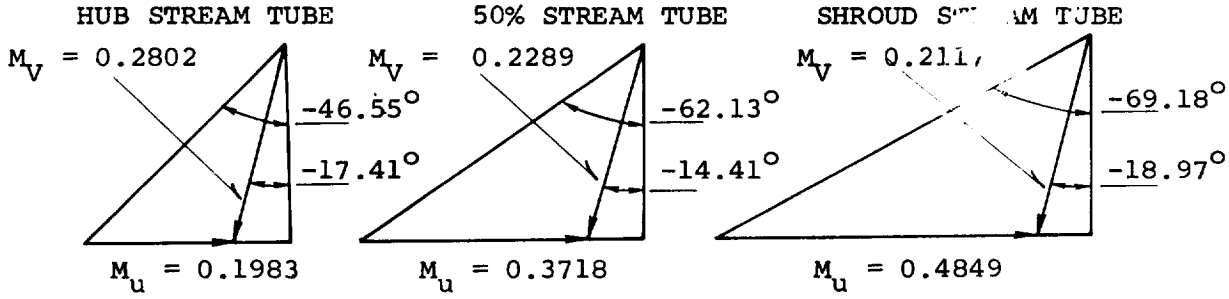
$M_u = u/a'_{cr}$



ROTOR INLET
(INSIDE BLADE ROW)



ROTOR EXIT
(INSIDE BLADE ROW)



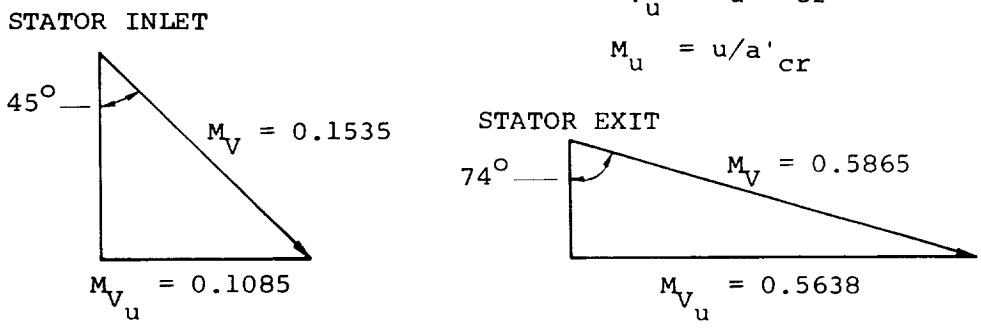
VECTOR DIAGRAMS FOR 24,000-RPM TAC

FIGURE 43

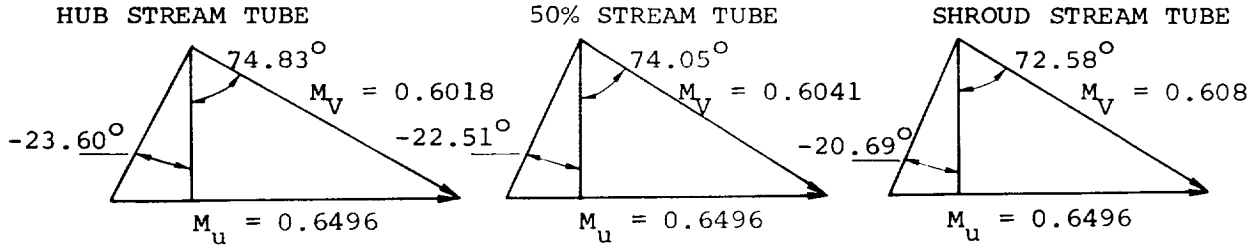
NOMENCLATURE: $M_V = V/a'_{cr}$

$M_{V_u} = V_u/a'_{cr}$

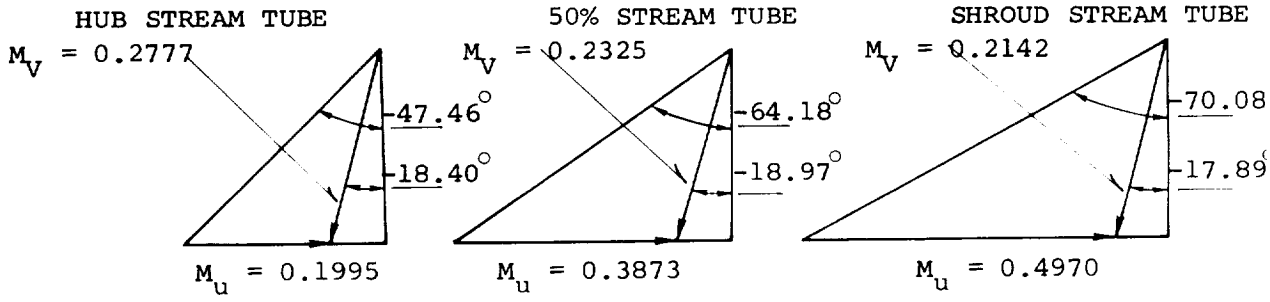
$M_u = u/a'_{cr}$



ROTOR INLET
(INSIDE BLADE ROW)



ROTOR EXIT
(INSIDE BLADE ROW)



VECTOR DIAGRAMS FOR 36,000-RPM TAC

FIGURE 44

A final boundary layer analysis was performed on all surfaces from the scroll inlet to the rotor exit to predict the fractional pressure loss associated with each surface for both wheels. For the blade splitter surfaces, calculations were made for the hub, mean, and shroud line stream tubes and the average value of fractional pressure loss was assigned to these surfaces. The hub surface loss was computed assuming the effective velocity profile was the average relative velocity at this location from the axi-symmetric solution. The shroud loss calculation was performed using the absolute velocity profile along the shroud line. The blade surface losses and mixing losses were calculated after the method of Stewart[4].

The two additional losses left before defining turbine performance are wheel backface loss and clearance loss. Backface loss was computed with the technique given by Reference 5 using a fluid viscosity based on static temperature and pressure at the rotor inlet. Clearance loss was estimated using the size/clearance correlation of Reference 6. Losses are negligible in the 24,000-rpm design due to large relative difference between size and clearance. The smaller 36,000-rpm wheel shows a clearance loss equivalent to an efficiency decrease of 0.67 percent.

5.3.2 Final Loss Distribution and Efficiency Predictions

The final loss distribution and efficiency predictions for both TAC turbines together with similar data for the BRU turbine is presented in Table 25. The loss distribution for the TAC turbines is similar to that estimated from BRU turbine data; however, due to a lower exit Mach number (i.e., approximately 0.16 vs 0.23) more diffusion takes place within the TAC rotors than in the BRU, resulting in less kinetic energy entering the diffuser. Therefore, for a given diffuser recovery, the TAC turbine will have lower losses in the diffuser and thus a higher total-to-total overall (scroll inlet to diffuser exit) efficiency.

TABLE 25

ESTIMATED DISTRIBUTION OF LOSSES:
TAC TURBINES - 24,000 AND 36,000 RPM

Losses Expressed in Work-Fraction	Data: BRU Turbine[1]		Prediction for TAC[2]	Calculated Efficiency[3]	
	Re_t = 76,000	Re_t = 176,000		TAC 24	TAC 36
Stator and Scroll Loss	0.0319	0.0276	0.0230	0.0268	0.0243
Rotor Loss	0.0502	0.0434	0.0520	0.0435	0.0478
Clearance Loss			0.0125	--	0.0067
Windage Loss	0.0049	0.0040	0.0125	0.0040	0.0036
Exit Velocity Head	0.0410	0.0400	0.0300	0.0260	0.0258
TOTAL Losses	0.1280	0.1150	0.1300	0.1003	0.1082
Resultant Static Efficiency (1 - total losses)	0.8720	0.8850	0.8700	0.8997	0.8918
TOTAL Rotor Efficiency	0.9130	0.9250	0.9000	0.9257	0.9176

[1]From Nusbaum and Kofskey (Ref. 2) loss distribution is estimated, static efficiency is test data

[2]Empirically extracted from Rohlik (Ref. 1).

[3]Based on a three-dimensional radial in-flow turbine design analysis, using a boundary layer calculation to predict losses.

NASA's selection of either the diffuser length or the diffuser exit Mach number will determine the value of overall efficiency as shown on Figure 45. The diffuser lengths plotted in Figure 45 are minimum total pressure loss diffusers obtained in the manner of Reference 8.

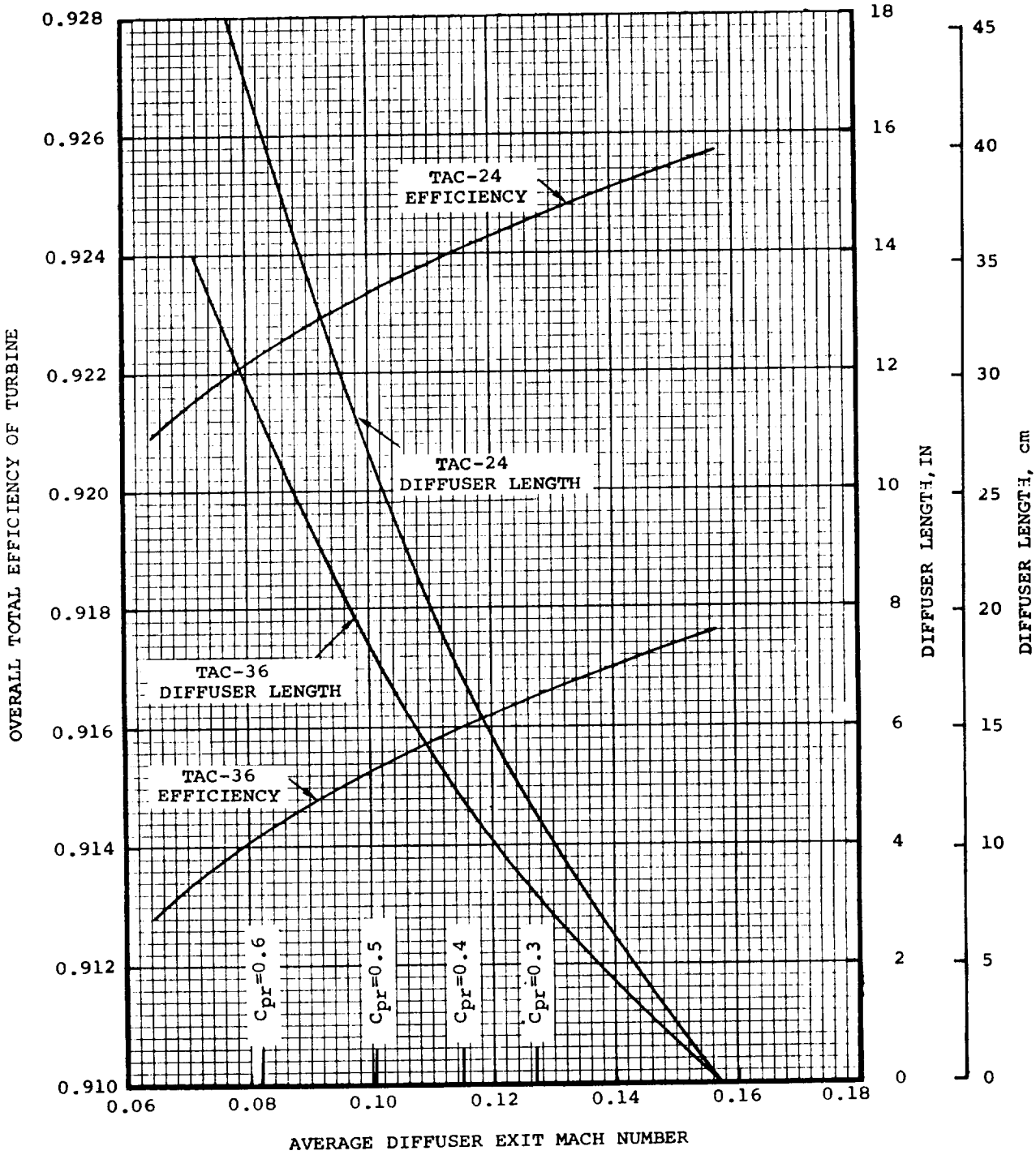
Test data relating efficiency to turbine Reynolds number ($m/\mu_2 r_2$) are presented in Figure 46. The static and total efficiencies at design-point operation (based on turbine-inlet, rotor-exit and diffuser-exit condition) are shown as functions of Reynolds number for the BRU turbine. It is observed that the TAC turbines operate at Reynolds numbers favorable to high efficiency.

5.3.3 Turbine Stress Analysis

The determination of the stress distribution in bladed asymmetrical disks (due to the centrifugal force of rotation, the axial and radial variation in temperature, the mechanical properties of the disk material, and the bending caused by axial pressure loading) is a problem best solved by utilizing finite element techniques. The finite element method has received extensive coverage in recent technical publications and is accepted as being the most accurate means of analysis for complex boundary value problems. This analysis has been expressed in numerical form and programmed for the high-speed digital computer. The assumptions, equations, and procedure are briefly stated below.

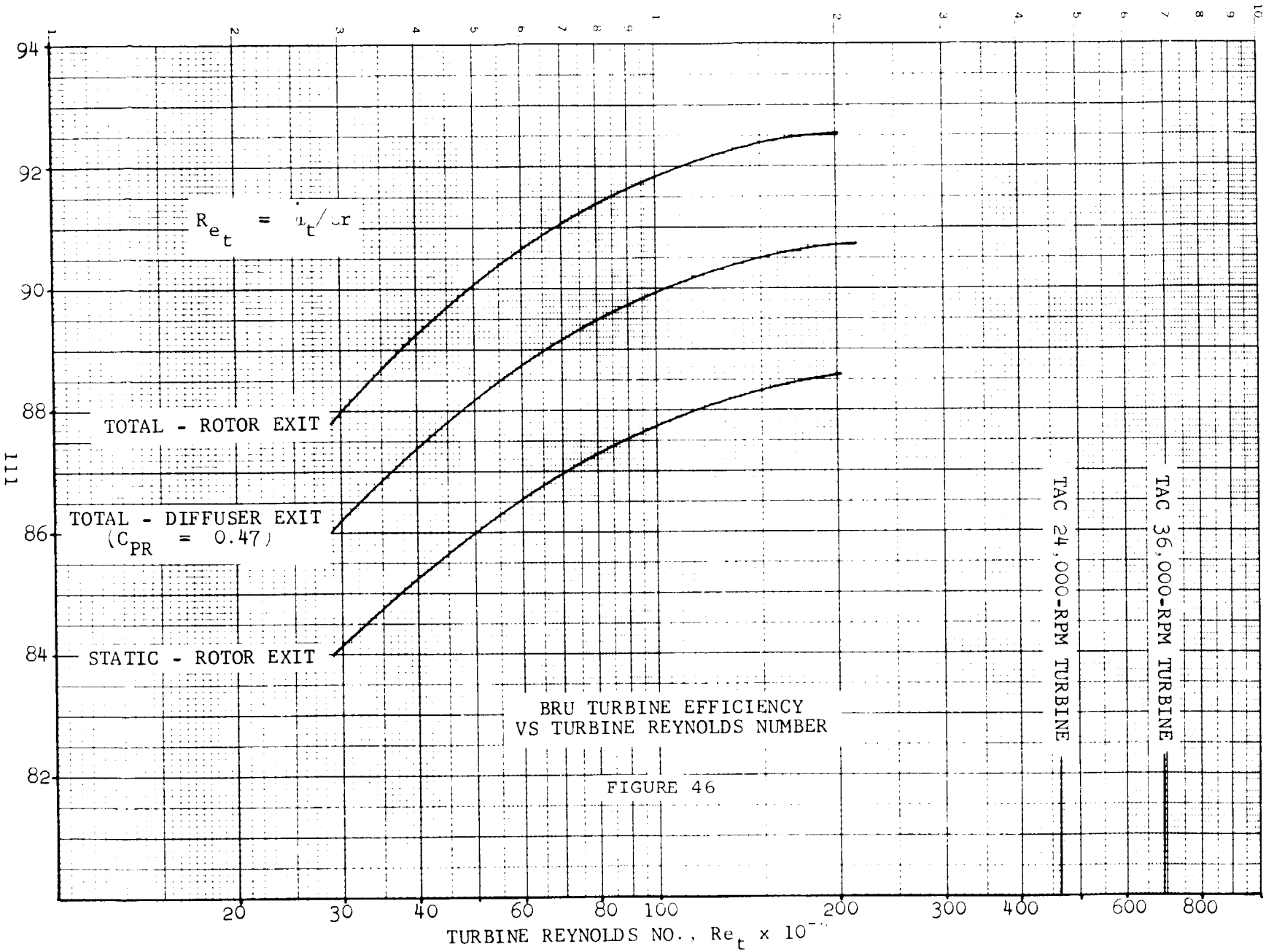
Assumptions

(a) Blades are utilized as plane stress elements (no circumferential stress component) with boundary conditions meeting both disk and blade requirements.



OVERALL TURBINE TO DIFFUSER EXIT TOTAL-TO-TOTAL EFFICIENCY AND DIFFUSER LENGTH AS FUNCTIONS OF DIFFUSER EXIT MACH NO.

FIGURE 45



BRU TURBINE EFFICIENCY
VS TURBINE REYNOLDS NUMBER

FIGURE 46

(b) The disk is considered circumferentially symmetrical with the blade loads distributed uniformly in the tangential direction. Axial, radial and tangential equilibrium and compatibility requirements are satisfied.

Equations

The finite element method is based upon an assumed displacement pattern of the disk or blade element given by

$$u = a_1 + a_2 r + a_3 z + a_4 rz$$

$$w = a_5 + a_6 r + a_7 z + a_8 rz$$

where

u	= radial displacement
w	= axial displacement
$a_1 \longrightarrow a_i$	= vector constants that are evaluated in terms of the elements corner displacements
r, z	= radial and axial coordinate variables, respectively

Utilizing the above-assumed displacement pattern, the finite element method forms the element equilibrium equation by equating the work down by the nodal forces to the strain-energy of the element. This results in the relationship

$$\left[k\right] \left\{u\right\} = \left\{F\right\}$$

where

k is denoted as the element stiffness matrix

F is applied forces, body forces and thermal forces

A separate stiffness matrix is formed for the disk elements (trapizoidal and triangular) and blade elements in that the tangential (circumferential) effects are included in the disk and are not included in the blade.

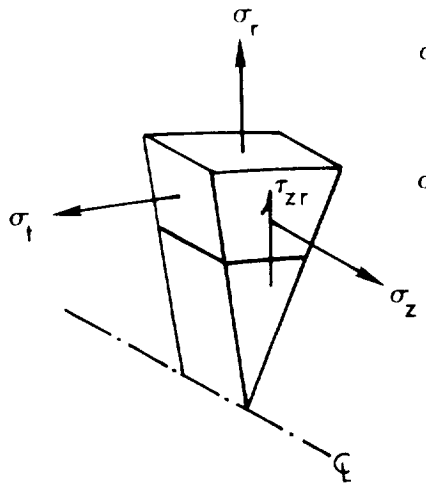
The final solution is then achieved by the simultaneous solution of the equations for the unknown displacements in both disk and blade.

$$\left[K_T\right] \left\{U_T\right\} = \left\{F\right\}$$

where

K_T is the complete stiffness matrix of the blade-disk configuration that is assembled from the individual element stiffness matrices.

Stresses acting on each element are obtained from the appropriate stress-displacement relationships of elasticity. Radial, tangential, axial and shear stresses are calculated and combined to form an equivalent stress as defined in Figure 47 for each finite element.



σ_e = Equivalent Stress

$$\sigma_e = \sqrt{\frac{1}{2}\left[\left(\sigma_r - \sigma_t\right)^2 + \left(\sigma_t - \sigma_z\right)^2 + \left(\sigma_z - \sigma_r\right)^2 + 6\,\tau_{zr}^2\right]}$$

FIGURE 47

The turbine geometry selected in 5.3.1 was used as input to the above program and the equivalent stress was calculated for the 24,000 and 36,000 rpm, (INCO 713) turbine designs (Figures 48, 49, and 50). The temperature distribution appearing in the above figures is a scale of known temperatures from the NASA BRU turbine which has similar thermal conditions.

It is important to note that within the computer program suitable restrictions were placed on the curvic end of the turbine wheel to simulate the connection to the remaining rotating assembly. Also important in the analysis is the way blading is treated. Input to the program for finite elements (of blades) is the number of blades and the tangential thickness of the blade at each element. Thus, the blades give accurate weight loadings to the disk.

Results of the stress program combined with material properties appear in Figures 51 and 52. These are plots of the peak equivalent stress computed at a constant axial location for both design and over-speed conditions.

Also plotted are the INCO 713 strength properties for each corresponding stress element with temperature effects taken into account. Both wheel stress levels appear sufficiently removed from the stress-rupture curve based on 50,000 hours design life.

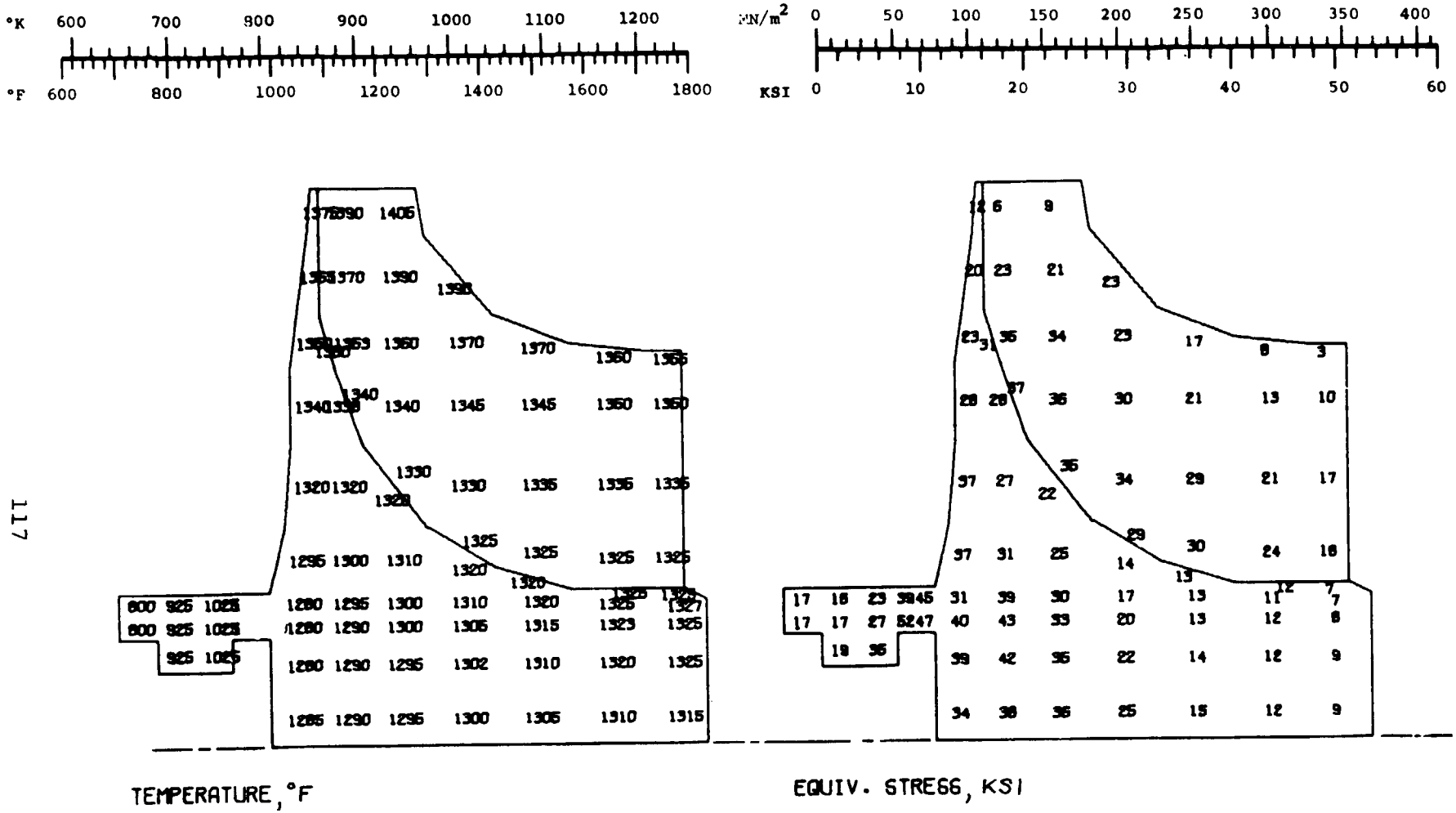
A detailed finite element creep analysis was performed for both wheels based on 50,000 hours. As can be seen from Figures 51 and 52, creep stress levels still fall below those permissible for 50,000 life at design speed.

24,000 RPM TAC TURBINE AT OVERSPEED AND OVERTEMPERATURE

FIGURE 48

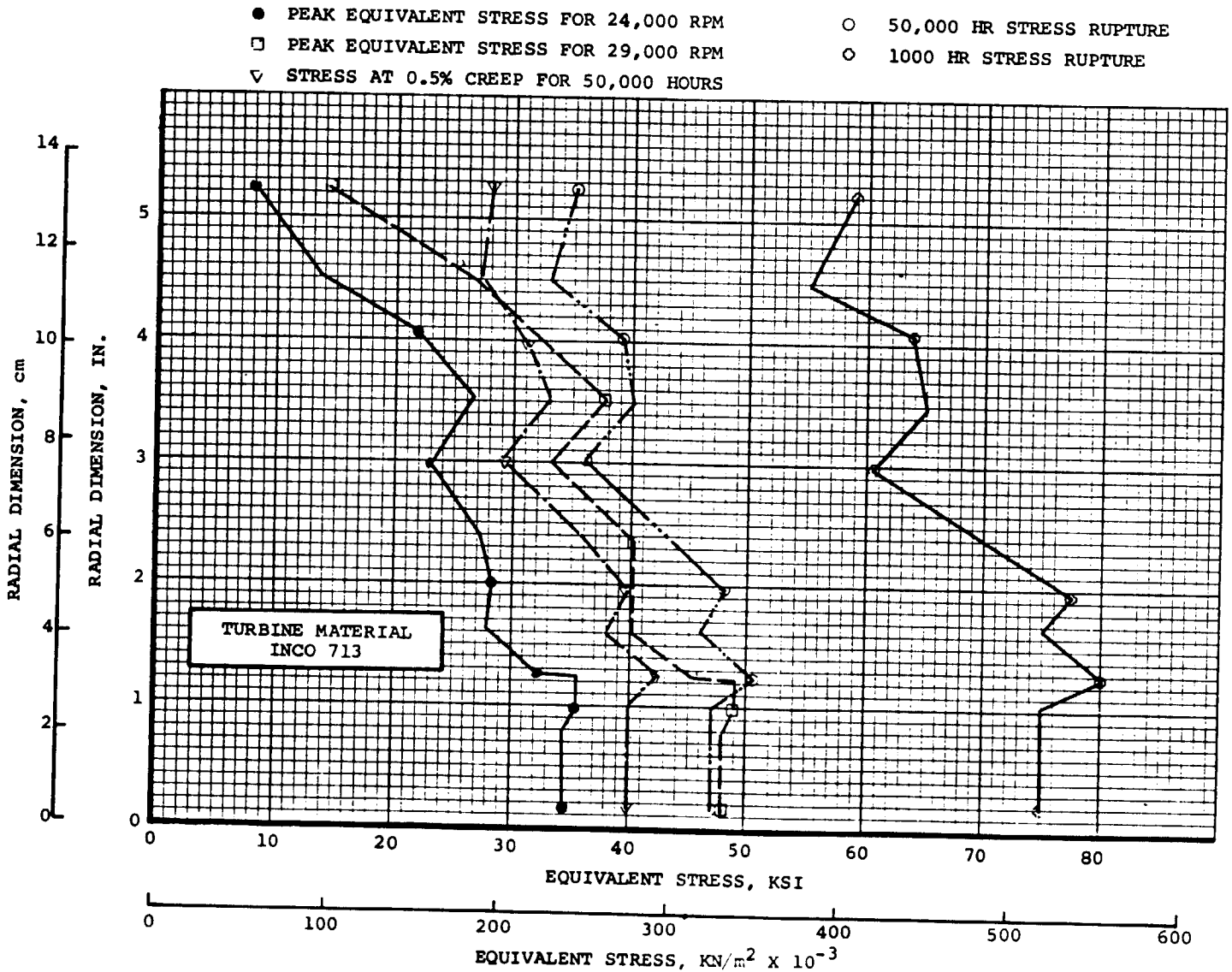
24,000 RPM TEST TURBINE AT OVERSPEED AND OVERTEMPERATURE

FIGURE 49



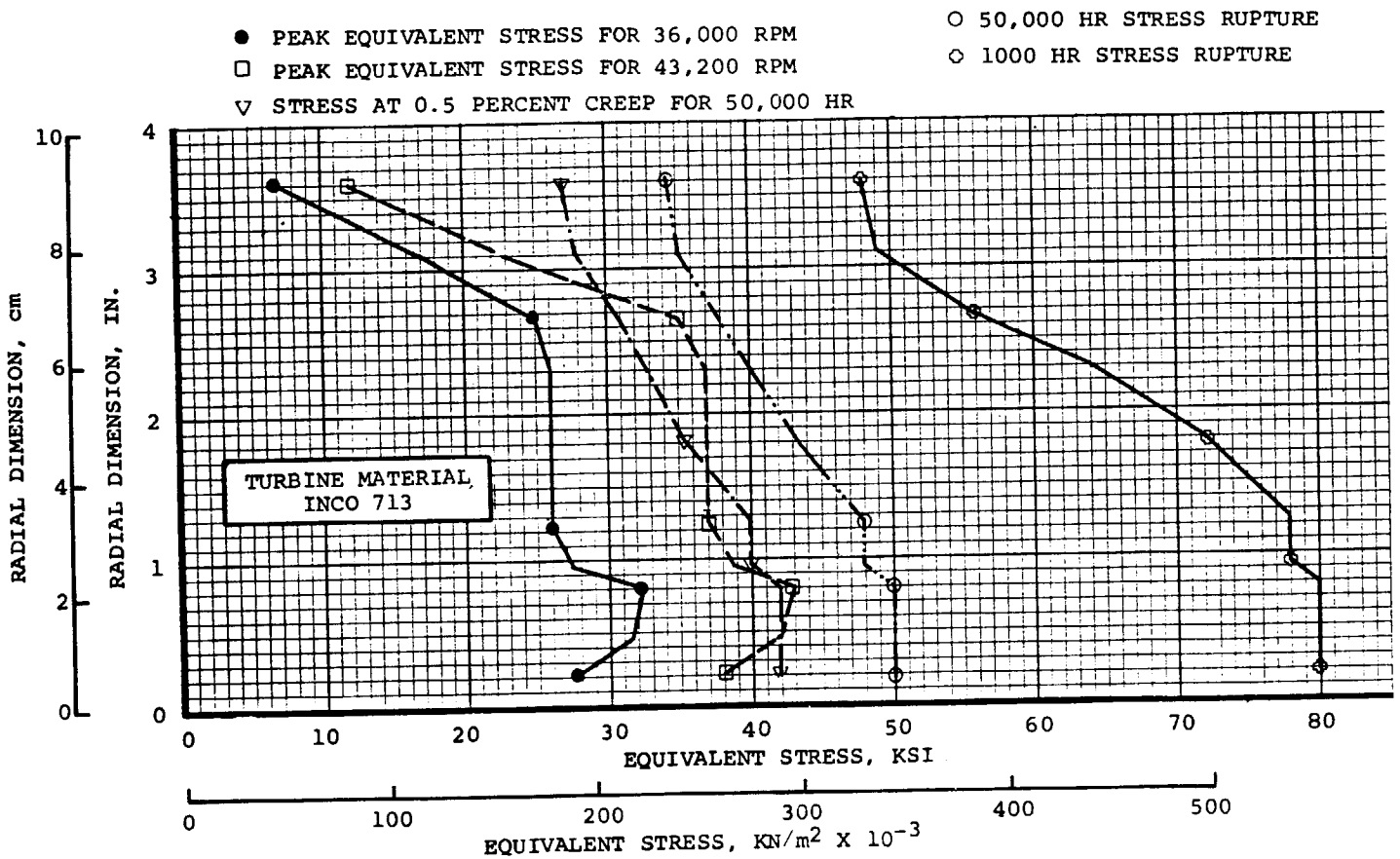
36,000 RPM TAC TURBINE AT OVERSPEED AND OVERTEMPERATURE

FIGURE 50



EQUIVALENT STRESS DISTRIBUTION VS RADIAL DIMENSION
TAC RADIAL TURBINE

FIGURE 51



EQUIVALENT STRESS DISTRIBUTION VS RADIAL DIMENSION
TAC RADIAL TURBINE

FIGURE 52

References for Section 5.3

1. Rohlik, Harold E., "Analytical Determination of Radial Inflow Turbine Design Geometry for Maximum Efficiency," NASA TN-D 4384, 1968

2. Perrone, George L. and Yasutoshi Senoo, "Unpublished Notes at AiResearch," 1963, Computer Program 5516.

3. Zweiful, O., "The Spacing of Turbo-Machine Blading, Especially with Large Angular Deflection," Brown Boveri Review, Vol. 32, Dec. 1945.

4. Stewart, Warner L., "Analysis of Two-Dimensional Compressible-Flow Loss Characteristics Downstream of Turbomachine Blade Rows in Terms of Basic Boundary-Layer Characteristics," NACA TN 3515, July 1955.

5. Schlichting, Hermann, "Boundary Layer Theory", Fourth Edition, McGraw Hill Book Co., New York, pp. 547-550, 1960.

6. Penny, Noel, "Rover Case History of Small Gas Turbines," SAE Preprint 634A, for the Automotive Engineering Congress, Detroit, Michigan, January 14, 1963.

7. Kofskey, Milton G. and William J. Nusbaum, "Cold Performance Evaluation of 4.97-In. Radial Inflow Turbine Designed for Single Shaft Brayton Cycle Space Power System," NASA TN D-5090, March 1969.

8. Sovran, Gino and Edward D. Klomp, "Experimentally Determined Optimum Geometries for Rectilinear Diffusers with Rectangular, Conical or Annular Cross-Section," General Motors Corporation, Research Labs, Warren, Michigan, Research Publication GMR-511, November 1965.

5.4 TAC Alternator Studies

5.4.1 Preliminary Screening Studies

Preliminary screening studies were conducted to evaluate both solid rotor inductor alternators and bonded rotor Lundell alternators for the TAC application. The overall performance specifications for this application are summarized in Table 26. Table 27 summarizes the speed and frequency configurations which were evaluated during this study.

The preliminary screening studies involved trial designs in which several parameters were systematically varied. Tables 28, 29 and 30 summarize the results of these trial design studies.

TABLE 26

TAC ALTERNATOR SUMMARY SPECIFICATIONS

Design output power, kw	160
Power output range, kw	40 to 160
Power factor	.75 lagging
KVA rating, kva	214
Speed, rpm	24,000 and 36,000
Overspeed capability, %	120
Design life, years	5
Coolant temperature, °R (°K)	956 (531)
Allowable hot spot temperature, °R (°K)	1260 (700)
Maximum voltage unbalance, %	9
Maximum windage, kw	9.6
Voltage - 3Ø, 120-v to 480-v L-N	
Frequency 400 to 2400-Hz, 400-Hz intervals	

TABLE 27

ALTERNATOR CONFIGURATIONS

Alternator Type	24,000 rpm		36,000 rpm	
	No. of Poles	Frequency (Hz)	No. of Poles	Frequency (Hz)
Lundell	2	400		
Lundell	4	800	4	1200
Lundell	6	1200		
Inductor	4	800	4	1200
Inductor	6	1200		
Inductor	8	1600	8	2400
Inductor	10	2000		
Inductor	12	2400		

From the alternators presented in the above tables, three were selected for further analyses:

(a) Lundell Alternator: 24,000-rpm, 6-pole, 1200-Hz

(b) Lundell Alternator: 36,000-rpm, 4-pole, 1200-Hz

(c) Inductor Alternator: 36,000-rpm, 4-pole, 1200-Hz

A Lundell-type alternator is the first choice for the 24,000- and 36,000-rpm units. This is primarily due to the lower windage losses of the Lundell-type that result from an inherently smooth rotor of a smaller diameter than a comparable inductor and higher overall efficiency.

TABLE 28

214 KVA LUNDELL GENERATOR DESIGN SUMMARY
0.75 PF (LAG)

Design Reference Number	Speed (rpm)	Poles	Frequency (Hz)	Volts per Phase	Rotor Steel	X_d Synchronous Reactance Per Unit[a]	Turns per Phase	Slots	Machine Dimensions (inches)			
									Stack Length	Frame Diameter	Overall Length	Rotor Diameter
									(cm)	(m)	(m)	(cm)
A-1	24,000	2	400	240	Hiperco 27	1.3	8	48	4.95 (12.58)	17.2 (.437)	14.2 (.361)	8. (20.31)
B-1	24,000	4	800	240	Hiperco 27	0.95	12	72	3.45 (8.76)	13.3 (.338)	8.0 (.203)	7. (17.78)
C-1	24,000	6	1200	240	4340 R_c 49	0.55	10	90	3.4 (8.63)	14.9 (.378)	10.8 (.274)	9.25 (23.48)
C-2	24,000	6	1200	240	4340 R_c 49	0.85	15	90	2.5 (6.35)	14.0 (.356)	9.3 (.236)	8.0 (20.31)
C-3	24,000	6	1200	240	4340 R_c 49	1.33	21	63	1.91 (4.85)	14.1 (.358)	8.15 (.207)	7.45 (18.91)
C-4	24,000	6	1200	240	4340 R_c 33	0.87	15	90	2.7 (6.86)	13.6 (.345)	9.5 (.241)	7.5 (19.04)
C-5	24,000	6	1200	120	4340 R_c 33	0.76	7	63	2.7 (6.86)	13.3 (.338)	9.5 (.241)	7.5 (19.04)
D-1	36,000	4	1200	120	H-11		8	96	3.56 (9.04)	13.3 (.338)	9.56 (.243)	7.5 (19.04)
D-2	36,000	4	1200	240	H-11	0.86	10	60	3.12 (7.92)	12.73 (.324)	9.22 (.234)	7.125 (18.09)
D-3	36,000	4	1200	240	4340 R_c 33	1.04	12	72	2.9 (7.37)	12.07 (.305)	8.7 (.221)	6.35 (16.11)

(a) Main Gap = 0.07 inches, (1.778 mm), auxiliary gap = 0.05 inches (1.27 mm)

(*) or 4340 @ 49 Rc

TABLE 29

214 KVA LUNDELL GENERATOR DESIGN SUMMARY
0.75 PF (LAG)

Design Reference Number	Densities			Losses (watts)				Efficiency (%)		Electric Weight (lbs)	Phase Balance, % 2/3 1Ø, 1. pF	Estimate Temperature °R (°F)
	Armature Amp/in^2	Field Amp/in^2	Rotor KL/in^2	Pole Face	Windage[b]	Field	Total	Electro-magnetic	Overall			
	(Amp/cm^2)	(Amp/cm^2)	(Weber/ m^2)							(kg)		
A-1	4700 (729)	2560 (397)	82 (127.0)	2207	5454	2138	16,919	93.31	90.43	618 (280)	8.0	790 (963)
B-1	4721 (732)	2465 (382)	97 (150.3)	586	2643	1392	11,251	94.89	93.45	295 (134)	8.0	679 (763)
C-1	5000 (775)	2099 (325)	70 (108.5)	3228	6567	1191	17,649	93.52	90.06	388 (176)	5.1	651 (712)
C-2	4760 (739)	2110 (327)	72 (111.6)	1906	3312	1312	13,204	94.18	92.38	285 (129)	9.7	679 (763)
C-3	4329 (671)	2074 (322)	72 (111.6)	3214	2420	1474	16,282	92.03	90.76	270 (122)	14.31	760 (909)
C-4	5072 (787)	2014 (312)	84 (130.1)	1551	2884	1158	12,736	94.20	92.63	279 (126)	8.9	691 (784)
C-5	4763 (741)	2078 (322)	88 (136.4)	2581	2884	1200	13,049	94.03	92.46	280 (127)	7.8	682 (768)
D-1	6750 (1046)	2000 (310)	67 (103.9)	1185		792				293 (133)	6.0	702 (804)
D-2	5625 (873)	2180 (338)	75 (116.2)	2524	13,065	1165	22,767	94.28	87.55	272 (123)	7.4	720 (837)
D-3	4980 (769)	2358 (365)	89 (138)	2185	9524	1312	19,125	94.34	89.32	221 (100)	9.25	694 (790)

(b) Windage based on 55 psia (37.92 nt/cm^2) at 24,000 rpm and 120 psia (82.74 nt/cm^2) at 36,000 rpm.

TABLE 30

214 KVA INDUCTOR ALTERNATOR DESIGN SUMMARY

DESIGN REFERENCE NUMBER	ALTERNATOR TYPE	RPM	ROTOR MATERIAL	POLES	FREQUENCY Hz	E.M.(1) EFFICIENCY %	WINDAGE(2) LOSS-KW	OVERALL EFFICIENCY %	E.M.(1) WEIGHT LBS (kg)	ROTOR WEIGHT LBS (kg)	ROTOR O.D. INCH (cm)	ROTOR LENGTH INCH (m)	RADIAL GAP LENGTH INCH (mm)	POLE `ACE LOSSES KW	% VOLT. UNBALANCE 2/3-SINGLE PHASE	STATOR HOT SPOT TEMP °F (°K)
I-1	INDUCTOR	24000	HIP-27	4	800	92.9	15.9	85.0	348 (158)	127 (58)	9.101 (23.1)	11.0 (.280)	.07 (1.78)	.99	8.4	898 (753)
I-2	INDUCTOR	24000	HIP-27	6	1200	92.6	10.3	87.4	265 (120)	100 (45)	8.275 (21.0)	10.56 (.268)	.07 (1.78)	1.35	9.9	862 (733)
I-3	INDUCTOR	24000	HIP-27	8	1600	92.8	10.6	87.5	238 (108)	98 (44)	8.335 (21.2)	10.23 (.260)	.07 (1.78)	1.15	8.0	784 (690)
I-4	INDUCTOR	24000	HIP-27	10	2000	91.9	12.3	85.8	237 (107)	103 (47)	8.422 (21.4)	10.38 (.263)	.07 (1.78)	0.96	6.0	738 (665)
I-5	INDUCTOR	24000	HIP-27	12	2400	91.1	9.7	86.3	192 (87)	79 (36)	8.070 (20.5)	9.02 (.229)	.07 (1.78)	1.31	8.9	743 (667)
I-6	INDUCTOR	36000	H-11	4	1200	92.8	>30.	<79.	231 (105)	83 (38)	8.848 (22.4)	7.87 (.200)	.08 (2.03)	1.19	10.7	885 (748)
I-7	INDUCTOR	36000	H-11	8	2400	92.4	>30.	<79.	161 (73)	61 (28)	8.575 (21.8)	6.55 (.166)	.08 (2.03)	0.93	6.8	763 (679)

(1) E.M. = electromagnetic components only.

(2) Preliminary estimates, assume 55 psia pressure for 24,000 rpm speed, 120 psia for 36,000 rpm.

Inductor I-6 was selected as the third alternator (second choice for 36,000 rpm) due to the good mechanical integrity inherent in the one-piece inductor rotor.

Twelve-hundred Hertz was selected as the output frequency for all alternators. This is the lowest that can be readily converted to 400 Hz with a natural cycloconverter. Twelve-hundred Hertz was the highest frequency investigated for the Lundell alternator.

5.4.2 Final Alternator Summary

A preliminary optimization of design and performance parameters of the recommended alternator configurations was performed and electrical performance determined at design power output and 0.75 lagging power factor. Table 31 presents a summary of the design details for the three alternator configurations.

5.4.2.1 24,000 RPM Lundell

Design C-4 was the final 24,000 rpm Lundell design. The layout of this design is shown in Figure 53 and the layout of the slot is shown in Figure 54. The saturation curves are shown in Figure 55. This design has an electrical efficiency of 94.2 percent, decreasing to 92.6 percent when windage is included. Figure 56 shows the efficiency variation with load. A breakdown of losses versus load (0.75 P.F.) is shown on Page 133.

TABLE 31

INTERNAL DESIGN DETAILS SUMMARY:

60° Phase Belts, 2/3 Pitch; 90% Stacking Factor:

	6-POLE LUNDELL (C-4) 24,000 RPM	4-POLE LUNDELL (D-2) 36,000 RPM	4-POLE INDUCTOR 36,000 RPM
Current Densities - Armature	5071 (786)	5625 (872)	4788 (741)
amps/in^2 (amps/cm^2) - Field	2014 (332)	1165 (181)	3885 (602)
Flux Densities - Back Iron	64 (99.2)	65 (101)	59 (91.5)
kl/in^2 (weber/m^2) - Teeth	129 (200)	124 (192)	135 (209)
- Main Air Gap	52 (80.6)	46 (71.3)	56 (86.8)
- Pole	84 (130)	75 (116)	80 (124)
- Frame	110 (171)	115 (178)	112 (174)
- Aux. Air Gap	57 (88.4)	57 (88.4)	N.A.
Rotor % Magnetic Steel -	55	55	N.A.
% Harmonics - Third	0	0	0
- Fifth	3.3	3.3	1.3
- Seventh	2.0	2.0	1.7
F.L. Losses - Pole Face	1552	2538	1089
(watts) - Back Iron	2213	2935	4771
- Teeth	1683	841	798
- Armature	3247	2236	3218
- Field	1158	1165	1990
- Windage	2884	13065	2080
(@ psia)	(55)	(120)	(1)
- Total	12.73%	22780	13.946
Overall Efficiency-	92.6%	87.6%	92.0%
No Load Loss -	5200	6000	----
Electrical Weights - Armature	13 (5.89)	9 (4.08)	16 (7.25)
pounds (kg) - Field	49 (22.2)	42 (19.0)	22 (10.0)
- Frame	85 (38.5)	88 (35.4)	36 (16.3)
- Stacks	35 (15.9)	41 (18.6)	81 (36.7)
- Rotor	98 (44.4)	92 (41.7)	83 (37.6)
- Total	280 (127)	272 (123)	238 (108)

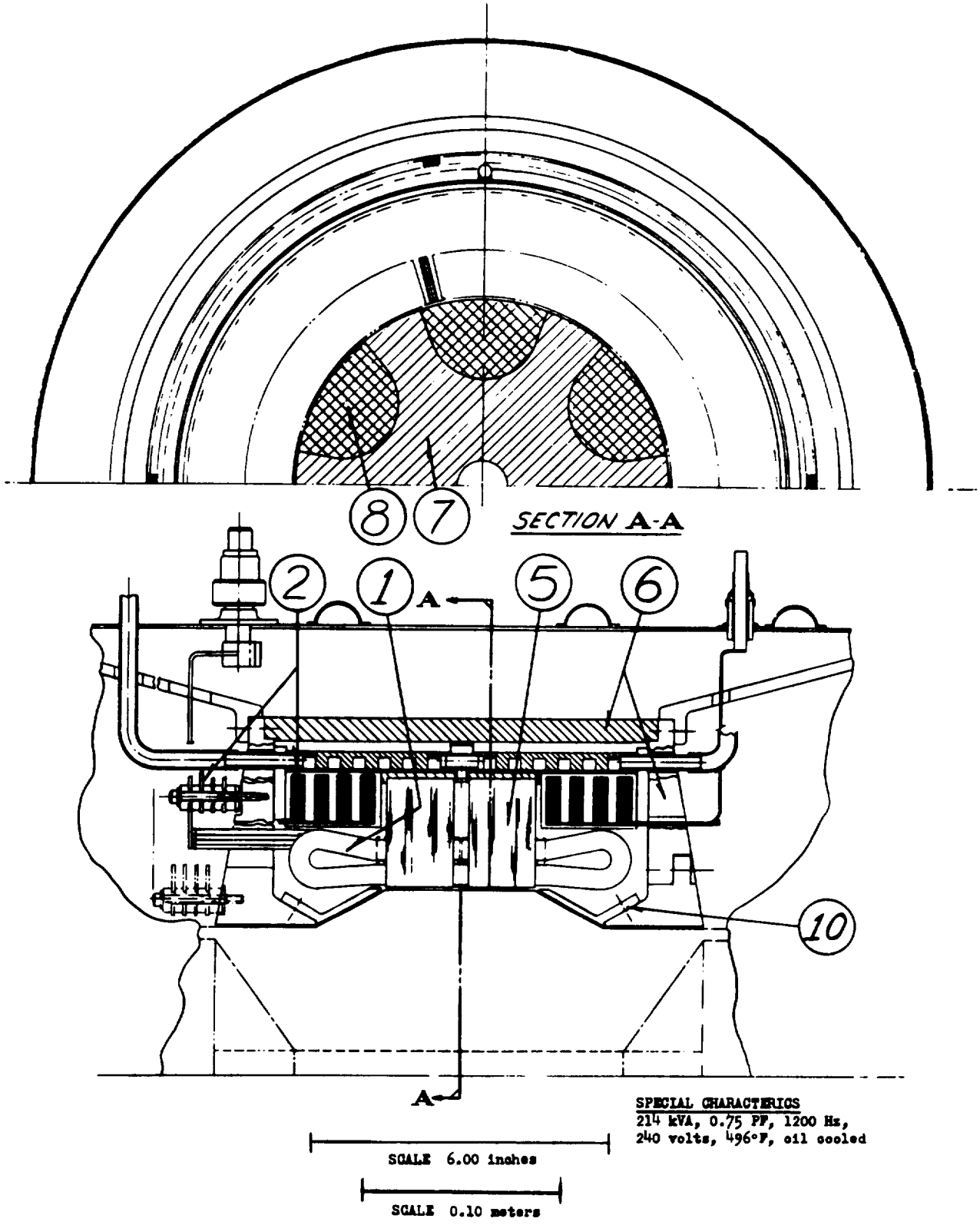
TABLE 31 (Cont'd)

INTERNAL DESIGN DETAILS SUMMARY:

60° Phase Belts, 2/3 Pitch; 90% Stacking Factor:

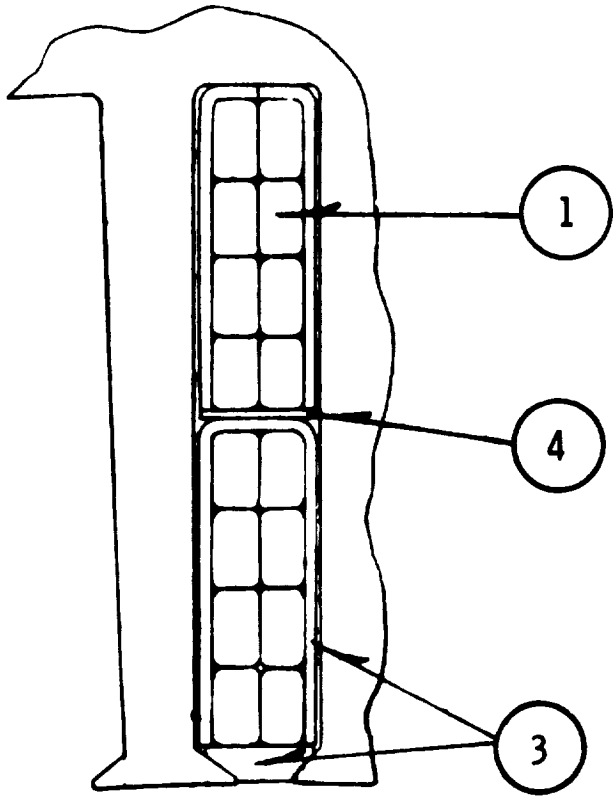
		6-POLE LUNDELL (C-4) 24,000 RPM	4-POLE LUNDELL (D-2) 36,000 RPM	4-POLE INDUCTOR 36,000 RPM
Dimensions inches	- Rotor O.D. (cm)	7.5 (19.05)	7.125 (18.097)	9.155 (23.254)
	- Rotor Length (m)	9.5 (.241)	9.22 (.234)	7.59 (.193)
	- Stack Length (cm)	2.7 (6.86)	3.12 (7.92)	2.856 (7.254)
	- Stack O.D. (m)	12.016 (.305)	11.305 (.287)	13.000 (.330)
	- Overall O.D. (m)	13.56 (.344)	12.73 (.323)	15.23 (.387)
	- Overall Length (m)	9.5 (.241)	9.22 (.234)	12.97 (.329)
Rotor Steel -		4340 R_c 33	4340 R_c 48	H-11
Number of Slots -		90	60	108
Conductors per Slot -		2	2	2
Series Turns -		15	10	9
Parallel Paths -		2	2	4
Parallel Strands -		8	6	2
Resistances, Hot (ohms)	- Armature (Per Phase)	0.0125	0.0084	0.0126
	- Field Coil	0.152	0.159	0.327
Main Gap, inch (mm) -		0.07 (1.78)	0.07 (1.78)	0.09 (1.78)
Auxiliary Gap, inch (mm) -		0.05 (1.27)	0.05 (1.27)	-- --
Reactances (P.U.)	- Xd (Unsat.)	0.867	0.86	1.216
	- X'd (Sat.)	0.462	0.33	0.341
	- X"d	0.462	0.33	0.341
	- Xq	0.434	0.41	0.594
	- X"q	0.434	0.41	0.594
	- X2	0.448	0.37	0.467
	- X0	0.0177	0.01	0.0119
Time Constants, Hot (seconds)	- T'D1[a]	0.403	0.37	0.156
	- T'D0	--	--	2.09
	- TA	0.004	0.005	0.0061
	- T_d"	0.0017	0.0017	--

(a) T'D1 is T'D0 except it does not assume a solid steel flux circuit.



LUNDELL ALTERNATOR, 24,000 RPM

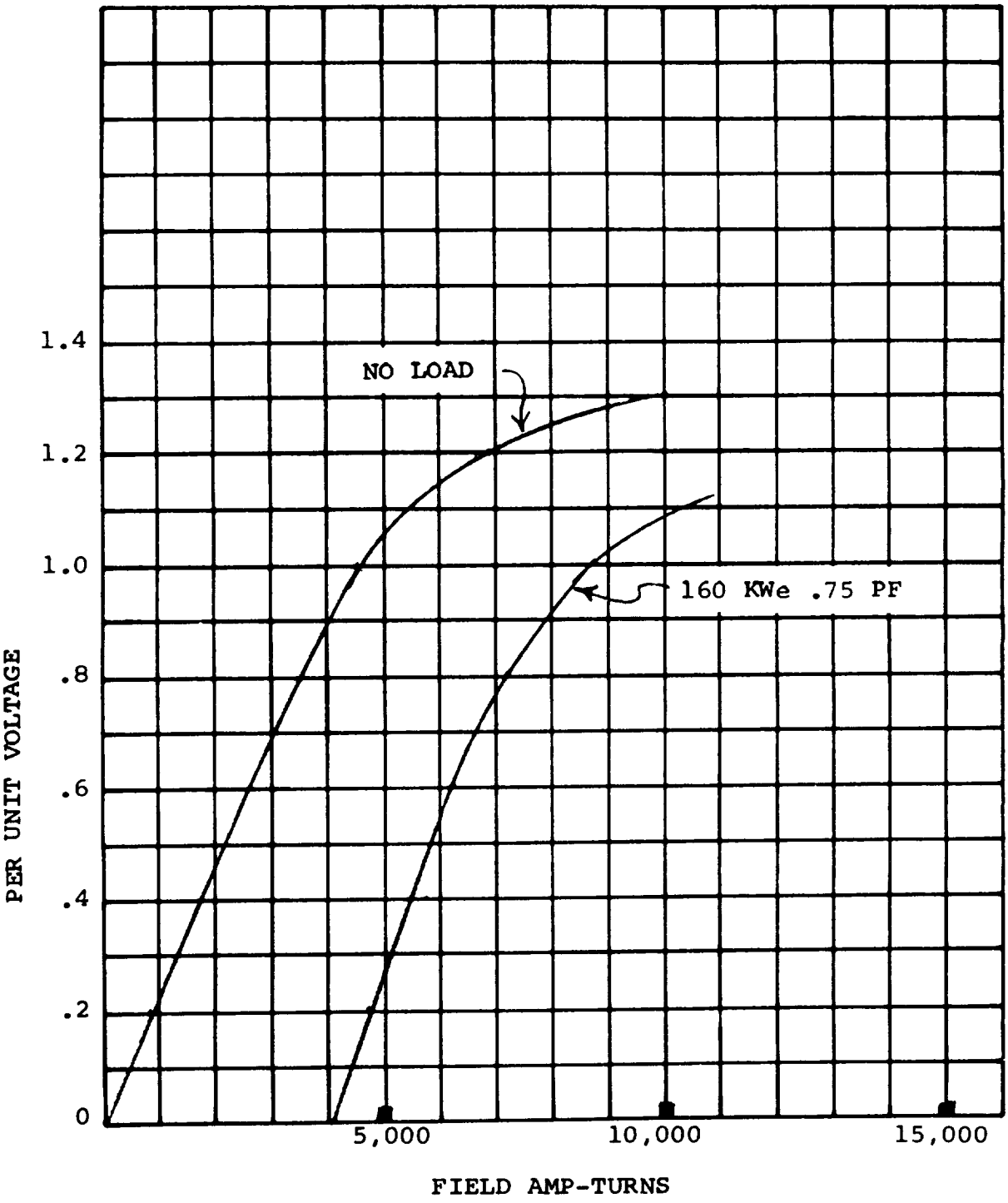
FIGURE 53



ENLARGED DETAIL OF STATOR SLOT
SCALE = 4:1

LUNDELL ALTERNATOR
24,000 RPM

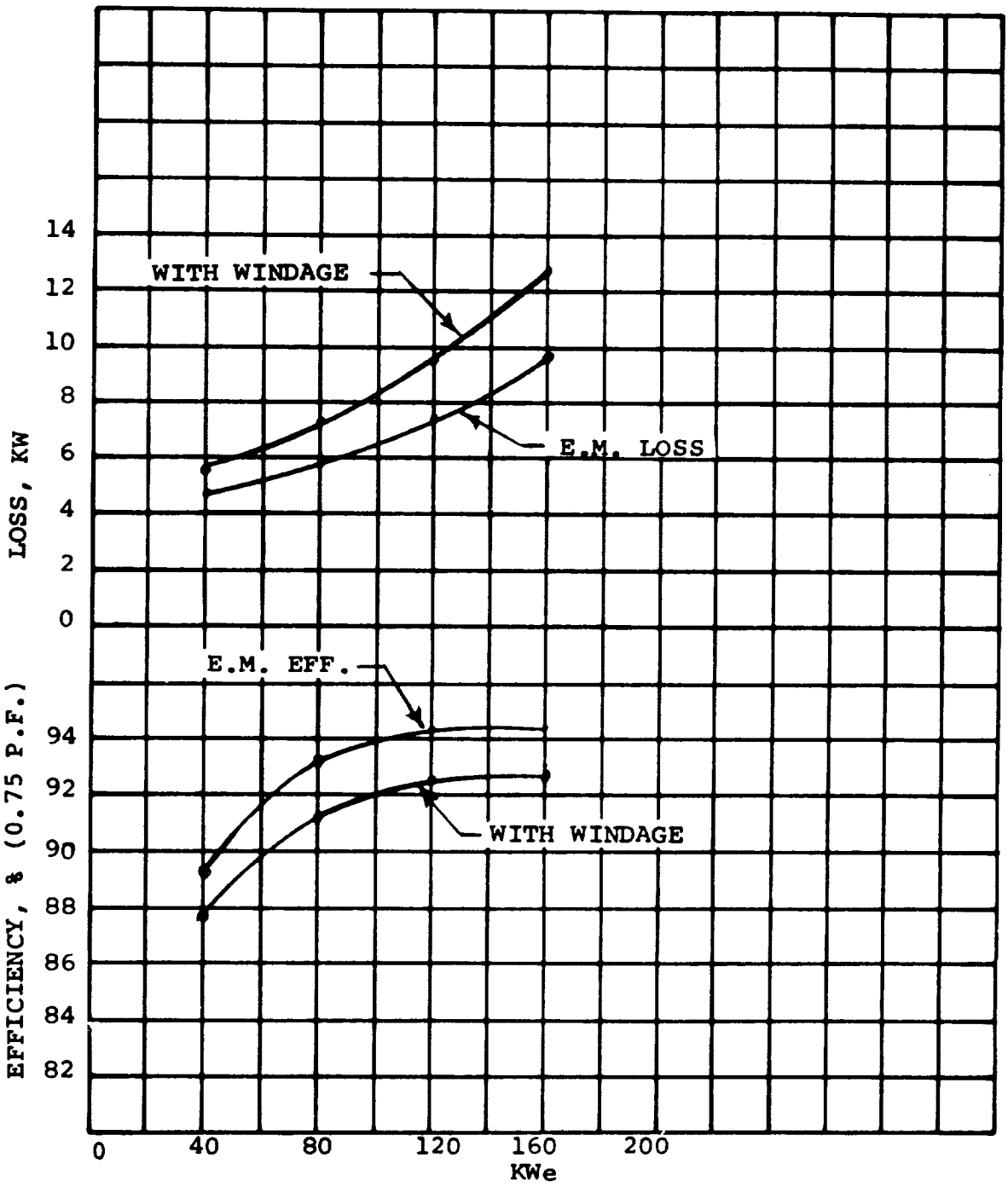
FIGURE 54



LUNDELL ALTERNATOR 24,000 RPM, 1200 Hz (C4)

SATURATION CURVES

FIGURE 55



LUNDELL ALTERNATOR 24,000 RPM, 1200 Hz (C-4)

EFFICIENCY

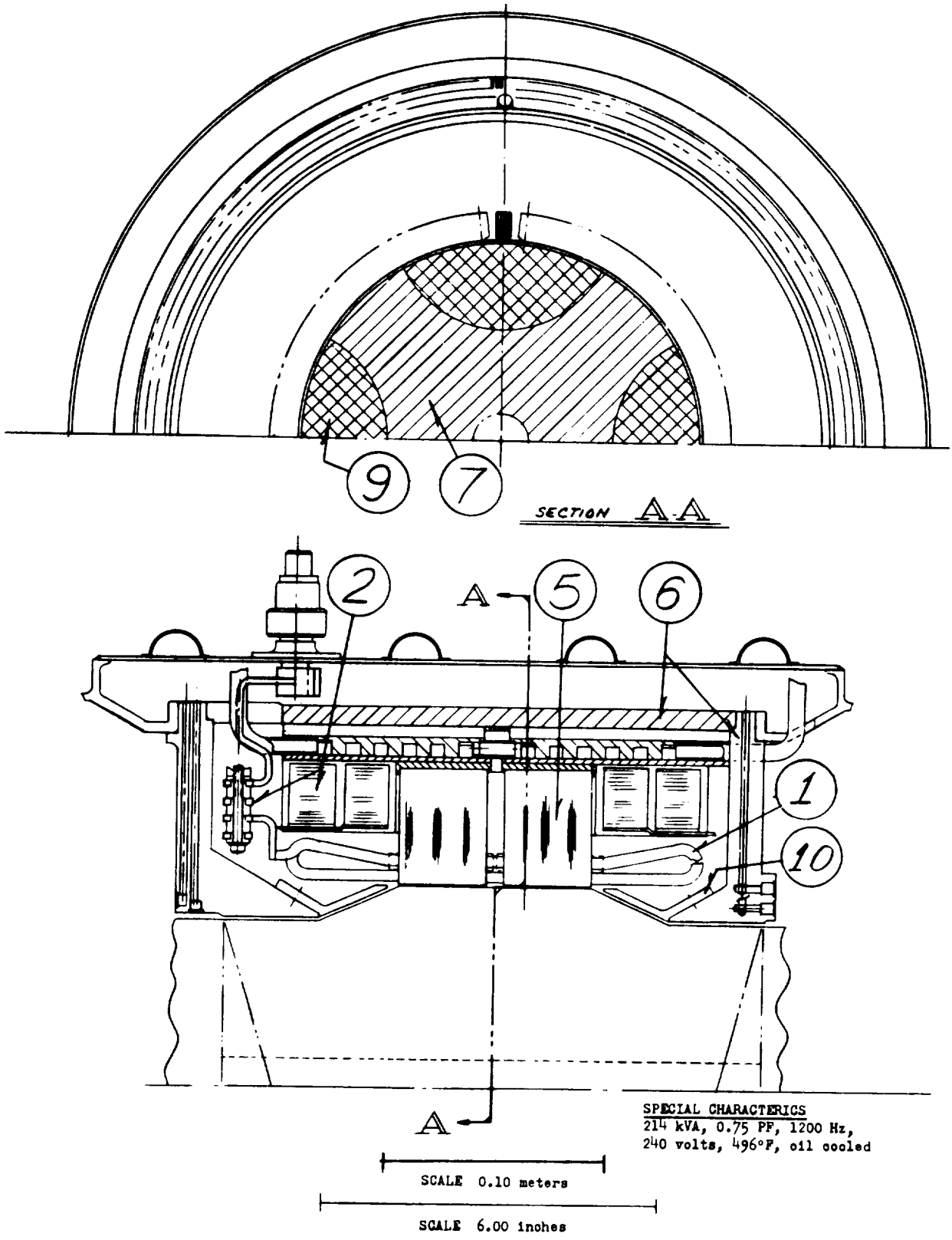
FIGURE 56

Power Output, kw_e	40	80	120	160
Losses, watts				
AC winding	180	732	1,732	3,247
Field winding	473	634	854	1,158
Pole Face	521	735	1,086	1,552
Teeth	1,560	1,600	1,642	1,683
DBS	2,051	2,104	2,158	2,213
Electromagnetic	4,875	5,805	7,472	9,853
Windage	768	1,471	2,158	2,884
Total loss	5,553	7,276	9,630	12,737
Efficiency, percent				
Electromagnetic	89.32	93.24	94.14	94.20
Overall	87.8	91.7	92.6	92.6

The efficiency is relatively constant from full load to half load but begins to fall off at 1/4 load.

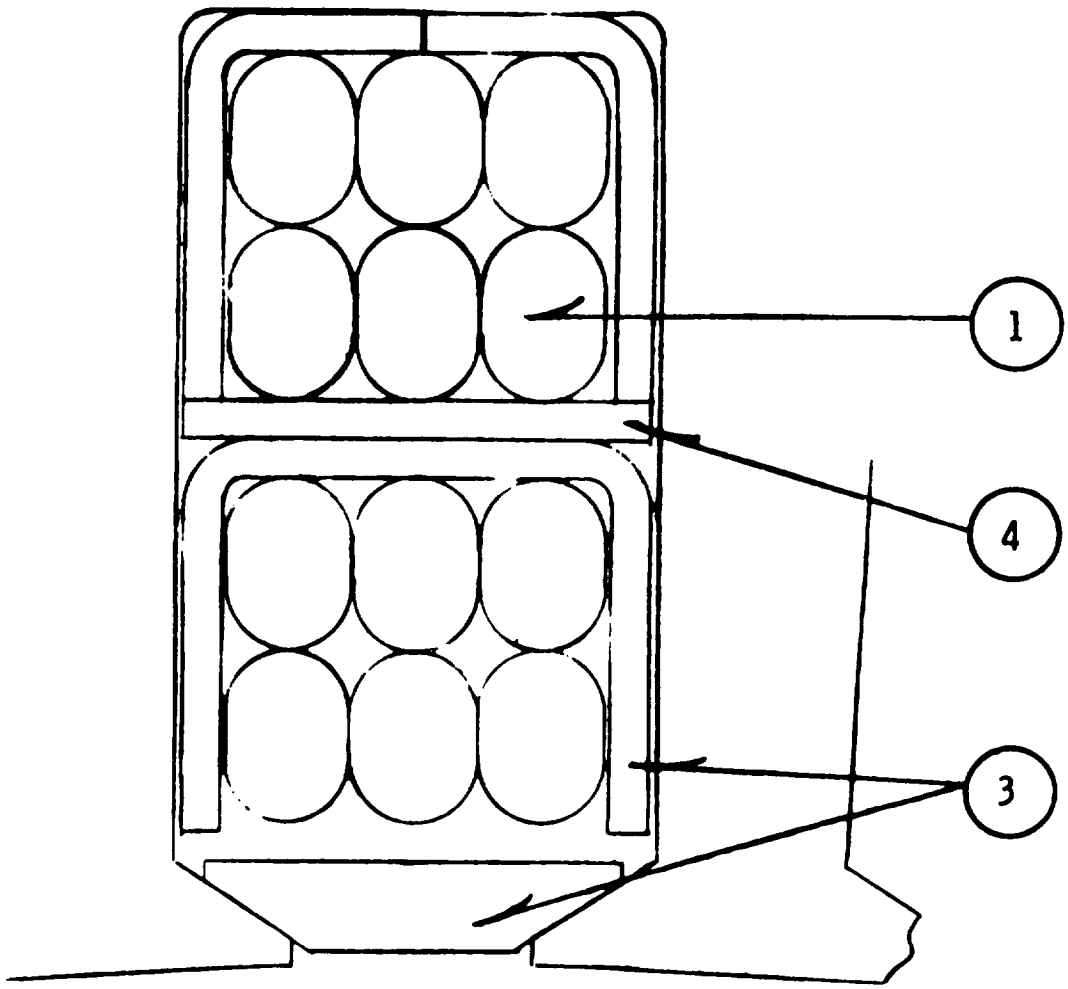
5.4.2.2 36,000 RPM Lundell

Design D-2 was the final 36,000 rpm Lundell design. The layout of this design and slot punching are shown in Figures 57 and 58. Saturation curves are shown in Figure 59. Efficiency curves are shown in Figure 60. A breakdown of generator losses versus load (0.75 P.F.) is shown on Page 138.



LUNDELL ALTERNATOR, 36,000 RPM

FIGURE 57

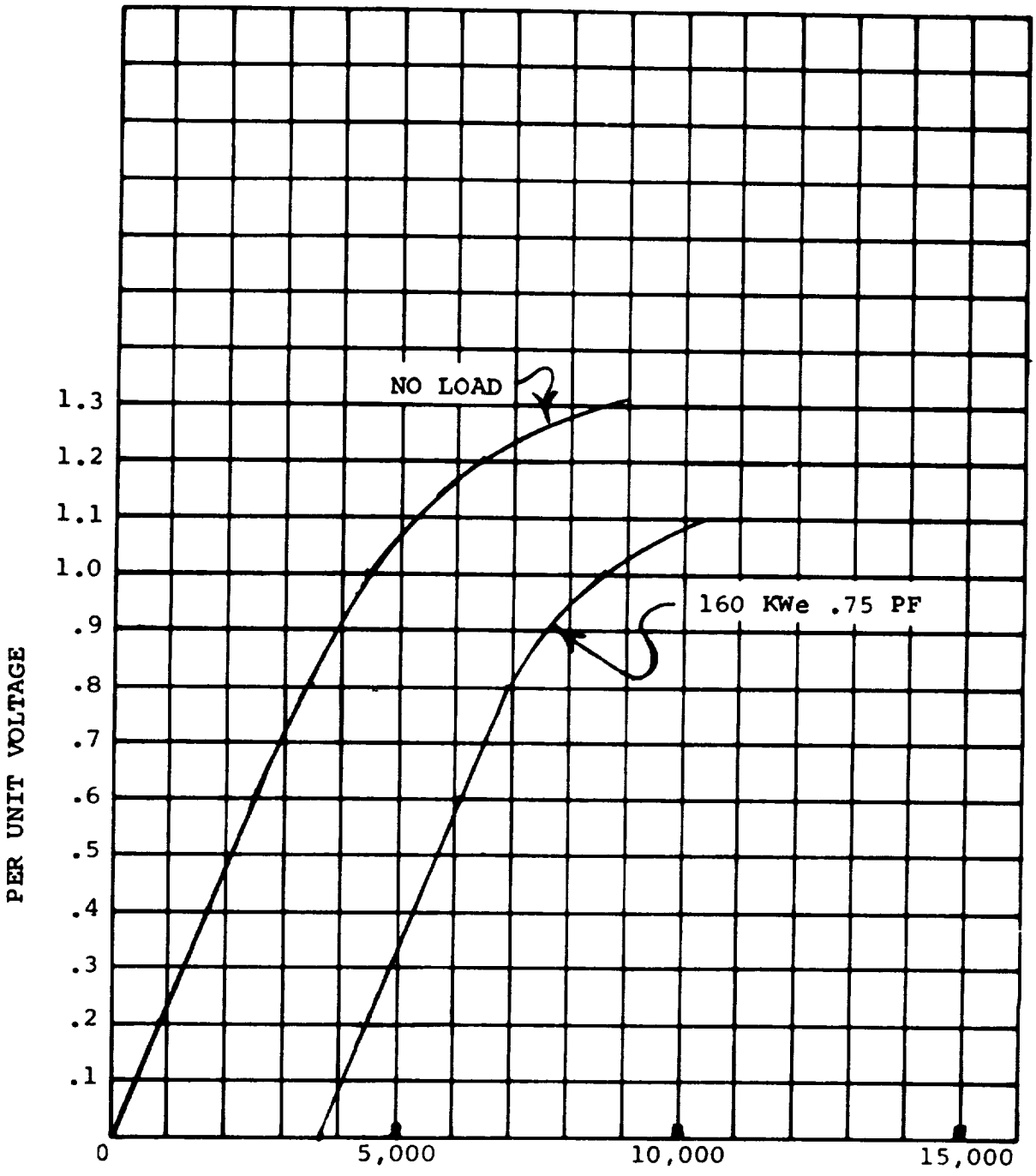


ENLARGED DETAIL OF STATOR SLOTS - 60 SLOTS SCALE 10/1

LUNDELL ALTERNATOR

36,000 RPM

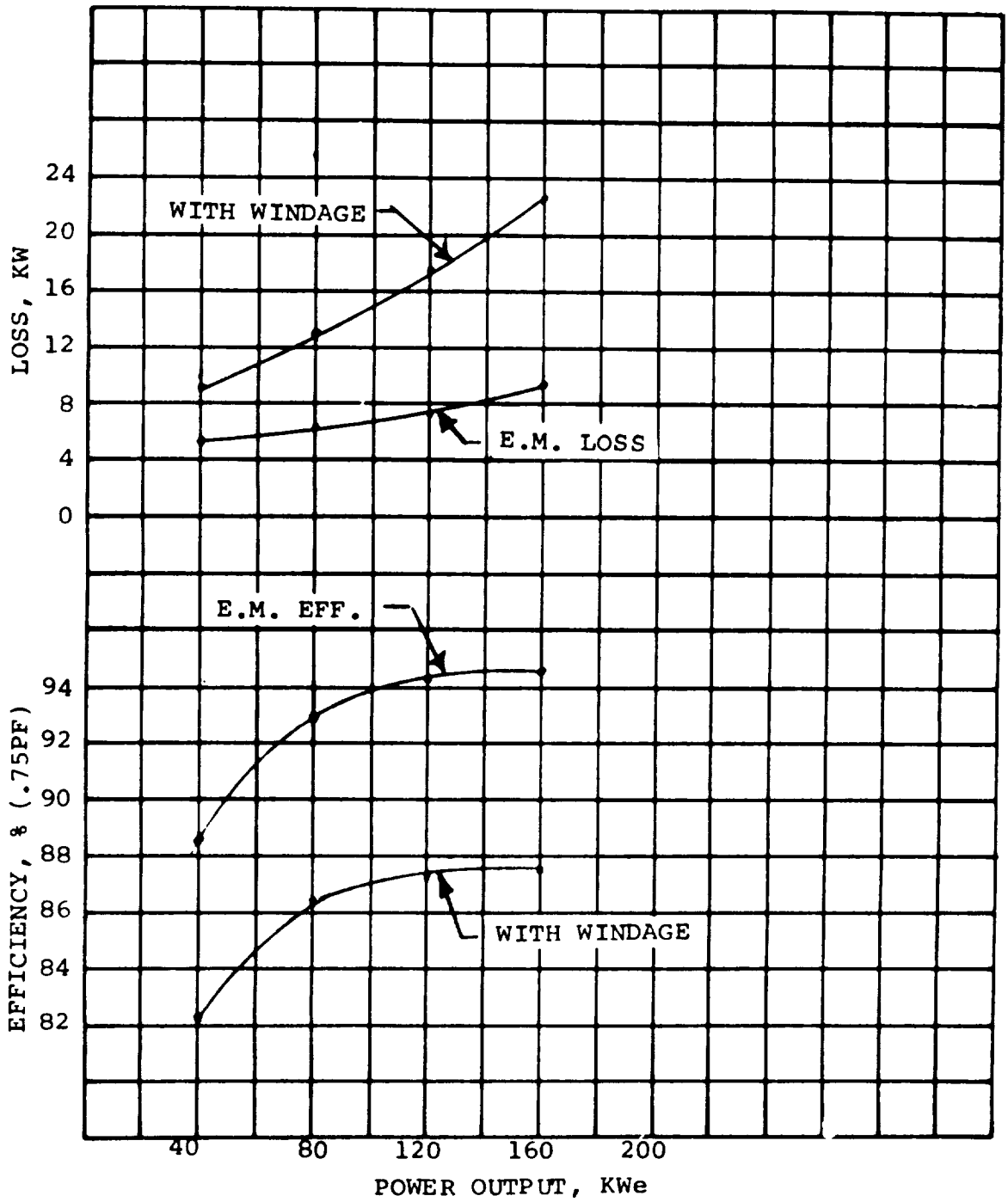
FIGURE 58



LUNDELL ALTERNATOR - 36,000 RPM, 1200 Hz (D2)

SATURATION CURVES

FIGURE 59



LUNDELL ALTERNATOR - 36,000 RPM, 1200 Hz (D2)

EFFICIENCY

FIGURE 60

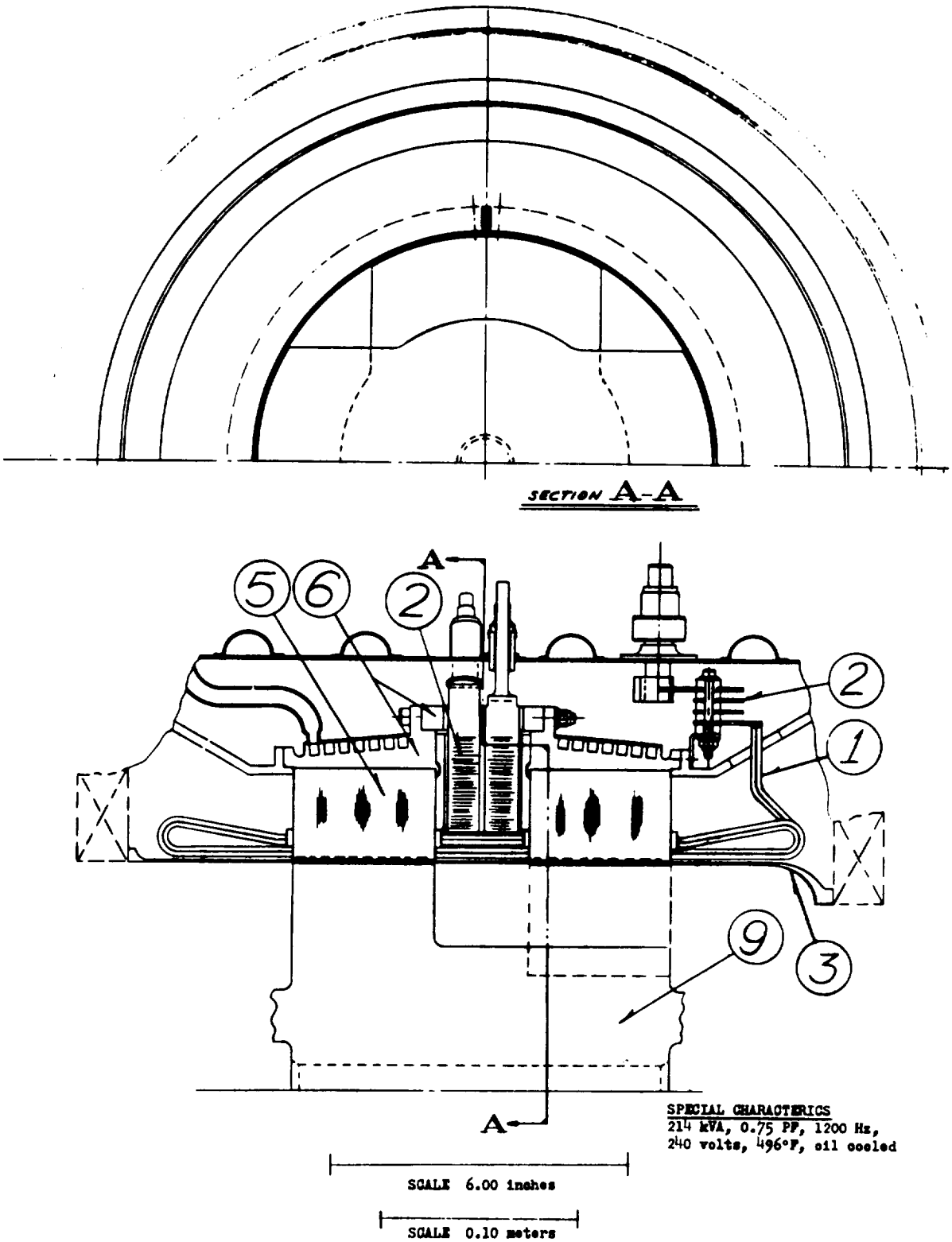
Power Output, kw_e	40	80	120	160
Losses, watts				
AC winding	117	484	1,157	2,236
Field winding	468	631	853	1,165
Pole face	915	1,246	1,784	2,524
Teeth	804	816	829	841
DBS	2,804	2,847	2,890	2,935
Total elec.	5,108	6,025	7,512	9,702
Windage	3,529	6,787	9,842	13,065
Total loss	8,637	12,812	17,354	22,767
Efficiency, percent				
Electromagnetic	88.68	93.00	94.11	94.28
Overall	82.24	86.20	87.36	87.56

5.4.2.3 36,000 RPM Inductor

The layout of the 4-pole inductor design is shown in Figures 61 and 62. Table 31 presents a summary of the design and performance details. Saturation curves are shown in Figure 63.

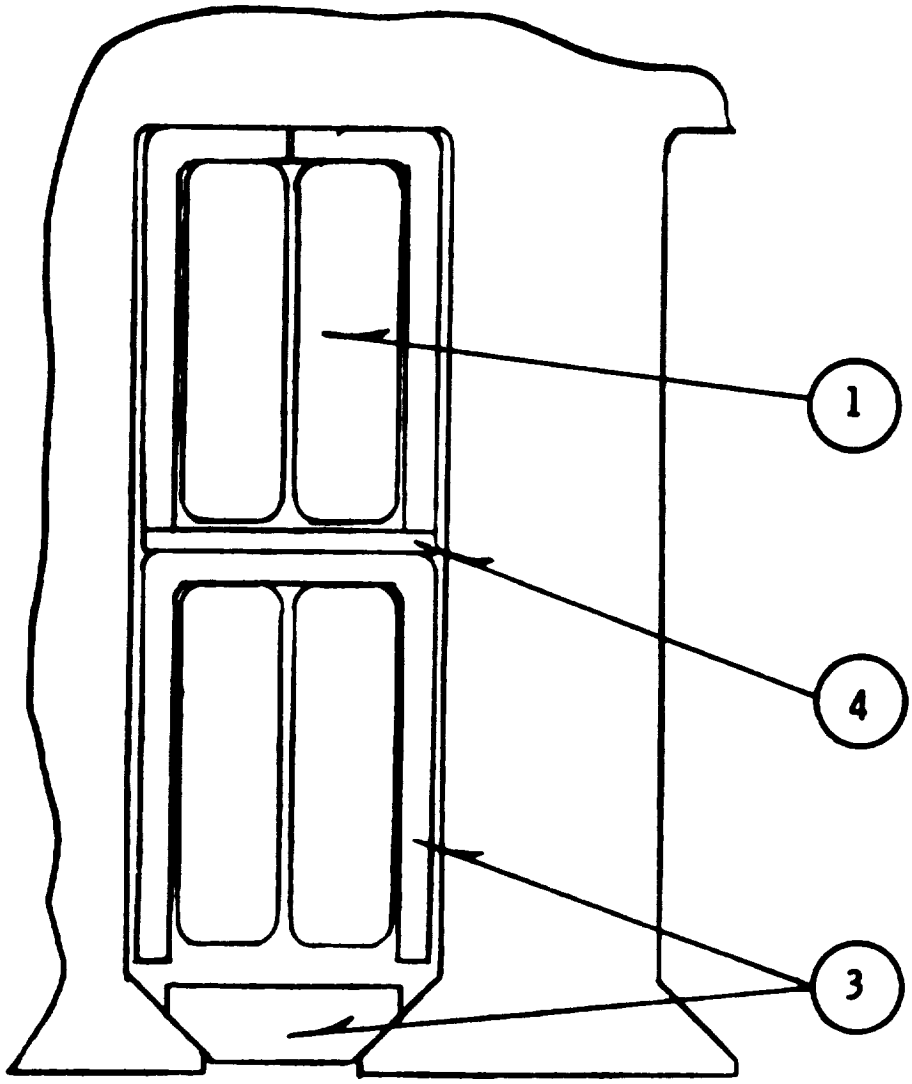
5.4.2.4 Mechanical Description

This section summarizes the mechanical details of the two final Lundell alternator designs and the final inductor alternator design. Figures 53, 54, 57, 58, 61, and 62 are the configuration layouts for the three designs. The ballooned numbers in these figures relate to the materials used for the indicated areas, the materials list being provided in Table 32. As seen on the figures, the basic alternator is made up of the rotor, the magnetic frame, the Hiperco-27 stacks, the armature coils, and the field coils. The rest of the configuration



INDUCTOR ALTERNATOR, 36,000 RPM

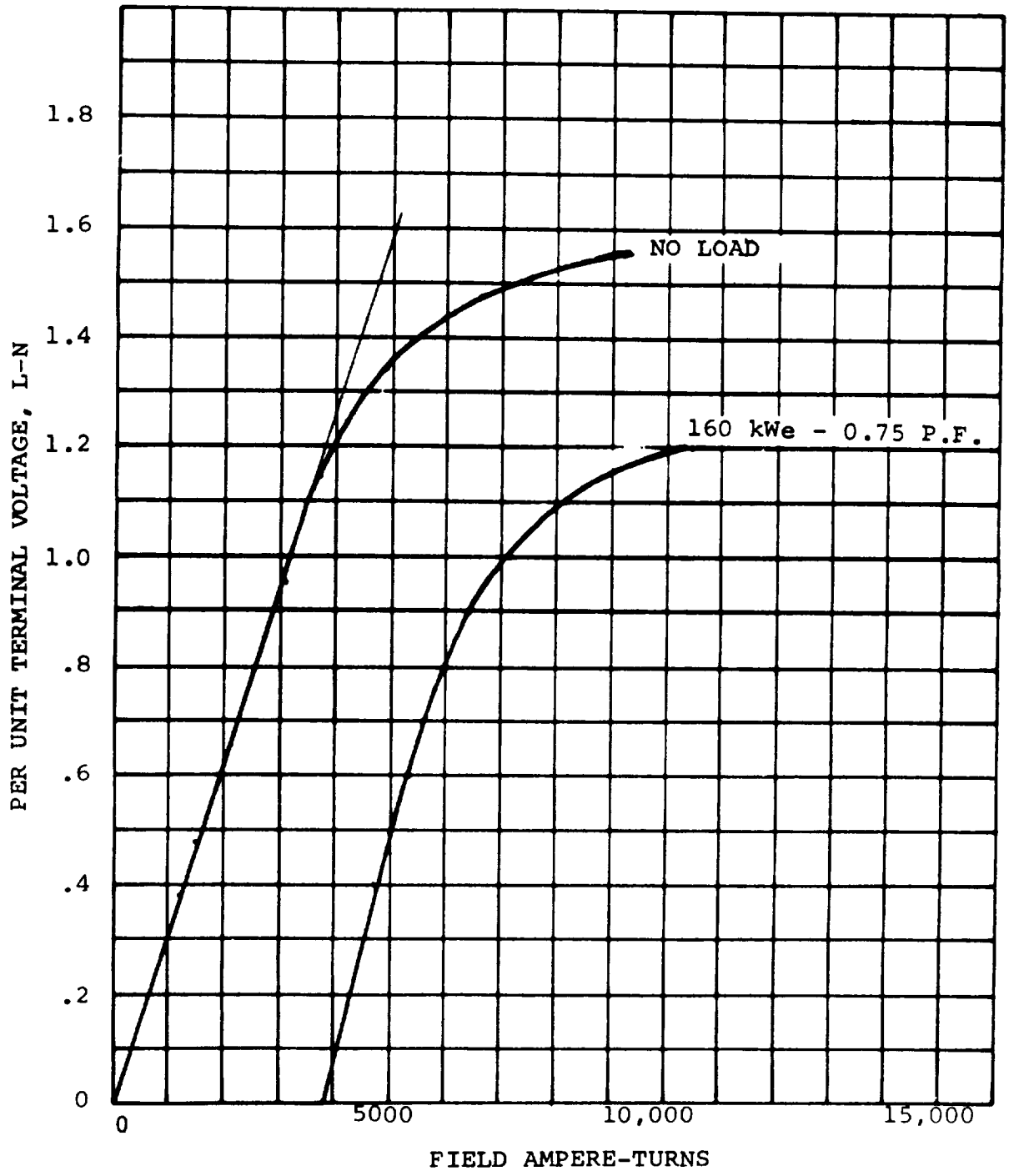
FIGURE 61



ENLARGED VIEW
OF STATOR SLOT
SCALE 10/1

INDUCTOR ALTERNATOR
36,000 RPM

FIGURE 62



INDUCTOR ALTERNATOR-36000 RPM, 1200HZ
SATURATION CURVES

FIGURE 63

TABLE 32

TAC ALTERNATOR MATERIALS LIST

1. Nickel Clad (20-28%) Silver - AC Windings
   (to be changed to AlSl-321 Clad Silver for Phase III)
2. CuBe Alloy (Dispersion Strengthened Copper Beryllium Alloy) - Field Coil and AC Bus Ring
3. Alumina (Al_2O_3) - Slot Liner, Slot Wedge, Bore Seal
4. Mica mat - Slot Cell Separator for Corona
5. Hiperco 27 Alloy, 0.004 inch Laminations, Magnetic-Stator Stack
6. Hiperco 27 Alloy, Forgings, Magnetic-Stator Frame, End Bells
7. Inconel 718, Non-Magnetic - Rotor
8. AlSl 4340 Steel, Magnetic - Rotor
9. AlSl H-11 Steel Forging, Magnetic - Rotor
10. To be selected, Non-Magnetic, Non-Conducting (Electrical)-Conical Baffle

around these fundamental components are to transfer the coolant in and out, transfer the power out and support the stator and rotor. The mounting of the bearing housings to the stator frame is a part of the total TAC configuration (not shown) and is done by mechanically fastening directly to the magnetic frame to utilize the structural rigidity associated with the relatively large magnetic frame.

The armature coil leads pass through the end bell to the bus rings on the 24,000 rpm design. In passing through the end bell, one-half inch spacing (1.27 cm) is required around each lead. This is to minimize eddy current heating due to the high frequency alternating flux surrounding the lead. This half-inch spacing is adhered to as a general rule for all the electrical leads of the ac armature coil.

The stators are hermetically sealed by the can mounting the terminals. This hermetic shroud is a thin wall reinforced can whose thickness is 30 to 40 mils (0.76 to 1.02 mm). There are reinforcing rings around the can.

The stator punchings are 0.004 in. thick (0.102 mm) Hiperco-27 magnetic alloy, have a semi-closed slot to reduce pole face losses, and are assembled into an unwelded stack to reduce iron losses. A 0.0004 inch (0.0102 mm) thick layer of plasma-arc sprayed alumina constitutes the interlaminar insulation. The block of material shown dotted on the ends of the stacks are small tabs on the ends of the slot liners. These hold and align the unwelded stacks to prevent the thin teeth from excessive flaring. The bottom slot liner must be slit into an "L" shape in order for the slot liner to be assembled into the semi-closed slot. The upper slot liners are "U" shaped and can be assembled from the ends of the stack at the time of winding.

The field coil is wound into series connected toroids of flat straps. They are electrically insulated from each other and the cooling ducts. There is a flat-to-round transition section between each coil bundle and terminal.

There are four bus rings in each generator. The parallel phase groups of the armature are connected to each bus ring in such a manner that the bus ring I^2R losses are held to a minimum. This permits the rings to be cooled by radiation to the stator cavity walls. The maximum bus ring temperature can be expected to be less than 800°F (700°K) with a 500°F (533°K) sink temperature. The bus rings are supported by ceramic insulation and a mechanical mount as illustrated in the various views. The rings are not continuous rings, but are partial arcs allowing for thermal expansion without diametral growth. The insulation pieces are spaced quite widely on the rings to permit a good field of view for radiation cooling. The leads come directly off the armature coil into bus rings as seen in the figures and the exposed lead ends are bonded into the bus rings. This is important to the design of the alternator since it simplified making a sound electrical joint at the time of final assembly. This is even more important should it be necessary to bake out the Anadur and fire it prior to assembly of the windings. This pre-bake will obtain a better slot fit-up at assembly by accounting for the 35 percent Anadur shrinkage prior to winding. Thus, by attaching the wire ends to the bus rings in readily accessible areas, bonding problems are minimized.

There is one terminal per bus ring, centrally located about the armature connections. Because of the temperatures brought on by the high current density and because of the limited space, special terminal studs are required. They are sized rather large to have sufficient cross sectional area to permit them to be self-cooled by radiation. Nickel plating is used to obtain an emmisivity of 0.4 on the outer surfaces. They can be cooled by radiation alone to less than 800°F (700°K) for a 500°F (533°K) ambient.

The features of the rotor design are found in the bonded construction and slotted pole faces. The slotted pole faces have 0.006 wide by 0.100 inch (0.153 by 2.54 mm) deep slots, approximately 30 per inch (12 per cm), that are cut with gangs of carbide cut-off wheels. The process for doing this has previously been developed by Westinghouse.

The central hole shown dotted in the rotor core serves an assembly function. It is not used for cooling and may not be necessary for the heat treatment to obtain the desired hardnesses. The angled lines, also dotted, on the two Lundells illustrate the minimum volume needed for magnetic flux carrying purposes.

The cooling system for the Lundell alternators (Figures 53 and 57 utilizes the nonmagnetic separation between the stacks and the frames. For each machine, this member would be constructed in two sections, one for each half of the stack. Liquid coolant flows through helical grooves near the inner surfaces, parallel grooves in each part being provided to meet the redundant cooling system requirement. The finned outer portion of this separator provides cooling passages for gas flowing from the end bell to the center of the stack. The gas will transport some of the pole face and windage losses from the "air"-gap to the separator to provide rotor cooling without overheating of the stator armature windings.

The stator can be assembled as a unit separate from the rotor and stub shaft assemblies. This is an important feature for assembly into the TAC or for separate assembly for TAC pre-assembly tests. The alternator is mounted to the TAC through conical frames that mechanically attach the magnetic frame.

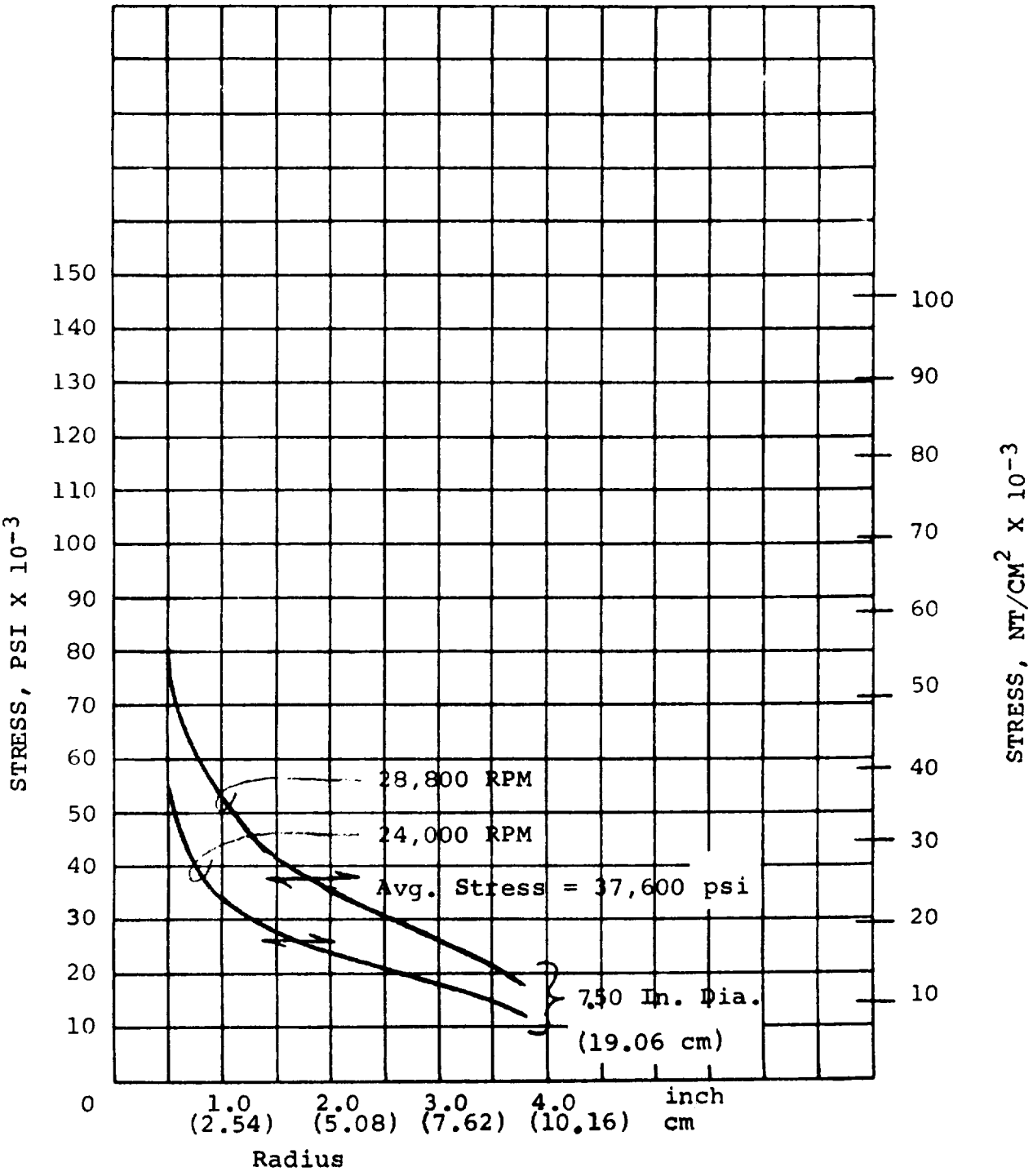
Most of the tubing for coolant flows, leads, etc., are not precisely shown due to the lack of definition at this stage of the design. The few tubes shown will actually be parallel tubes spaced 180 degrees apart to equalize the disturbances due to the penetrations. This equalizing rule will be adhered to for all penetrations in general.

5.4.3 Alternator Rotor Stress and Fabrication Considerations

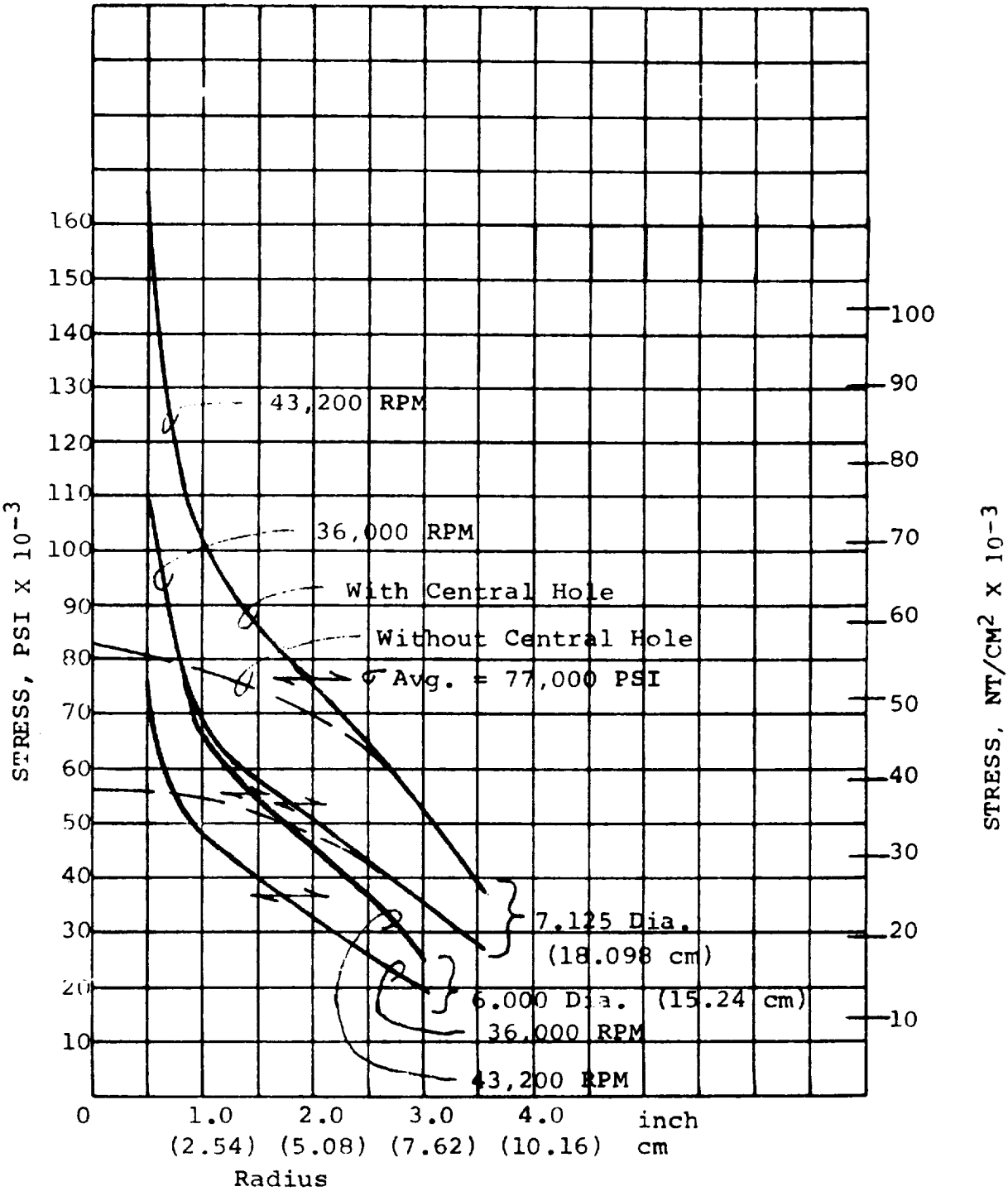
The preferred materials for the Lundell rotor are SAE 4340 and Alloy 718. This combination of materials can be diffusion bonded in an autoclave. Compaction of a loose-fitting assembly is produced by gas pressure at an elevated temperature and thermally activated diffusion bonds are produced. The time-temperature-pressure cycle in the autoclave, which has been developed for bonding rotors with lesser strength requirements, should be modified to produce a higher strength SAE 4340 alloy. This can be accomplished by aging alloy 718 at a temperature which prevent transformation of the 4340 steel from austenite to pearlite. The assembly should then be cooled from the aging temperature before transformation occurs to obtain an adequate hardness and strength for the TAC application.

The maximum stress intensity within the 24,000 rpm Lundell rotor will be 81,000 psi (558,000 kN/m^2) at 20 percent overspeed as shown in Figure 64. A hardness between R_c25 and R_c32 in the SAE 4340 steel is required to obtain adequate strength for the overspeed condition.

The maximum stress intensity within the 7.125 inch (18.1 cm) diameter 36,000 rpm Lundell rotor without a central hole at 20 percent overspeed is 83,000 psi (572,000 kN/m^2) as shown in Figure 65. This stress intensity is only slightly higher than the peak stress in the 24,000 rpm alternator with a central hole but would have higher average stress. The 36,000 rpm design with a hole has unacceptably high stresses.



24,000 RPM LUNDELL STRESS
FIGURE 64



36,000 RPM LUNDELL ROTOR

FIGURE 65

The stress intensities within the 36,000 rpm inductor rotor with a central hole are excessive. A rotor without a central hole is marginal from the standpoint of strength, having a maximum stress of 138,5000 psi (955,000 kN/m^2) at overspeed which is 92 percent of the 0.2 yield strength of H-11.

5.4.4 Corona Considerations for Voltage Selection

The ambient atmosphere in which the stator winding of the TAC alternator will be operating is composed of a mixture of helium and xenon gases, approximately 72 percent helium and 28 percent xenon by volume. Dr. T. Dakin of Westinghouse Research and Development Laboratories was consulted for information regarding the properties of the helium-xenon gas mixture in the stator cavity. According to Dr. Dakin, helium will have a predominant influence on the gas mixture's electrical characteristics. Therefore, the properties given by Paschen's curve for helium are used to determine the maximum permissible voltage of the armature winding to preclude corona.

The minimum spacing between phase conductors is 0.029 in. (0.737 mm), equal to the thickness of the slot liner and conductor double insulation thickness. An ac winding voltage of 415 volts rms or 587 crest volts line to line is assumed for this analysis. The corresponding crest voltage is 881 volts when allowance is made for a 50 percent voltage transient. The minimum pressure for voltage breakdown at 881 volts and 0.029 in. (0.737 mm) gap is 25 psia (172 kN/m^2 abs) according to the Paschen's curve for helium, which would be the case for a break in the insulation.

The case of a helium gap in series with solid insulation between conductors must also be considered. A basic law of electrostatics states that the total voltage "E_T" across series dielectrics is divided in proportion to the ratio of the thicknesses "t_n" of the

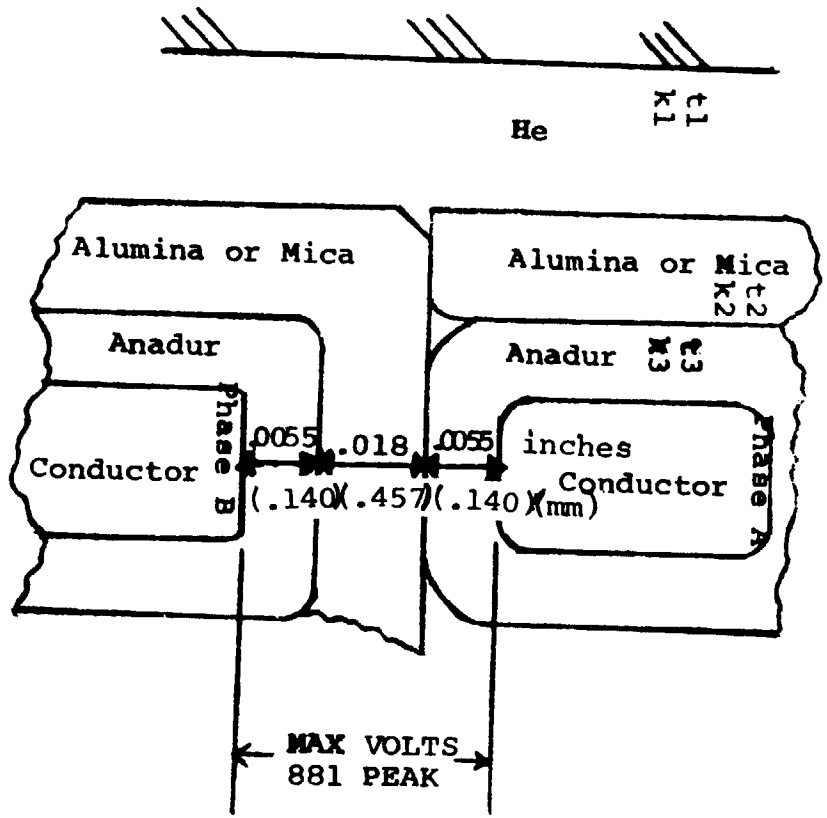


FIGURE 66

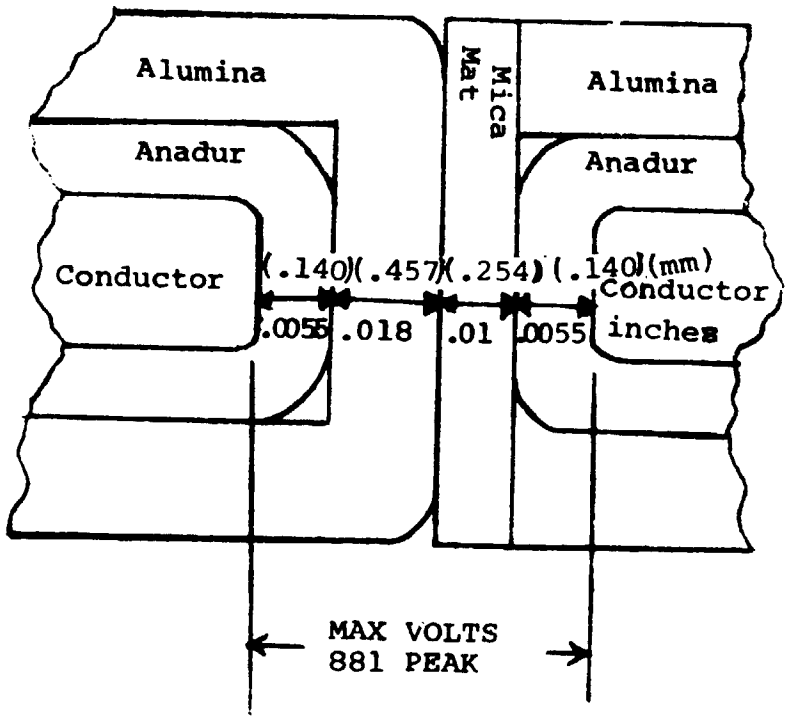


FIGURE 67

ndividual dielectrics to the respective dielectric constants "K_n" as ndicated below:

$$E_T = \frac{D}{\epsilon_o}\left[\frac{t_1}{K_1} + \frac{t_2}{K_2} + \frac{t_3}{K_3} \cdots\right]$$

= electrostatic flux density

$_o$ = permittivity of free space

A result of this relation is the concentration of voltage across ıe low dielectric constant media, such as a gas, when it appears in ɜries with high dielectric constant solid materials. Ceramic insula- ions are particularly poor in this respect because of their relative- ɣ high dielectric constant.

For the TAC alternator, there are two insulating materials Anadur and alumina) of known thicknesses in series with a gas filled ap of unknown thickness. The dielectric constant of alumina is ɔpproximately 10 while the dielectric constant of Anadur is estimated ɜ equal to that of Borosilicate glass at 662°F (623°K), which is ɔout 5.6. The dielectric constant of helium is assumed equal to that f free space, that is 1.0. Thickness of the alumina is 18 mils).457 mm) and the double thickness of Anadur is 11 mils (0.280 mm) ɔr phase-to-phase voltage in the slot (see Figure 66).

The thickness of the gas filled gap cannot be determined as it is variable quantity throughout the winding. However, it is not neces- ɪry to establish an exact value for the gap in order to determine the ɪnimum pressure below which ionization of the gas will occur. The ɜrcent voltage, "percent V_{HE}", across any helium gap length can be ɜtermined by solution of the equation below for various values of ɪp length.

$$\%V_{HE} = \frac{100}{1 + \left(\frac{t_2}{K_2} + \frac{t_3}{K_3}\right) \frac{K_1}{t_1}}$$

where: t_1 = gap length

K_1 = dielectric constant of gas in gap

t_2, t_3 = thickness of solid insulations in series with gap

K_2, K_3 = dielectric constants of solid insulations

Solution of the above equation for the case under consideration results in the curve given in Figure 68. The maximum voltage across the various gap lengths can now be determined from the product of "V_{HE}" and the maximum expected winding voltage as previously determined. The pressure (p) times spacing (d) value, "pd", is determined from Paschen's curve for the gas in question and corresponding to the voltages calculated above. The minimum pressure below which ionization of the gas will occur is determined by dividing Paschen's pd value by the gap length used in determining the gap voltage. A plot of minimum pressure versus length of gap for the TAC alternator, assuming helium gas in the gap, is presented in Figure 69. This curve shows that ionization of the helium gas in the stator cavity will not occur for pressures greater than 66 psia (455 kN/m^2 abs) regardless of the length of gap (containing helium) in series with the Anadur and alumina insulation, assuming, of course, that the maximum expected winding voltage is not exceeded. The gap length at which ionization would occur is 0.004 in (0.102 mm) from Figure 69. The probability of this gap length occuring in the alternator is very high and therefore it can be concluded that stator cavity pressure must exceed 66 psia to prevent ionization of the gas mixture in the stator cavity for the insulation configuration and voltage described in Figure 66.

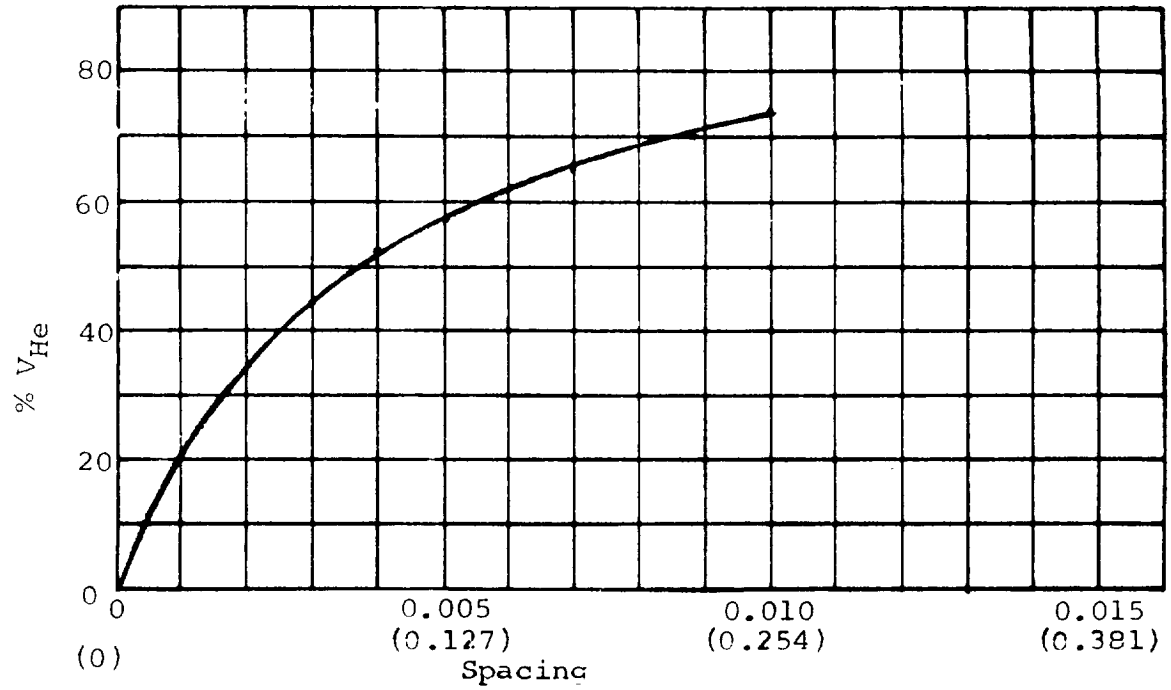


Figure 68

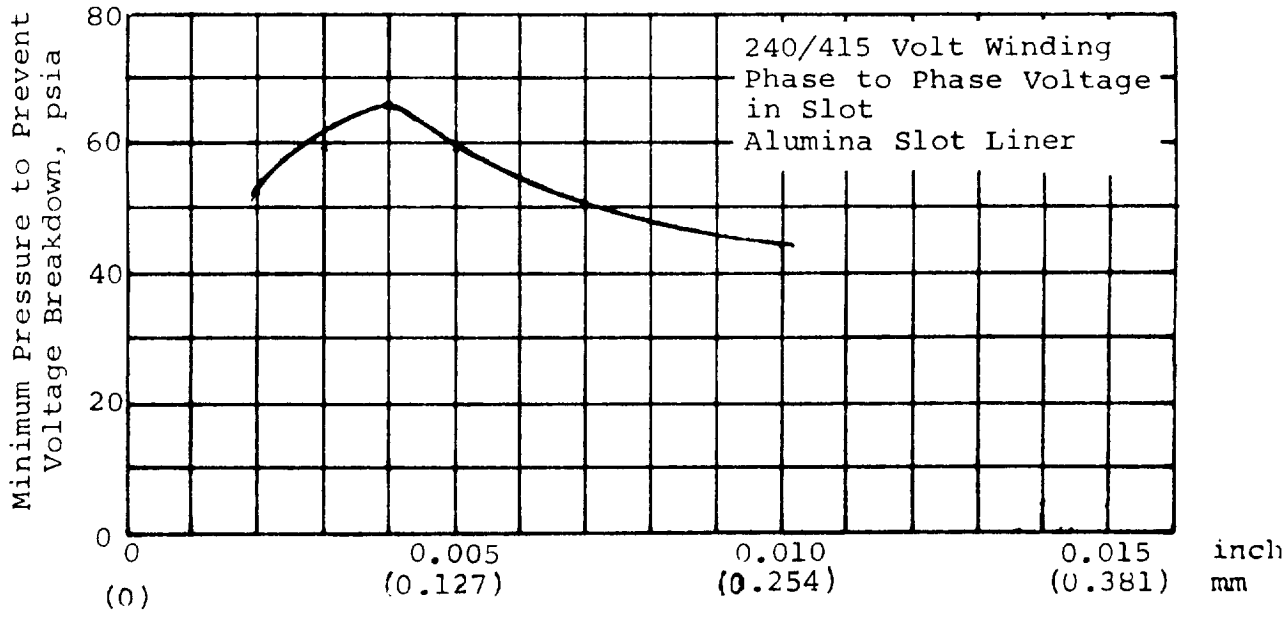


Figure 69

Other conditions investigated are conductor-to-stack voltage in the slot, Figure 70, phase-to-phase voltage in the slot with mica slot liners, Figure 66, phase-to-phase voltage in the slot with alumina slot liner and 10 mil (0.254 mm) mica mat phase separator, Figure 67, and 120/208 volt connected winding. Results are presented in Figure 71.

The pressure in the stator cavity will decrease when system load is decreased. For this reason, it is recommended that the 120/208 alternator voltage be selected.

A voltage transient of 50% was assumed in the corona analysis. If actual systems voltage transients are less or if a gas with a better Paschen's characteristic is selected, the minimum pressure values given in Figure 71 would be lower. In any case, the minimum allowable stator cavity pressure should be determined by test under conditions selected for the final configuration. At present, however, a minimum cavity pressure of 16 psia (110 kN/m^2 abs) is recommended.

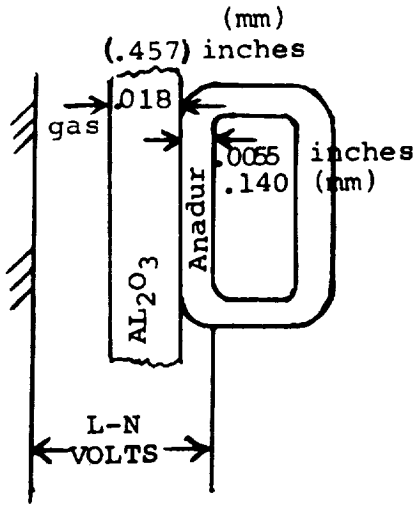
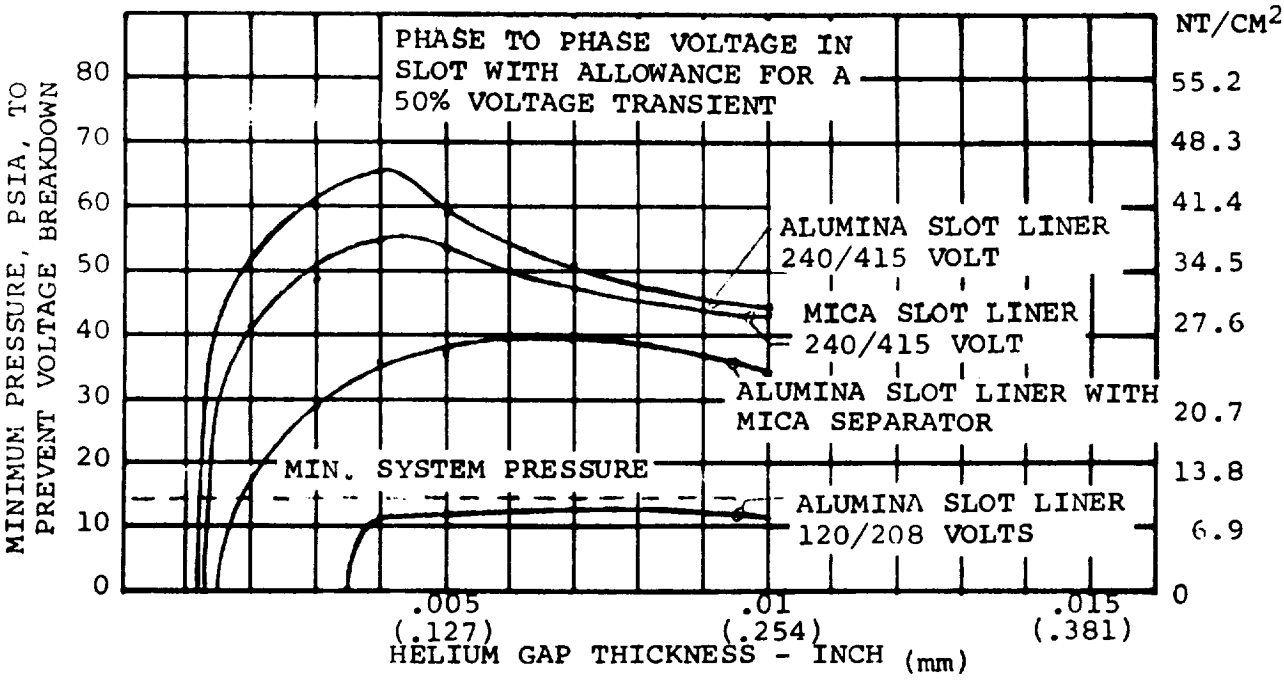


Figure 70



ALTERNATOR VOLTAGE WYE CONNECTED	MINIMUM ALLOWABLE PRESSURE TO PREVENT IONIZATION OF GAS, PSIA (nt/cm^2)		
	PHASE TO PHASE IN SLOT	PHASE TO STACK IN SLOT	HELIUM GAP OF 29 MILS (0.737 mm) NO INSULATION
240/415	40 (with Mica (27.6) separator)	26 (17.9)	25 (17.2)
120/208	13 (8.95)	2 (1.38)	8 (5.52)
240 DELTA CONNECTED	13 (with Mica 8.95 separator)	26 (17.9)	10 (6.90)

IONIZATION OF HELIUM IN TAC ALTERNATOR

FIGURE 71

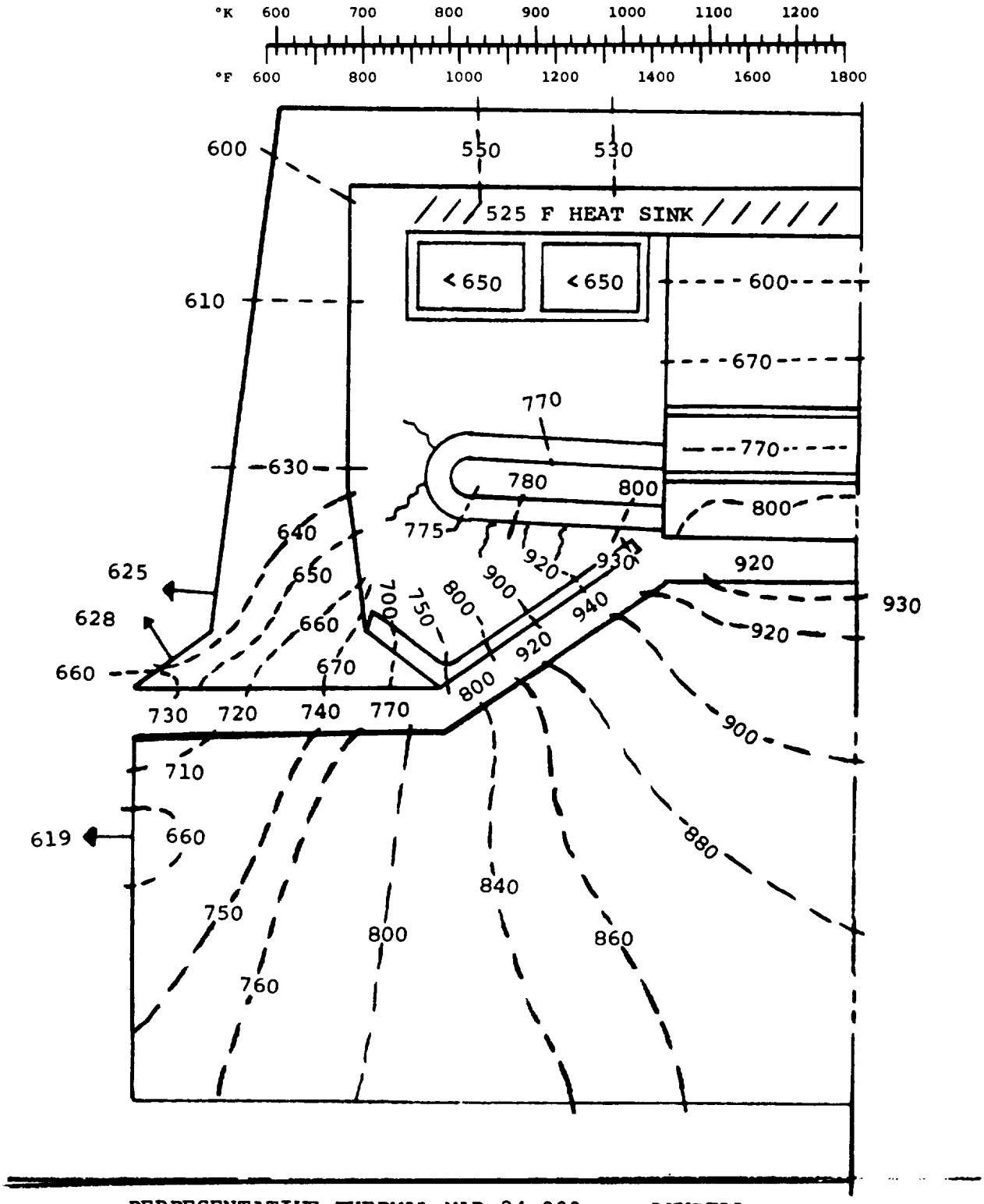
5.4.5 Alternator Thermal Analysis

A number of preliminary thermal maps were generated using Westinghouse computer analysis routines. Analysis was limited to the recommended 24,000 rpm TAC alternator but the techniques are applicable to the 36,000 rpm designs and the trends shown here will also apply to the 36,000 rpm designs.

5.4.5.1 Alternator Thermal Maps

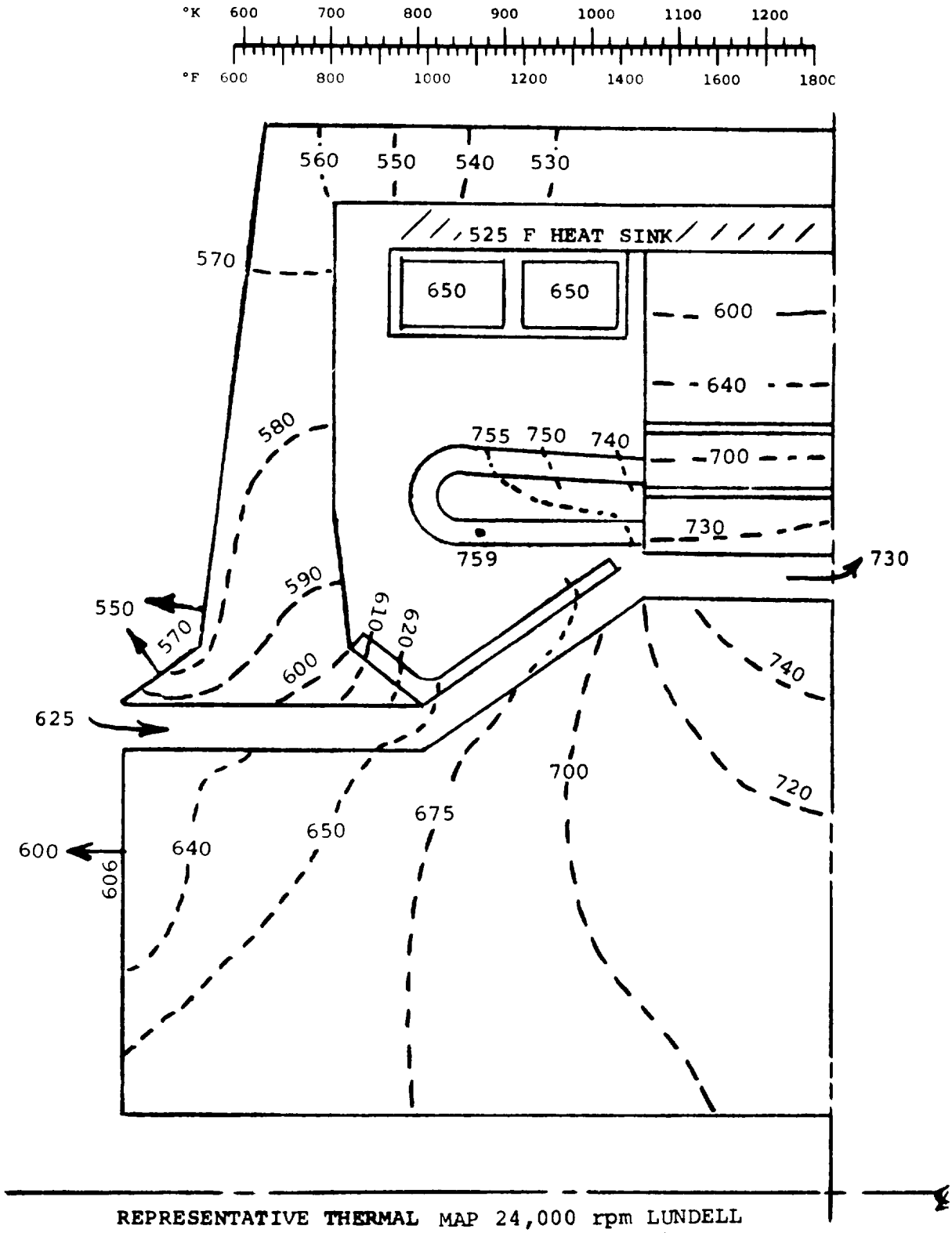
The first thermal analyses were performed assuming little, or no, gas flow in the air gap, but providing coolant for the end bell. Figure 72 presents the thermal map for one such case in which about 700 watts (15%) of the windage and pole face losses were carried out by the gas. This thermal map illustrates that with no gas flow, and nearly all windage and pole face losses passing through the gap to the stack or the end bell, the maximum rotor temperature will exceed 900°F (756°K). In the highly stressed center hole region, the temperature would reach 870°F (739°K). For the proposed materials, the temperature would be excessive. In addition, the armature winding temperatures are slightly in excess of the specified hot-spot limitation of 796°F (698°K).

To reduce the rotor and winding temperatures, gas was permitted to flow through the gap. Assuming a gas temperature rise of 100°F (56°K) as it flows through the auxiliary, conical, and main gaps to the center of the stack, the maps of Figures 73 and 74 are obtained. As these maps show, it is desirable to assure a coolant temperature of not more than 625°F (603°K) at the entry to the auxiliary gap. If this condition is met, the maximum rotor temperature at the central hole would be about 705°F (648°K). Calculations of the heat transfer in the heat sink area indicate that the gas will leave the finned passage at about 30°F (17°K) above the heat sink temperature, or about 555°F (563°K) Assuming some heating before entering the auxiliary gap, it is probable that the gas temperature at this point will be in the range between 580 and 625°F (578 and 603°K) as shown in the figures.



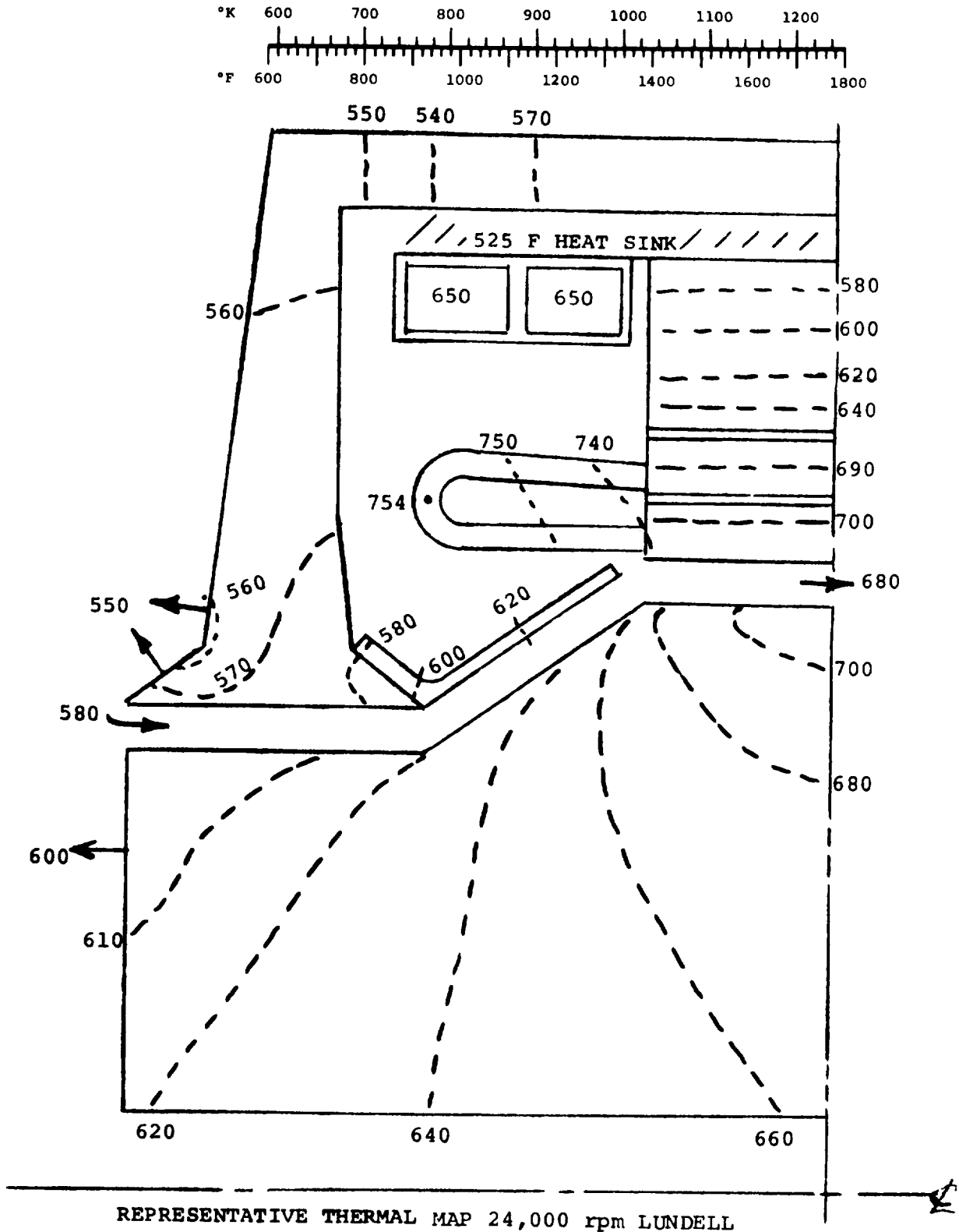
REPRESENTATIVE THERMAL MAP 24,000 rpm LUNDELL
COOLED END BELL, NO GAS FLOW

FIGURE 72



REPRESENTATIVE THERMAL MAP 24,000 rpm LUNDELL COOLED END BELL, GAS FLOW IN GAP

FIGURE 73



REPRESENTATIVE THERMAL MAP 24,000 rpm LUNDELL COOLED END BELL, GAS FLOW IN GAP

FIGURE 74

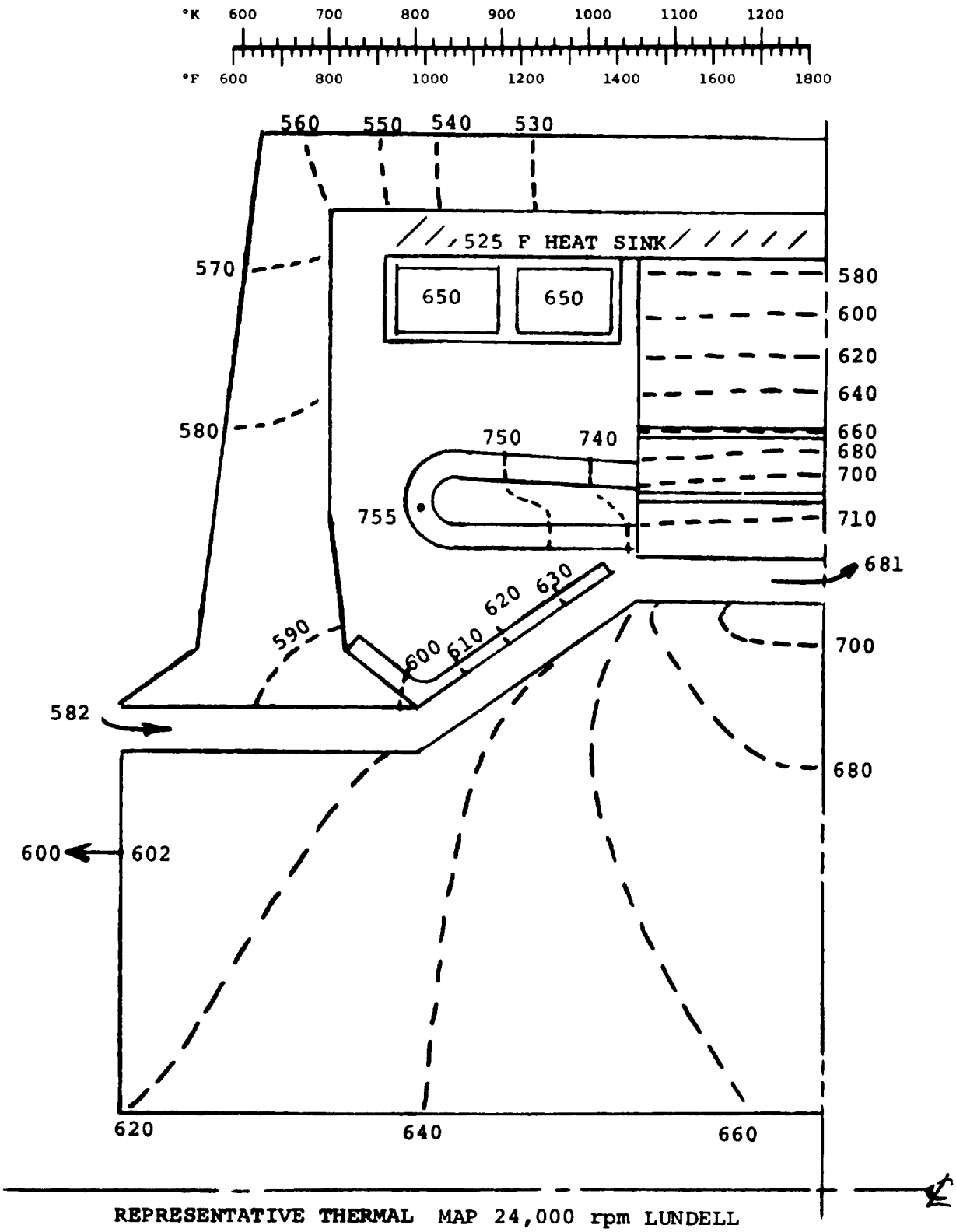
The inclusion of end bell cooling ducts adds considerable complexity to the end bell, and with a failure of one flow path, a circumferential or diametral temperature gradiant would be created in the end bell. To evaluate the necessity for end bell cooling, the map of Figure 75 was obtained. This map can be compared directly with Figure 74. The comparison indicates that only the end bell and baffle temperatures are significantly affected by elimination of the end bell cooling ducts. However, this cooling method was retained for consideration in the next phase of study in that it may prove of greater merit at that time (see Section 6.3.3).

During the final stages of the Phase I TAC effort, it became apparent that the provision of a flow path for the gas from the heat sink to the outside of the end bell could be difficult. Therefore, a study was made of the thermal performance obtained when the gas was constrained to enter the auxiliary gap near the conical section. The thermal map, Figure 76 shows that while the rotor and end bell temperatures near the gap are increased (as compared to Figure 74), they are still well within acceptable limits.

The thermal map of Figure 77 shows the effect of using a liquid coolant at SNAP-8 temperatures. All temperatures within the alternator are well within the 300°F (167°K) hot spot temperature rise limitation of the TAC program.

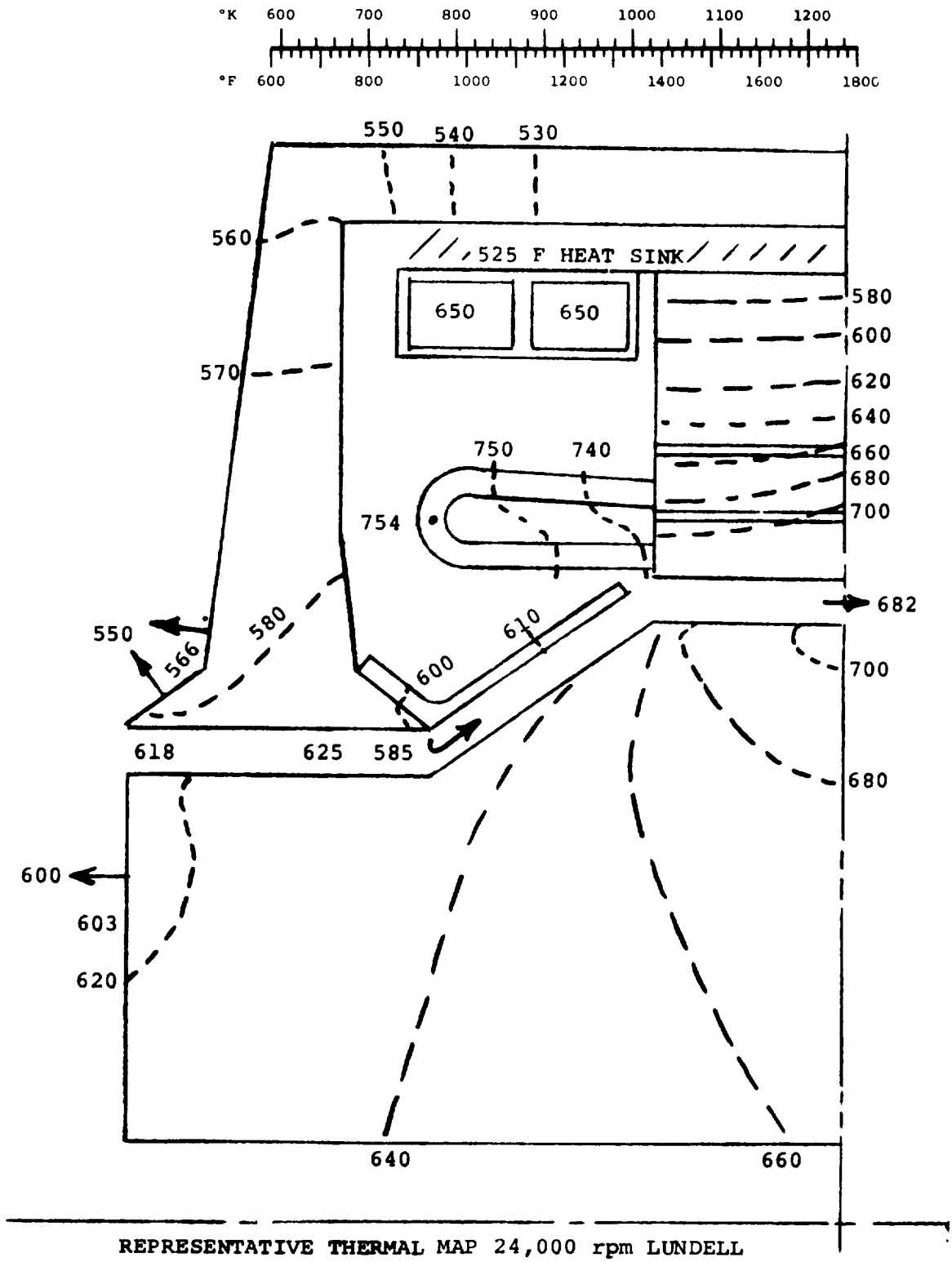
5.4.5.2 Field Coil Thermal Analyses

The TAC 24,000 rpm Lundell alternator field coil was analyzed utilizing the same program as for the basic alternator. A total of up to 155 nodes were considered. These studies indicated that with the proposed spiral-wound strap conductors, the maximum temperature can be within about 150°F (83°K) of the liquid coolant temperature. This will require the use of thin insulations between turns, and high thermal conductivity ceramic plates at the ends of each section to



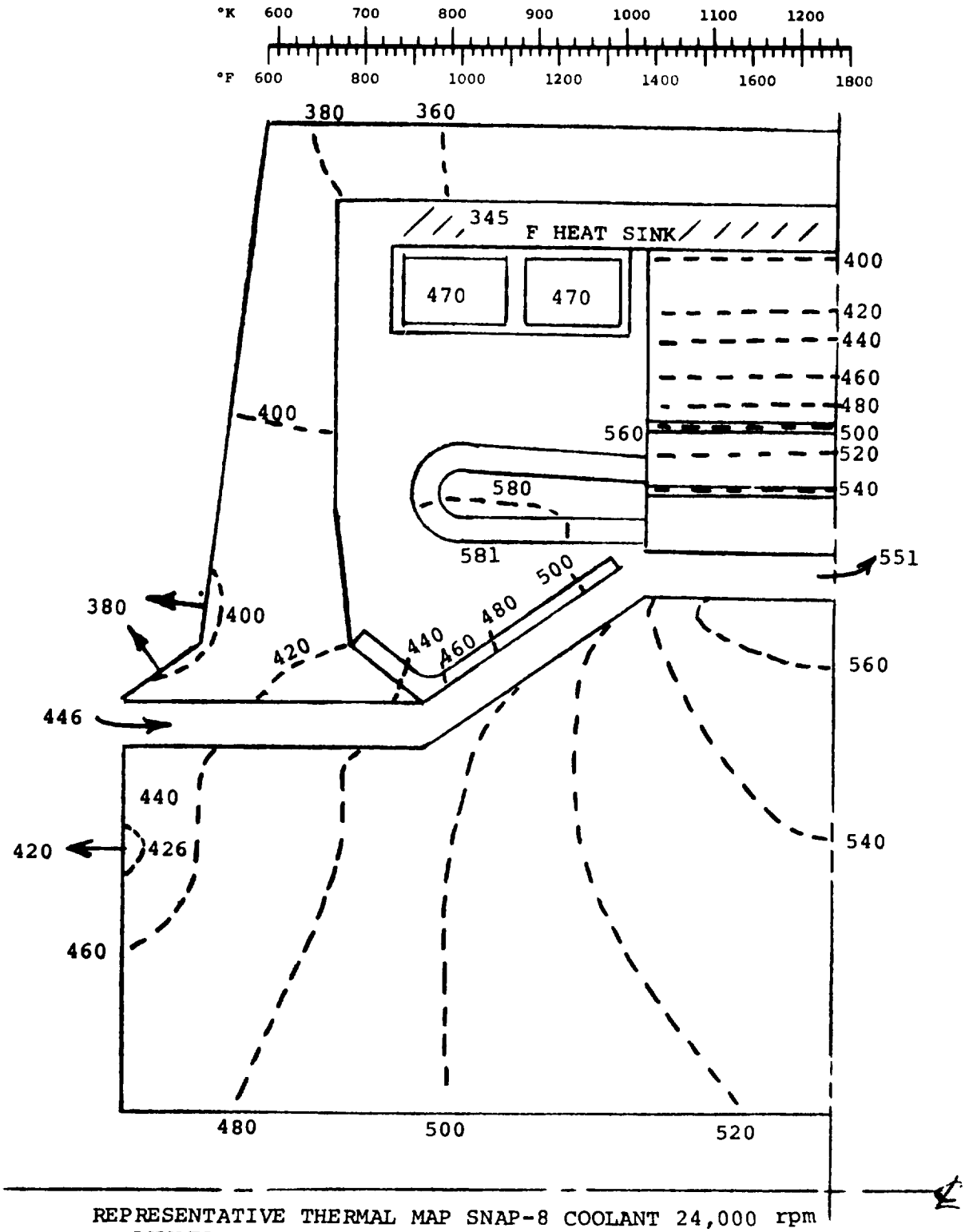
REPRESENTATIVE THERMAL MAP 24,000 rpm LUNDELL
GAS FLOW IN GAP

FIGURE 75



REPRESENTATIVE THERMAL MAP 24,000 rpm LUNDELL COOLED END BELL, GAS FLOW IN CONICAL AND MAIN GAPS

FIGURE 76



REPRESENTATIVE THERMAL MAP SNAP-8 COOLANT 24,000 rpm
LUNDELL COOLED END BELL GAS FLOW IN
GAP

FIGURE 77

assure low radial temperature drops. In addition, it may be feasible to reduce the proposed field coil dimensions, since the electrical resistance will be decreased at the indicated temperatures, resulting in decreased losses.

5.4.5.3 Phase I Alternator Thermal Analysis Summary

The preliminary thermal analyses discussed above demonstrate that Lundell alternators can be cooled to meet the TAC program hot-spot limitations. Significant findings are enumerated below:

(a) To limit the axial temperature gradient of the alternator to about 25°F (14°K), a liquid flow rate (nominal) of about 1.668 lb/sec (0.756 kg/sec) is required. Pumping power for the coolant, from alternator inlet to outlet, will be about 1230 watts, dropping to 615 watts when the gradient exists due to blockage of one coolant path.

(b) Gas flow through the rotor to stator gap must be provided to limit the rotor temperature to 700°F (643°K).

(c) The "air" gap gas flow can be restricted to the conical and main gap regions with little effect upon the rotor temperature

(d) Addition of liquid coolant passages in the end bells has no significant effect on rotor cooling. However, such coolant passages could reduce the axial temperature gradient caused by loss of one of the redundant cooling flows.

(e) Hot spot temperatures, occuring in the armature winding end turns, will be less than 300°F (167°K) above the liquid coolant temperature.

(f) Field coil temperatures will not exceed the hot spot temperature specified for the TAC alternator.

(g) If the coolant temperature is changed, all alternator temperatures will change by approximately the same magnitude. However, some deviation from the patterns will result from changes in the losses due to temperature level.

5.4.6 Alternator Overall Conclusions and Recommendations

The recommended alternator design is the 24,000 rpm, 6-pole Lundell at 120 volts (L-N), the latter being limited by corona considerations which in turn limits the minimum stator cavity pressure (and minimum system pressure indirectly) to 16 psia (110 kN/m^2 abs). Testing is recommended to verify this prior to "freezing" the minimum specified pressure. The rotor for this configuration is constructed of SAE 4340 and Inconel 718, diffusion bonded and hardened to 33 R_c and 38 R_c respectively in an autoclave. The hardness requirements are dictated by the strength requirement and are within the realm of practicality for hardening as a bonded unit within the autoclave. No significant gains could be identified utilizing other magnetic materials having superior magnetic properties or more compatible "heat-treat-as-a-unit" characteristics.

The impact of designing without a central hole in the rotor was found to be significant to the design choice. With the hole, the 36,000 rpm designs are overstressed and impractical; the 24,000 rpm designs require the magnetic steel to be hardened to 33 R_c. Without the hole, the 36,000 rpm Lundell only requires hardening the 4340 to 33 R_c to make it strong enough; the 24,000 rpm Lundell 4340 may be left in a fully annealed state (R_c11) for adequate strength.

Windage losses are well below the 9.6 kw limit but are very significant to the choice of cooling configuration. A circulating gas completely within the alternator is required to limit hot spot and

rotor temperatures below safe levels. This gas flow is generated by the dynamic head created in the conical sections of the rotor and the flow need not pass through the auxiliary air-gap sections for adequate cooling. Preliminary calculations indicate the inherent gas flow to be two times the minimum requirement.

End-bell cooling appears to be unnecessary but was retained for further study in Phase III relative to redundancy requirement in case only one of the two parallel cooling paths is operative.

The alternator meets electrical specifications but further improvements are expected in the Phase III design. In particular, the 8.9 percent calculated voltage unbalance appears to be conservatively high and with improved calculation techniques, should drop below the 6 percent goal. Also, the efficiency at 1/4 P.U. load will be improved

The location of electrical leads, bus rings, terminals and cooling tubes are significant to the TAC assembly configuration. Preliminary agreement on basic configurations must be reached early in Phase III prior to initiating the detailed design analyses as their location can affect all components with the TAC unit.

5.4.7 References for Section 5.4

1. Belt, R.N.: Silent Electrical Power Generators for Tactical Applications. U.S. Army MERDC, Report No. 1954, Appendix E, June 1969.

2. Bagwell, D.: TOSS, An IBM 7090 Code for Computing Transient c Steady-State Temperature Distributions. Union Carbide Nuclear Co., Oak Ridge Gaseous Diffusion Plant, AEC R&D Report No. K-1494, 1963.

3. Becker, K.M., and Kaye, J.: Measurements of Diabatic Flow in an Annulus with an Inner Rotating Cylinder. Trans. ASME, Series C, Vol. 84, pp. 97-105, 1962.

4. Bjorklund, I.S., and Kays, W.M.: Heat Transfer Between Concentric Rotating Cylinders. Trans. ASME, Series C, Vol. 81, pp. 175-186, 1959.

.5 Rotor Dynamics

During Phase I, critical speed and bearing load studies were erformed for all candidate TAC configurations. Such studies indicate hat effect radial bearing spring rate, bearing span and rotating roup weight and stiffness distribution will have on critical speeds nd dynamic bearing loads. A typical "finite element" mass and stiff- ess distribution model is shown in Figure 78 for TAC-A.

Design iterations on the above parameters are repeated until nalysis indicates that the following criteria are met:

(a) Rigid body critical speeds will occur at the lower end of the rotational spectrum away from the operating speed range

(b) Bending mode criticals will occur well above the 120 percent overspeed point

Table 33 summarizes bearing and rotating group characteristics or the final TAC configurations. Vertical rotor orientation or ero-g operation was assumed in all analyses with a mass eccentricity f 0.0001 in. (0.00254 mm) chosen to simulate the "worst case" mass nbalance condition.

The usual procedure in designing a rotating group is to calculate he critical speeds with consideration of rotor and bearing flexibility nd then adjust the rotor bearing design such that criticals do not oincide with the operating speed range. Included in such calculations re such essential effects as:

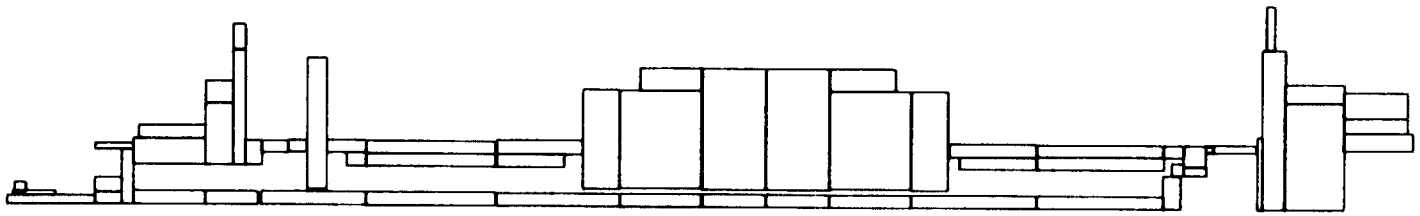
Gyroscopic moments

Shaft flexibilities

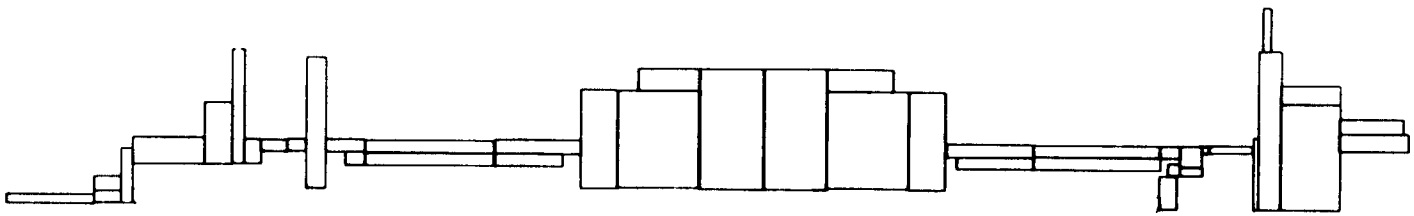
Linear and nonlinear bearing flexibilities and damping

Static and dynamic rotor unbalance

Rotor mass distribution



MASS ELEMENTS OF ROTATING ASSEMBLY



STIFFNESS ELEMENTS OF ROTATING ASSEMBLY

TABLE 33

SUMMARY OF BEARING AND ROTATING GROUP
CHARACTERISTICS USED IN CRITICAL SPEED* ANALYSIS

TAC No.	SKP No.	Shaft Speed, rpm	Compressor Design	Bearing Design	Bearing Spring Constant, lb./in. (N/cm)		Bearing Span, in. (cm)	Rotating Group Weight, lbs. (kg)			
									Components		
					Compressor	Turbine		Total	Compressor	Rotor	Turbine
TAC-A	21511	24,000	Radial	Gas	60,000 (105,000)	60,000 (105,000)	18.2 (46.2)	200 (90.7)	9.10 (4.1)	115 (52)	40 (18)
TAC-B	21510	24,000	Axial	Gas	60,000 (105,000)	60,000 (105,000)	29.8 (75.7)	207 (93.9)	15.00 (6.8)	115 (52)	40 (18)
TAC-C	21495	36,000	Radial	Rolling Element	40,000 (70,000)	40,000 (70,000)	24.5 (62.2)	124 (56.2)	5.75 (2.6)	97 (44)	12 (5.4)
TAC-D	21513	36,000	Axial	Rolling Element	100,000 (175,000)	500,000 (876,000)	34.0 (86.4)	133 (60.3)	13.00 (5.9)	97 (44)	12 (5.4)
TAC-E	21494	36,000	Radial	Oil-Film	100,000 (175,000)	100,000 (175,000)	25.8 (65.5)	126 (57.2)	5.75 (2.6)	97 (44)	12 (5.4)
TAC-F	21512	36,000	Axial	Oil-Film	100,000 (175,000)	100,000 (175,000)	35.6 (90.4)	132 (59.9)	13.00 (5.9)	97 (44)	12 (5.4)

*For each case a radial eccentricity of 0.0001 in. (0.0003 cm) was assumed to simulate rotating group unbalance.

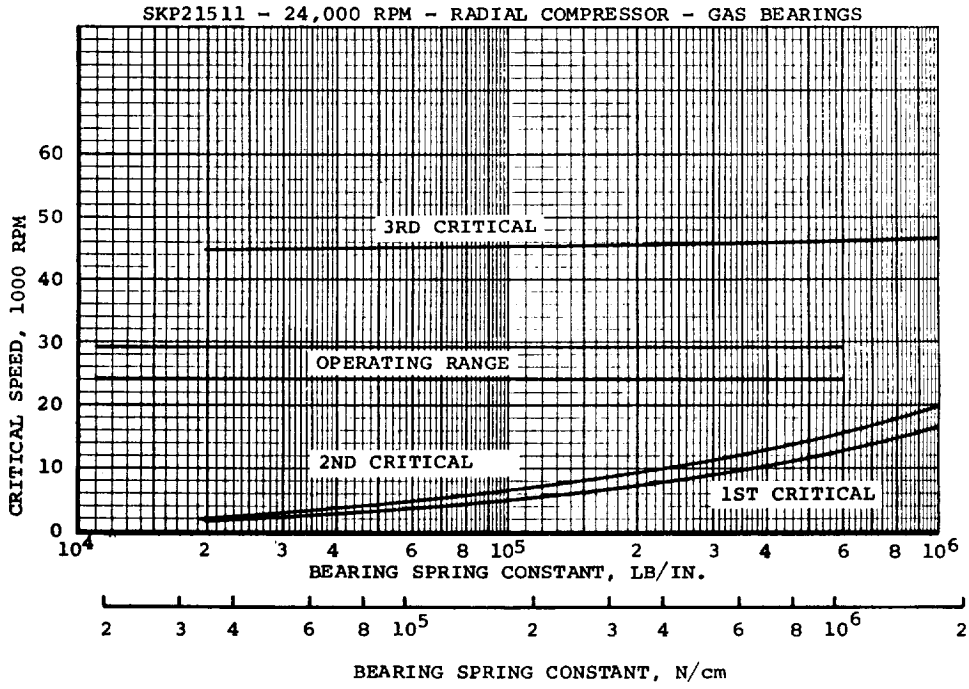
No problems were encountered in these areas for both gas bearing configuration, TAC-A and TAC-B. The large shaft diameter necessary for journal bearing load capacity also lends bending stiffness to the rotating group. Pivoted-pad gas bearings of 60,000 ppi spring rate (105,000 N/cm) were used in each configuration. Figures 79 and 80 present rotor dynamics for TAC-A and TAC-B, respectively. Bearing loads are slightly higher for TAC-B due to a longer bearing span and the heavier axial compressor.

In order to meet the 50,000 hour design life, TAC-C and D employed 30-mm roller bearings. Therefore, to allow enough shaft diameter about the alternator rotor for sufficient rotor stiffness, the bearings were mounted outboard of the turbine and compressor.

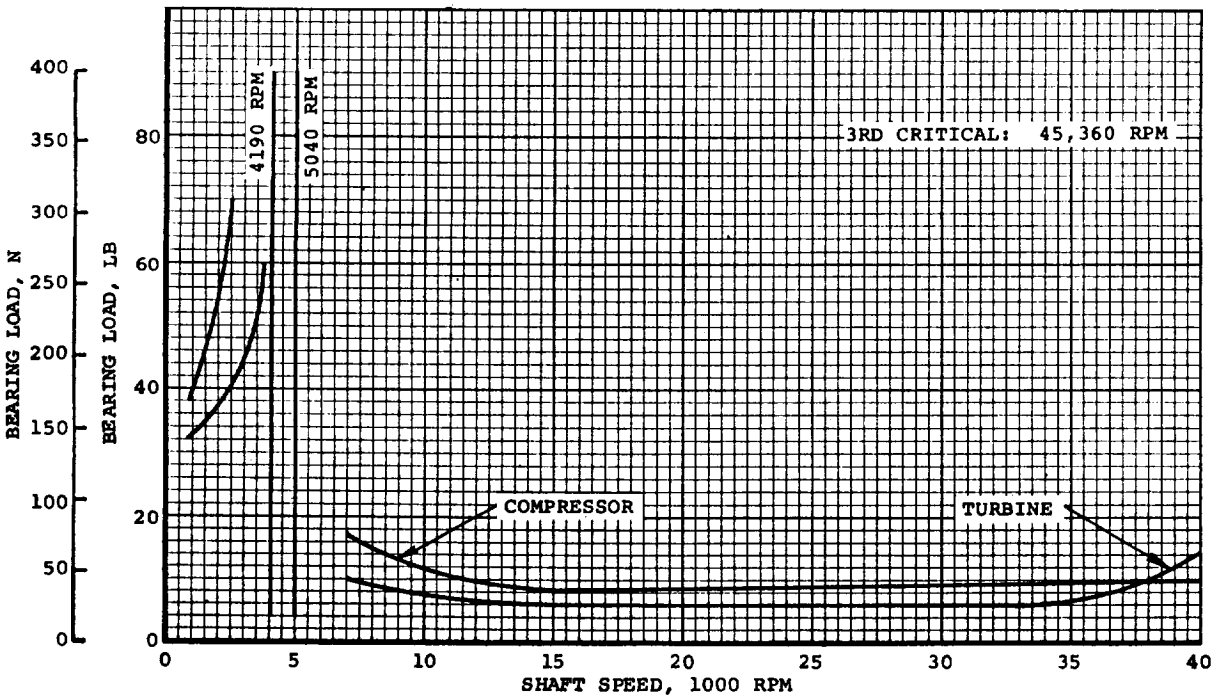
The roller bearings as mounted in the TAC structure will exhibit spring rates of approximately 500,000 ppi (875,600 N/cm). As can be seen from Figure 81 for TAC-C this places the second critical squarely in the operating range. This was corrected by mounting both bearings in a flexible mount of 40,000 ppi equivalent spring rate (70,000 N/cm).

A similar problem existed for TAC-D (see Figure 82) although it required only the turbine end bearing to be flexibly mounted with a spring rate equivalent to 100,000 ppi (175,000 N/cm).

Initially, TAC-E and -F utilized inboard oil film journal bearings. However, the large journal diameters dictated by bending stiffness considerations also entailed prohibitive viscous losses. Therefore, the bearings were mounted outboard on a 1.0-in. diameter shaft extension (2.54 cm) thereby decreasing overhung weight while simultaneously allowing increased center stiffness through larger diameter internal shafting. Figures 83 and 84 present satisfactory rotor behavior with a bearing spring rate of 100,000 ppi (175,000 N/cm).



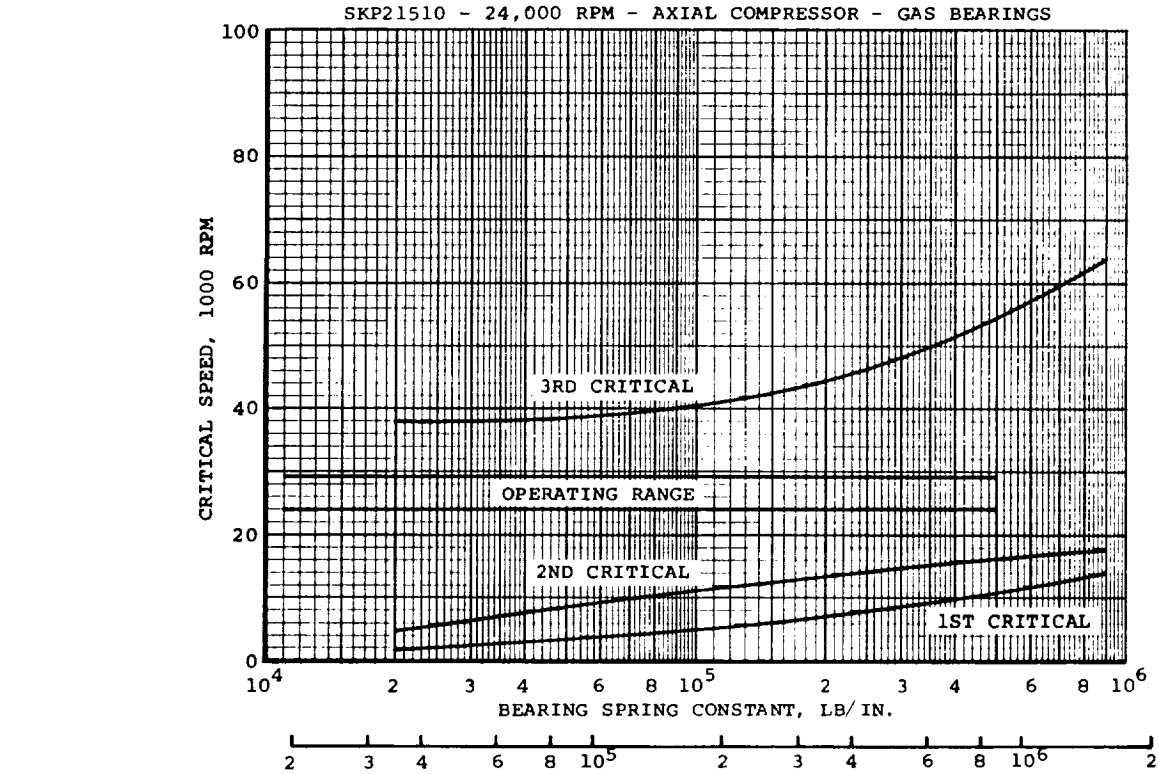
CRITICAL SPEED VERSUS BEARING SPRING CONSTANT



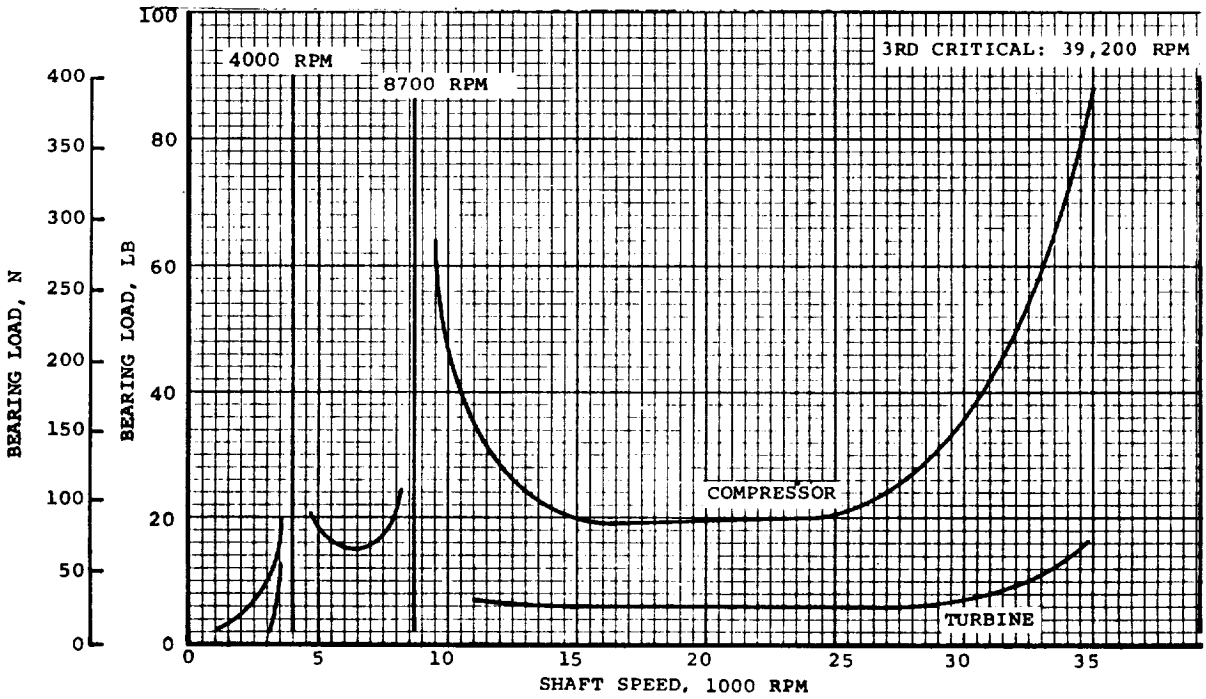
BEARING LOAD AND CRITICAL SPEED ANALYSIS

TAC - A

FIGURE 79



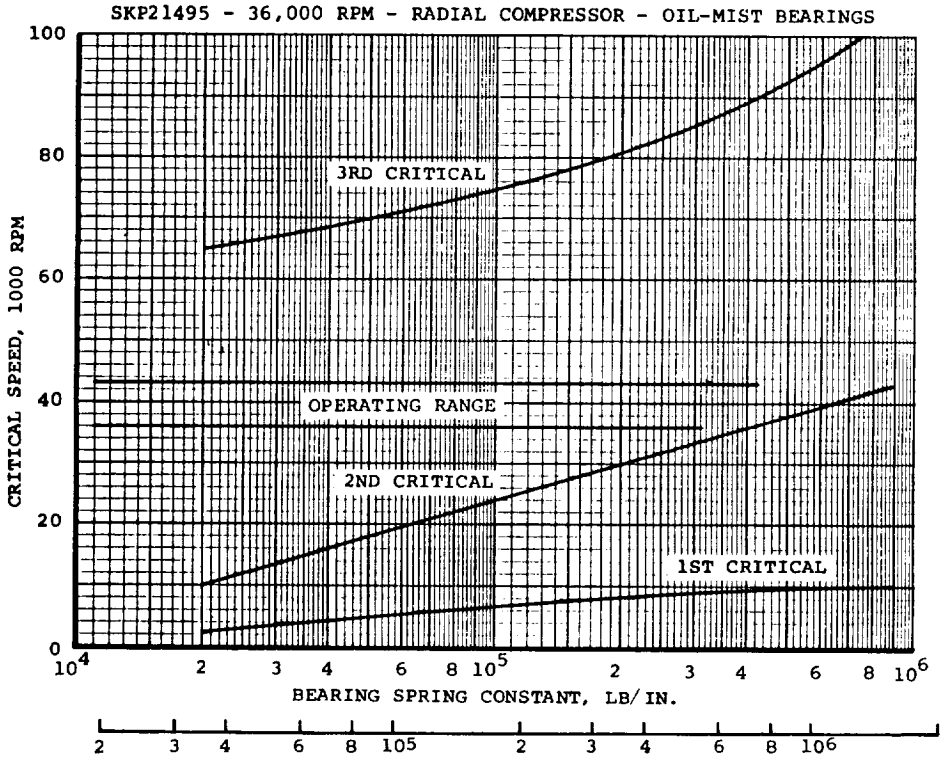
CRITICAL SPEED VERSUS BEARING SPRING CONSTANT



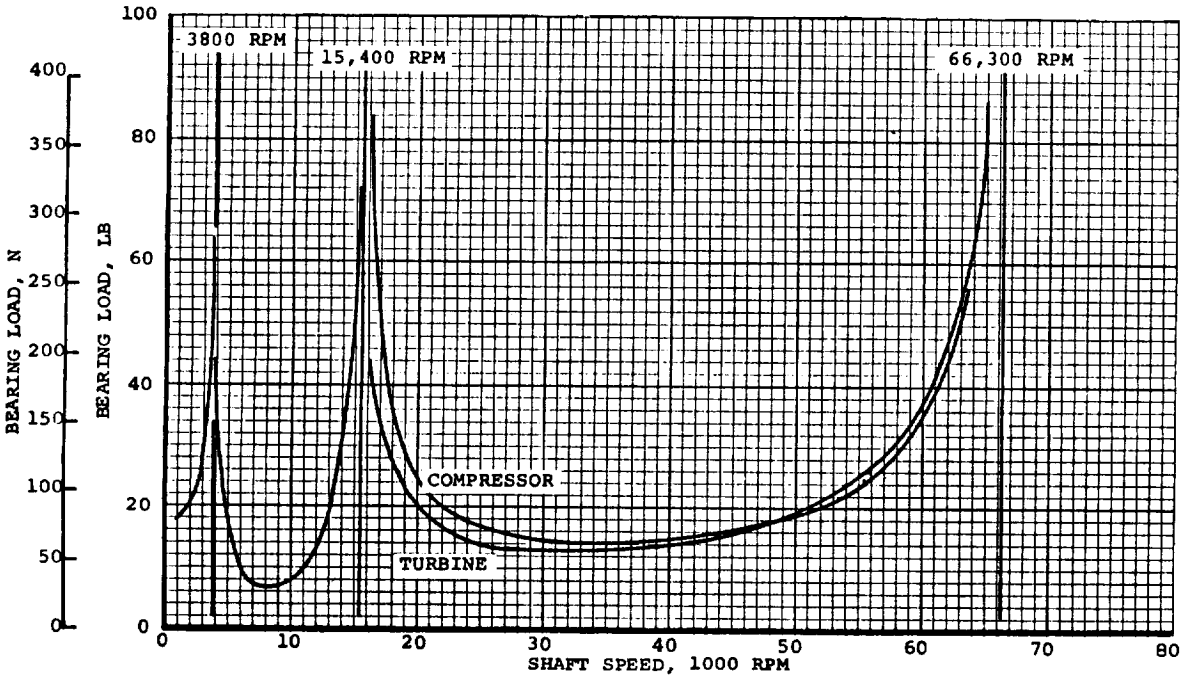
BEARING LOAD AND CRITICAL SPEED ANALYSIS

TAC - B

FIGURE 80



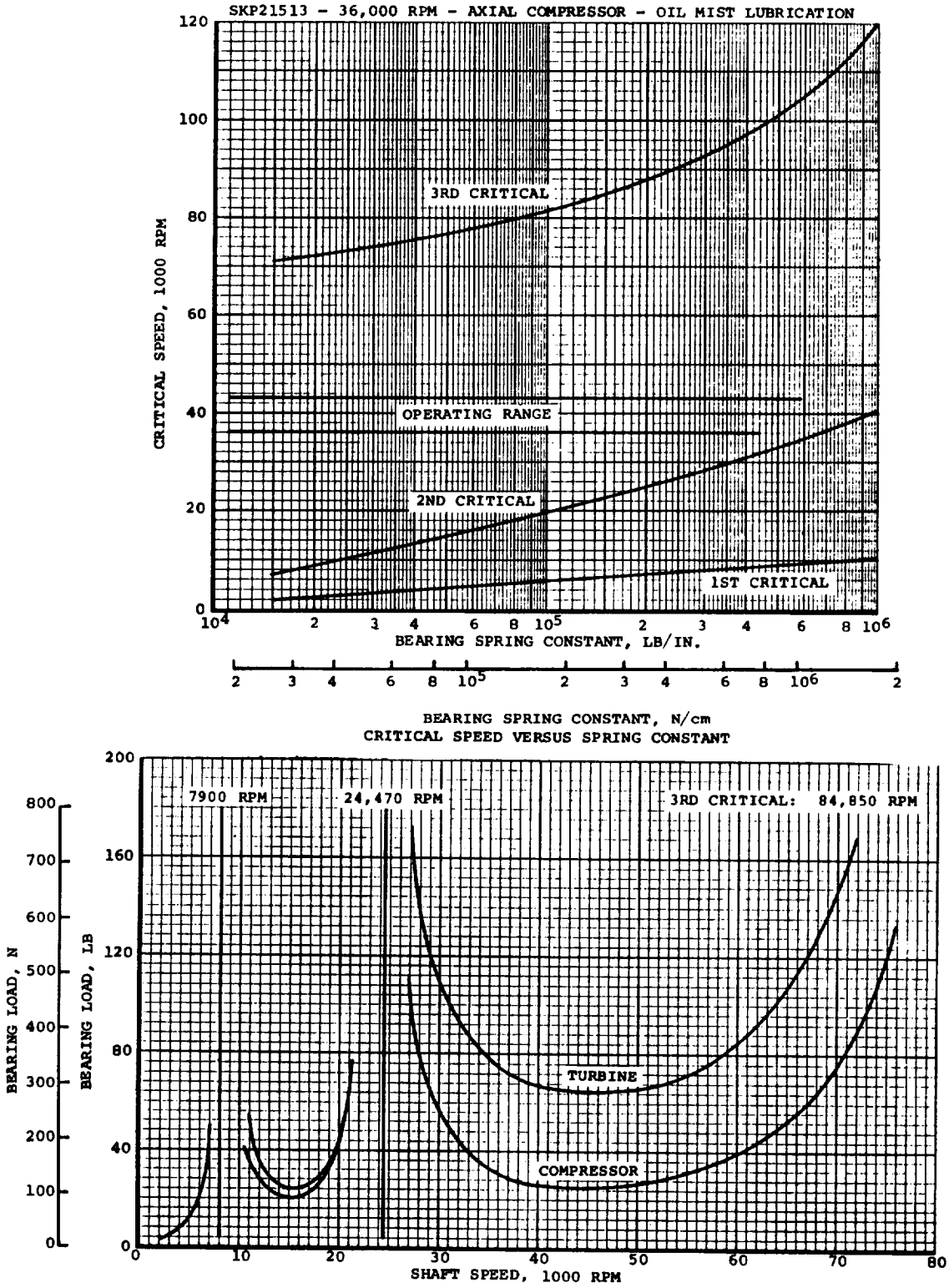
CRITICAL SPEED VERSUS SPRING CONSTANT



BEARING LOAD AND CRITICAL SPEED ANALYSIS

TAC - C

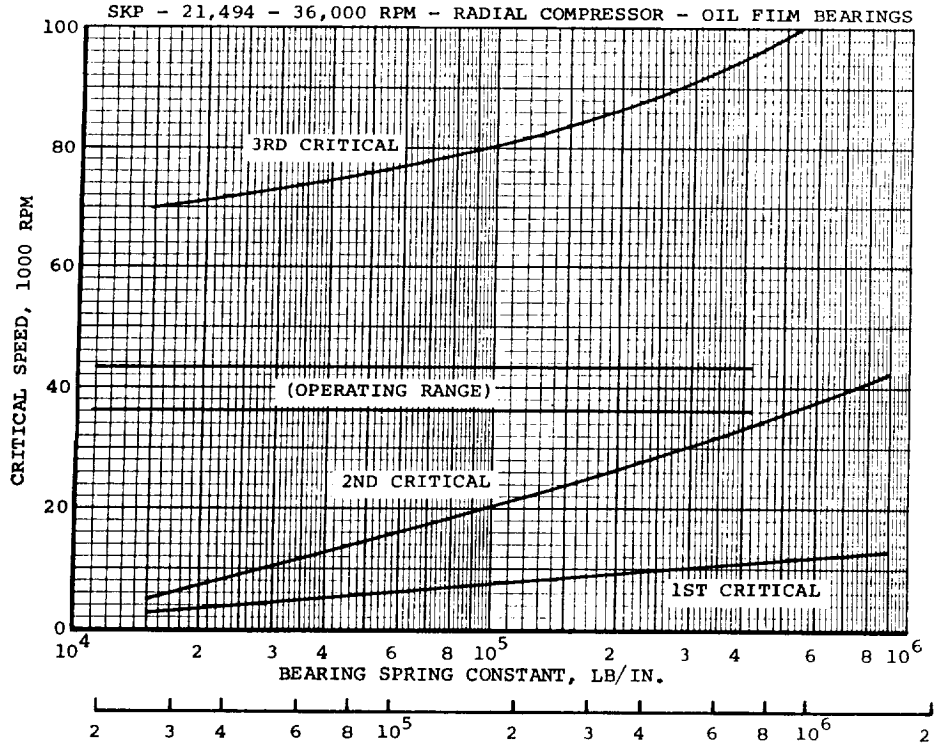
FIGURE 81



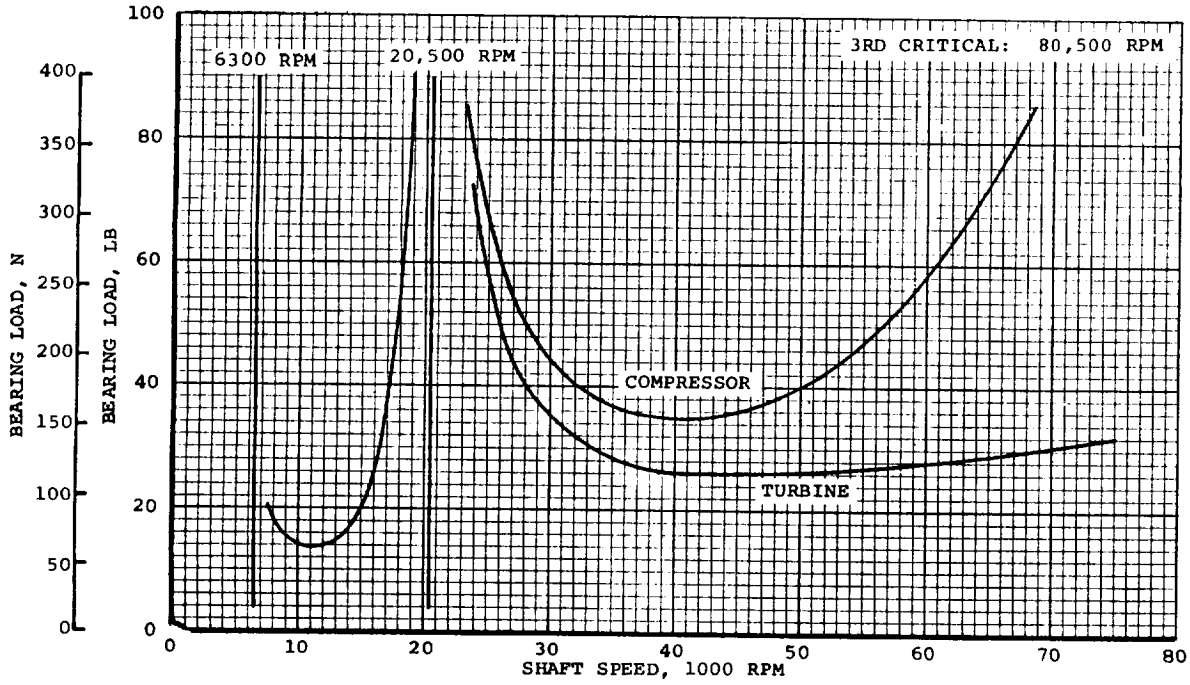
BEARING LOAD AND CRITICAL SPEED ANALYSIS

TAC - D

FIGURE 82



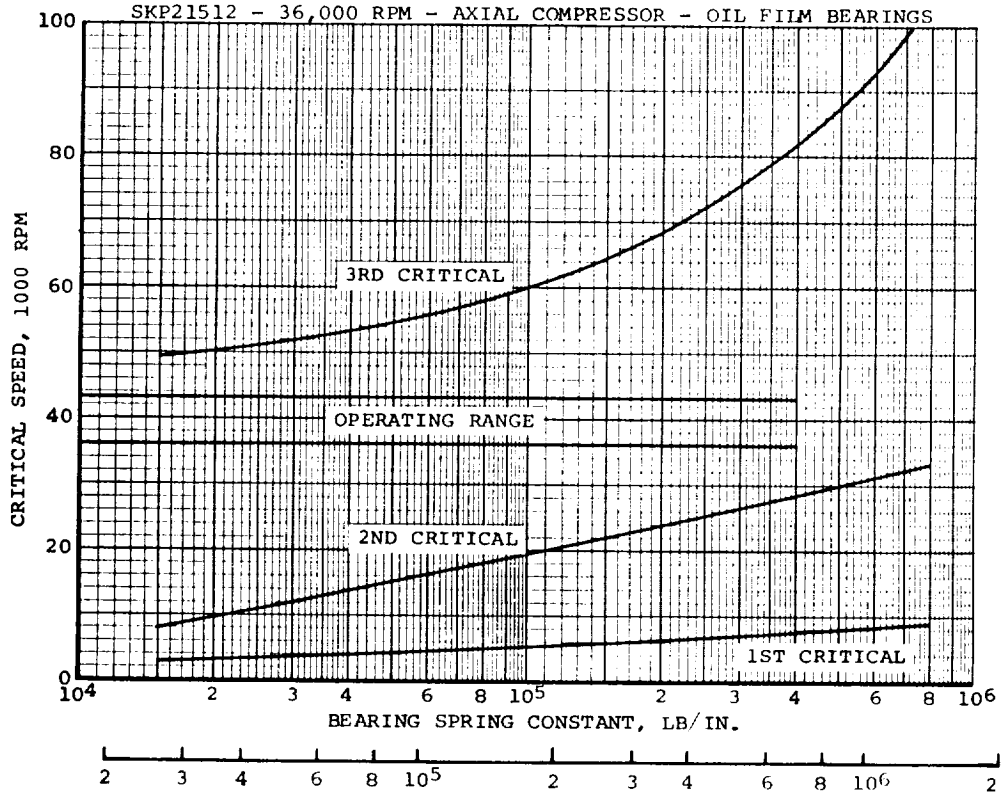
CRITICAL SPEED VERSUS SPRING CONSTANT



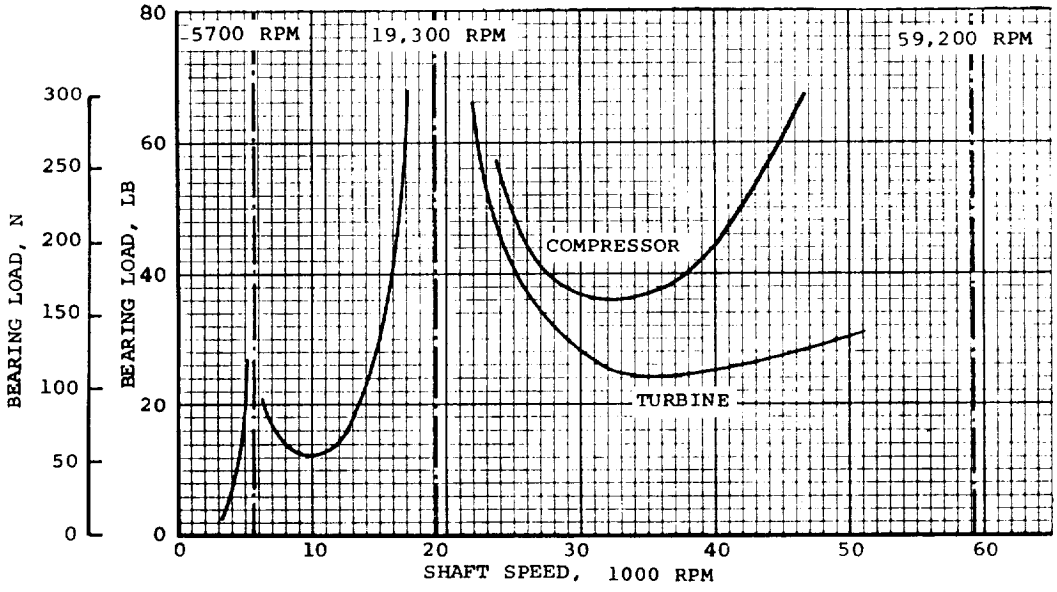
BEARING LOAD AND CRITICAL SPEED ANALYSIS

TAC - E

FIGURE 83



CRITICAL SPEED VERSUS SPRING CONSTANT



BEARING LOAD AND CRITICAL SPEED ANALYSIS

TAC - F

FIGURE 84

5.6 TAC Bearing Configurations

5.6.1 Gas Lubricated Bearing System

The journal bearing concept chosen for both the radial and axial flow 24,000 rpm TAC units is a three-pad configuration with one pad resiliently mounted to accommodate journal centrifugal growth and thermal gradient effects.

Analyses were performed by computer techniques using the following assumed constants:

(a) Gas lubricant (working fluid) molecular weight, He-Xe mixture - 39.944

(b) Rotating assembly angular speed, 24,000 rpm

(c) Pad length-to-diameter ratio (L/D), arbitrary choice - 1.00

(d) Pad-wrap angle, arbitrary choice - 100-deg arc

(e) Pad-pivot location - 65 percent back from pad leading edge

(f) Journal bearing design load - one-half the weight of the TAC rotating assembly, i.e., 100 lb (444.8 N)

(g) Bearing cavity ambient pressure - a range as follows:

TAC Net Output, kw_e	P_a (Bearing Cavity Ambient Pressure), psia	kN/m^2abs
40.0	25.0	172.4
160.0	100.0	689.5

(h) Journal (lubricant) temperature - a range arbitrarily selected between 860 and 1260°R (477.5 and 696°K)

5.6.1.1 Journal Bearing Design Load

The radial aerodynamic component version of the TAC machine is conceptually a scale-up of the NASA BRU. The rotating group mass of the BRU is approximately 22 lb (9.96 kg). Preliminary estimates of the 24,000-rpm TAC indicated that the rotating group, scaled from the BRU geometry, would weight close to 200 lb (90.5 kg). Design practice dictates that each journal bearing should, as a minimum, support one-half of this weight during self-acting operation with the TAC operating horizontally in a 1 g environment.

5.6.1.2 Journal Bearing Design Minimum Film Thickness

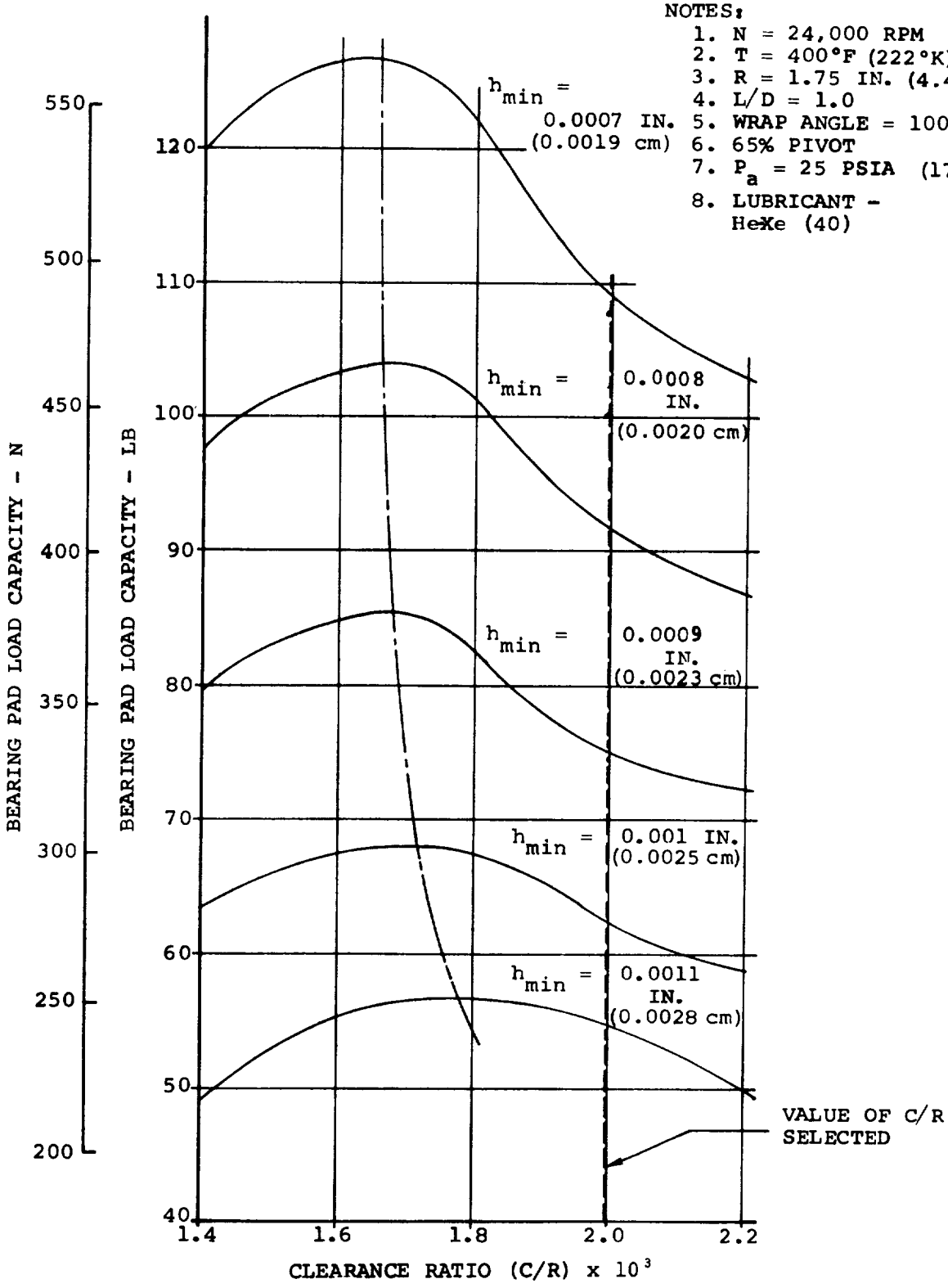
In the design of a gas bearing/rotor suspension system for turbomachinery such as the TAC, the bearing load capacity (minimum film thickness requirements are of paramount importance. The lowest bearing cavity ambient pressure level (to meet the lower power level output operating conditions) will establish the journal diameter. Preliminary studies revealed that a 3.5-in.-dia journal (8.89 cm) would provide the required 100-lb (444.8 N) load capacity at "worst-case" conditions of 25.0 psia (172.4 kN/m^2abs) and 860°R (477.5°K) while providing a minimum film thickness (h_{min}) of approximately 0.75 mil (0.01905 mm).

5.6.1.3 Clearance Ratio Selection

The influence of clearance ratio upon pad-load capacity was investigated for the two selected bearing cavity pressures and journal/lubricant temperature extremes. Figures 85 and 86 are plots of bearing pad load capacity versus clearance ratio for various constant minimum film thicknesses (h_{min}). Note that in each figure a given clearance ratio is optimum for only one value of minimum film thickness. It is desirable to choose a clearance ratio that is to the right of the peak load curve. With such a choice for clearance ratio, slight decreases in clearance, such as those due to centrifugal effects, will actually increase the lubricant film thickness. Based on the results in Figures 85 and 86, a clearance ratio (C/R) of 0.002 has been selected.

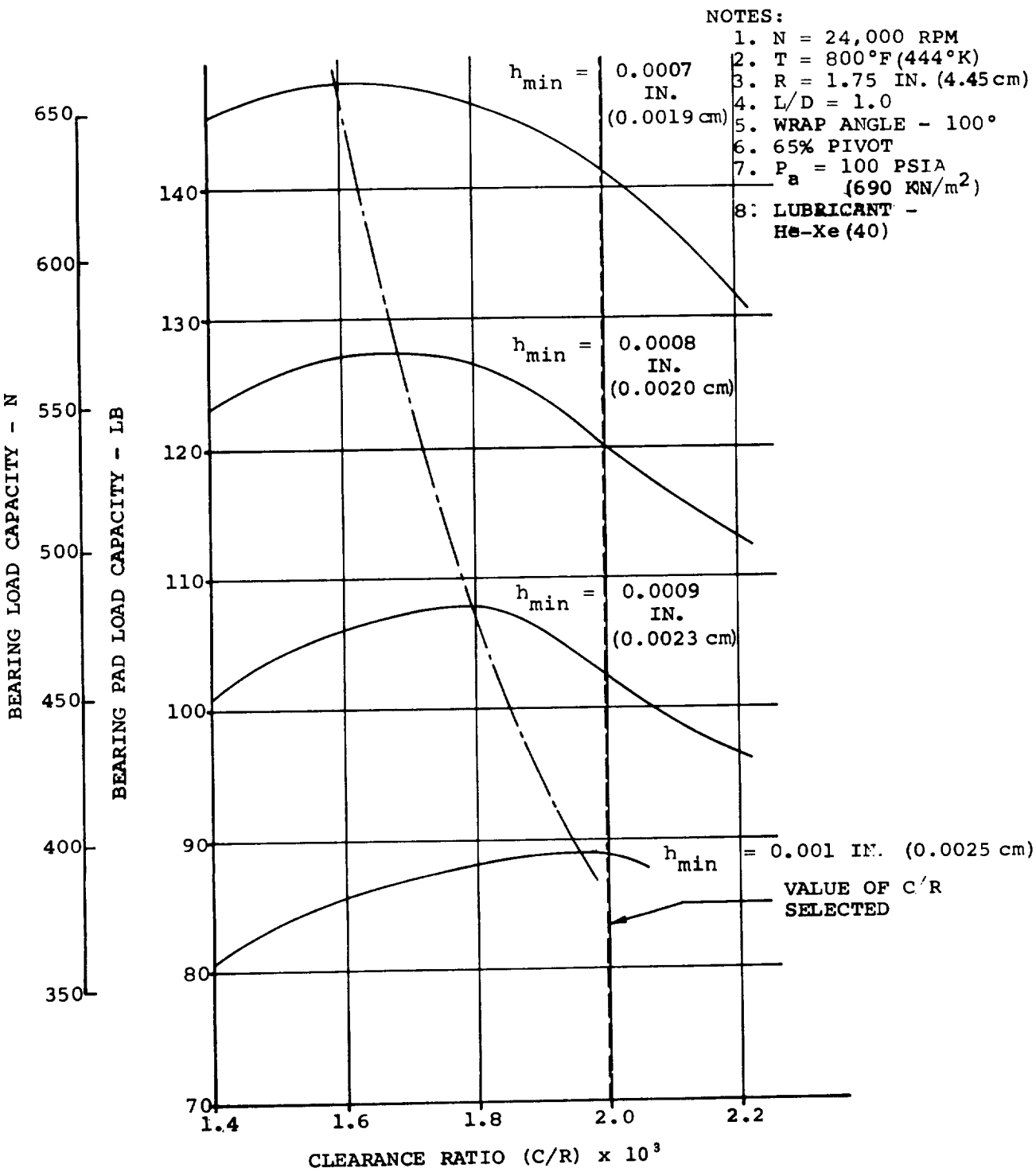
5.6.1.4 Predicted Bearing Pad Performance

The predicted bearing pad self-acting performance for a clearance ratio of 0.002 is shown in Figures 87 and 88. It should be noted that the stability-limit curve superimposed on Figure 87 applies only to a vertically oriented TAC rotor or a 0-g environment. The stability-limit curve is derived from data obtained during testing conducted under Contract NAS 3-7633 and reported in NASA CR-54939. Figure 89 from that study presents experimentally obtained operating conditions at which the on-set of self-excited rotor whirl occurred. These conditions are in dimensionless form (pad eccentricity ratio, ε, versus pad compressibility number, Λ) to enable the prediction of self-excited whirl in three-pad gas bearings of similar geometry but with dimensions different from those tested. The upper boundary curve was used to predict the journal bearing geometric preload for the BRU machine built under Contract NAS 3-9427. Subsequent time transient orbital studies of the BRU gas journal bearing system, performed by the Franklin Institute Research Laboratories under a subcontract to AiResearch, demonstrated the validity of the empirical stability criteria. When applied to the TAC bearing pad performance in Figure 87, the stability criteria



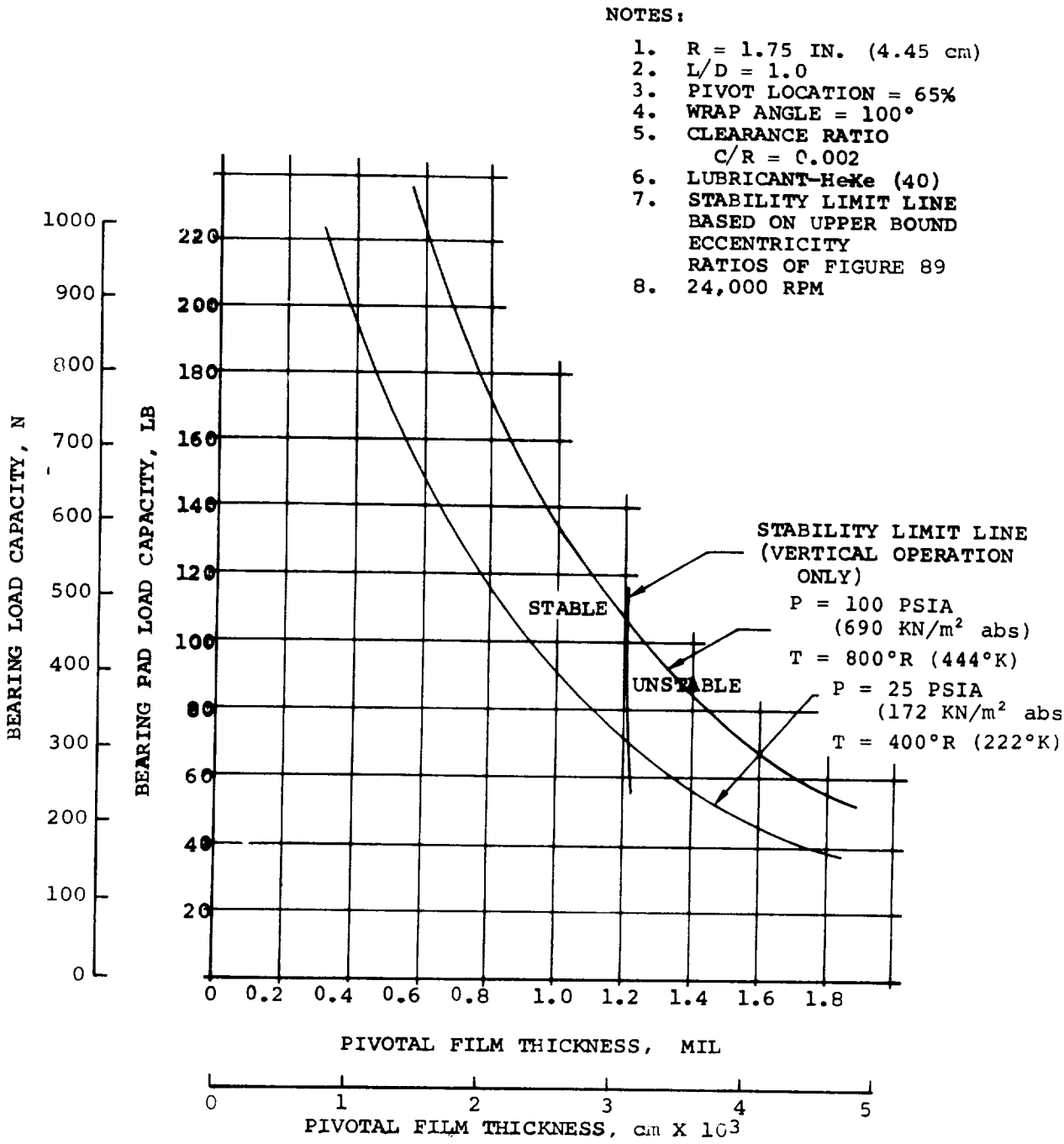
TAC GAS JOURNAL BEARING LOAD CAPACITY VS CLEARANCE RATIO

FIGURE 85



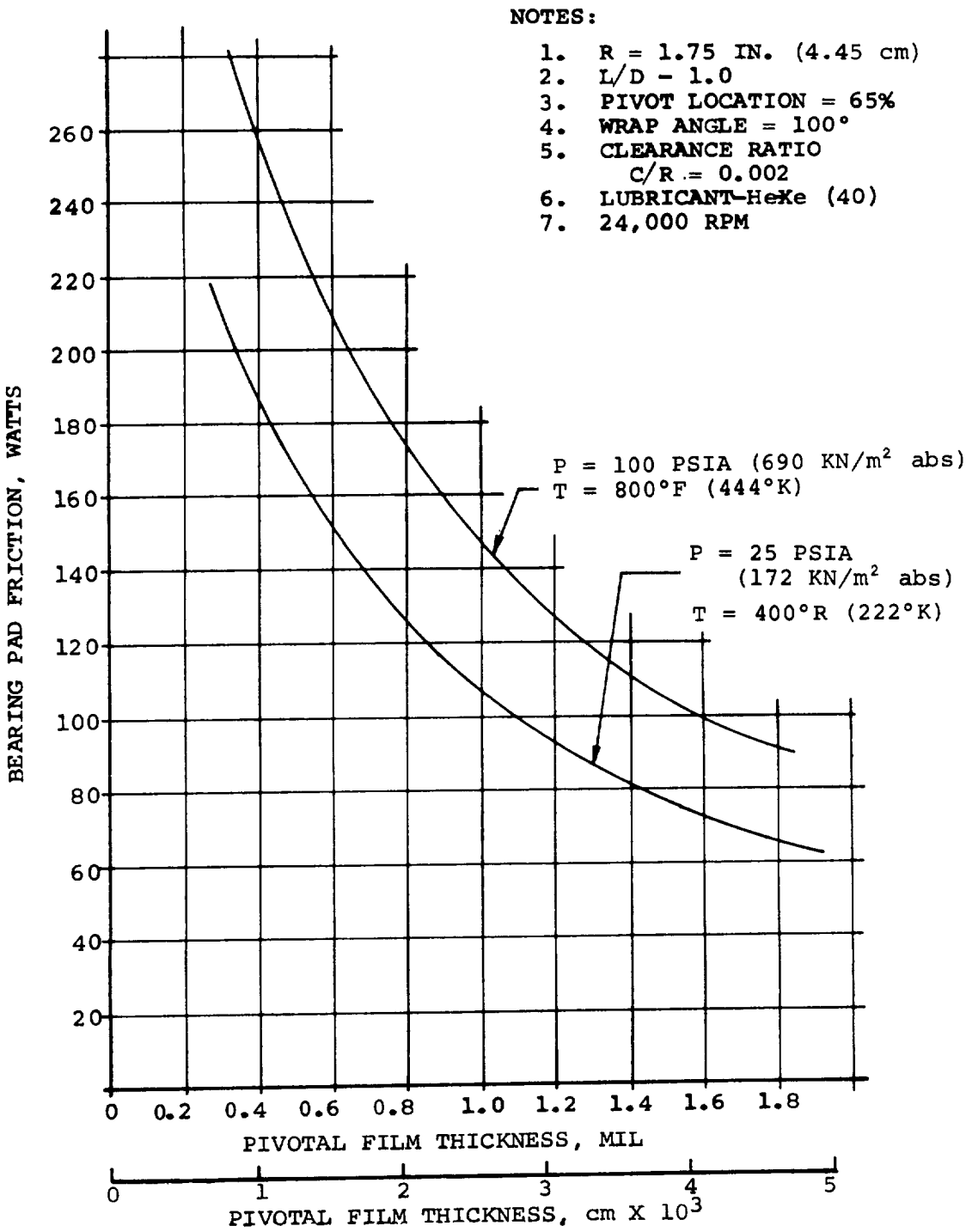
TAC GAS JOURNAL BEARING LOAD CAPACITY VS CLEARANCE RATIO

FIGURE 86



TAC GAS JOURNAL BEARING PAD LOAD CAPACITY VS PIVOTAL FILM THICKNESS

FIGURE 87

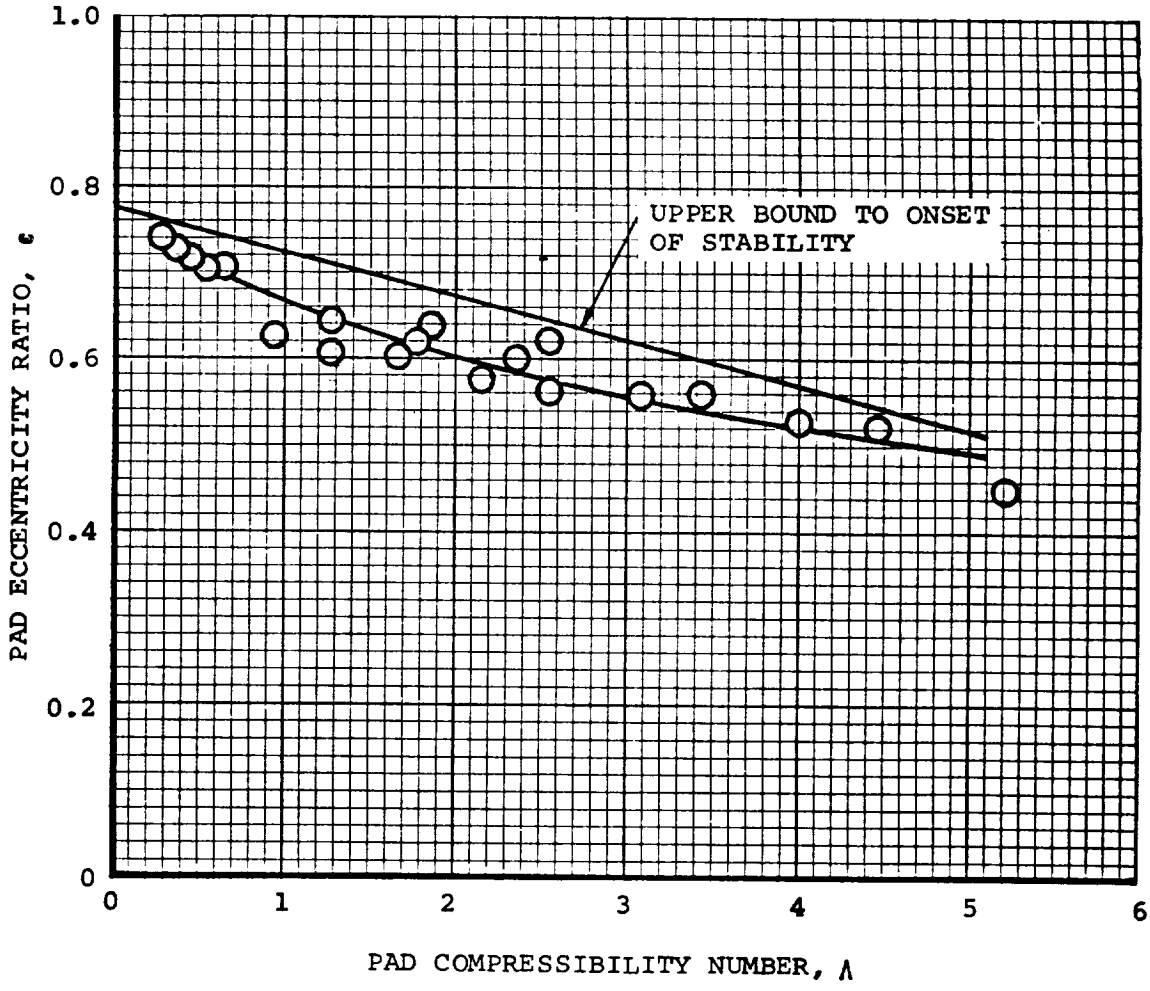


TAC GAS JOURNAL BEARING PAD LOAD CAPACITY VS
PIVOTAL FILM THICKNESS

FIGURE 88

NOTES:

1. CONFIGURATION: THREE PIVOTED PADS, TWO RIGID AND ONE FLEXIBLE MOUNT AT 2000 LB/IN. (3502 N/CM)
2. LINES ARE BEST FIT CURVES THROUGH DATA POINTS
3. DATA POINTS REFER TO ONSET OF SELF-EXCITED INSTABILITY
4. P_a = AMBIENT PRESSURE
5. $\Lambda = \frac{6\mu\Omega}{P_a}(R/C)^2$
6. Ω = JOURNAL VELOCITY, RAD/SEC
7. μ = VISCOSITY, REYNS
8. R = JOURNAL RADIUS, IN.
9. C = RADIAL JOURNAL CLEARANCE, IN.
10. $\epsilon = 1 - \frac{h_{min}}{C}$
11. h_{min} = MINIMUM FILM THICKNESS, IN.



REDUCED TEST DATA
GAS BEARING STABILITY STUDY

FIGURE 89

imply that the bearing geometric preload must be such that the pivotal film thickness should not exceed 0.0012 in. (0.03045 mm) at steady-state self-acting conditions.

5.6.1.5 Gas Lubricated Journal Bearing Performance

Figures 90 and 91 show typical predicted journal bearing performance for a bearing cavity ambient pressure of 100 psia (689.5 kN/m^2 abs) and an assumed lubricant temperature of 1260°R (696°K). The special case of zero journal bearing load (vertical TAC operation on earth or zero "g" operation) occurs at zero displacement between fixed pivots. When the TAC units are in a horizontal position during terrestrial operation, the load on each journal is essentially 100 lb (44.8 N). The displacement between the fixed pivots will be 1.06 mil (0.0269 mm) as shown on Figures 90 and 91.

Therefore the expected performance of each TAC journal bearing is as follows:

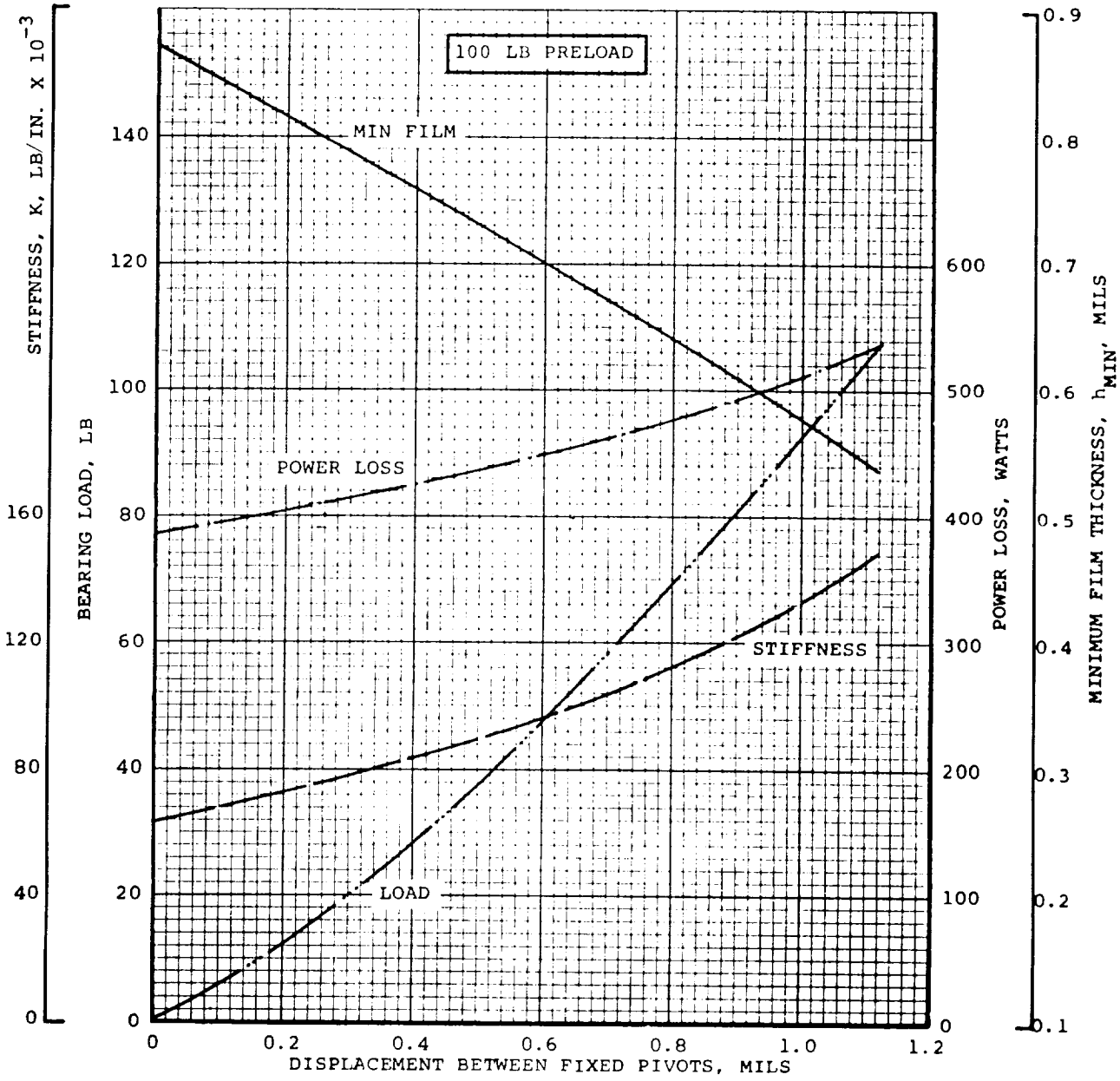
	Vertical or Zero "g" Operation	Horizontal Terrestrial Operation
Journal bearing load, lb (N)	0	100 (444.8)
Minimum film thickness, mil (mm)	0.87 (0.0221)	0.556 (0.0141)
Bearing power loss, watts	385	524
Bearing stiffness, lb/in. (N/cm)	64,000 (112,081)	140,000 (245,178)

5.6.1.6 Gas Lubricated Thrust Bearing

The thrust bearing selected for the gas lubricated TAC units is a preloaded pair of identical stator plates of the Rayleigh step-sectored

NOTES:

1. NO. OF PADS: 3
2. σ = 100°
3. D = 3.5 IN.
4. N = 24,000 RPM
5. P_a 100 PSIA
6. a/c = 0.65
7. L/D 1.0
8. μ = 7.5×10^{-9} REYNS

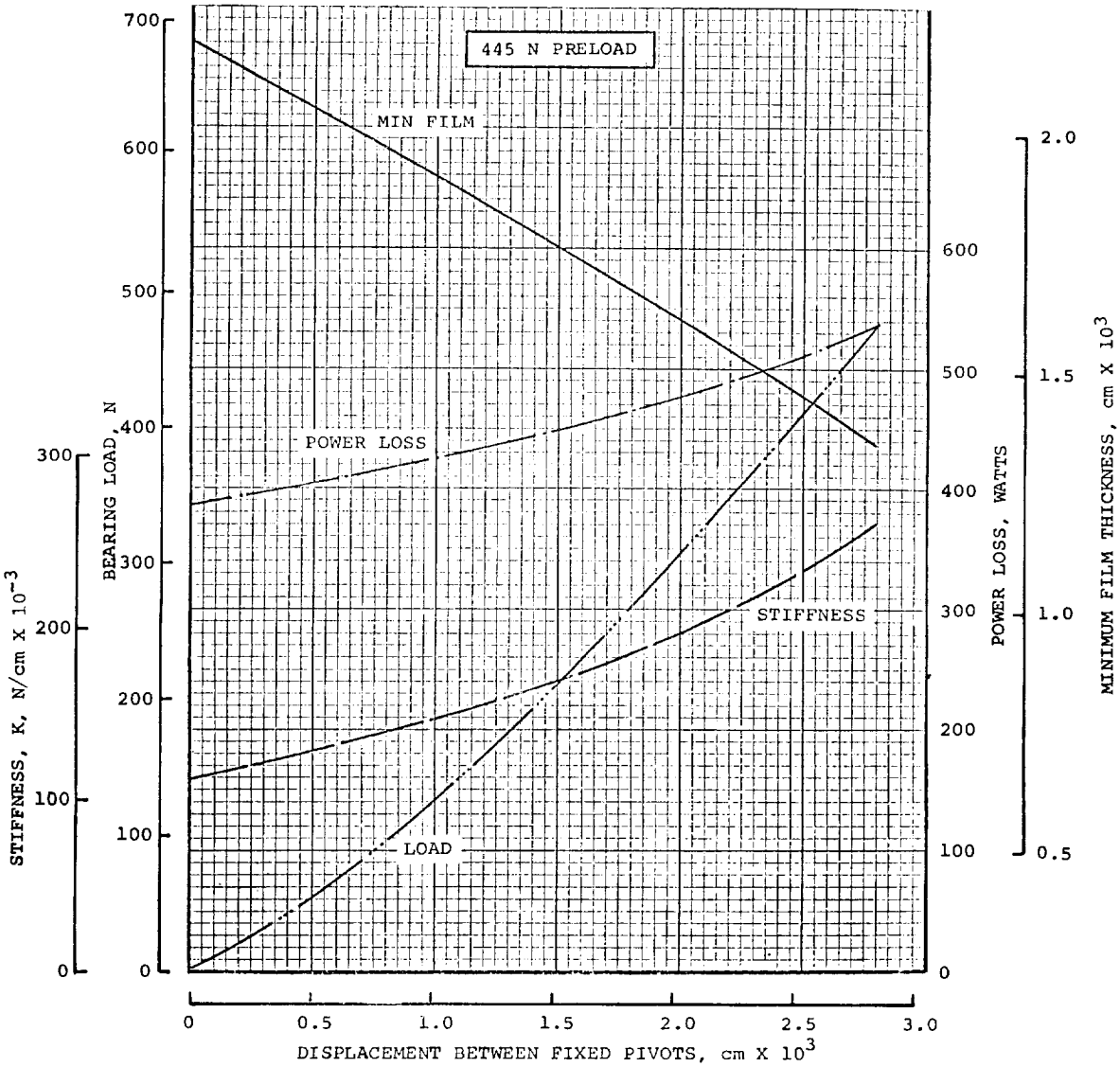


TILTING PAD GAS JOURNAL BEARING PERFORMANCE
XeHe LUBRICANT (MW = 39.94)

FIGURE 90

NOTES:

1. NO. OF PADS: 3
2. γ = 100°
3. D = 8.89 cm
4. N = 24,000 RPM
5. P_a = 690 KN/m^2
6. θ/α = 0.65
7. L/D = 1.0
8.



TILTING PAD GAS JOURNAL BEARING PERFORMANCE
X_eH_e LUBRICANT (MW = 39.94)

FIGURE 91

type. Figures 92 and 93 present the predicted steady-state performance of the chosen 8.0 in. (20.32 cm) O.D. two-sided thrust bearing system as a function of axial displacement of the thrust runner.

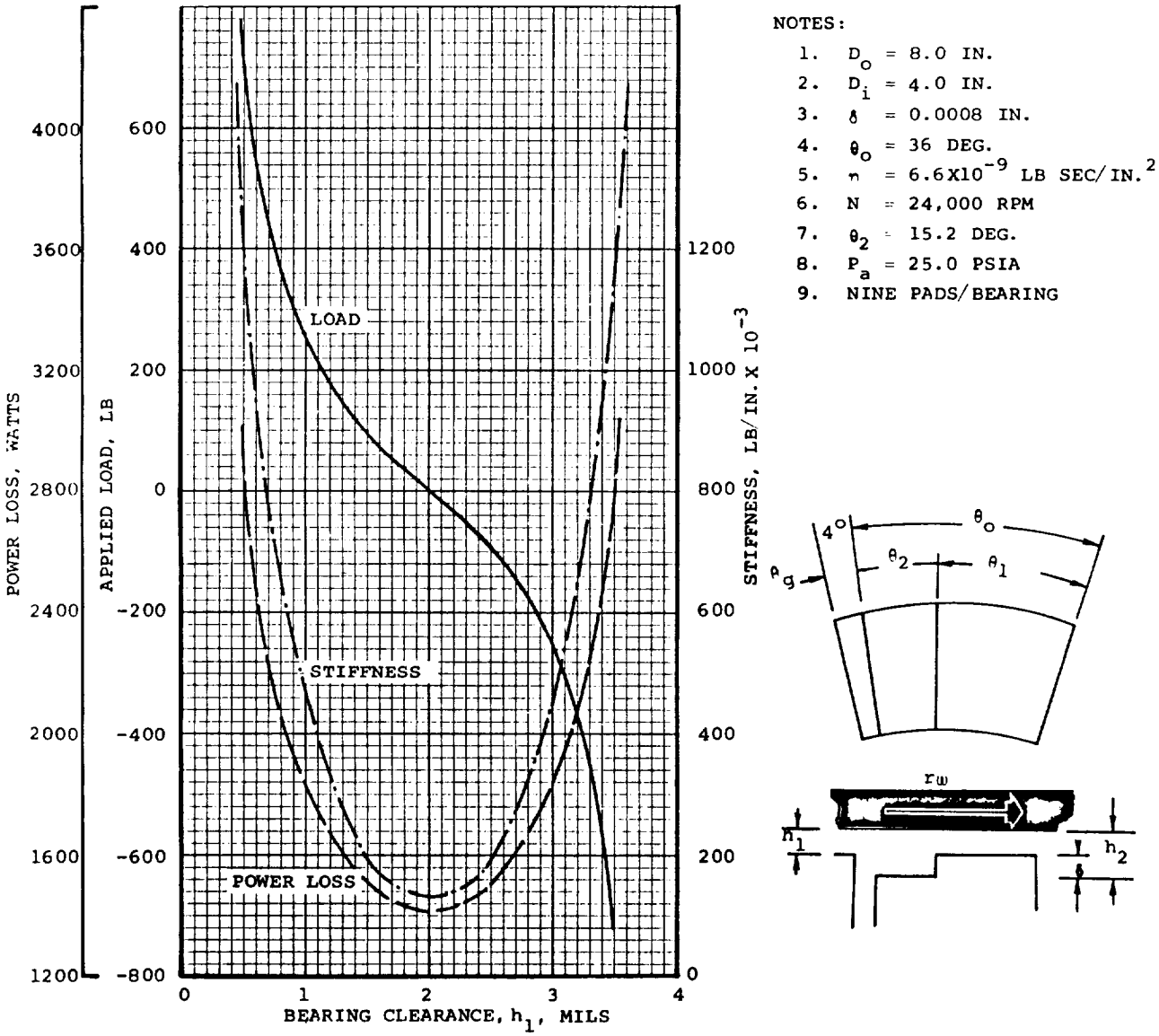
Anticipated thrust bearing performance for two orientations is as follows:

	Vertical Terrestrial Operation	Horizontal or Zero "g" Operation
Load, lb (N)	300 (1334)	100 (445)
Minimum bearing clearance, in. (mm)	0.00092 (0.0234)	0.00148 (0.0376)
Lubricant film stiffness, lb/in. (N/cm)	450,000 (788,072)	195,000 (341,498)
Total power loss, watts	1930	1520

5.6.1.7 Combined Bearing System Losses

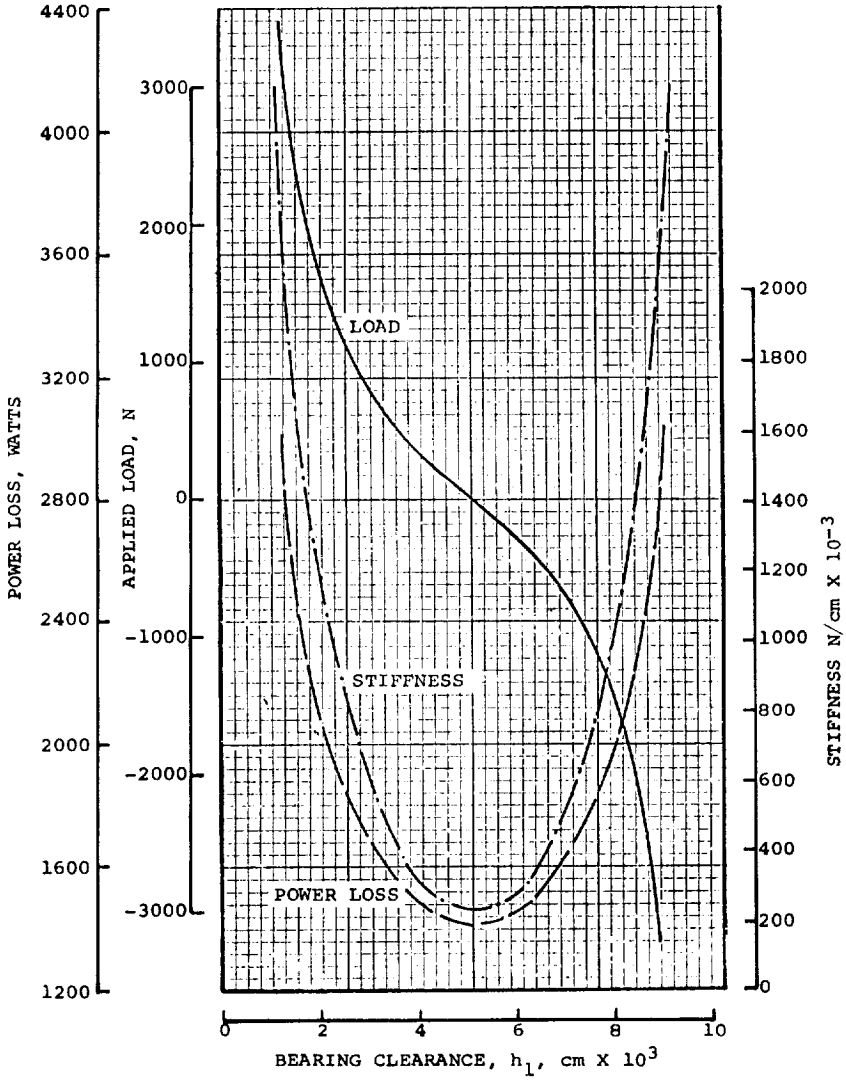
Comparison of the journal and thrust bearing losses at two orientations indicate that vertical terrestrial operation will be the worst case. Total combined gas bearing losses are 2.7 kw versus 2.568 kw for the other orientation. These losses were used in the final definition of the TAC-A and -B machines.

Labyrinth seals are used to isolate the aerodynamic components and the alternator rotor cavity from the bearing cavity. Leakage of these seals for the TAC-A and -B configurations are summarized in Tables 34 and 35. The alternator cavity is vented to the compressor inlet to minimize the cavity pressure and thus windage loss without external pumping. Additional discussion of alternator windage is included in Section 5.7.



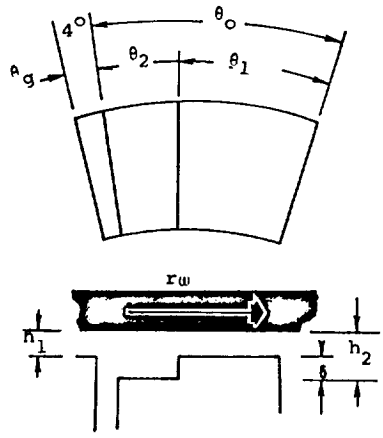
PERFORMANCE OF GAS-LUBRICATED DOUBLE-ACTING
STEP THRUST BEARING
XeHe LUBRICANT (MW = 39.94)

FIGURE 92



NOTES:

1. D_o = 20.3 cm
2. D_i = 10.2 cm
3. δ = 0.002 cm
4. θ_o = 36 DEG
5. η = 4.6 X 10^{-5} N SEC/m^2
6. N = 24,000 RPM
7. θ_2 = 15.2 DEG
8. P_a = 172 KN/m^2 abs
9. NINE PADS/BEARING



PERFORMANCE OF GAS-LUBRICATED DOUBLE-ACTING
STEP THRUST BEARING
X_eH_e LUBRICANT (MW = 39.94)

FIGURE 93

TABLE 34

TAC-A SEAL LEAKAGES

	BACKFACE SEALS		ALTERNATOR ISOLATION SEALS	
	COMP. END	TURB. END	COMP. END	TURB. END
Seal Diameter, in (cm)	3.5 (8.9)	3.5 (8.9)	3.5 (8.9)	3.5 (8.9)
Seal Clearance, in (cm)	0.005 (0.0127)	0.005 (0.0127)	0.005 (0.0122)	0.005 (0.0127)
Bearing Compartment Pressure, psia (KN/m^2 abs)	104.5 (720)	104.5 (720)	104.5 (720)	104.5 (720)
Downstream Pressure, psia (KN/m^2 abs)	69.0 (476)	69.0 (476)	55 (379)	55 (379)
Leakage Flow, lb/sec (kg/sec)	0.0305 (0.0138)	0.0305 (0.0138)	0.035 (0.016)	0.035 (0.016)
Total Flow, lb/sec (kg/sec)	0.061 (0.028)		0.070 (0.032)	

TABLE 35

TAC-B SEAL LEAKAGES

	BACKFACE SEALS		ALTERNATOR ISOLATION SEALS	
	COMP. END	TURB. END	COMP. END	TURB. END
Seal Diameter, in (cm)	3.5 (8.9)	3.5 (8.9)	4.9 (12.5)	3.5 (8.9)
Seal Clearance, in (cm)	0.005 (0.0127)	0.005 (0.0127)	0.005 (0.0127)	0.005 (0.0127)
Bearing Compartment Pressure, psia (KN m^2 abs)	104.5 (720)	104.5 (720)	104.5 (720)	104.5 (720)
Downstream Pressure, psia (KN m^2 abs)	55 (379)	69.0 (476)	55 (379)	55 (379)
Leakage Flow, lb sec (kg sec)	0.035 (0.016)	0.0305 (0.0138)	0.049 (0.022)	0.035 (0.016)
Total Flow, lb sec (kg sec)	0.0655 (0.0297)		0.084 (0.038)	

5.6.2 Oil/Mist Lubrication with Rolling Element Bearings

5.6.2.1 Bearing Selection

A preliminary analysis of rolling element bearings was conducted for an operating speed of 36,000 rpm and rotor masses up to 400 lbs (181.4 kg). The long life requirement (5 years) necessitates a bearing system that has two roller bearings to support radial loads and a ball bearing to support the axial loads.

Figures 94 and 95 present the bearing life as a function of load for a range of roller and ball bearings. A system that uses 30-mm bore bearings (106-size roller bearings and a 206-size ball bearing) was selected for the TAC application. The 30-mm bore size was judged the minimum that could be utilized with the lubrication system discussed in the next section. The B_1 design life (43,800 hours) can be obtained with the roller bearings at radial loads less than 265 lb (1.18 kN). The ball bearing B_1 fatigue-life that can be expected is approximately 26,000 hours with a thrust load of 65 to 75 lb (289 to 334 N). This is the lowest thrust load which should be imposed on the ball bearing to ensure that no ball-skidding occurs. Aerodynamic thrust loads could be balanced to provide the 65- to 75-lb (289 to 334 N) minimum load while the unit is operating horizontally in a 1- to 0-g field. For operation in the vertical orientation in a 1-g field, the rotor weight (130 lb or 478 N) should oppose the aerodynamic thrust load to give a net thrust of approximately 65 lb (289 N).

The bearing lives calculated in this analysis were based on present-day bearing manufacturing technology. They do not reflect such advanced techniques as Ausforming the rings, for which there is some indication of potentially great life improvement, but which is not yet a well-developed, reliable manufacturing technique. It is possible that such techniques will be perfected within the next few years, and

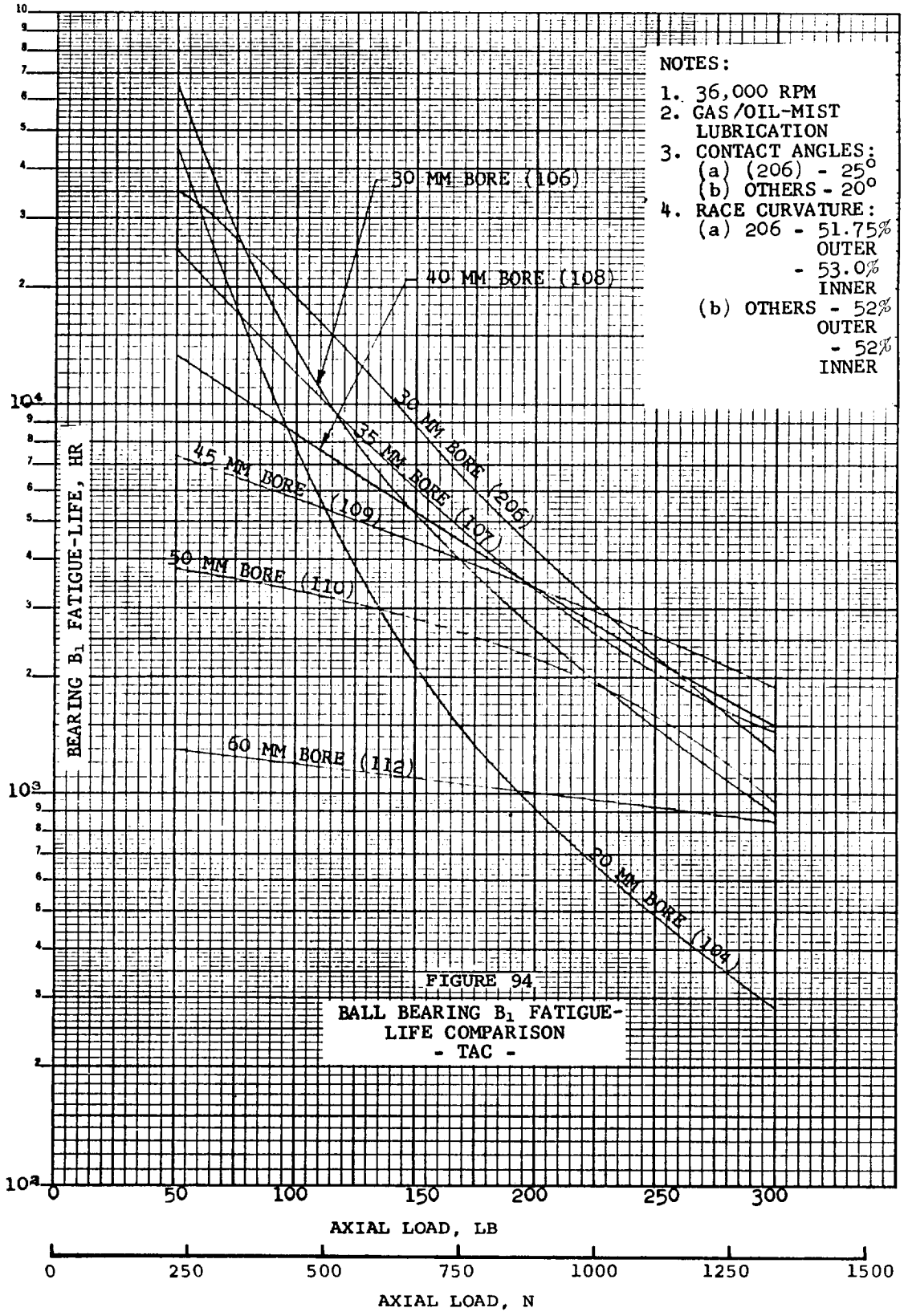


FIGURE 94

BALL BEARING B_1 FATIGUE-LIFE COMPARISON
- TAC -

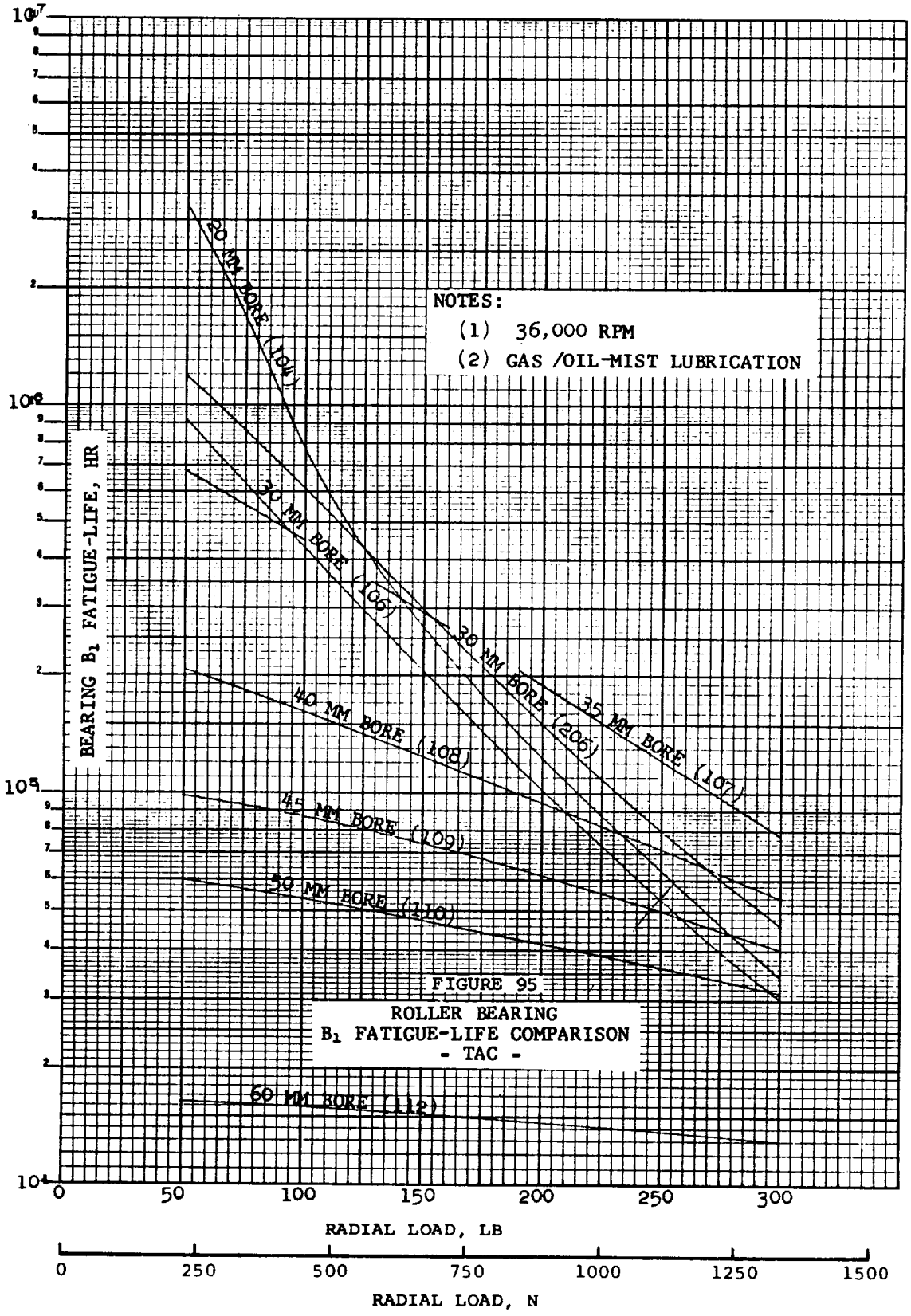


FIGURE 95

ROLLER BEARING
B_1 FATIGUE-LIFE COMPARISON
- TAC -

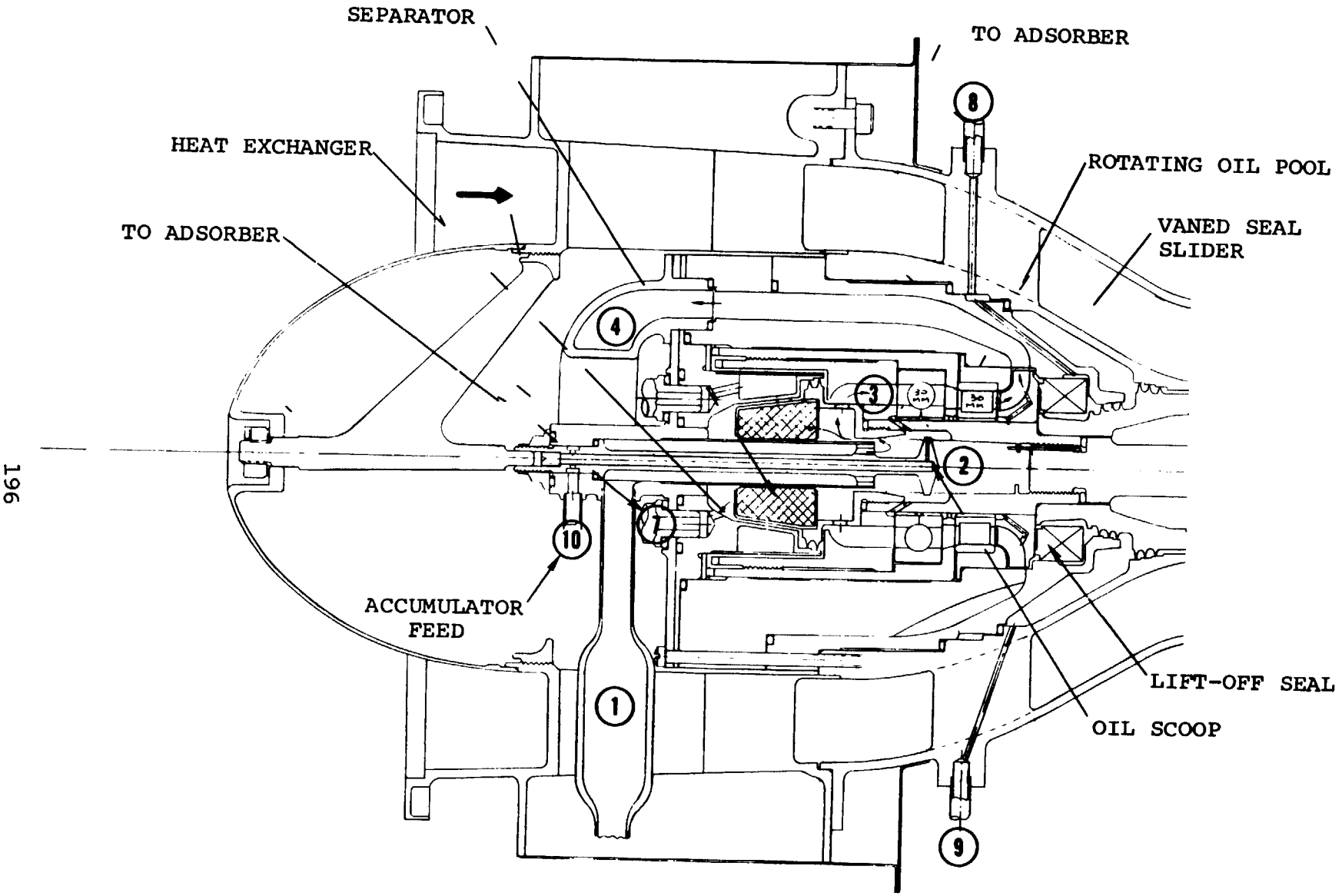
if so, it is conceivable that ball bearing fatigue-lives of 40,000 to 50,000 hours could be achieved in this application.

Details of the selected bearings are presented below:

	Roller Bearing	Ball Bearing
Bore size, mm	30	30
Basic bearing size	106	7206
Radial play, in (mm)	0.0005 (0.0127)	--
Contact angle, deg	--	25
Race curvature, percent of ball dia.		
Inner race	--	53
Outer race	--	51.75
Material	CEVM M-50	CEVM M-50
Material life factor	10.7	10.7
Number of elements	14	12
Element diameter, in. (mm)	0.275 (6.98)	11/32 (8.725)
Roller length, in. (mm)	0.275 (6.98)	--
Power loss, watts	225	350

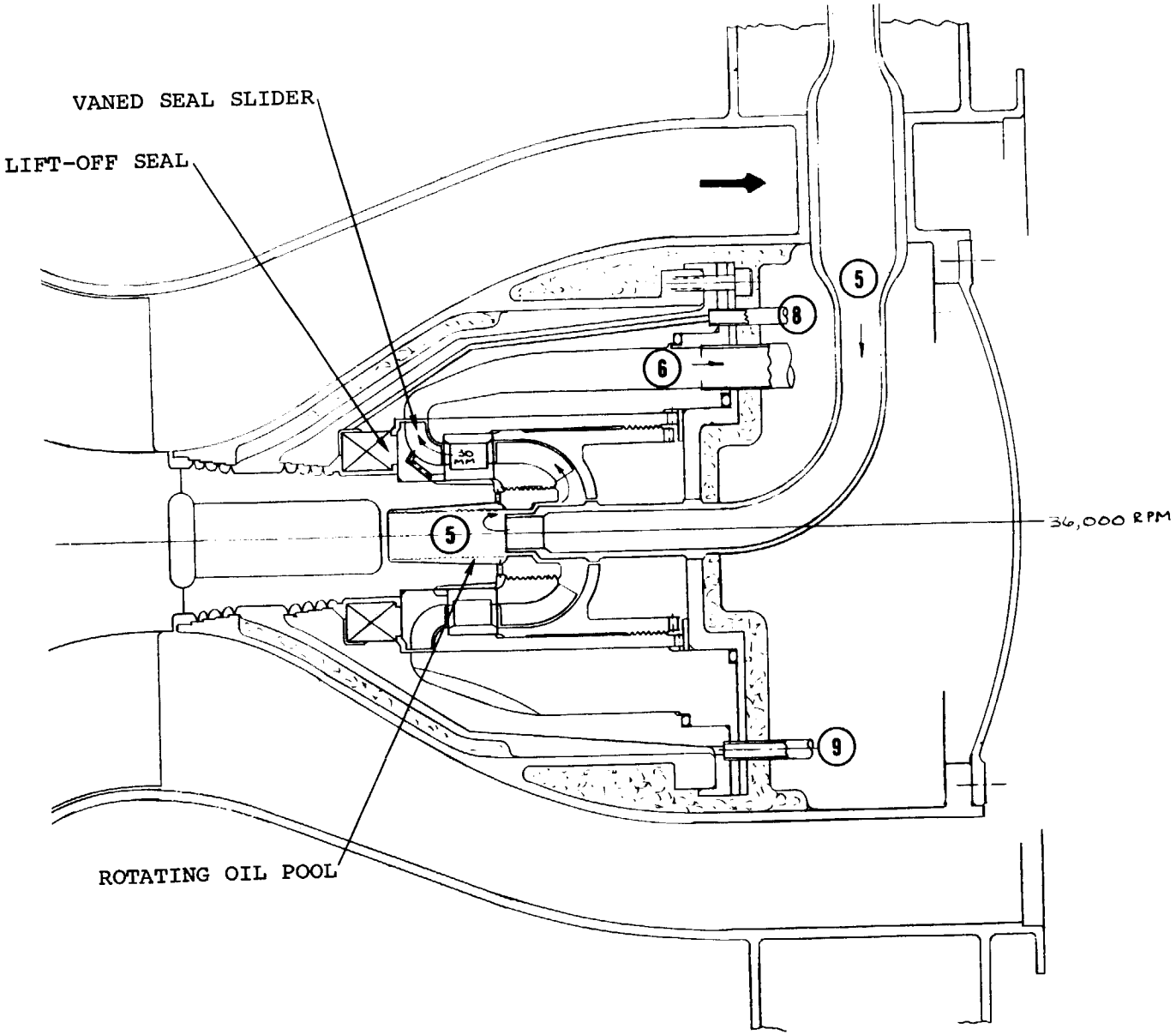
5.6.2.2 Oil-Gas Lubrication System

Details of the mechanical arrangement of the compressor end and turbine end bearing compartments are shown in Figures 96 and 97, respectively. This lubrication system is an adapted TAC version of the concept presented in NASA CR-1229 and United Aircraft Corporation report PWA-3549.



COMPRESSOR END BEARING COMPARTMENT

FIGURE 96



TURBINE END BEARING COMPARTMENT
FIGURE 97

The concept includes under race pressurized oil cooling of the bearings as well as oil-mist cooling and lubrication of the rolling elements. Operation of the system is as follows: Gas-oil flow from location 1 in Figure 96 is injected to location 2 through the concentric tube. Most of the oil flows into the rotating pool where it is subsequently pumped through the inner race of the ball and roller bea: ings. The gas/oil mist turns the corner and flows between the rollin bearing elements, the pressure then increased across the vaned seal slider. The gas/oil mist and liquid oil at location 4 is pumped via external piping to location 5 on Figure 97. The flow is similarly split at the turbine end compartment. Between locations 6 and 1 a he: exchanger is used to remove the heat from the oil and gas mixture.

Pressures have been tentatively selected for several of the loca· tions as shown below:

OIL/GAS LUBRICATION PRESSURES

Location	Pressure	
	psia	kN/m^2 abs
2	122	842
5	122	842
7	121	835
8	135	931
9	180	966
10	140	1241

Pressure rise across the two vaned seal sliders is approximately 8.4 psi (57.9 kN/m^2) each. This should be sufficient, in fact one of the vaned sliders may be removed after the entire system is defined and th pressure drop through each pipe and component determined. The oil

)op is used to regulate the oil capacity within the closed lubrication ;tem. This scoop is 0.75 in. (1.905 cm) in diameter and operates)50 in. (1.27 mm) submerged in the rotating pool. Pressure at the). of the oil scoop is approximately 18 psi (124 kN/m^2) over the gas :ssure at location 2. Thus the accumulator pressure is set at 140 :a (1241 kN/m^2 abs). If the oil level drops (inside radius increases) : differential pressure between the gas and the accumulator pressure ıses more oil to be forced into the closed system. If the oil level :reases the resulting pressure rise in the rotating pool forces oil :o the accumulator.

A seal system in each bearing compartment consists of a buffered)yrinth seal set followed by a face seal with a lift-off hydrodynamic ; bearing surface built into the seal nose. This face seal is the ne diameter and general configuration as the hydrodynamic seal built r the NASA BRU-R under Contract NAS 3-9428. A summary of the geo- try, leakage and power loss for these seals is included as Table 36. th the low frictional losses generated by the hydrodynamic seals, : drilled passages in the seal slider may not be required. However, ese passages will facilitate atomization of the oil into the gas ream at locations 4 and 6 of Figures 96 and 97, respectively.

The flow rate through the rotating separator is set by the gas akage across the hydrodynamic seal. The separator condenses and)arates the oil from this flow before discharging it to the absorber. small heat exchanger outside the separator provides a heat sink to fect the condensation. Based on the vapor pressure of Conaco DN-600 l at 660°R (367°K) which is 0.000298 mm Hg, the oil-to-gas mass flow tio discharged to location 7 is 0.543×10^{-6}. Based on the results)wn in Table 36, a gas mass flow of 1.04 lb/hr (0.472 kg/hr) must ss through the separator. The total oil discharged to the absorber 12.9 grams in 50,000 hours operation. The effectiveness of the parator is a function of the residence time in the separator based the gas velocity. The gas velocity and separator length as shown

TABLE 36

BEARING COMPARTMENT SEAL SUMMARY

Hydrodynamic Face Seal (Typical Both Ends)	
Outside diameter, inch (cm)	2.150 (5.461)
Inside diameter, inch (cm)	1.550 (3.937)
Gas bearing mean diameter, inch (cm)	1.75 (4.445)
Seal surface mean diameter, inch (cm)	2.050 (5.207)
Seal land width, inch (cm)	0.100 (0.254)
Operating clearance, inch (cm)	0.0002 (0.0005)
Upstream pressure, psia (KN/m^2 abs)	135 (931)
Downstream pressure, psia (KN/m^2 abs)	130 (896)
Gas temperature, °R (°K)	940 (522)
Isothermal flow leakage, lb/hr (kg/hr)	0.502 (2.233)
Power loss, watts	60

	Comp End		Turbine End	
Labyrinth Seals	Inboard	Outboard	Inboard	Outboard
Mean diameter, in. (cm)	2.20 (5.59)	1.70 (4.32)	1.70 (4.32)	1.55 (3.94)
No. of teeth	4	4	4	4
Radial clearance, in. (cm)	0.003 (0.008)	0.003 (0.008)	0.003 (0.008)	0.003 (0.008)
Inlet pressure, psia, (KN/m^2 abs)	180 (1240)	180 (1240)	180 (1240)	180 (1240)
Downstream pressure, psia (KN/m^2 abs)	120 (827)	135 (931)	124 (855)	135 (931)
Leakage flow, lb/sec (kg/sec)	0.0259 (0.1152)	0.0177 (0.0787)	0.01944 (0.0865)	0.01615 (0.0718)

NOTE: The hydrodynamic face seal leakage is a small portion of the outboard labyrinth seal leakage for each bearing compartment.

in Figure 96 results in a residence time 20 times that for the separator design summarized in PWA-3549.

A labyrinth seal is shown between the separator inlet and discharge. This seal has a very small pressure drop and a relatively large clearance due primarily to dimensional stacking of the stationary and rotating parts. An alternative would be a viscoseal arrangement between the separator and heat exchanger, which could operate with a wider clearance without detrimental effects.

The absorber is used to purify the gas being returned to the cycle from the buffered labyrinth seal system. The operating principal is to condense the oil vapor and other condensibles in the gas and to subsequently absorb the oil and oil decomposition products. Glass wool and polyurethane foam have been identified as excellent oil removal materials. The removal of oil decomposition products is accomplished with molecular sieve materials in the form of pellets. The absorber design shown in PWA-3549 should fulfill the requirements of the TAC system since this design is based on 22.5 grams of oil for 10,000 hours versus the TAC requirement of 12.0 grams in 50,000 hours. Since the bulk temperature of the lubricant is limited to 710°R (394°K), no detectable decomposition is expected. Thus, the molecular sieve requirements are not defined. Based on an abosrber efficiency of 99.78 percent, as defined in PWA-3549, the amount of oil discharged into the main cycle is 0.0283 grams in 50,000 hours of operation.

The bearing and windage losses that are rejected to the oil for the two-bearing compartments are shown below.

HEAT LOSSES REJECTED TO OIL

	Compressor End	Turbine End
Ball bearing loss, w	350	-
Roller bearing loss, w	225	225
Hydrodynamic seal windage, w	60	60
Compartment heat gain, w	-	450
Total heat rejected, w	1370	

The required oil flow rate is 200 lb/hr (90.7 kg/hr) on the basis of 660°R (367°K) inlet temperature with a total temperature rise of 50°F (27.8°C). Gas flow rate was determined by assuming 0.5 in. (1.27 cm) I.D. tubing between the two compartments and a volumetric flow parameter $[(Q_l + Q_g)/A]^2/gD$ equal to 1000 for vertical annular flow where

Q_l = liquid volumetric flow rate, ft^3/sec

Q_g = gas volumetric flow rate, ft^3/sec

A = tube flow area, ft^2

D = tube inside diameter

Gas volumetric flow is 175.8 cu ft/hr (4.955 m^3/hr); the mass flow rate is 123 lb/hr (56.75 kg/hr) for the design conditions of 120 psia (827 kN/m^2 abs) loop pressure.

The total parasite power charged to the bearing compartments is:

POWER LOSS SUMMARY

	Compressor End	Turbine End
Ball bearing, w	350	-
Roller bearing, w	225	225
Hydrodynamic seal windage, w	60	60
Gas pumping, w	179	179
Oil pumping, w	279	279
Probe disc drag, w	11	-
Separator drag, w	15	-
	1119	743
Total Parasite Losses, w	1862	

Control of the lubrication system is quite simple for startup and transient load (pressure) changes. The accumulator pressure is set at 1.17 times compressor inlet pressure (P_1). The buffer gas for the labyrinth seals is at a pressure of 1.5 P_1. These reference pressures are achieved by tapping the compressor scroll at the appropriate locations. Thus the percent of P_1 should be maintained. At start initiation the bearing compartment is effectively isolated from the main gas loop by the buffered labyrinth seal system. At some low speed, for example 10,000 rpm, the hydrodynamic seal will start to lift off and the bearing compartment pressure will quickly reach P_1. The accumulator pressure will cause oil to enter the system until the required oil level is reached and the bearing cavity pressure increased to shut off the oil flow. Since the lubrication system controls are referenced to P_1 the system should follow the main gas loop. An isolation check

valve will be required between the absorber and the main gas loop to prevent reverse flow and adverse pressure gradients during startup. Although not necessary for space operation, a shut off valve should be included between the accumulator and location 10 of Figure 96. This valve would be used to prevent flooding the bearing compartment if the accumulator were higher than the bearing compartment. It could be turned on at some predetermined speed such as 10,000 rpm, after the hydrodynamic seal had lifted-off.

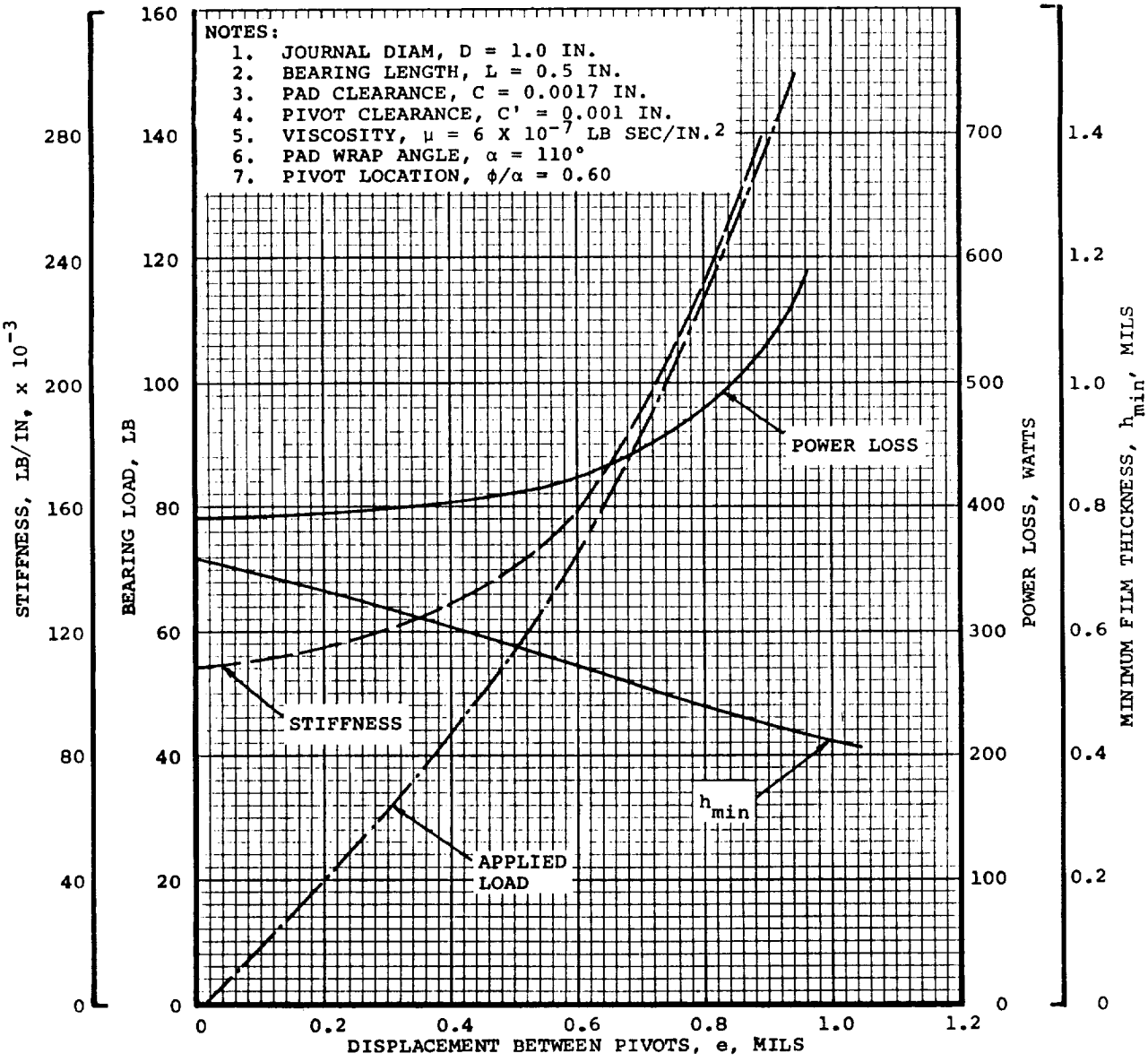
5.6.3 Oil Film Bearings

5.6.3.1 Journal Bearings

The journal bearing concept chosen for the 36,000 rpm oil lubricated TAC units is of the three-segment pivoted-pad type. This bearing is inherently stable. In addition the journal diameter and resultant power losses will be minimized by using this bearing.

The predicted performance of a 1.0-in.-dia (2.54 cm) journal bearing is shown in Figures 98 and 99. Vertical shaft or zero "g" operation can be determined from this figure by selecting parameters at zero displacement between fixed pivots. The rotating group mass of TAC units E and F is approximately 130 lb (59 kg). Therefore, for terrestrial horizontal operation each journal bearing would support 65 lb (289 N). Referring to Figures 98 and 99, the performance for this condition is found by selecting parameters at 0.55 mil (0.014 mm) displacement between pivots.

The predicted performance of a single oil film journal bearing as related to its orientation is as follows:



PERFORMANCE OF OIL LUBRICATED JOURNAL BEARING
(36,000 RPM)

FIGURE 98

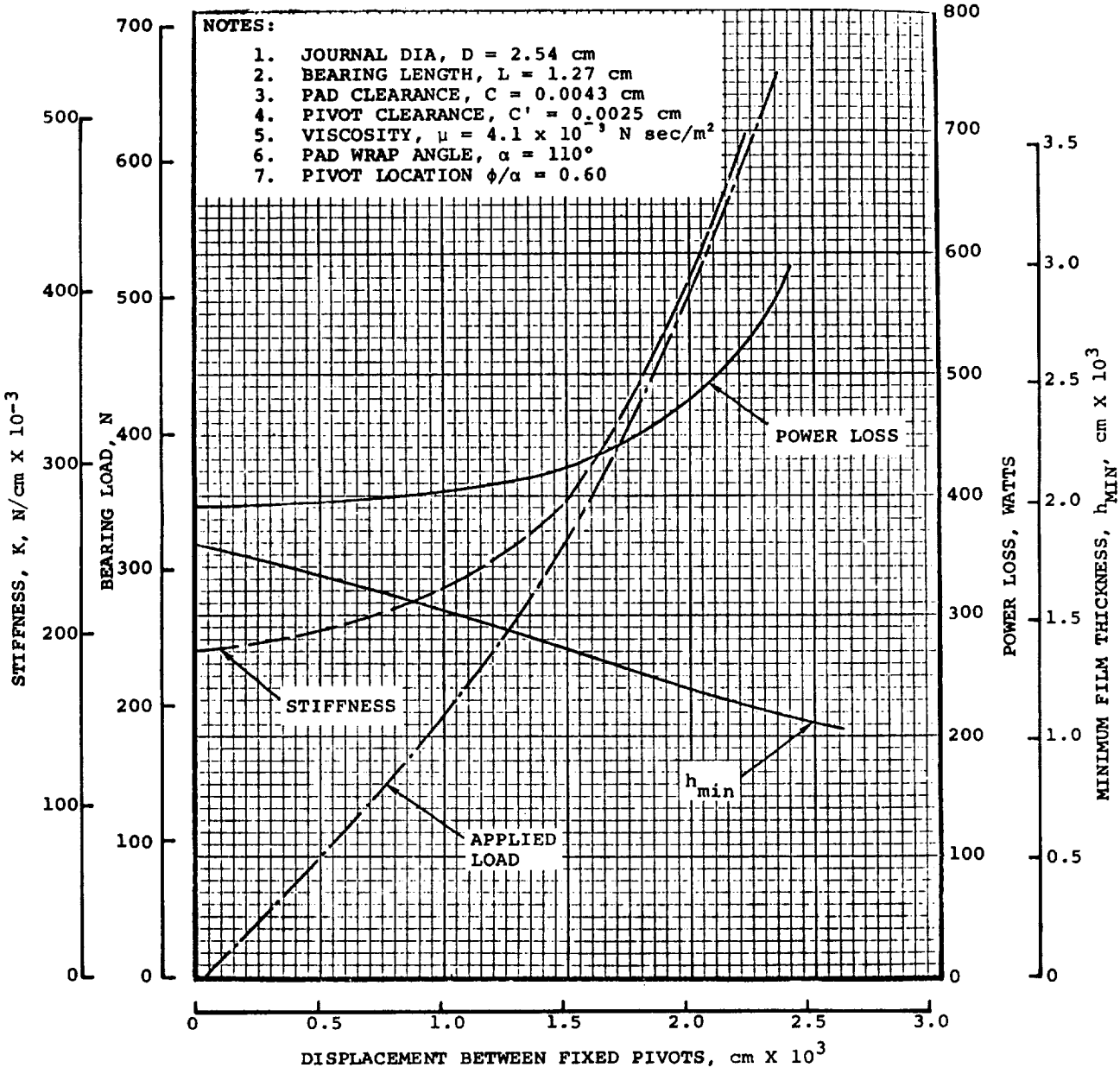

NOTES:
1. JOURNAL DIA, D = 2.54 cm
2. BEARING LENGTH, L = 1.27 cm
3. PAD CLEARANCE, C = 0.0043 cm
4. PIVOT CLEARANCE, C' = 0.0025 cm
5. VISCOSITY, μ = 4.1 x 10⁻⁹ N sec/m²
6. PAD WRAP ANGLE, α = 110°
7. PIVOT LOCATION φ/α = 0.60
STIFFNESS
POWER LOSS
APPLIED LOAD
h min
STIFFNESS, K, N/cm X 10⁻³
BEARING LOAD, N
POWER LOSS, WATTS
MINIMUM FILM THICKNESS, h MIN, cm X 10³
DISPLACEMENT BETWEEN FIXED PIVOTS, cm X 10³

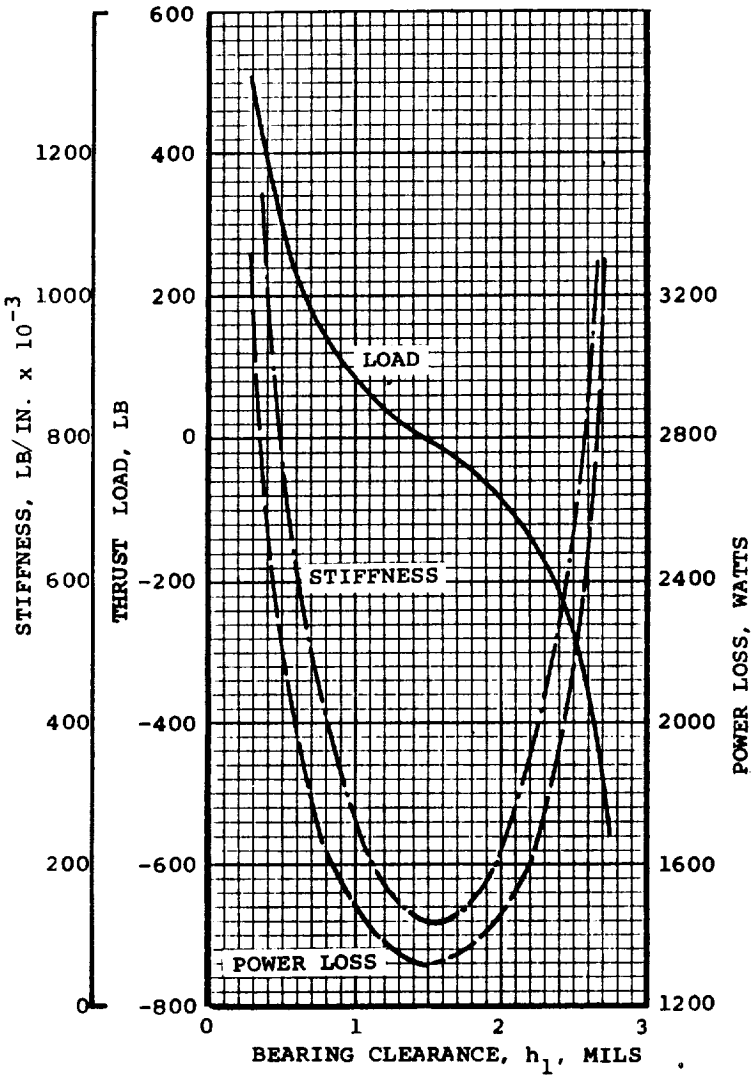
FIGURE 99

	Vertical or Zero "g" Operation	Horizontal Terrestrial Operation
Journal bearing load, lb (N)	0	65 (289)
Minimum film thickness, mil (mm)	0.72 (0.0183)	0.550 (0.014)
Bearing power loss, w	390	415
Bearing stiffness, lb/in. (N/cm)	108,000 (189,137)	150,000 (262,691)

5.6.3.2 Oil Thrust Bearing

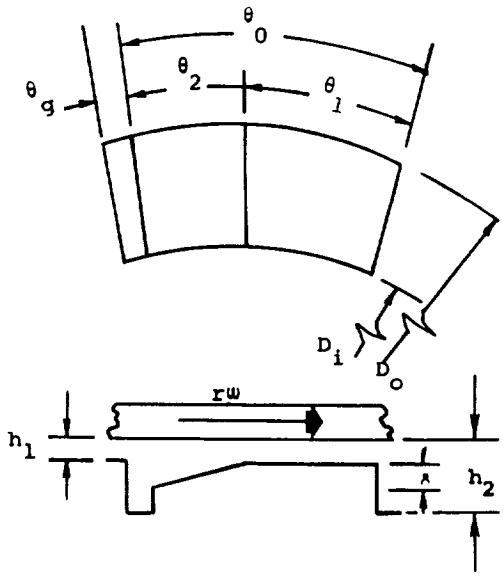
The thrust bearing analyzed for TAC units E and F, consists of a double-acting tapered land bearing. Performance of the 2.025-in.-dia (5.15 cm) bearing is shown in Figures 100 and 101. From this data and with an assumed total design thrust load of 200 lb (890 N)--rotor weight plus axial thrust--the following information is noted:

	Vertical Terrestrial Operation	Horizontal or Zero "g" Operation
Thrust bearing load, lb (N)	200 (890)	70 (312)
Minimum bearing clearance, in. (mm)	0.00065 (0.0165)	0.00105 (0.0179)
Lubricant film stiffness, lb/in. (N/cm)	550,000 (963,199)	230,000 (402,792)
Total power loss, watts	1860	1450



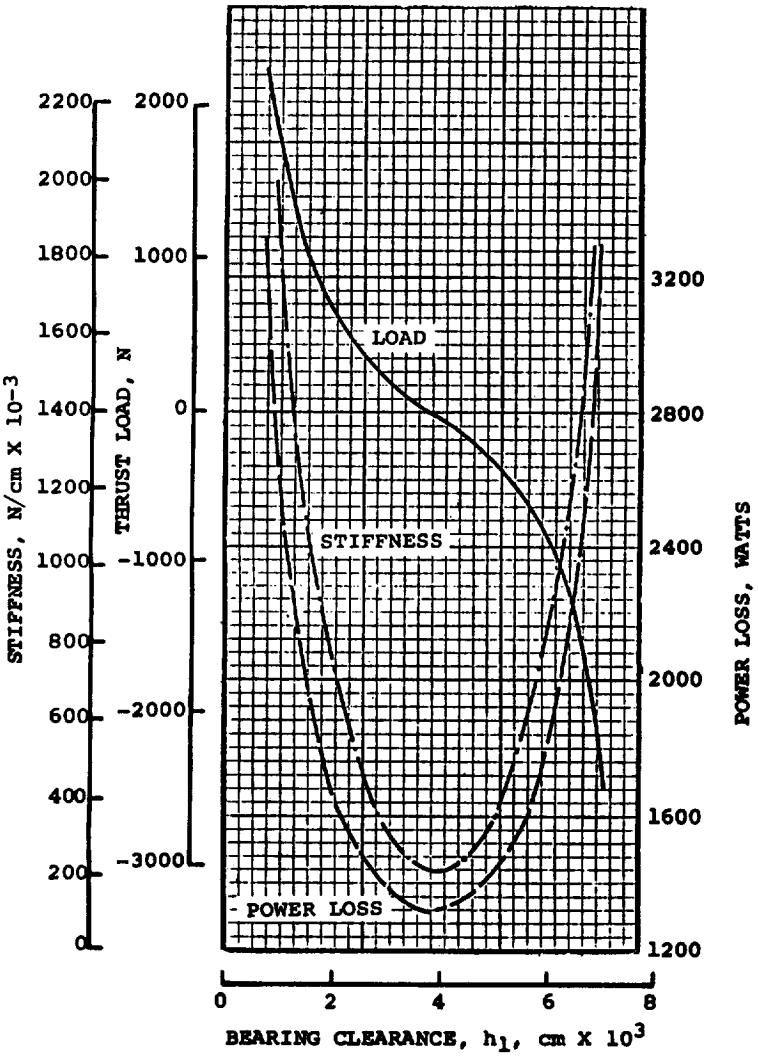
NOTES:

1. D_o = 2 025 IN
2. D_1 = 1.125 IN.
3. ϵ = 0 0008 IN.
4. θ = 37.5 DEG.
5. η = $6X10^{-7}$ LB-SEC/IN^2
6. N = 36,000 RPM
7. θ_2 = 22.5 DEG.



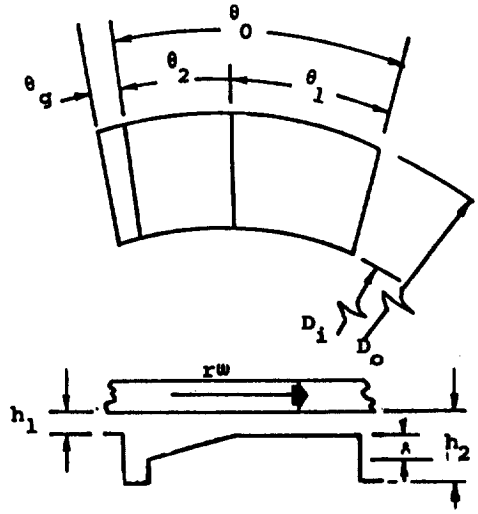
PERFORMANCE OF OIL-LUBRICATED DOUBLE-ACTING TAPERED LAND 8-PAD THRUST BEARING

FIGURE 100



NOTES:

1. D_o = 5.144 cm
2. D_i = 2.860 cm
3. δ = 0.002 cm
4. θ = 37.5 DEG
5. η = 4.1 X 10^{-3} N SEC/m^2
6. N = 36,000 RPM
7. θ_2 = 22.5 DEG



PERFORMANCE OF OIL-LUBRICATED DOUBLE-ACTING TAPERED LAND 8-PAD THRUST BEARING

FIGURE 101

5.6.3.3 Combined Bearing Losses

Comparison of the journal and thrust bearing losses at two orientations indicate that vertical terrestrial operation will be the worst case. Total combined oil bearing losses are 2.64 kw versus 2.28 for the other orientation. These losses were used in the final definition of the TAC-E and -F configurations.

5.6.3.4 Bearing Compartment Losses

Since both bearing compartments are flooded with liquid oil, high windage losses will result. These losses were estimated as follows:

Compressor end	
Peripheral losses, w	2487
Disc losses, w	941
Turbine end	
Peripheral losses, w	1315
Disc losses, w	957
Total windage losses, w	5700

Sealing of the flooded compartment is accomplished with a spiral groove lift-off seal that will establish a liquid vapor interface. Buffered labyrinth seals on the turbine end and buffered hydrodynamic gas lift-off seals on the compressor end complete the lubrication seal system. Total power losses for these seals are:

Liquid/vapor seal, w	810
Hydrodynamic seals, w	120
Total seal losses, w	930

Thus the total compartment losses for the two bearing compartments are 6.63 kw plus bearing losses of 2.64 kw. These losses were used in the definition of the final TAC-E and -F configurations. Seal leakages were estimated for the hydrodynamic seals as 0.0086 lb/sec (3.9 g/sec). The labyrinth seals on the turbine end are the same as those summarized in Table 36, Page 200, [leakage of 0.0356 lb/sec(16.159 g/sec)]. Thus total leakage charged to the bearing compartments is 0.0442 lb/sec (20.05 g/sec).

5.7 Alternator Windage Loss Summary

5.7.1 Windage Loss Analysis

The rotor radial gap friction coefficient was calculated from th following empirical expressions suggested by Wendt[1,2].

$$C_d = \frac{0.46 \left[\frac{\Delta}{R}\left(1 + \frac{\Delta}{R}\right)\right]^{0.25}}{(Re_p)^{0.5}} \qquad 400 > Re_p > 10^4$$

$$C_d = \frac{0.073 \left[\frac{\Delta}{R}\left(1 + \frac{\Delta}{R}\right)\right]^{0.25}}{Re_p\ 0.3} \qquad Re_p > 10^4$$

Where

C_d = friction coefficient $= \frac{W_p}{\pi \rho U^3 RL}$

Re_p = peripheral Reynolds number $= \frac{\rho U \Delta}{\mu}$

Δ = radial gap

R = rotor radius

L = rotor length

ρ = gas density

μ = gas viscosity

U = rotor tip speed

W_p = peripheral windage loss

The above equations allow a reasonably good correlation with ooth cylinder friction data reported by Taylor[3]. However, Westing-use results (unpublished) suggest a multiplying factor of 1.1 to count for the extra losses due to stator slots.

The rotor face (disc) loss of a homopolar inductor alternator can estimated by applying the following equations as recommended by hlichting[4] for a disc confined in a housing:

$$C_M = \frac{2.67}{(Re_R)0.5} \qquad (10^4 < Re_R < 1.64 \times 10^5)$$

$$C_M = \frac{0.0727}{(Re_R)^{0.2}} \qquad (Re_R) > 1.64 \times 10^5)$$

ere

C_M = moment coefficient $= \frac{4W_R}{\rho U^3 R^2}$

Re_R = disc Reynolds number $= \frac{\rho UR}{\mu}$

W_R = disc loss per side

The friction coefficients defined above are plotted versus ynolds number in Figure 102. In the absence of experimental data for ndell alternators, it was recommended that windage losses for the tor conical sections be estimated by first calculating a full disc ss and then scaling it by a geometric factor, (slant length/delta dius), to account for the additional surface area.

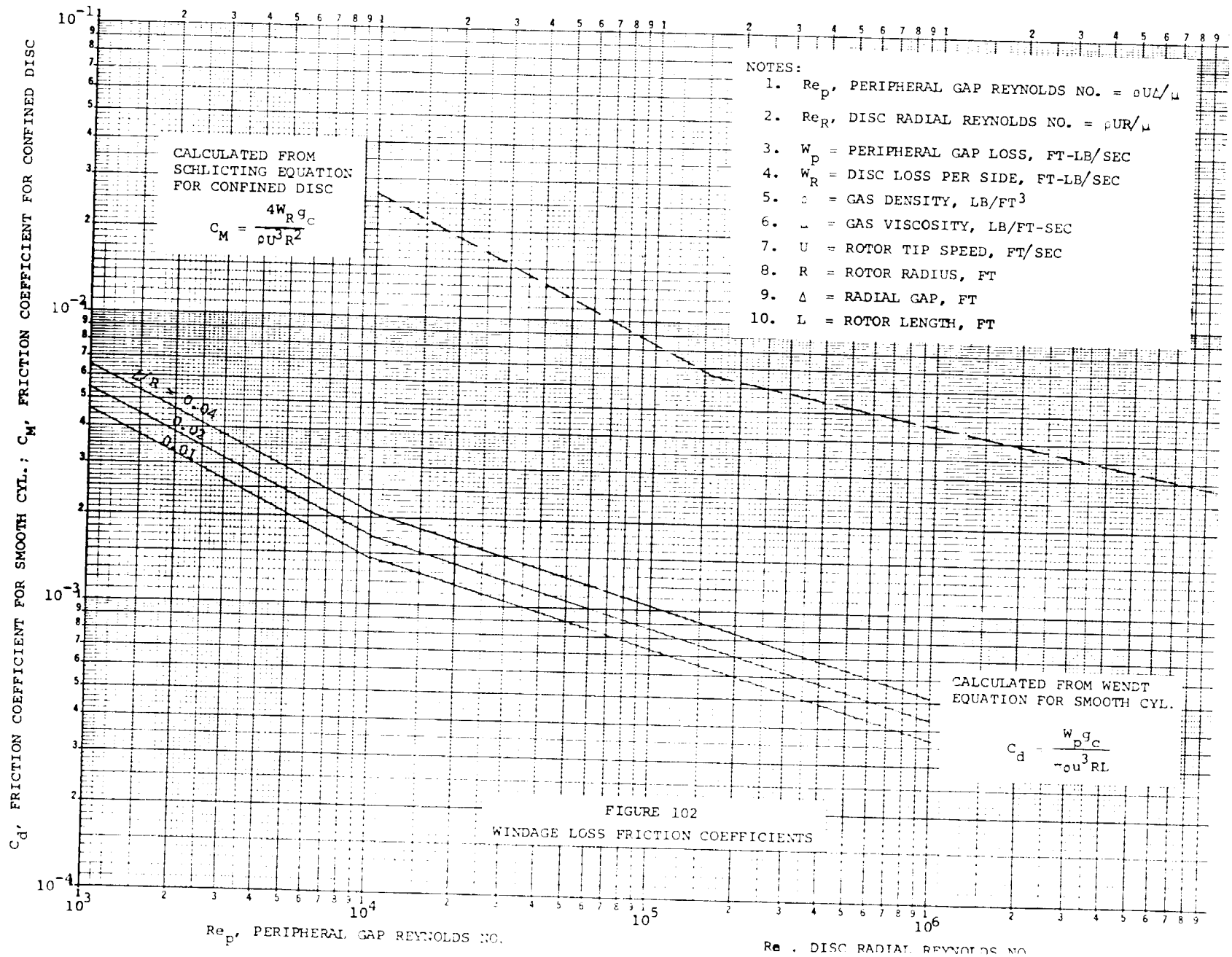


FIGURE 102

WINDAGE LOSS FRICTION COEFFICIENTS

Alternator windage losses were calculated according to the above thod for the final selected alternators for the 24,000 and 36,000 n machines. These results are shown in Figure 103 as a function of e alternator cavity pressure. Due to anticipated alternator rotor ɔling problems, a limit of 9.6 kw was placed on the windage loss.

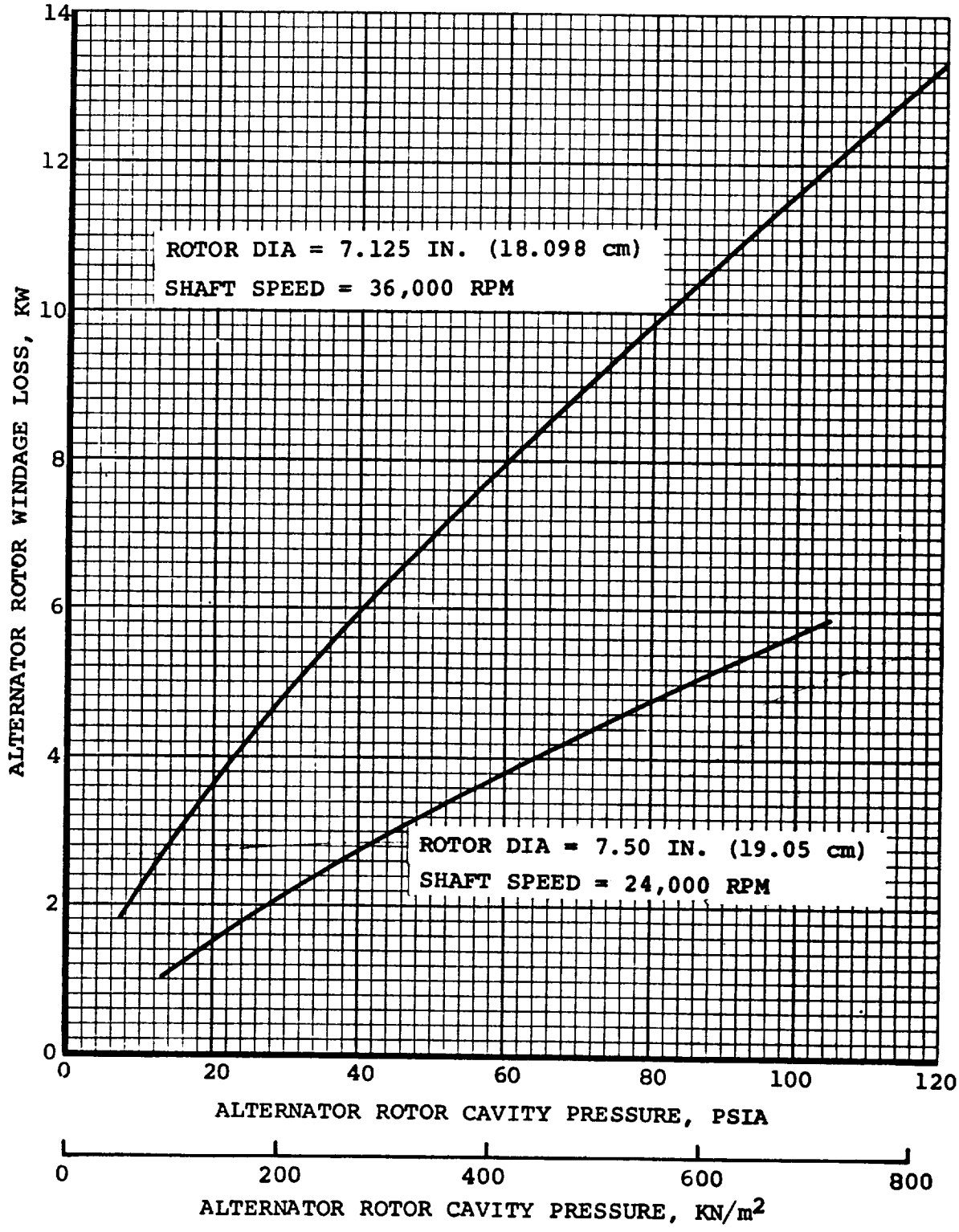
The 24,000 rpm systems could run the alternator cavity at any asonable cavity pressure without severe problems. Venting of the ternator cavity to the compressor inlet (55 psia or 379 kN/m^2 abs) s selected to minimize the windage loss without additional complica- ɔns. Seals are required to limit the amount of cycle bleed leakage rough the alternator cavity.

For the 36,000 rpm systems, the 9.6 kw windage loss limit allows naximum cavity pressure of approximately 77 psia (530 kN/m^2 abs). is will require that the rotor cavity be sealed and pumped below the mpressor inlet pressure (120 psia or 827 kN/m^2 abs). Seals will be quired to limit the amount of gas that must be exhausted from the tor cavity.

7.2 Isolation Seals

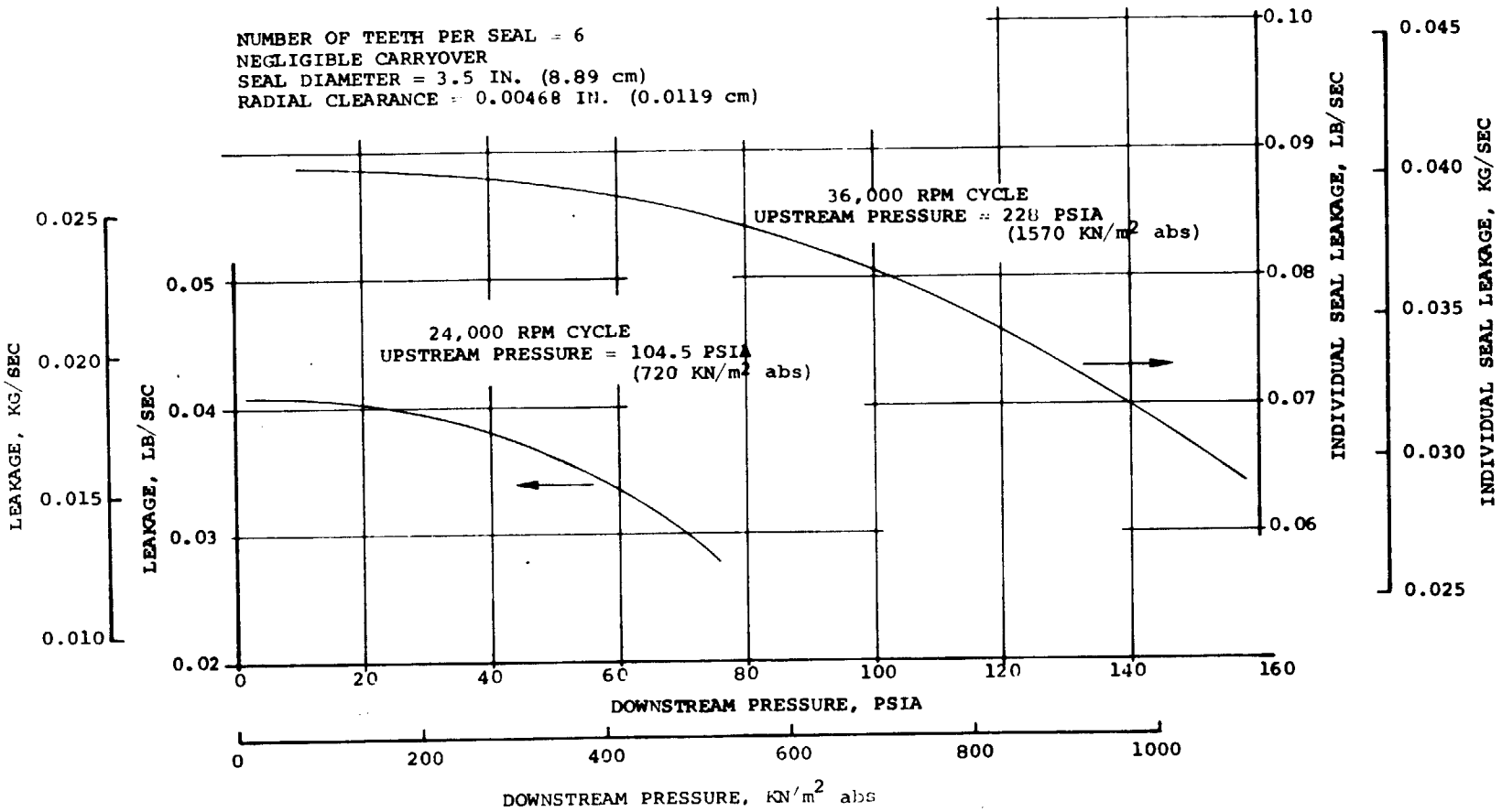
Either labyrinth or gas lift-off seals may be used to isolate the ternator cavity. Preliminary sizing indicated that a 3.5-in.-dia 89 cm) labyrinth seal would fulfill the isolation seal requirement. ch tooth of the seal is at a slightly lower radius than the previous ɔth, to reduce the pressure recovery. Figure 104 shows the results the seal leakage analysis. The upstream pressures correspond to compressor discharge pressure for each shaft speed at design (160) output power.

The hydrodynamic gas lift-off consists of a standard face seal ch a hydrodynamic bearing surface machined into a portion of the



TAC ALTERNATOR WINDAGE LOSS VS CAVITY PRESSURE

FIGURE 103



TAC LABYRINTH SEAL LEAKAGE

FIGURE 104

nose. At zero or low-shaft speeds, the nose is in contact with the seal slider. As the shaft speed increases, the hydrodynamic bearing surface forces the nose away from the slider to establish a finite clearance between the slider and the nose. If the alternator rotor cavity pressure is less than the bearing cavity pressure, a finite gas flow across the seal will exist during normal operation.

Estimates of the seal leakage were made on the basis that isothermal (rather than adiabatic) flow occurred across the seal. The isothermal flow assumption is justified, since the heat-transfer effectiveness of the seal is very high at small flow rates. The seal leakage rate may be estimated from the laminar isothermal flow equation:

$$W_S = \frac{gB\delta^3}{2\mu RTL} (P_1^2 - P_2^2)$$

where

B = flow width

δ = clearance

μ = gas viscosity

P_1 = inlet pressure

P_2 = cavity pressure

R = gas constant

T = temperature

L = flow length

W_S = static seal leakage

If the higher pressure exists at the inner radius, the dynamic leakage will exceed the static leakage by virtue of the shaft rotation. The appropriate correction factor can be estimated from the NASA Technical Note, TND-5344:

$$\frac{\Delta W}{W_S} = \frac{3}{5} R_2^2 \left(\frac{\omega^2}{gRT}\right)$$

where

ω = angular velocity

R_2 = seal radius

Two hydrodynamic seal configurations were required, depending upon whether a radial or an axial compressor was utilized. If a radial compressor is used the alternator cavity pressure is approximately 156 psia (1075 kN/m^2 abs); the axial compressor delivers a static pressure at the last stage of approximately 220 psia (1517 kN/m^2 abs) for the 36,000 rpm machines. The clearance was set at 0.00015 in. (0.00381 mm) for the radial compressor seal. However, the larger seal required with the axial compressor dictated a larger clearance of 0.0002 in. (0.00508 mm). Presented below is a summary of the two configurations.

	Radial Comp Seal	Axial Comp Seal
Outside diameter, in. (cm)	3.7 (9.40)	4.7 (11.93)
Inside diameter, in. (cm)	3.1 (7.87)	4.1 (10.41)
Axial clearance, in. (mm)	0.00015 (0.00381)	0.0002 (0.00508)
Upstream pressure, psia (kN/m^2 abs)	156 (1075)	220 (1517)
Seal land width, in. (mm)	0.100 (2.54)	0.100 (2.54)
Windage loss for two seals, kw	1.31	1.89

Figure 105 shows the estimated seal leakage for the two seals.

Comparison of these results with the labyrinth seal results indicates a quantum change in the leakage rate at the same pressure and size conditions for the labyrinth seal.

5.7.3 Alternator Cavity Pressure Reduction

The simplest method of maintaining a low alternator cavity pressure entails the use of an ejector, operating from compressor bleed and discharging to the compressor inlet. The available driving pressure ratio (primary inlet to discharge) is approximately equal to the cycle compressor pressure ratio under these conditions.

An ejector optimization study was conducted with the aid of an AiResearch computer program to ascertain the flow geometry that yields the best pumping characteristics. The computation method assumes constant area mixing with static pressure equilibrium between the primary and secondary jets at the mixing-tube entrance. The diffuser inlet conditions are based on the subsonic solution of the nonfrictional mixing function, thereby allowing a normal shock loss in the mixing tube. An additional Fanno line solution for wall-friction loss is superimposed, with friction factors as input.

Both single and two-stage ejectors were analyzed for this application. The two-stage utilized less bleed flow to pump the 36,000 rpm alternator cavity. The ejector performance is shown in Figure 106.

5.7.4 TAC Loss Summary

The 24,000 rpm TAC machine alternate windage loss is 3.55 kw as shown in Figure 103. Bearing losses and seal leakages are summarized in Tables 34 and 35.

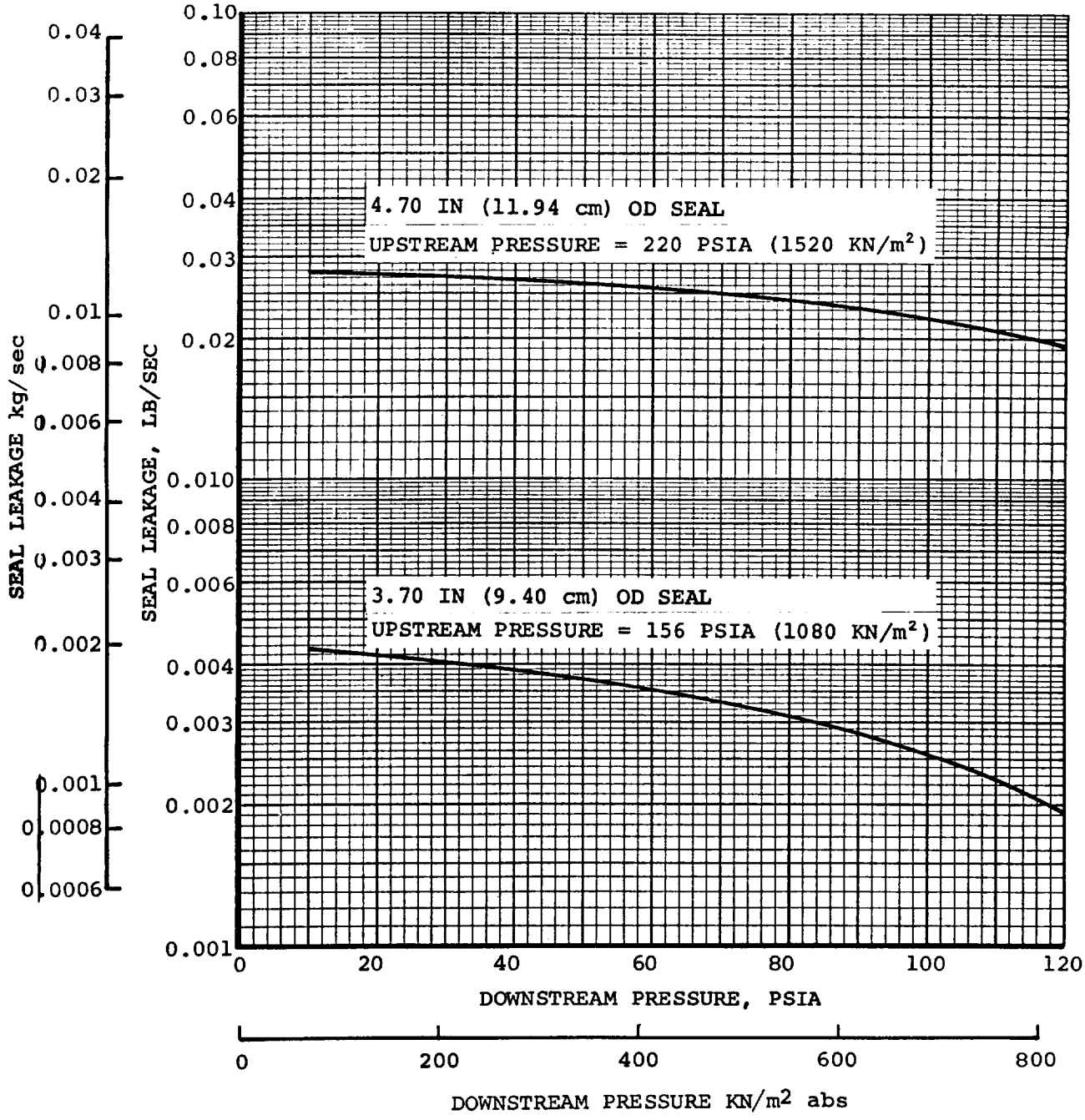

SEAL LEAKAGE kg/sec
0.04
0.03
0.02
0.01
0.008
0.006
0.004
0.003
0.002
0.001
0.0008
0.0006
SEAL LEAKAGE, LB/SEC
0.10
0.08
0.06
0.04
0.03
0.02
0.010
0.008
0.006
0.004
0.003
0.002
0.001
4.70 IN (11.94 cm) OD SEAL
UPSTREAM PRESSURE = 220 PSIA (1520 KN/m²)
3.70 IN (9.40 cm) OD SEAL
UPSTREAM PRESSURE = 156 PSIA (1080 KN/m²)
0
20
40
60
80
100
120
DOWNSTREAM PRESSURE, PSIA
0
200
400
600
800
DOWNSTREAM PRESSURE KN/m2 abs

FIGURE 105

NOTES:

1. 36,000 RPM CYCLES
2. PRIMARY NOZZLE:
   INLET PRESSURE = 228 PSIA (1570 KN/m²)
   INLET TEMPERATURE = 943°R (524°K)
   EFFICIENCY = 0.9
3. DISCHARGE PRESSURE = 120 PSIA (827 KN/m²)
4. SUCTION INLET TEMPERATURE = 1160°R (644°K)
5. DIFFUSER EFFICIENCY = 0.6

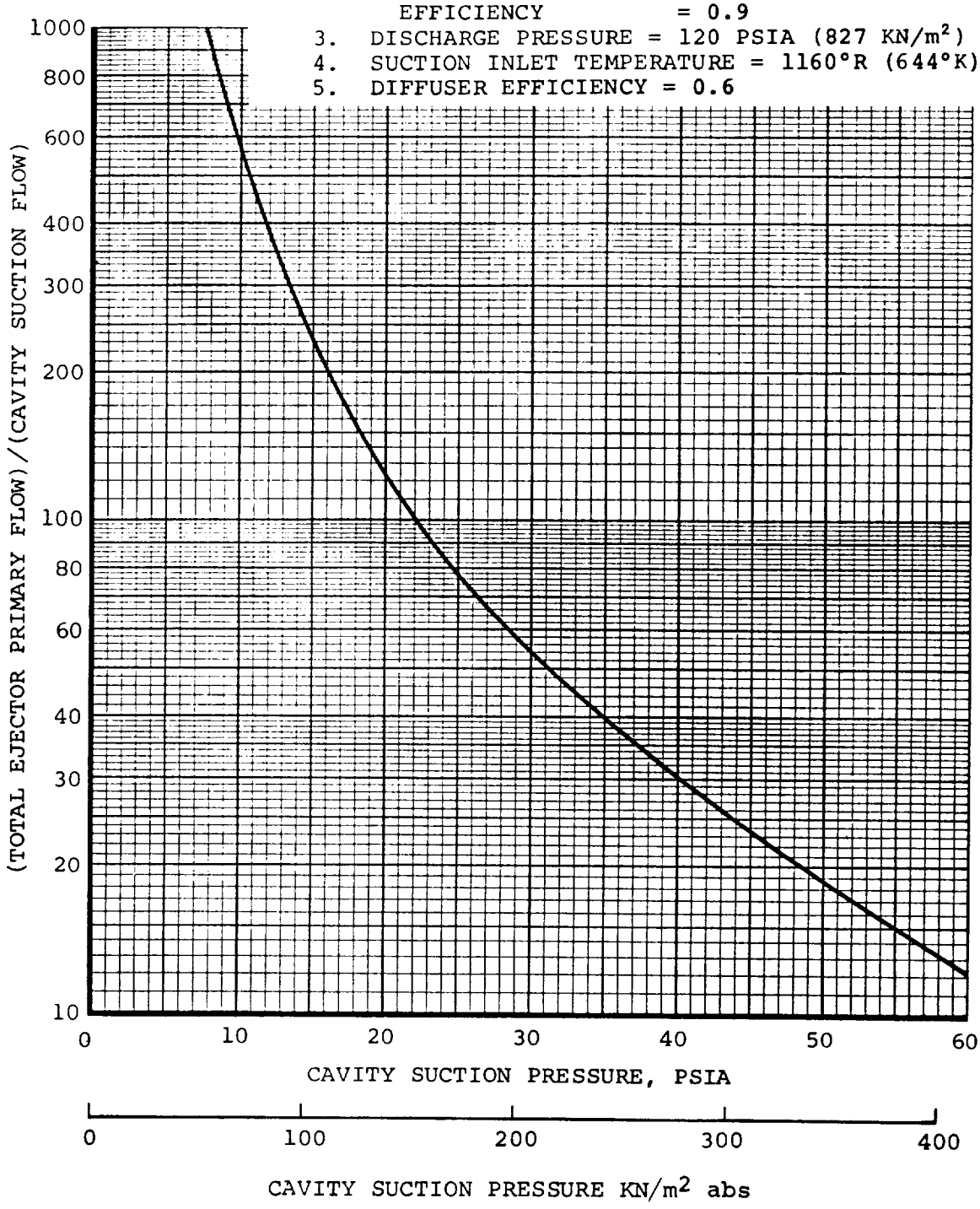


FIGURE 106

Table 37 summarizes the losses for the 36,000 rpm TAC configurations. The alternator cavity pressure for the radial compressor configurations was selected as the minimum pressure at which the alternator could be maintained without excessive bleed flow required by the ejector. The axial compressor configurations required a larger bleed flow due to the larger hydrodynamic seal. The alternator cavity pressure for these configurations was determined by the combined alternator rotor and isolation seal windage loss fixed at 9.6 kw. this resulted in an allowable alternator windage loss of 7.71 kw or a cavity pressure of 56 psia (386 kN/m^2 abs) as shown in Figure 103.

The turbine backface seal for the radial compressor configurations has a pressure drop of 6 psi (156 versus 150 psia) across the 3.5 in. dia seal. The axial machines impose a pressure of 220 psia on one side of the turbine backface seal with a downstream pressure of 150 psia. This results in a much larger leakage flow for the turbine backface seal of the axial configuration.

References for Section 5.7

1. Wendt, F., "Ingenieus-Archiv," Vol. 4, 1933, p. 577.

2. Donnelly, R. J. and N. J. Simon, "An Empirical Torque Relation for Supercritical Flow Between Rotating Cylinders," Journal of Fluid Mechanics, Vol. 7, 1959, p. 401.

3. Taylor, G. I., "Friction Between Rotating Cylinders," Proceedings of the Royal Society of London, Series A, Vol. 157, 1936, pp. 546 to 578.

4. Schlichting, M., "Boundary Layer Theory," McGraw-Hill, New York, 1960.

TABLE 37

TAC LOSS SUMMARY

Configuration Bearing Type Compressor	TAC-C Oil-Mist Radial	TAC-D Oil-Mist Axial	TAC-E Oil-Film Radial	TAC-F Oil-Film Axial
Shaft losses, kw				
Bearing compartments	1.860[a]	1.86	9.27[b]	9.27
Isolation seals	1.31	1.89	1.31	1.89
Alternator windage[d]	6.0	7.71	6.0	7.71
Total	9.17	11.46	16.58	18.87
Bleed flow required, lb/sec (kg/sec)				
Bearing compartments	0.0792[a] (0.0359)	0.0792 (0.0359)	0.0442[b] (0.0200)	0.0442 (0.0200)
Turbine backface labyrinth	0.0108 (0.0049)	0.0622 (0.0282)	0.0108 (0.0049)	0.0622 (0.0282)
Isolation seals[c]	0.00389 (0.00176)	0.026 (0.0118)	0.00389 (0.00176)	0.026 (0.0118)
Ejector primary flow[e]	0.1168 (0.0530)	0.374 (0.167)	0.1168 (0.0530)	0.374 (0.167)
Total	0.2107 (0.0955)	0.5414 (0.2455)	0.1757 (0.0797)	0.5064 (0.2297)
Ejector flow ratio	30	14.4	30	14.4
Alternator cavity pressure, psia (KN/m^2)	40 (276)	56 (386)	40 (276)	56 (386)
Isolation seal upstream pressure, psia (KN/m^2)	156 (1076)	220 (1520)	156 (1076)	220 (1520)

a. See Section 5.6.2
b. See Section 5.6.3
c. See Figure 105
d. See Figure 103
e. See Figure 106

6. PHASE III COMPONENT SUMMARY

6.1 Compressor Design

Table 38 compares the Phase I and Phase III compressor design point. Changes in the corrected speed and mass flow made it necessary to re-evaluate the governing design parameters such as blade exit angle, number of impeller blades, relative velocity ratio, inlet Mach number, vaned and vaneless diffuser losses, etc., to establish optimized compressor design.

TABLE 38

COMPRESSOR DESIGN COMPARISON

	Phase I	Phase III
Shaft speed, rpm	24,000	24,000
Mass flow, lb/sec (kg/sec)	10.13 (4.60)	13.73 (6.23)
Pressure ratio	1.9	1.9
Inlet pressure, psia (kN/m^2 abs)	55 (379)	70 (483)
Inlet temperature, °R (°K)	700 (389)	580 (322)
Corrected speed, rpm	20,659	22,696
Corrected flow, lb/sec (kg/sec)	3.144 (1.427)	3.0481 (1.383)

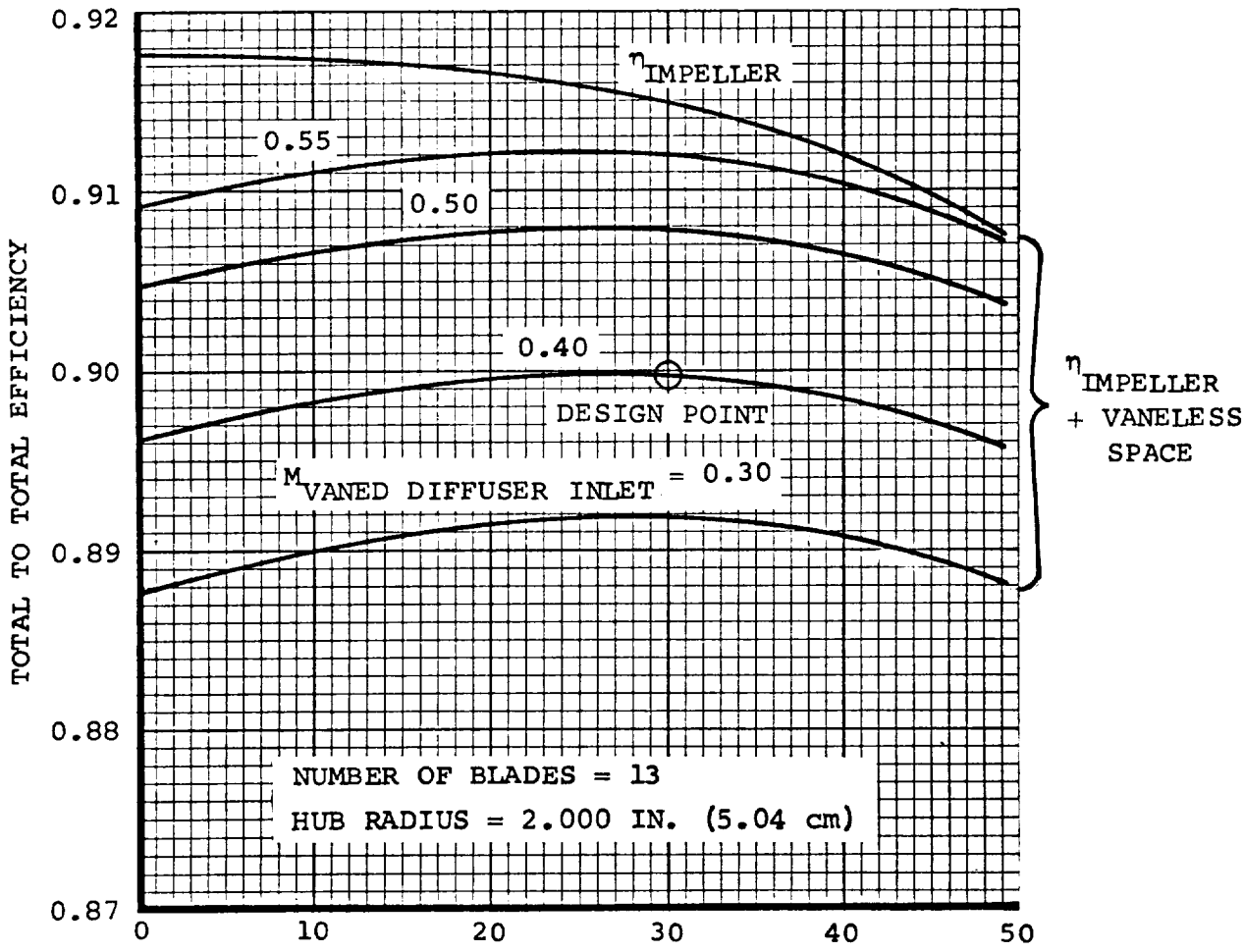
6.1.1 Preliminary Design Optimization

The optimization procedure for the Phase III compressor was the same as described in Section 5.2.1. The relative velocity ratio and number of blades were selected as 0.58 and 13 respectively.

The hub inlet radius was kept at 2 inches. Losses were calculated using the same method as in Phase I, except for the blade exit mixing loss calculation, which was improved slightly. The overall estimated total to total compressor efficiency, including scroll, is 0.865, compared to 0.87 in the Phase I design. Figure 107 shows how efficiency levels up to the inlet of the vaned diffuser vary with blade exit angle for different vaned diffuser inlet Mach number. The peak occurs at a blade exit angle of 30 degrees for vaned diffuser inlet Mach number from 0.3 to 0.5, agreeing with results from the Phase I study.

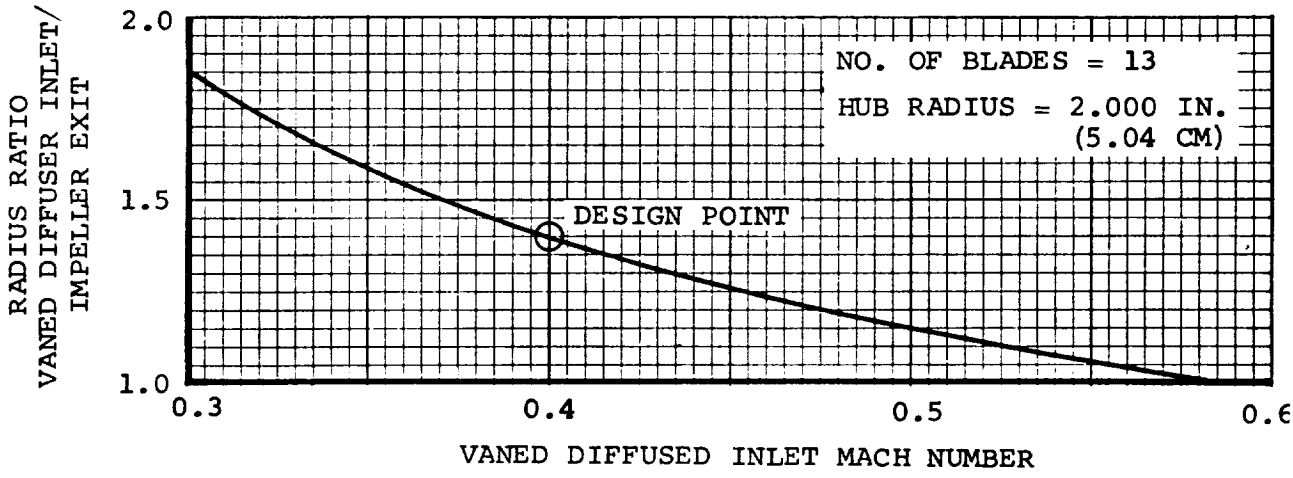
A low system gas flow velocity is required to maintain the heat exchanger pressure losses at acceptable levels. This requirement dictates a low exit velocity from the diffuser. Figure 108 shows the variation in overall total-to-total efficiency as a function of the impeller exit angle and vaned diffuser inlet Mach number with the diffuser exit Mach number fixed at 0.12. The vaned diffuser to rotor exit radius ratio is also shown for a 30 degree blade exit angle. A vaned diffuser inlet Mach number of 0.4 was selected as a good compromise between efficiency and vaneless diffuser radius ratio. (See Section 5.2.1 for addition discussions.)

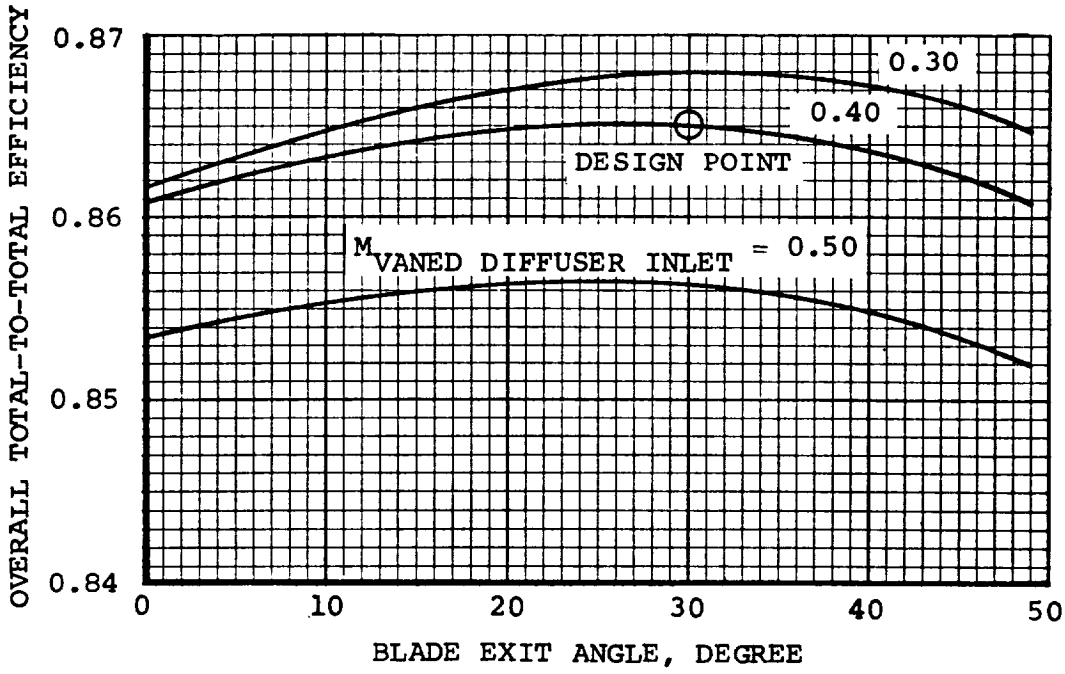
Table 39 presents a summary of the Phase III compressor design.



TAC PHASE III COMPRESSOR

FIGURE 107





TAC PHASE III COMPRESSOR

FIGURE 108

TABLE 39

PHASE III COMPRESSOR DESIGN

Speed, rpm	24,000
Inlet total press, psia (kN/m^2 abs)	70.0 (483)
Inlet total temperature, °R (°K)	580 (322)
Pressure ratio	1.9
Flow, lb/sec (kg/sec)	13.73 (6.23)
Specific speed, $\frac{N/Q_{in.}}{g^{3/4} H_{ad}^{3/4}}$	0.1129
Number blades	13
$\Delta T/T$ overall	0.3384
η overall	0.865
Exit total temperature, °R (°K)	776.2 (431)
Impeller tip dia, in. (cm)	8.718 (22.14)
Vaned diffuser inlet dia, in. (cm)	11.873 (30.16)
Vaned diffuser exit dia, in. (cm)	18.275 (46.42)
Number of diffuser vanes	20
Impeller tip speed, ft/sec (m/sec)	913.1 (231.9)
Impeller exit blade height, in. (cm)	0.582 (1.478)
Impeller exit blade angle, deg	30.0
Inducer tip dia, in. (cm)	4.982 (12.65)
Inducer hub dia, in. (cm)	2.000 (5.02)
Axial clearance, in. (cm)	0.010 (0.025)
Rey No., $\frac{\rho U_{tip} D_{tip}}{\mu}$	15.686×10^6

6.2 Turbine Phase III Design Point

Table 40 compares the Phase I and Phase III turbine design point Since the corrected speed and flow changed the preliminary design was repeated. Overall estimated total-to-total efficiency, including diffuser losses is 0.918 for the new turbine design.

TABLE 40

TURBINE DESIGN COMPARISON

	Phase I	Phase III
Shaft speed, rpm	24,000	24,000
Mass flow, lb/sec (kg/sec)	9.93 (2.19)	13.52* (3.005
Pressure ratio	1.786	1.824
Inlet pressure, psia (kN/m^2 abs)	101.4 (701)	130.0 (898)
Inlet temperature, °R (°K)	2060 (1144)	1610 (894)
Corrected speed, rpm	12,043	13,622
Corrected flow, lb/sec (kg/sec)	2.869 (0.633)	2.693 (0.593)

*Turbine mass flow rate is based on 1.5 percent compressor bleed flow.

6.2.1 Preliminary Design Optimization

An initial velocity diagram was established for an assumed loss distribution in the blade rows by satisfying continuity and work requirements. When the velocity distribution was calculated from the optimized geometry loss assumptions were checked from the boundary layer calculations. It must be noted that these calculated losses did not include secondary flow losses or losses from the disturbance of the tip shroud vortex on the bulk of the fluid. Additional losses must be assumed, based on experimental data.

The turbine rotor exit Mach number of 0.18 was set with the required diffuser exit Mach number of 0.1 and an assumed diffuser recovery of 50 percent, based on a limited diffuser length with an area ratio of 1.782. A selection of the optimized jet/speed ratio, based on total to rotor exit static pressure ratio, defined the tip speed. The turbine work requirement further defined the moment of angular momentum at the rotor inlet for a zero exit swirl design. A 20 bladed rotor design with a slip factor of 0.885 was selected for minimum rotor inlet loss. The exducer hub radius was maintained the same as the Phase I design and a 74 degree nozzle angle was used to define the meridional shape of the rotor. The reaction ratio from inlet to the exducer mean radius of this rotor was calculated as 2.155, which is comparable with other designed high performance turbines.

Satisfactory blade loadings were achieved after several iterations. During this analysis, the blading was assumed to be radial elements with a blade thickness distribution similar to a centrifugal compressor due to the low temperature and low tip speed of this turbine. The blade loading was further checked with a modified NASA

computer program TANDEM which analyzes blade rows with tandem arrangements. From this program, effects of leading edge incidence, number of full blade and/or spitter, as well as the location of spitter vanes, on blade loading could be analyzed. Results were compared with the previously calculated blade loading; they showed about the same rate of reaction and loading distribution, except in the wake of the splitters. The NASA based program showed continuous loading while the previous method results indicated sudden increase in loading where the splitters ended.

6.2.2 Turbine Design Results

As a result of the preliminary optimization, the turbine design parameters summarized in Table 41 are recommended for the TAC Phase II application. More detailed analysis will be necessary to consider reducing blade numbers. It is possible that the surface friction loss thereby reduced will be greater than the additional losses associated with higher blade loading.

TABLE 41

PHASE III TURBINE DESIGN

Shaft speed, rpm	24,000
Inlet temperature, °R (°K)	1610 (894)
Overall pressure ratio	1.824
Corrected flow, lb/sec (kg/sec)	2.693 (1.220)
Tip speed, ft/sec (m/sec)	1051 (267)
Inducer tip radius, in. (cm)	5.018 (12.75)
Exducer tip radius, in. (cm)	3.511 (8.91)
Exducer hub radius, in. (cm)	1.387 (3.52)
Inducer blade width, in. (cm)	0.898 (2.28)
Wheel axial length, in. (cm)	3.04 (7.72)
Exit swirl angle, deg	0
Nozzle angle, deg	74
Diffuser pressure recovery factor	0.50
Exducer exit Mach number	0.180
Number of blades/splitters	20/10
Velocity factor	1.0
Overall efficiency	0.918

6.3 Phase III Alternator Study

6.3.1 Alternator Requirements

Specified electrical and mechanical specification requirements for the alternator are listed below:

(a) The alternator shall have a maximum continuous rating of 160 kw_e with a 3-phase output at a 0.75 lagging load power factor and an overload rating of 320 kva at 0.9 lagging load power factor for 5 seconds after temperature equilibrium has been reached. Rated voltage shall be 240 volts L-N, 3 phase, wye connected initially; however, the stator winding design shall permit reconnecting the above coils to produce 480 volts L-N. In addition, the feasibility of bonding a high magnetic permeability pole face material to the rotor (in order to reduce pole face losses) shall be investigated. If the above is deemed feasible, a stator shall be designed which then permits 120, 240, or 480 volts L-N windings.

(b) The alternator shall be capable of operating at 120 percent of design speed without a catastrophic failure under all loads up to and including rated TAC load conditions (160 kw_e, 0.75 lagging power factor) for a limited time.

(c) The design life criteria for the alternator shall be 5 years operating time under the specified conditions for the TAC assembly.

(d) For systems radiator size and weight considerations, it is desired to operate the alternator stator at elevated temperatures. The alternator shall utilize high-temperature magnetic, electrical and insulation materials which include

stainless steel or Inconel-clad silver for the conductors, Anadur "S" for the insulation between conductors, and high-purity ceramic, 99.5 percent alumina, for the slot insulators. A maximum of 300°F (167°K) temperature increase shall be permitted between the coolant supply temperature and the alternator hot spots at the 160 kw_e power level.

The alternator stator winding shall permit the direct substitution of organic insulated windings at some future date with a reduced coolant supply temperature of 107°F (315°K).

(e) The alternator shall be designed to the maximum extent possible so as to reduce to a minimum windage losses. A windage loss less than 6 percent of the rated output for a full-load pressurized rotor cavity shall be considered a design goal. Windage losses will be determined with Helium-Xenon mixture in the rotor cavity at a pressure of 70 and 86 psia (483 and 593 kN/m^2 abs) for 466°F (514°K) coolant.

(f) The alternator shall be in accordance with MIL-G-6099A (ASG) in accordance with the latest revision in effect for the following:

1. Short-Circuit Capacity. Paragraph 4.5.12 for a minimum time of 5 seconds for each occurrence.

2. Phase Balance. Paragraphs 4.5.10, 4.5.10.1 and 4.5.10.2 except that paragraph 4.5.10.1 is amended to read "...the individual phase voltages shall not deviate from the average by more than 2.25, 4.5, and 9 percent, respectively."

3. Waveform. Paragraph 4.5.16* - In addition the total rms harmonic content of the line-to-neutral voltage wave, when the alternator is operating into a purely resistive load, shall be less than 5 percent from 10 to 100 percent maximum design load of 160 kw_e.

4. Output Voltage Modulation.* Paragraph 4.5.13, except that modulation shall not exceed 0.5 percent.

(g) Shock, Vibration, and Acceleration - The alternator shall be in accordance with the environmental specifications NASA Nos. P2241-1 and P2241-2 except paragraph 2.3.3.1 of Specification P2241-1 shall be replaced with paragraph 3.5.1.4 from environmental Specification No. 417-2, Revision C, dated June 1, 1969. Assumed acceleration is 1.5 g's in both directions along mutually perpendicular axes.

(h) Radiation Environment - The design radiation environment shall be 10^7 rads, 10^{13} nvt fast neutrons per square centimeter (>1 Mev) unless otherwise specified.

(i) Position Sensitivity - The alternator shall be designed to operate in any position in both zero "G" and one "G" environments.

(j) Voltage-Regulator-Exciter and Speed Control - While the VRE, speed control, and power conditioning equipment were not a part of the study, their effects on the alternator shall be considered in the design study. The speed control of transient load changes shall be of the phase-controlled parasitic load type. Frequency regulation shall be assumed

*This shall be a design goal without analytical verification.

to be within ±1 percent of design frequency for a change in external load of from 10 percent to full design output power. Some form of system gas pressure modulation is contemplated for long term or scheduled control of power level.

Preliminary design and performance parameters for a 400 Hz, 2-pole 240 volt L-N Lundell alternator with high temperature insulation were established to determine the design feasibility specifically with regard to the following:

a. Weight and efficiency at design power output.

b. Magnetic and mass unbalanced forces on the rotor.

c. Rotor stresses at 24,000 rpm and 20 percent overspeed.

d. Temperature distribution for coolant temperatures of 325°F (436°K) and 466°F (514°K) with argon in the gap except that windage losses for the HeXe mixture shall be used to determine the temperature distribution.

e. Voltage limitations due to corona as a function of pressure of a helium gas.

6.3.2 Electrical Design

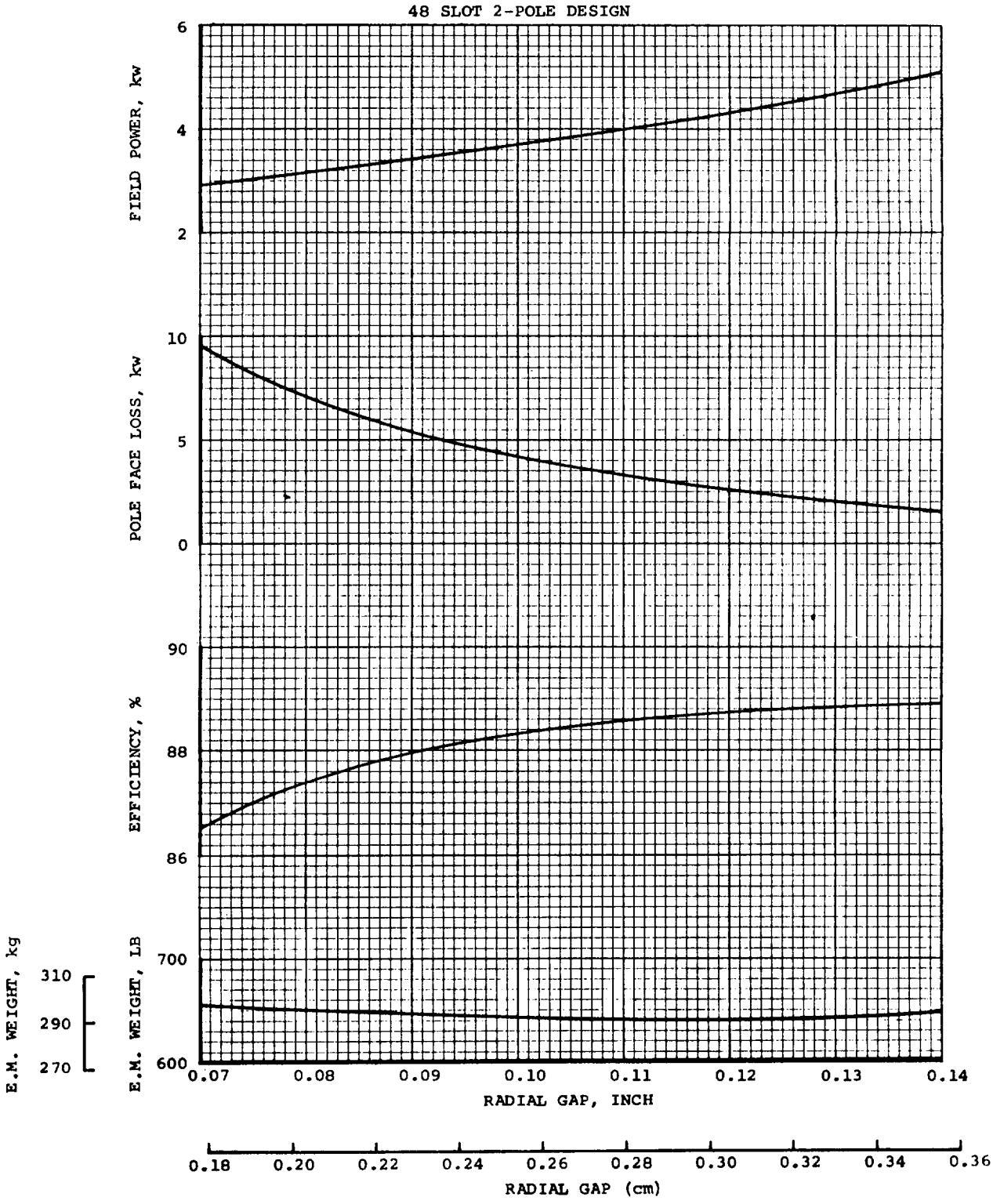
6.3.2.1 Configuration Design Selection and Features

During the Phase I studies, a preliminary 2-pole, 400 Hz Lundell alternator design was derived. This design had 48 stator slots, 8 series turns per phase, an 8 in. (20.4 cm) diameter rotor and used Hiperco 27 for the rotor magnetic material.

SAE 4340 alloy was selected for the rotor magnetic material for the Phase III, 2-pole, 400 Hz alternator design and a design analysis using the Phase I selected parameters (48 slots) was performed with the SAE 4340 magnetic alloy in the rotor. This design required a rotor diameter of 8.4 inches (21.4 cm) and had pole face losses which were approximately 3.4 times as large as the previous design. The higher pole face losses were caused by the lower permeability of the SAE 4340 as compared to Hiperco 27. A radial gap study was performed to evaluate the effect, on alternator weight and efficiency, of increasing the radial gap to reduce pole face losses. Results of this study are shown in Figure 109. Radial gaps in the range of 0.100 to 0.120 in. (0.254 to 0.305 cm) provide optimum results regarding alternator weight and efficiency. Pole face losses decrease and stationary field coil losses increase with increasing radial gap. Increasing the radial gap transfers some of the rotor surface losses to the stator field which normally is desirable from heat transfer considerations. A radial gap of 0.120 inches (0.305 cm) was selected; however, this can be reduced to as low as 0.100 inches (0.254 cm) if this later seems desirable.

Preliminary indications were that the 8.4 in. (21.3 cm) diameter rotor was too large. The stator slots were increased to 60, thereby increasing the number of stator turns per phase from 8 to 10 for the 240 volt L-N case. This configuration resulted in a rotor diameter of 8.0 in. (20.4 cm), and reduced the total pole face loss. This is because the greater number of slots decreased the tooth ripple (or no-load) component of pole face loss (which was predominant for the 48 slot design). The load harmonic component of pole face loss became predominant for the 60-slot design, and a further increase in the number of stator slots (and turns) would further increase this loss component.

It is most probable that a higher number of stator turns and slots can be tolerated from a pole face loss standpoint if a further reduction in rotor diameter is deemed necessary. However, the 60 slot



RADIAL GAP STUDY

FIGURE 109

configuration was selected because of considerations regarding the gas recirculation scheme utilized for cooling. The pressure for gas circulation is created in the tapered cone section of the rotor. Preliminary indications were that the larger radius and height of the cone section provided by the 8 in. (20.4 cm) rotor diameter design would be desirable to provide satisfactory pumping head for forced convection cooling, and that rotor stress levels were satisfactory. Later thermal analysis indicated it ensured a conservative design; further optimization may show that a smaller rotor diameter would still produce adequate forced convection cooling for a 2-pole machine.

The 60 slot alternator configuration was designed for 240 volts L-N; however, the alternator windings can be reconnected to produce 480 volts L-N. This is accomplished by connecting the two parallel circuits in series. Because the stator is wound for the minimum of two conductors per slot and the maximum number of parallel circuits is two, the 60 slot stator cannot be reconnected or rewound to produce 120 volts L-N. In order to provide a stator that can be reconnected and/or rewound to provide 120, 240, or 480 volts L-N, a 30 slot stator design was made. For the 120 volt configuration, the 30 slot stator is wound with two conductors per slot and two paralleled paths. The two paralleled paths are reconnected in series to provide 240 volts L-N. To obtain 480 volts L-N, the stator must be rewound with four conductors per slot. As a consequence of reducing the stator slots fr 60 to 30, the rotor pole face losses increased by a factor of approximately 5.5. This is caused by the larger slot pitch and slot opening of the 30 slot design which increases the amplitude of the rotor surfa flux pulsations. The high pole face losses of this configuration can be reduced to approximately one-fourth by bonding a high magnetic permeability pole face material such as SAE 1010 to the rotor.

Because some question existed (see Section 6.3.4) regarding the feasibility of pole face bonding and because the higher voltage levels are preferred, the 60 slot design was selected for all performance calculations. The 60 slot alternator configuration and the slot

configuration for the various slot designs are shown in Figure 110. There are some small dimensional differences between the 30 slot alternator design and 60 slot alternator design shown; however, the configuration in Figure 110 is representative of both for all practical purposes. A summary of design details for the different slot designs is given in Table 42.

The two pole Lundell rotor consists of two magnetic pole sections cantilevered from flux collector rings located at each end of the rotor. The space between the magnetic pole sections is filled with non-magnetic Inconel 718. This material is bonded to the magnetic pole sections to provide a homogeneous structure to reduce rotor stress and provide a smooth rotor surface to minimize windage losses. The flux from a given rotor pole face passes radially through the adjacent radial gap into the stator teeth and then passes circumferentially through the depth behind the slot to and through the teeth and radial gap adjacent to the other pole. After entering the pole, the flux passes axially through the pole body to the flux collector ring. The flux then passes through the auxiliary radial gap, into the stator frame where it returns axially to the other end of the alternator and to the pole of origin through the other auxiliary gap.

The stationary field coils are located above the end extensions of the ac winding. As shown in Figure 110, there is an excess of space available for the field coils; as a result, the size of the field coil can be increased to reduce the field coil losses and amperes required from the voltage regulator-exciter.

Because the end extensions are long and the depth of the magnetic section behind the slots is large for 2-pole machines, the 2-pole configuration does not lend itself to efficient cooling by conduction of losses to the stator O.D. Because of this, forced convection cooling was adopted to cool the end extensions. The stator stack was divided into two sections to allow room for a 0.5 in. (1.27 cm) passageway for

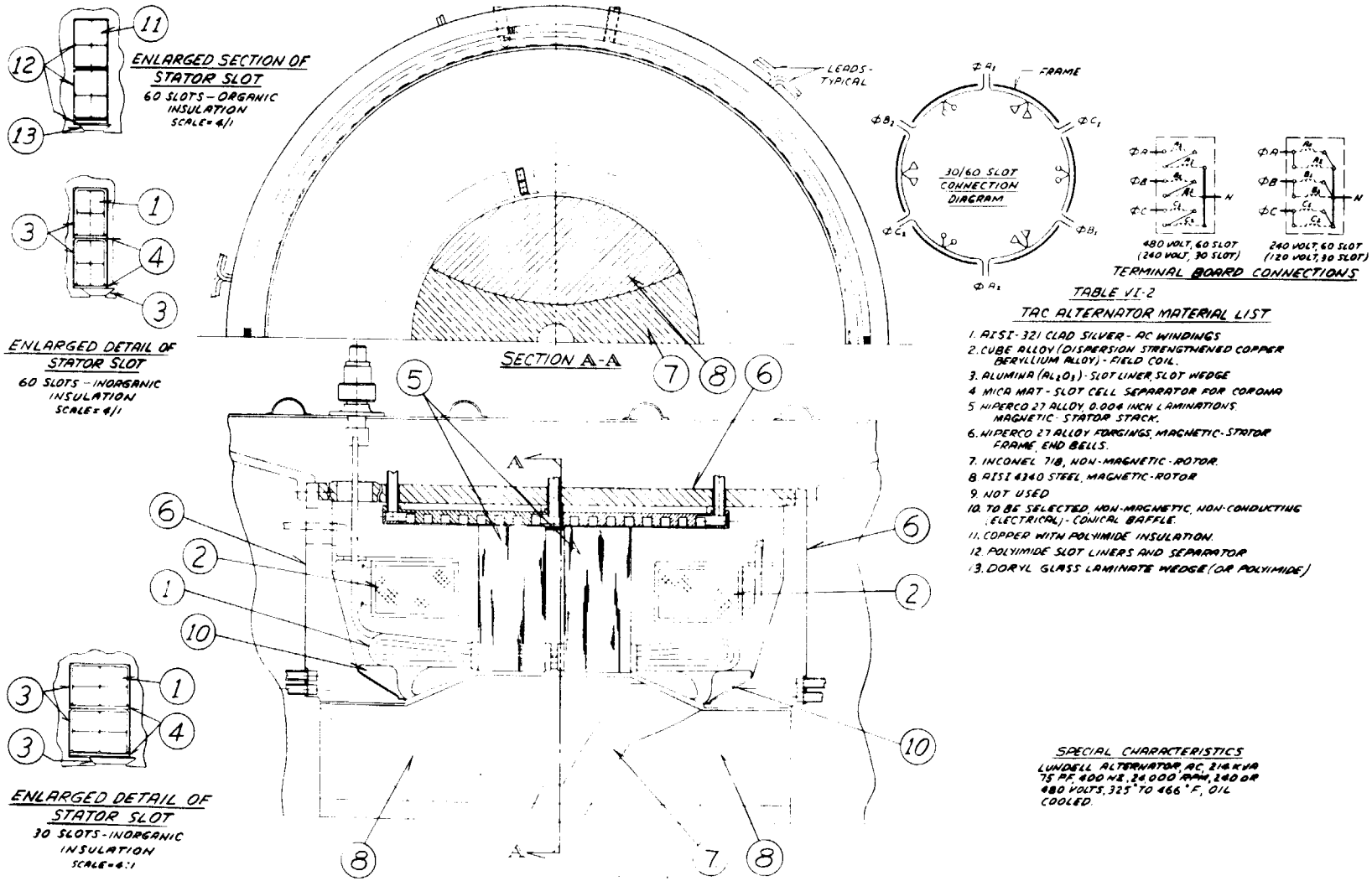


TABLE VI-2

TAC ALTERNATOR MATERIAL LIST

1. AISI-321 CLAD SILVER - AC WINDINGS
2. CUBE ALLOY (DISPERSION STRENGTHENED COPPER BERYLLIUM ALLOY) - FIELD COIL.
3. ALUMINA (AL_2O_3) - SLOT LINER, SLOT WEDGE
4. MICA MAT - SLOT CELL SEPARATOR FOR CORONA
5. HIPERCO 27 ALLOY, 0.004 INCH LAMINATIONS. MAGNETIC - STATOR STACK.
6. HIPERCO 27 ALLOY FORGINGS, MAGNETIC - STATOR FRAME, END BELLS.
7. INCONEL 718, NON-MAGNETIC - ROTOR.
8. AISI 4340 STEEL, MAGNETIC - ROTOR
9. NOT USED
10. TO BE SELECTED, NON-MAGNETIC, NON-CONDUCTING (ELECTRICAL) - CONICAL BAFFLE.
11. COPPER WITH POLYIMIDE INSULATION.
12. POLYIMIDE SLOT LINERS AND SEPARATOR
13. DORYL GLASS LAMINATE WEDGE (OR POLYIMIDE)

SPECIAL CHARACTERISTICS

LUNDELL ALTERNATOR, AC, 214 KVA 75 PF, 400 HZ, 24,000 RPM, 240 OR 480 VOLTS, 325° TO 466° F, OIL COOLED.

TAC PHASE III ALTERNATOR LAYOUT

TABLE 42

TAC PHASE III ALTERNATOR DESIGN SUMMARY

Number of slots	60		60	30
Design voltage	240/416		240/416	480/832
Reconnectable voltage	480/832		480/832	240/416
Rewind voltage	-		-	120/208
Coolant Temperature: °F (°K)	466 (514) and 325 (436)		107 (315)	466 (514)
Dimensions: in.				
Rotor O.D.	8.0 (20.4)		8.0 (20.4)	8.0 (20.4)
Rotor length	13.04 (33.2)		13.04 (33.24)	12.32 (32.6)
Stack length (overall)	4.22 (10.7)		4.22 (10.7)	3.5 (8.9)
Stack O.D.	16.21 (41.2)		16.21 (41.2)	16.51 (42.0)
Overall O.D.	18.5 (47.0)		18.5 (47.0)	
Overall length	13.9 (35.0)		13.9 (35.0)	
Electromagnetic weights: lbs (kg)				
Armature	26.9 (12.2)		26.9 (12.2)	26.2 (11.9)
Field	43.3 (19.6)		43.3 (19.6)	44.4 (20.1)
Frame	211.7 (95.9)		211.7 (95.9)	204.3 (92.8)
Stacks	135.5 (61.5)		135.5 (61.5)	136.3 (61.9)
Rotor	153.1 (69.5)		153.1 (69.5)	145.0 (65.7)
Total	570.5 (258.7)		570.5 (258.7)	556.2 (252.4)
Materials:				
AC conductors	321 sst clad silver		Copper	321 sst clad silver
Field conductors	Cube copper alloy		Copper	Cube copper alloy
Armature laminations	0.004 in. (0.102 mm) thick Hiperco 27		0.004 in. (0.102 mm) thick Hiperco 27	0.004 in. (0.102 mm) thick Hiperco 27
Frame	Hiperco 27 forgings		Hiperco 27 forgings	Hiperco 27 forgings
Rotor magnetic	SAE 4340 @ Rc 33		SAE 4340 @ Rc 33	SAE 4340 @ Rc 33
Rotor nonmagnetic	Inconel 718 @ Rc 38		Inconel 718 @ Rc 38	Inconel 718 @ Rc 38
Insulation				
AC winding	Anadur		Polyimide, Doryl varnish	Anadur
Slot liner	Alumina		Polyimide	Alumina
Slot separator	Synthetic mica		Polyimide - glass	Synthetic mica
Field winding	Synthetic mica		Polyimide	Synthetic mica
Winding details:				
Number of slots	60		60	30
Conductors per slot	2		2	4
Series turns per phase	10		10	20
Parallel paths	2		2	1
Parallel strands	4		4	2
Phase belts	60°		60°	60°
Pitch	2/3		2/3	2/3
Bare conductor dimensions, in. (mm)	0.081 x 0.144(2.06 x 3.66)		0.102 x 0.162(2.59 x 4.12) and 0.102 x 0.144(2.59 x 3.66)	0.182 x 0.128(4.62 x 3.25)
Rotor tip speed (24,000 rpm): ft/sec (m/sec)	837 (255)		837 (255)	837 (255)
Main gap: in. (mm)	0.120 (3.05)		0.120 (3.05)	0.120 (3.05)
Auxiliary gap: in. (mm)	0.050 (1.27)		0.050 (1.27)	0.050 (1.27)
Current densities: amps/in.^{2} (amps/cm^2)				
AC winding	3425 (530)		2512 (389)	3304 (513)
Field winding	3757 (581)		3757 (581)	3921 (607)
Flux densities: KL/in.^{2} (Webers/m^2)				
Back iron	76 (118)		76 (118)	75 (116)
Teeth	113 (175)		113 (175)	103 (160)
Main air gap	46 (71)		46 (71)	55 (85)
Pole	86 (133)		86 (133)	85 (132)
Frame	98 (152)		98 (152)	102 (158)
Auxiliary air gap	58 (90)		58 (90)	58 (90)
Percent harmonics:				
Third	0		0	0
Fifth	2.71		2.71	2.71
Seventh	2.18		2.18	2.33
Reactances: P.U.				
Xd	1.21		1.21	1.1
X'd	0.277		0.28	0.262
X"d	0.244		0.245	0.230
Xq	0.55		0.55	0.504
X"q	0.048		0.052	--
X2	0.146		0.105	--
Xo	0.008		0.0085	0.007
Time constants, hot seconds				
T'do	0.291		0.291	0.234
T'D	0.059		0.060	0.051
T"A	0.0052		0.006	--
T"d	0.0051		0.005	0.005
Coolant temperature: °F (°K)	466 (514)	325 (436)	107 (315)	466 (514)
F.L. losses: w				
Pole face	1166	1258	1259	1485
Back iron	3782	4355	4940	3762
Teeth	564	650	737	468
Armature	2132	1709	1069	2324
Field	3513	3513	3539	3946
Electromagnetic subtotal	11158	11484	11543	11985
Windage	8610	9150	10200	8600
Total	19768	20634	21743	20585
Efficiency: percent				
Electromagnetic	93.2	93.3	93.3	93.0
Overall	89.0	88.6	88.0	88.6

radial gas flow. A detailed description of the forced convection cooling scheme is presented in Section 6.3.3.1.

The configurations of the alternator slots are designed so that the alternators can be rewound using an inorganic insulation system for the 107°F (315°K) coolant temperature condition. Two different sizes of quadruple layer polyimide insulated rectangular wire are used to obtain a proper fit in the slot. The slot liners are composed of a double layer, polyimide film insulation. The slot liners are overlapped between phases to provide added high voltage protection as shown by the slot detail in Figure 110. Organic insulations degrade with time and temperature; therefore, if long life is desired, the operating temperature of the insulation must be limited to achieve the desired life. Available data for a selected polyimide insulation system indicates that the winding temperatures must be less than 417°F (487°K) to achieve 5 years thermal life. Average winding temperatures using a coolant temperature of 107°F (315°K) are well below this limit, as indicated in Section 6.3.3.4. A summary of the design for the low temperature inorganic insulated 60 slot TAC alternator is given in Table 42.

6.3.2.2 Performance Summaries

Alternator electrical performance was determined for loads corresponding to 1/4, 1/2, 1 and 1-1/2 times rated power output at load power factors of 0.75 lagging and 1.0 respectively. Breakdowns of losses, current densities, flux densities, efficiencies, and field ampere turns are given in Tables 43 through 46 for coolant temperatures of 325°F (436°K) and 107°F (315°K) and for rotor cavity pressures of 70 psia (483 kN/m^2 abs) and 86 psia (593 kN/m^2 abs) respectively. To show potential part-load efficiency improvements the stack length was arbitrarily increased 1.0 in. (2.54 cm) with the results as shown in Table 43.

TABLE 43

COOLANT TEMPERATURE = 325°F (436°K)
INORGANIC INSULATION
CAVITY PRESSURE AT FULL LOAD = 70 PSIA (483 kN/m^2)

POWER FACTOR	0.75				1.00				0.9
OUTPUT POWER, KW P.U. LOAD	40 1/4	80 1/2	160 1	240 1 1/2	40 1/4	80 1/2	160 1	240 1 1/2	320 KVA O.L.
LOSSES: WATTS									
ARMATURE	99	401	1,709	4,313	55	222	918	2,195	4,311
FIELD	1,199	1,730	3,513	8,151	868	984	1,465	2,342	6,111
POLE FACE	511	659	1,258	2,269	485	565	891	1,443	2,261
TOOTH	624	633	650	667	618	620	625	630	657
BACK IRON	4,184	4,241	4,355	4,471	4,143	4,158	4,188	4,221	4,404
TOTAL ELECTROMAGNETIC	6,616	7,664	11,484	19,872	5,169	6,549	8,087	10,831	17,744
WINDAGE	3,550	5,710	9,150	12,080	3,550	5,710	9,150	12,080	13,640
OVERALL	10,166	13,374	20,634	31,952	9,719	12,259	17,237	22,911	31,384
EFFICIENCIES: %									
ELECTROMAGNETIC	85.81	91.26	93.30	92.35	88.64	92.43	95.19	95.68	94.20
OVERALL	79.73	85.68	88.58	88.25	80.45	86.71	90.27	91.28	90.17
CURRENT DENSITIES: AMPS/IN^2									
ARMATURE CURRENT	856	1,713	3,425	5,138	640	1,280	2,560	3,840	5,138
FIELD CURRENT	2,187	2,627	3,743	5,702	1,861	1,981	2,418	3,057	4,937
FLUX DENSITIES: KL/IN^2									
BACK IRON	74	75	76	77	74	74	74	74	76
TOOTH	110	111	112	114	109	109	110	110	113
MAIN GAP	44	45	46	46	44	44	44	45	46
POLE	72	77	86	95	69	70	74	80	92
FRAME	78	84	98	112	74	75	81	89	108
AUX. AIR GAP	46	50	58	75	44	45	48	53	64
FIELD AMP TURNS	7,654	9,195	13,101	19,957	6,514	6,933	8,462	10,698	17,280
INCREASED STACK LENGTH DESIGN [5.22 IN (13.3 cm)]									
TOTAL EM LOSSES, WATTS	5647	6719	10,849	24,991					
EM EFFICIENCY:	87.63	92.25	93.65	90.57					

Amps/in^2 times 0.155 = amps/cm^2
KL/in^2 times 1.55 = Webers/m^2

TABLE 44

COOLANT TEMPERATURE = 325°F (436°K)
INORGANIC INSULATION
CAVITY PRESSURE AT FULL LOAD = 86 PSIA (593 kN/m^2)

POWER FACTOR	0.75				1.0				0.9
OUTPUT POWER, KW P.U. LOAD	40 1/4	80 1/2	160 1	240 1 1/2	40 1/4	80 1/2	160 1	240 1 1/2	320 KVA O.L.
LOSSES: WATTS									
ARMATURE	99	401	1,709	4,313	55	222	918	2,195	4,311
FIELD	1,199	1,730	3,513	8,151	868	984	1,465	2,342	6,111
POLE FACE	511	659	1,258	2,269	485	565	891	1,443	2,261
TOOTH	624	633	650	667	618	620	625	630	657
BACK IRON	4,184	4,241	4,355	4,471	4,143	4,158	4,188	4,221	4,404
TOTAL ELECTROMAGNETIC	6,617	7,663	11,485	20,872	6,170	6,548	8,088	10,831	17,744
WINDAGE	4,060	6,520	10,440	13,800	4,060	6,520	10,440	13,800	15,580
OVERALL	10,677	14,183	21,925	34,672	10,230	13,068	18,525	24,631	33,324
EFFICIENCIES: %									
ELECTROMAGNETIC	85.81	91.26	93.30	92.00	86.64	92.43	95.19	95.68	94.20
OVERALL	78.93	84.94	87.95	87.38	79.63	85.96	89.62	90.69	89.63
CURRENT DENSITIES: $AMPS/IN^2$									
ARMATURE CURRENT	856	1,713	3,425	5,318	640	1,280	2,560	3,840	5,138
FIELD CURRENT	2,187	2,637	3,743	5,702	1,861	1,981	2,418	3,057	4,937
FLUX DENSITIES: KL/IN^2									
BACK IRON	74	75	76	77	74	74	74	74	76
TOOTH	110	111	112	114	109	109	110	110	113
MAIN GAP	44	45	46	46	44	44	44	45	46
POLE	72	76	86	95	69	70	74	80	92
FRAME	78	84	98	112	73	75	81	89	107
AUX. AIR GAP	46	50	58	66	44	45	48	53	64
FIELD AMP TURNS	7,654	9,195	13,101	19,957	6,514	6,933	8,462	10,698	17,280

$Amps/in^2$ times 0.155 = $amps/cm^2$
KL/in^2 times 1.55 = $Webers/m^2$

TABLE 45

COOLANT TEMPERATURE = 107°F (315°K)
ORGANIC INSULATION
CAVITY PRESSURE AT FULL LOAD = 70 PSIA (483 kN/m^2)

POWER FACTOR	0.75				1.0				0.9
OUTPUT POWER, KW	40	80	160	240	40	80	160	240	320 KVA
P.U. LOAD	1/4	1/2	1	1 1/2	1/4	1/2	1	1 1/2	O.L.
LOSSES: WATTS									
ARMATURE	61	250	1,077	2,774	34	138	574	1,369	2,769
FIELD	1,201	1,736	3,539	8,358	869	985	1,471	2,356	6,188
POLE FACE	511	660	1,259	2,271	485	564	890	1,442	2,261
TOOTH	707	717	737	757	699	701	705	710	744
BACK IRON	4,738	4,804	4,940	5,078	4,685	4,699	4,729	4,761	4,988
TOTAL ELECTROMAGNETIC	7,217	8,266	11,552	19,239	6,771	7,087	8,369	10,628	16,950
WINDAGE	3,960	6,360	10,200	13,480	3,960	6,360	11,200	14,800	15,200
OVERALL	11,177	14,626	21,752	32,719	10,731	13,447	19,569	25,428	32,150
EFFICIENCIES: %									
ELECTROMAGNETIC	84.72	90.64	93.27	92.58	85.52	91.86	95.03	95.76	94.44
OVERALL	78.16	84.54	88.03	88.00	78.85	85.61	89.10	90.42	89.96
CURRENT DENSITIES: AMPS/IN^2									
ARMATURE CURRENT	628	1,256	2,512	3,767	469	939	1,877	2,816	3,767
FIELD CURRENT	2,189	2,631	3,757	5,774	1,861	1,982	2,422	3,065	4,968
FLUX DENSITIES: KL/IN^2									
BACK IRON	74	75	76	77	74	74	74	74	76
TOOTH	110	111	113	114	109	109	110	110	113
MAIN GAP	44	45	46	46	44	44	44	44	46
POLE	72	77	86	95	69	70	74	80	92
FRAME	78	84	98	112	74	75	81	90	108
AUX. AIR GAP	46	50	58	66	44	44	48	53	64
FIELD AMP TURNS	7,660	9,210	13,150	20,209	6,515	6,937	8,478	10,729	17,389

Amps/in^2 times 0.155 = amps/cm^2
KL/in^2 times 1.55 = Webers/m^2

TABLE 46

COOLANT TEMPERATURE = 107°F (315°K)
ORGANIC INSULATION
CAVITY PRESSURE AT FULL LOAD = 86 PSIA (593 kN/m^2)

POWER FACTOR	0.75				1.0				0.9
OUTPUT POWER, KW	40	80	160	240	40	80	160	240	320 KVA
P.U. LOAD	1/4	1/2	1	1 1/2	1/4	1/2	1	1 1/2	O.L
LOSSES: WATTS									
ARMATURE	61	249	1,069	2,761	34	138	571	1,369	2,710
FIELD	1,201	1,736	3,539	8,358	869	985	1,471	2,356	6,188
POLE FACE	511	660	1,259	2,271	485	564	890	1,442	2,261
TOOTH	707	717	737	757	699	701	705	710	744
BACK IRON	4,738	4,804	4,940	5,078	4,685	4,699	4,729	4,761	4,988
TOTAL ELECTROMAGNETIC	6,818	8,166	11,543	19,181	6,772	7,087	8,366	10,638	16,891
WINDAGE	4,480	7,210	11,550	15,260	4,480	7,210	11,550	15,240	17,210
OVERALL	11,298	15,376	23,093	34,441	11,252	14,297	19,916	25,878	34,101
EFFICIENCIES: %									
ELECTROMAGNETIC	85.44	90.74	93.27	92.60	85.52	91.86	95.03	95.76	94.46
OVERALL	77.98	83.88	87.39	87.45	78.04	84.84	88.93	90.27	89.41
CURRENT DENSITIES: AMPS/IN^2									
ARMATURE CURRENT	628	1,256	2,512	3,767	469	939	1,877	2,816	3,767
FIELD CURRENT	2,189	2,631	3,757	5,774	1,861	1,982	2,422	3,065	4,968
FLUX DENSITIES: KL/IN^2									
BACK IRON	74	75	76	77	74	74	74	74	76
TOOTH	110	111	113	114	109	109	110	110	113
MAIN GAP	44	45	46	46	44	44	44	44	46
POLE	72	77	86	95	69	70	74	80	92
FRAME	78	84	98	112	74	75	81	90	108
AUX. AIR GAP	46	50	58	66	44	44	48	53	64
FIELD AMP TURNS	7,660	9,210	13,150	20,209	6,515	6,937	8,478	10,729	17,389

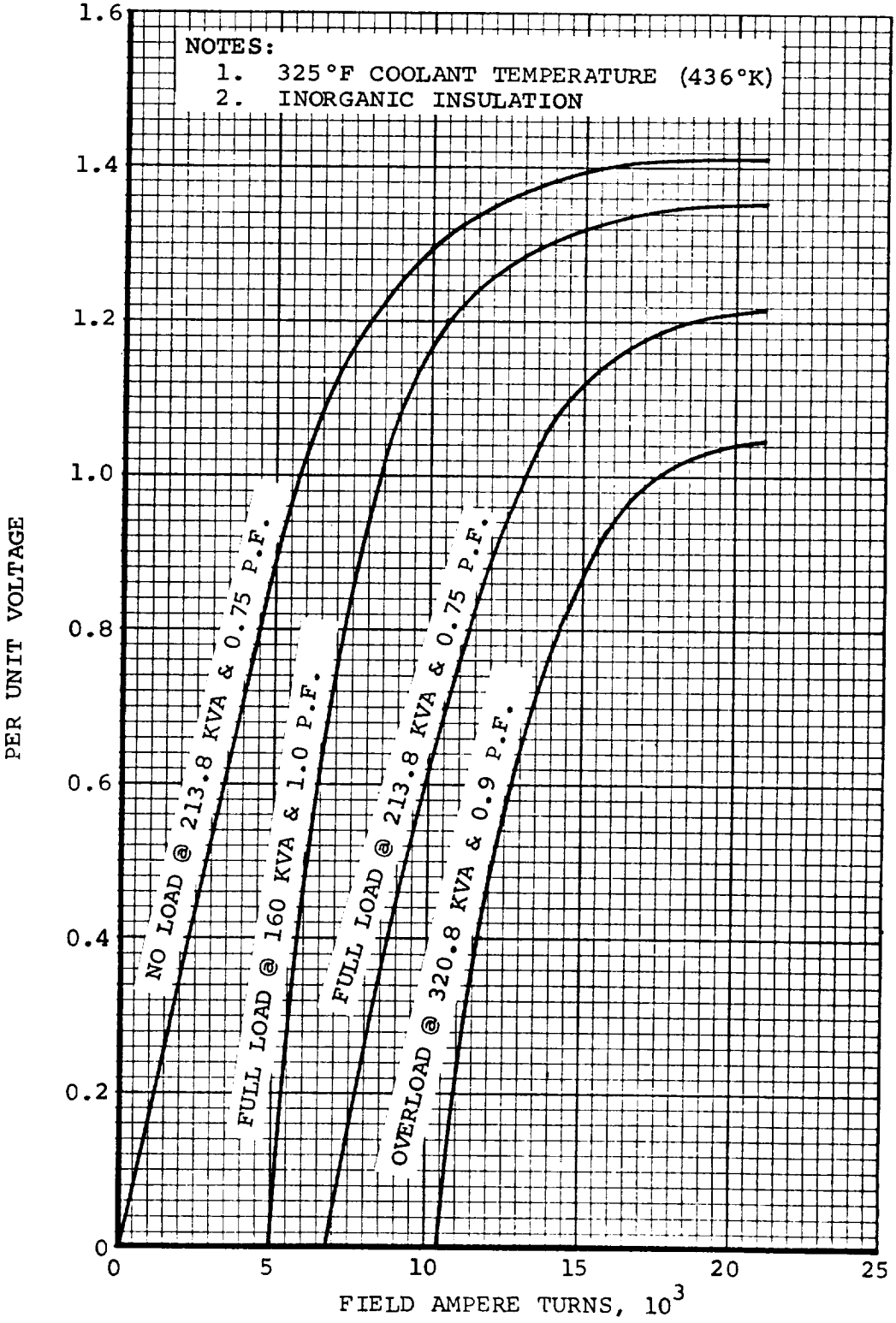
$Amps/in^2$ times 0.155 = $amps/cm^2$
KL/in^2 times 1.55 = $Webers/m^2$

Load and no-load saturation curves are given in Figures 111 and .12 for the high temperature and low temperature alternators, respec-:ively. Calculations performed for the overload conditions of 320 kva ıt 0.9 P.F. lagging indicate a winding temperature rise of 376°F (290°K) .n five seconds assuming the highest coolant temperature of 466°F (514°K). The calculation assumes all of the heat is stored in the ac ;inding during the 5 second time period and is somewhat pessimistic. :he average winding temperature at the end of 5 seconds would be about)44°F (779°K). This temperature is well below the melting point of ;ilver, 1761°F (1234°K) and within the temperature limits of the ;elected inorganic insulation.

5.3.2.3 Miscellaneous Electrical Design Considerations

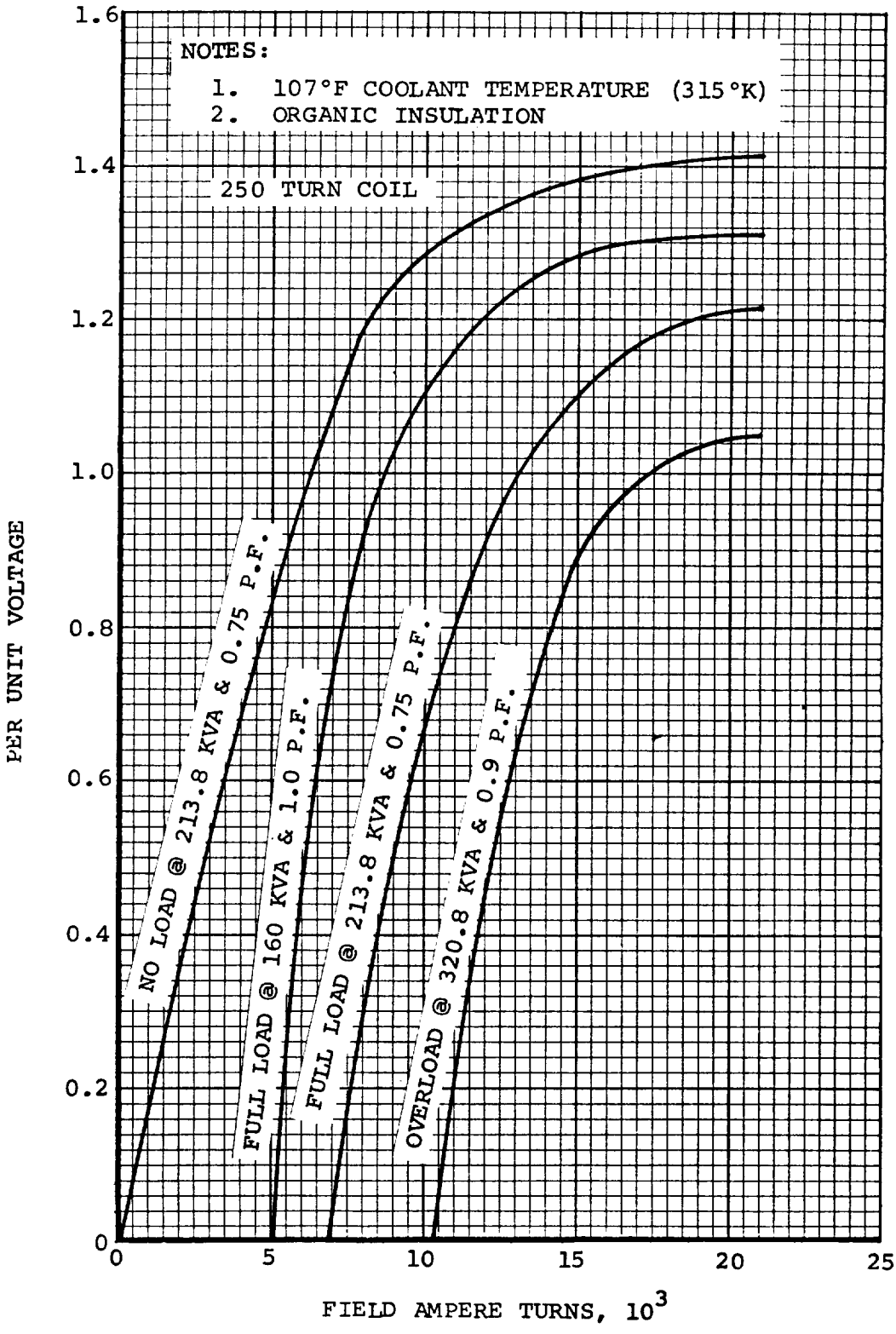
The ac winding of the alternator is surrounded with a helium-xenon gas mixture. The gas pressure is assumed to vary as a linear function of load ranging from 1/4 load to 1-1/2 times rated load. It is known from Paschen's characteristic curves for gases that the inception of corona is a function of voltage, gas pressure, and electrode spacing. The voltage gradient through the gas is dependent upon the dielectric constant and thickness of the insulation materials between the electrodes. Because the gas pressure in the stator cavity of the alternator is variable, calculations were made to determine the minimum allowable pressure to prevent ionization (corona) of the gas for the three specified alternator voltages. Results of these calculations are presented in Table 47.

The first three lines in the table present results for the inorganic, high temperature insulation system. In order to portray the effects of increasing the insulation thickness on minimum allowable pressure, calculations were repeated for the case of phase-to-phase voltage in the slot assuming that all insulation thickness are doubled. The results indicated in Table 47 show that the minimum pressure is reduced to approximately one half of the previous quantities.



SATURATION CURVES

FIGURE 111



SATURATION CURVES

FIGURE 112

TABLE 47

MINIMUM ALLOWABLE PRESSURES
BASED ON CORONA CONSIDERATIONS

		Minimum Allowable Pressure to Prevent Ionization of Gas, Psia (kN/m^2)	
Alternator Voltage (No Transients)	Insulation	Phase to Phase in Slot	Phase to Stack in Slot
120/208	Inorganic	No Limit	No Limit
240/416	Inorganic	14 (97) *6 (41)	8 (5.5)
480/832	Inorganic	53 (370) *26 (*180)	49 (340)
120/208	Organic, no varnish	No Limit	No Limit
240/416	Organic, no varnish	15 (100)	No Limit
480/832	Organic, no varnish	56 (390)	41 (280)

*For double insulation thicknesses

Calculations were repeated for the organic, low temperature insulation system assuming that the winding is not impregnated with a varnish. The minimum allowable pressures calculated for this case are approximately the same as for the inorganic insulation system. This is surprising in view of the lower dielectric constant of the organic insulation; however, the insulation thicknesses selected were less than for the inorganic insulation system. This was done primarily because of higher available dielectric strength and poorer heat transfer properties. Increasing the thickness of the insulation would result in lower minimum allowable pressures as indicated previously for the inorganic insulation system.

The fact that no varnish impregnation was assumed in the organic insulation system calculations is significant. If it is assumed that the winding is completely impregnated with a compatible varnish, then the minimum pressure for corona inception cannot be accurately calculated. Theoretically, a varnished winding is solid and does not contain any gas filled spaces. In reality, however, small bubbles or cavities do occur. The type of gas and the pressure in these cavities cannot be accurately predicted. In general, the use of a varnish impregnation will significantly increase the corona resistance of the winding. The mechanism of failure would be caused by the presence of corona pulses occurring in the entrained cavities in the solidified insulation. The electrons and ions in the gas bombard the insulation on each pulse and erode away the insulation. Harmful chemical reactions can occur. In general, for insulating materials, the time-to-failure at any applied voltage is a measure of corona resistance. Inorganic insualtions are much better in this respect than organic insulations. An inorganic insulating material such as alumina may induce corona in a gas at a lower voltage than for an organic material such as polyimide, but it is better able to withstand the effects of the corona pulses. Long life can be achieved for organic insulations by operating the insulation at reduced voltage stress levels.

The unbalance in the three-phase voltage of the alternator when operating with a single-phase current load equal to 2/3 of the rated current was determined for the alternator designs presented in Phase I and Phase III. The method of calculating one of the reactance values that indirectly effects voltage unbalance was changed during the Phase I to Phase III interim. The quadrature-axis sub-transient reactance (X"q) which is used in determining the negative sequence reactance (X_2) was previously determined by neglecting the quadrature axis damping provided by eddy currents flowing in the solid rotor surface. The procedure now used for calculating X"q is based on a modification of procedures which accounts for sub-transient damping effects. A check on the new calculation procedure was made by comparing calculated results and test results for the 1200 Hz alternator of the Brayton Rotating Unit (BRU).[1] The value of voltage unbalance obtained by test is 5.2 percent for a 2/3 rated current, single phase, unity power factor load. The calculated value is 5.85 percent. It was previously calculated to be 11.8 percent using the initial methods of Phase I.

6.3.3 Thermal Analysis

6.3.3.1 Method of Cooling

Direct conduction of the internal losses to heat sinks on the magnetic frame was not considered for the two-pole alternator since previous studies of the six-pole alternator, which offered more favorable conditions for direct conduction, revealed this mode of cooling was not adequate. A portion of the losses generated within the pole faces, conductors and gas must be transported by forced convection.

Forced convection within the alternator is obtained by recirculating the cavity gas through the conical gap around the rotor whereby the rotor produces a pumping action on the gas. The gas then passes through the main gap between the stator and rotor. A split stack

[1] Final Report, 1200 Hz Brayton Electrical Research Components. NASA CR-72564, 1968.

provides a radial passage from the main gap to a heat-exchanger which is located between the stack and the magnetic frame. The heat exchanger also serves as a nonmagnetic separator between the back-iron and the frame. After the gas passes through the heat-exchanger, it flows around the field coil and through the end extensions of the windings. Special baffles are used around the conical sections of the rotor. These baffles are designed to (1) cause the gas to enter the conical gap near the end of the auxiliary radial gap, (2) cause the gas to flow into the main gap with minimum leakage at the ends of the stacks, and (3) cause some of the gas to flow through the ends of the windings.

6.3.3.2 Gas Flow Rate

Pumping of the gas is produced by the action of the conical surfaces upon the gas within the gap. The head developed by this action was estimated from:

$$\Delta P = \rho (K\omega)^2 \, (R_o^2 - R_i^2)/2g$$

where

ΔP = pressure head

ρ = gas density

ω = rotor speed, 800 π radian/sec

R_o = rotor radius (main gap) = 4.0 in. (10.16 cm)

R_i = rotor radius (auxiliary gap) = 3.25 in. (8.255 cm)

K = 0.5

g = 386.4 lb_m in. lb_f^{-1} sec^{-2}

The pressure drop within the gas flow circuit was estimated from:

$$\Delta P = \rho/2g \left[V_H^2 \left(\frac{fl}{D} + \Sigma C_{ch}\right) + V_R^2 \Sigma C_{dR} \right]$$

where

V_H = velocity of gas in the heat-exchanger

V_R = velocity of gas in baffles and gap around the rotor

C_{dh} = loss coefficients for heat-exchanger (entrance, exit, turning, etc.)

C_{dR} = loss coefficient for baffles and gaps

fl/D = friction factor for heat exchanger

V_H/V_R = constant = 3 $in.^2$/2.75 $in.^2$ = 1.091

With an allowance of one dynamic head loss for each entrance, turn and exit plus an adequate allowance for the friction factor, the pressure drop for the flow circuit is:

$$\Delta P = 1/2\ \rho\ V_H^2 \quad (9.34)$$

and equating the pump head to the pressure drop gives:

$$V_H \approx 80 \text{ ft/sec } (24.4 \text{ m/sec})$$

$$V_R \approx 73.2 \text{ ft/sec } (22.3 \text{ m/sec})$$

The volumetric flow rate through the circuit was considered constant since Reynolds number effects upon the friction and other loss coefficients was neglected.

The flow rate based upon a velocity of 80 ft/sec (24.4 m/sec) in the heat-exchanger is given in Figure 113 as a function of pressure and the average temperature of the gas. These flow rates were used for the heat transport calculations.

The surface area on the gas side of the heat-exchanger is 7.51 ft^2 (0.697 m^2, both sides of the split stack). Each side consists of 275 parallel passages 4.38 in. (11.1 cm) long with a flow area per passage of 0.01 $in.^2$ (0.2 by 0.05 in.; 0.508 by 0.127 cm and 0.0645 cm^2).

6.3.3.3 Windage Losses

Windage losses were calculated for HeXe gas since this gas produces a lower Reynolds number (higher drag coefficient) than argon gas at the same conditions. Windage losses as a function of gas gemperature are given in Figures 114 and 115. Drag coefficients from NASA TMX-52851[2] were used. A comparison of the windage loss in the main gap obtained by the method used for the Phase I study and by the recent data reported in TMX-52851 showed that the new data gives approximately 30 percent higher loss. Therefore, the new data was used for the cooling studies.

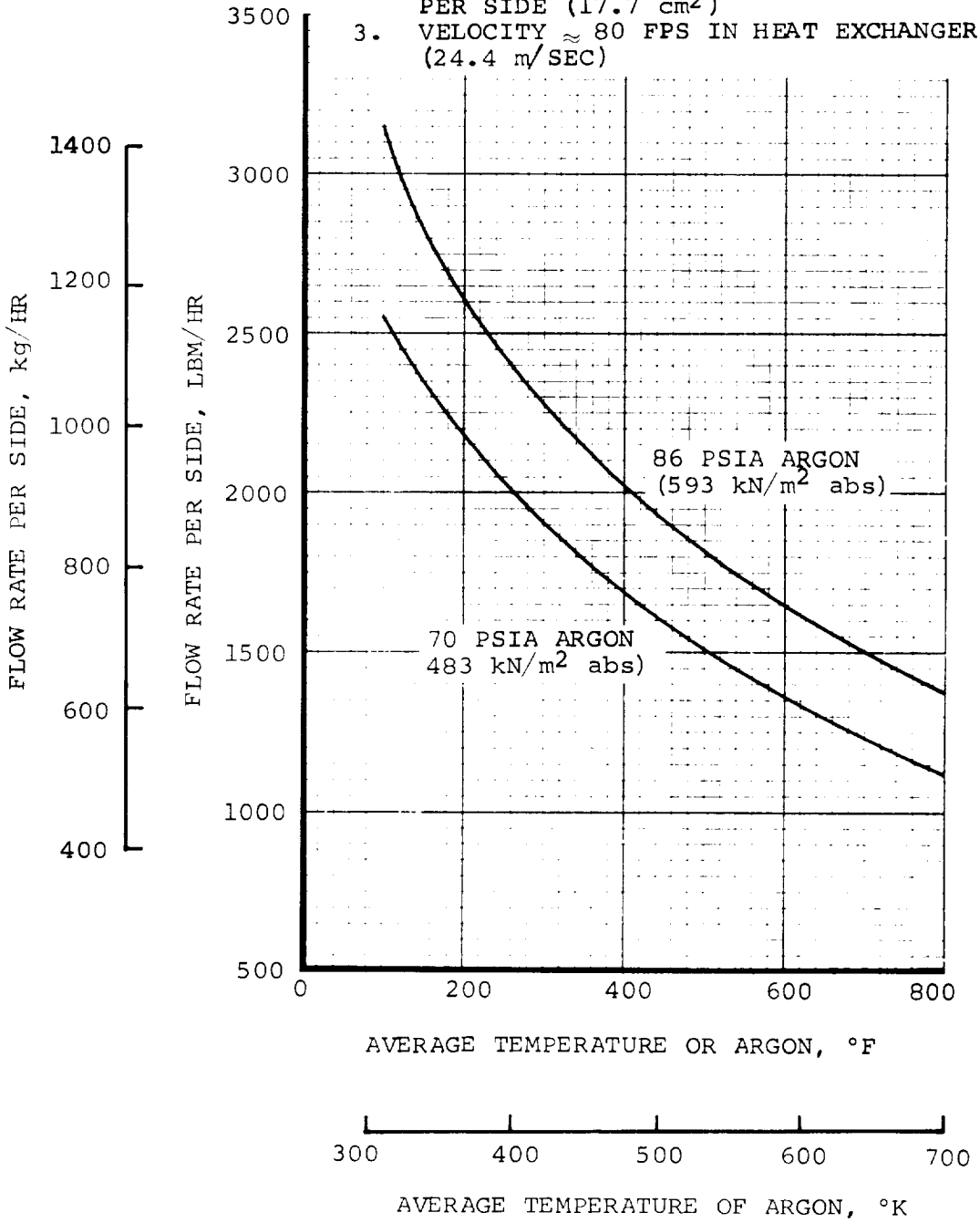
6.3.3.4 Thermal Maps

Computer programs were utilized to perform all analyses excepting the temperature rise of the liquid coolant and the maximum and minimum temperature of the gas. A 30°F (17°K) temperature rise of the liquid coolant was used for all calculations. The mean temperature difference between the gas and liquid in the heat-exchanger and the temperature rise of the gas were obtained by iterative calculations. The gas temperature rise of the gas were obtained by iterative calculations. The gas temperatures were treated as boundary temperatures which were improved after each iteration until the temperature rise of the gas

[2] Gorland, S.; Kempke, E.; and Lumannick, S.: Experimental Windage Losses for Close Clearance Rotating Cylinders in the Turbulent Flow Regime. NASA TMX-52851.

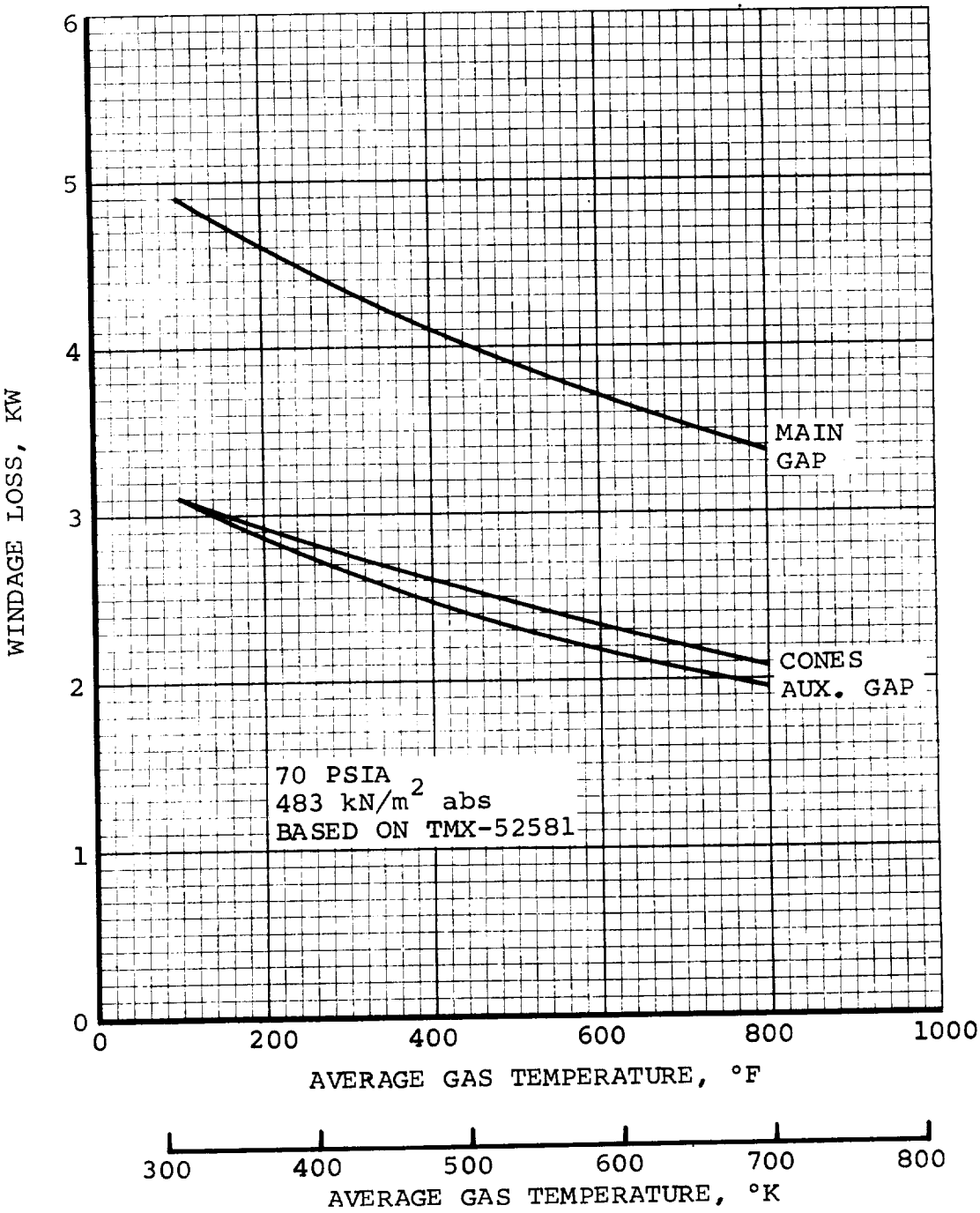
NOTES:

1. FLOW AREA IN BAFFLES AND GAP AROUND THE ROTOR = 3.0 IN.^{2} PER SIDE (19.4 cm^2
2. FLOW AREA IN HEAT EXCHANGER = 2.75 IN.^{2} PER SIDE (17.7 cm^2)
3. VELOCITY $\approx$ 80 FPS IN HEAT EXCHANGER (24.4 m/SEC)



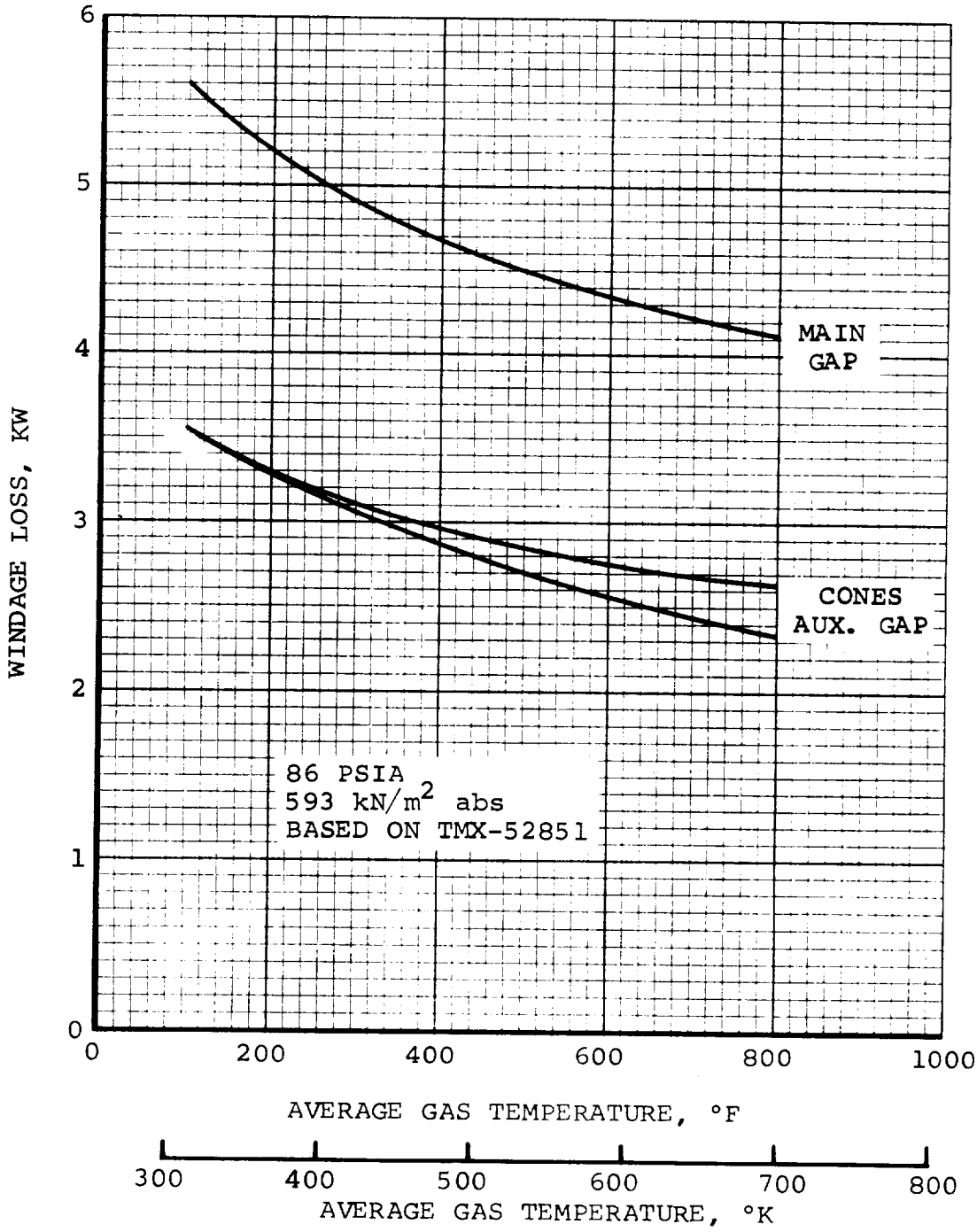
COOLING GAS FLOW RATE

FIGURE 113



ALTERNATOR WINDAGE LOSSES

FIGURE 114



ALTERNATOR WINDAGE LOSSES

FIGURE 115

rrelated with the heat flow into the gas at each point along the flow
th. The analysis did not include the alternator field coils since
eir thermal state is relatively independent of other alternator
mperatures. The field coils can be cooled by coolant coils which
e an intimate part of the field coil package. The field coils do
t represent difficult cooling problems as indicated in the Phase I
udies where a more compact field coil design was analyzed.

Thermal maps are presented in Figures 116 through 126 for the con-
tions and situations listed in Table 48.

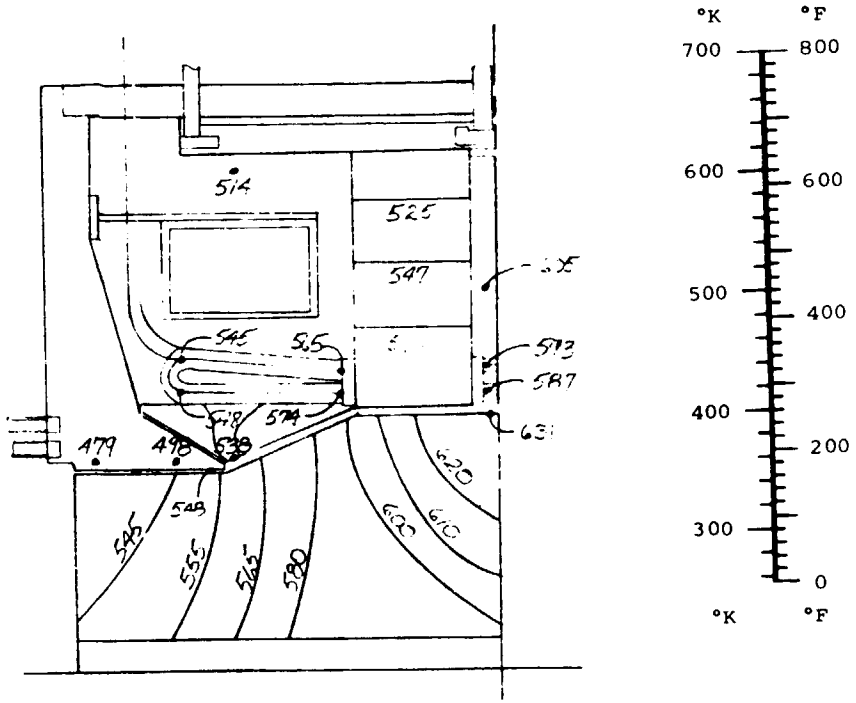
All of the cooling configurations and conditions that were inves-
gated fulfilled the requirement of the investigation since the hot-
ot temperature for all designs was less than 300°F (167°K) above
ıe coolant supply temperature.

Design No. 5 from Table 48 represents the design with the least
ɜrit for a coolant supply temperature of 466°F (514°K) since the
ɜmperature at an adiabatic interface between the rotor and bearings is
gh, 693°F (640°K). Approximately one kilowatt of heat must be con-
ıcted through the interface to decrease the interface temperature
)0°F (55°K). Addition of coolant within the end bell, as represented
/ Design No. 4, decreased the temperature of the adiabatic interface
:om 693° to 623°F (640° to 602°K). Similarly, the addition of a small
ıs flow through the auxiliary gap without coolant in the end bell, as
ɜpresented by Design No. 2, decreased the temperature of the adiabatic
ıterface from 693° to 561°F (640° to 567°K). Design No. 1 has coolant
ı the end bell plus forced circulation of gas through the auxiliary
ıs. This combination of cooling modes decreased the temperature of
ıe adiabatic interface from 693° to 538°F (640° to 553°K). The rate
: gas flow through the auxiliary gap for this case was made equal to
ıe leakage rate which was anticipated for the seals between the bear-
ıg compartment and the rotor cavity. Subsequent seal analysis (see
ɜction 6.6) indicated a leakage rate approximately 1.3 times the flow

TABLE 48

LISTING OF THERMAL MAPS

Design No.	Coolant Supply Temperature °F (°K)	Cavity Pressure psia (nt/cm^2)	Coolant in End Bell	Flow Through Aux. Gap	Full Flow Through End Extensions	Heat Flow In or Out of Rotor	Figure No. Thermal Map	Maximum Hot Spot Temperature °F (°K)	Maximum Pole Face Temperature °F (°K)	Maximum Winding Temperature °F (°K)	Bearing Stub Shaft Interface Temperature °F (°K)
1	466 (514)	70 (48.3)	Yes	Yes	Yes	No	116	631 (606)	631 (606)	593 (585)	538 (553)
2	466 (514)	70 (48.3)	No	Yes	Yes	No	117	636 (608)	636 (608)	593 (585)	561 (567)
3	466 (514)	70 (48.3)	No	Yes	No	No	118	636 (608)	636 (608)	610 (593)	561 (567)
4	466 (514)	70 (48.3)	Yes	No	Yes	No	119	645 (613)	645 (613)	593 (585)	623 (602)
5	466 (514)	70 (48.3)	No	No	Yes	No	120	712 (650)	658 (621)	593 (585)	693 (640)
6	325 (436)	70 (48.3)	Yes	Yes	Yes	No	121	517 (542)	517 (540)	450 (525)	463 (513)
7	325 (436)	70 (48.3)	Yes	Yes	Yes	Out	122	492 (529)	492 (529)	451 (507)	345 (448)
8	325 (436)	70 (48.3)	Yes	Yes	Yes	In	123	551 (561)	551 (561)	451 (507)	628 (603)
9	325 (436)	86 (59.3)	Yes	Yes	Yes	No	124	502 (535)	502 (535)	445 (503)	452 (506)
10	107 (315)	70 (48.3)	Yes	No	Yes	No	125	264 (402)	264 (402)	208 (371)	247 (383)
11	107 (315)	86 (59.3)	Yes	No	Yes	No	126	260 (400)	260 (400)	208 (371)	251 (396)



466°F (514°K) COOLANT
70 PSIA (483 kN/m² abs) CAVITY PRESSURE

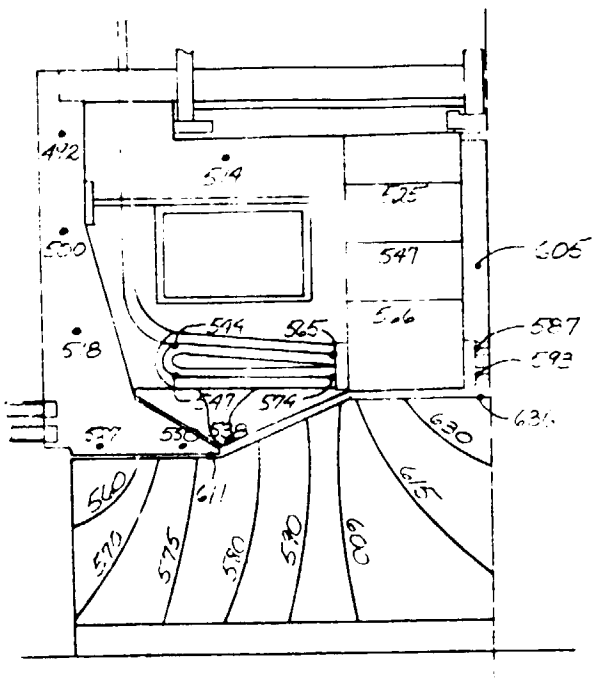
Special Conditions:
Gas Flow in Auxiliary Gap

Avg. Pole Face Temperature: 621°F (601°K)
Avg. Winding Temperature: 567°F (570°K)

Windage	Avg. Gas Temp., °F	Windage Loss Watts (HeXe)
Main Air Gap	583 (579°K)	3,750
Cone Gap	547 (558°K)	2,380
Aux. Air Gap	505 (537°K)	2,290
Total Windage		8,420

Gas Circulation Rate: 1410 lbm/hr per side (0.178 kg/sec)
Aux. Gap Gas Flow Rate: 191 lbm/hr per side (0.024 kg/sec)
Aux. Gap Gas Flow Inlet Temperature: 400°F (478°K)

FIGURE 116



466°F (514°K) COOLANT
70 PSIA (483 kN/m² abs) CAVITY PRESSURE

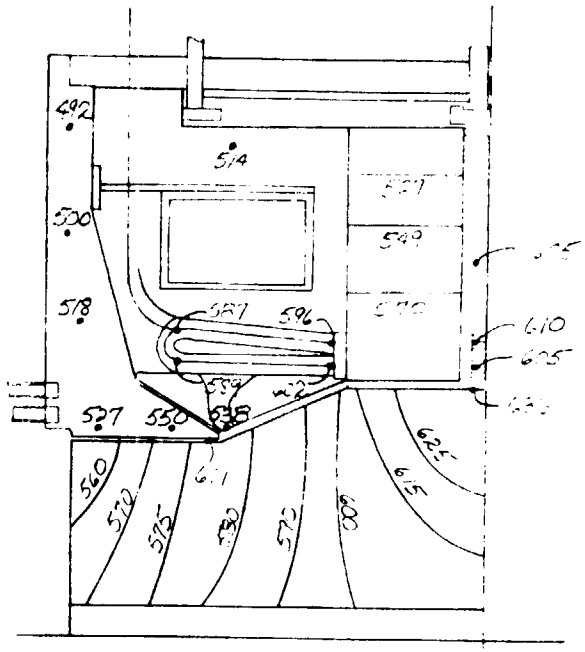
Special Conditions:
Gas Flow in Auxiliary Gap
End Bell without Coolant

Avg. Pole Face Temperature: 626°F (603°K)
Avg. Winding Temperature: 567°F (570°K)

Windage	Avg. Gas Temp., °F	Windage Loss Watts (HeXe)
Main Air Gap	583 (560°K)	3,750
Cone Gap	547 (558°K)	2,380
Aux. Air Gap	540 (555°K)	2,240
Total Windage		8,370

Gas Circulation Rate: 1410 lbm/hr per side (0.175 kg/sec)
Aux. Gap Gas Flow Rate: 191 lbm/hr per side (0.024 kg/sec)
Aux. Gap Gas Flow Inlet Temperature: 400°F (478°K)

FIGURE 117



466°F (514°K) COOLANT
70 PSIA (483 kN/m² abs) CAVITY PRESSURE

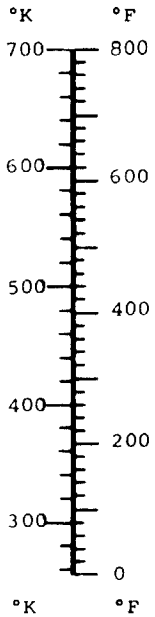
Special Conditions:
Gas Flow in Auxiliary Gap
End Bell without Coolant
Partial Gas Flow over End Extensions

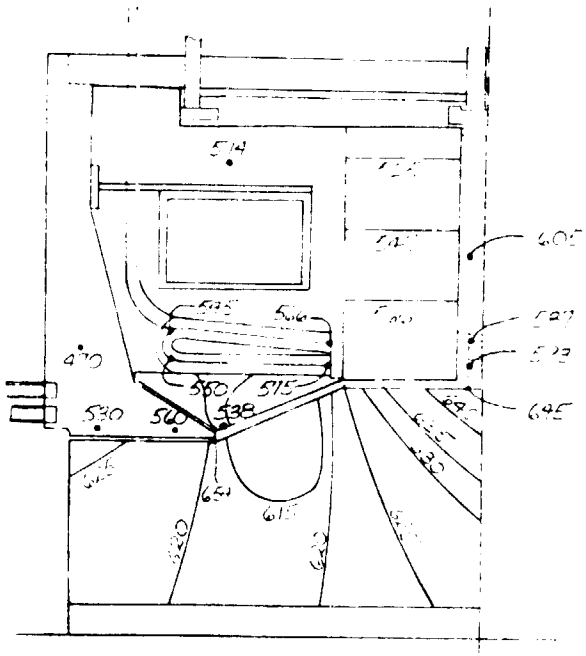
Avg. Pole Face Temperature: 626°F (603°K)
Avg. Winding Temperature: 587°F (582°K)

Windage	Avg. Gas Temp., °F	Windage Loss Watts (HeXe)
Main Air Gap	583 (580°K)	3,750
Cone Gap	547 (588°K)	2,380
Aux. Air Gap	540 (555°K)	2,240
Total Windage		8,370

Gas Circulation Rate: 1410 lbm/hr per side (0.178 kg/sec)
Aux. Gap Gas Flow Rate: 191 lbm/hr per side (0.024 kg/sec)
Aux. Gap Gas Flow Inlet Temperature: 400°F (478°K)

FIGURE 118





466°F (514°K) COOLANT
70 PSIA (483 kN/m² abs) CAVITY PRESSURE

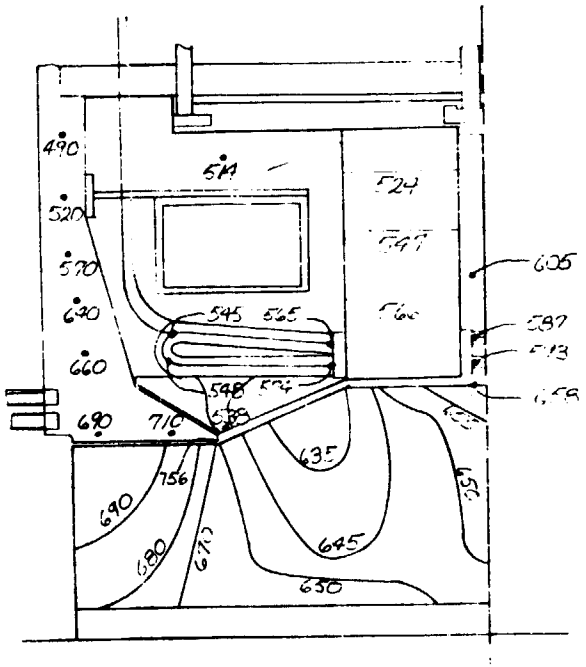
Special Conditions: None

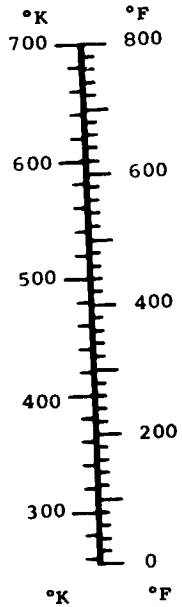
Avg. Pole Face Temperature: 636°F (608°K)
Avg. Winding Temperature: 568°F (571°K)

Windage	Avg. Gas Temp., °F	Windage Loss Watts (HeXe)
Main Air Gap	583 (580°K)	3,750
Cone Gap	547 (558°K)	2,380
Aux. Air Gap	643 (613°K)	2,120
Total Windage		8,250

Gas Circulation Rate: 1410 lbm/hr per side (0.178 kg/sec)
Aux. Gap Gas Flow Rate:
Aux. Gap Gas Flow Inlet Temperature

FIGURE 119





466°F (514°K) COOLANT
70 PSIA (483 kN/m^2 abs) CAVITY PRESSURE

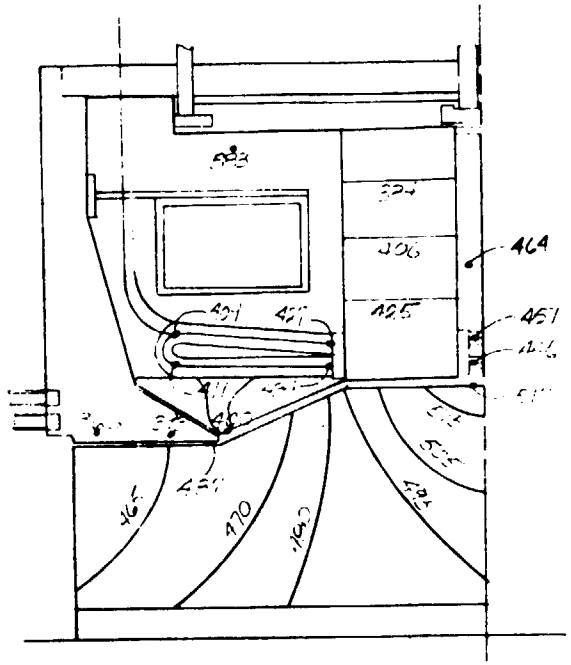
Special Conditions: End Bell without Coolant

Avg. Pole Face Temperature: 652°F (637°K)
Avg. Winding Temperature: 568°F (570°K)

Windage	Avg. Gas Temp., °F	Windage Loss Watts (HeXe)
Main Air Gap	583 (580°K)	3,750
Cone Gap	548 (559°K)	2,380
Aux. Air Gap	758 (676°K)	2,000
Total Windage		8,130

Gas Circulation Rate: 1410 lbm/hr per side (0.178 kg/sec)
Aux. Gap Gas Flow Rate
Aux. Gap Gas Flow Inlet Temperature

FIGURE 120



325°F (436°K) COOLANT
70 PSIA (483 kN/m^2 abs) CAVITY PRESSURE

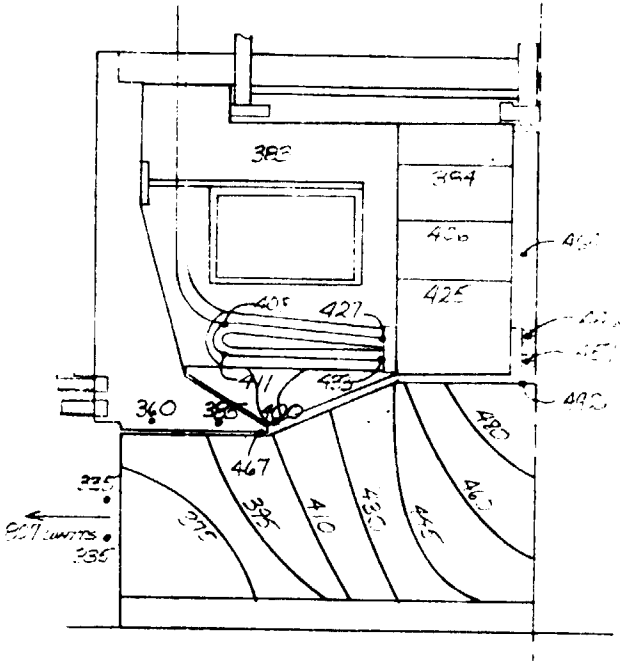
Special Conditions: Gas Flow in Auxiliary Gap

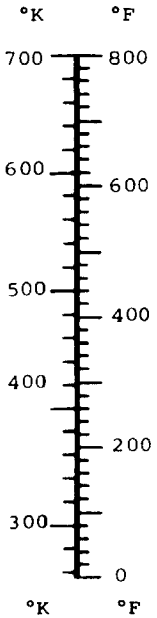
Avg. Pole Face Temperature: 509°F (538°K)
Avg. Winding Temperature: 429°F (484°K)

Windage	Avg. Gas Temp., °F	Windage Loss Watts (HeXe)
Main Air Gap	444 (502°K)	4,030
Cone Gap	408 (478°K)	2,580
Aux. Air Gap	458 (510°K)	2,360
Total Windage		8,970

Gas Circulation Rate: 1610 lbm/hr per side (0.203 kg/sec)
Aux. Gap Gas Flow Rate: 191 lbm/hr per side (0.024 kg/sec)
Aux. Gap Gas Flow Inlet Temperature: 400°F (478°K)

FIGURE 121





325°F (436°K) COOLANT
70 PSIA (483 kN/m^2 abs) CAVITY PRESSURE

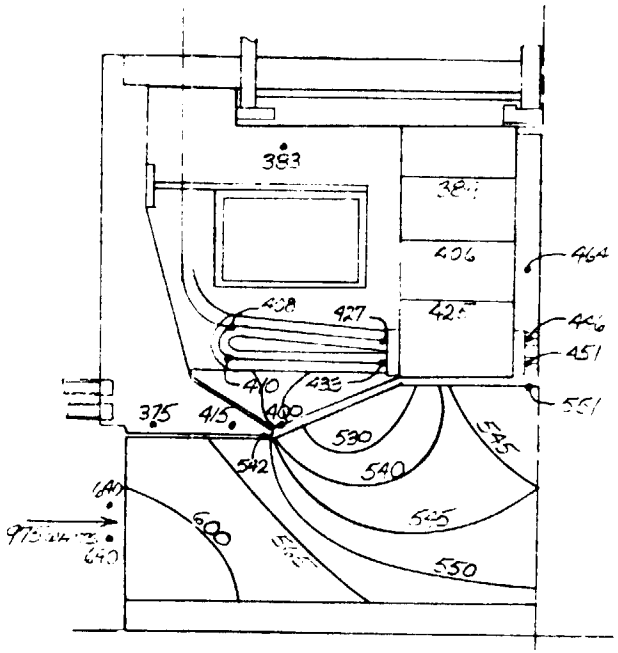
Special Conditions:
- Gas Flow in Auxiliary Gap
- Heat Flow out of Rotor
- Copper Heat Shunt in Rotor

Avg. Pole Face Temperature: 480°F (522°K)
Avg. Winding Temperature: 430°F (494°K)

Windage	Avg. Gas Temp., °F	Windage Loss Watts (HeXe)
Main Air Gap	443 (502°K)	4,030
Cone Gap	407 (474°K)	2,580
Aux. Air Gap	443 (502°K)	2,380
Total Windage		8,990

Gas Circulation Rate: 1610 lbm/hr per side (0.203 kg/sec)
Aux. Gap Gas Flow Rate: 191 lbm/hr per side (0.024 kg/sec)
Aux. Gap Gas Flow Inlet Temperature: 400°F (478°K)

FIGURE 122



325°F (436°K) COOLANT
70 PSIA (483 kN/m^2 abs) CAVITY PRESSURE

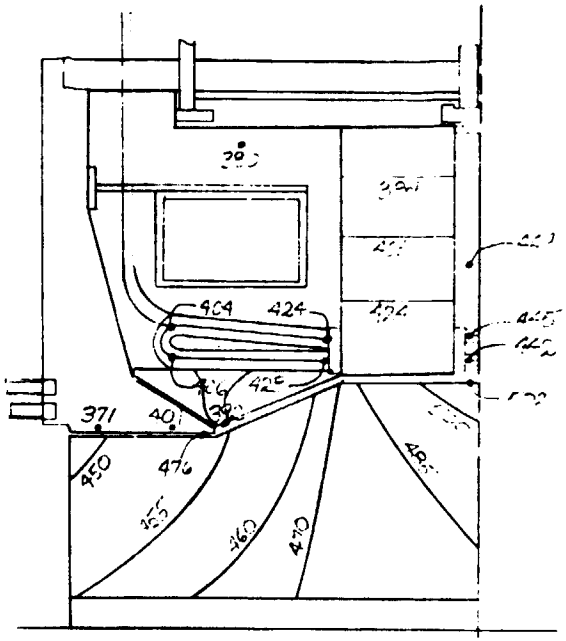
Special Conditions:
- Gas Flow in Auxiliary Gap
- Heat Flow into Rotor
- Copper Heat Shunt in Rotor

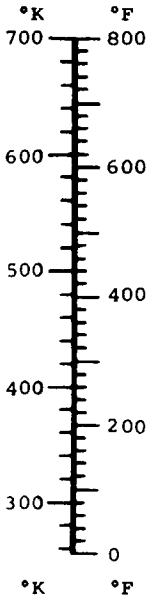
Avg. Pole Face Temperature: 546°F (558°K)
Avg. Winding Temperature: 435°F (497°K)

Windage	Avg. Gas Temp., °F	Windage Loss Watts (HeXe)
Main Air Gap	445 (503°K)	4,030
Cone Gap	409 (483°K)	2,580
Aux. Air Gap	495 (530°K)	2,300
Total Windage		8,910

Gas Circulation Rate: 1,610 lbm/hr per side (0.203 kg/sec)
Aux. Gap Gas Flow Rate: 191 lbm/hr per side (0.024 kg/sec)
Aux. Gap Gas Inlet Temperature: 400°F (478°K)

FIGURE 123





325°F (436°K) COOLANT
86 PSIA (593 kN/m^2 abs) CAVITY PRESSURE

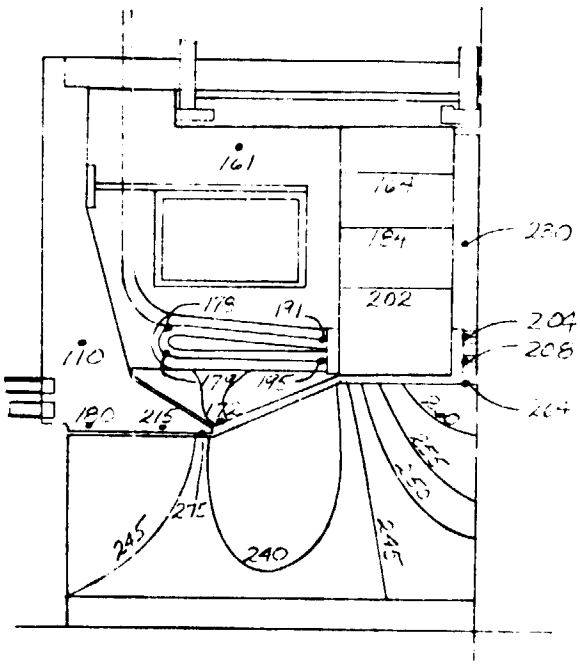
Special Conditions:
Gas Flow in Auxiliary Gap

Avg. Pole Face Temperature: 495°F (530°K)
Avg. Winding Temperature: 424°F (491°K)

Windage	Avg. Gas Temp., °F	Windage Loss Watts (HeXe)
Main Air Gap	436 (484°K)	4,580
Cone Gap	399 (477°K)	2,940
Aux. Air Gap	451 (507°K)	2,760
Total Windage		10,280

Gas Circulation Rate: 1990 lbm/hr per side (0.251 kg/sec)
Aux. Gap Gas Flow Rate; 236 lbm/hr per side (0.030 kg/sec)
Aux. Gap Gas Flow Inlet Temperature: 400°F (478°K)

FIGURE 124



107°F (315°K) COOLANT
70 PSIA (483 kN/m^{2}abs) CAVITY PRESSURE

Special Conditions: None

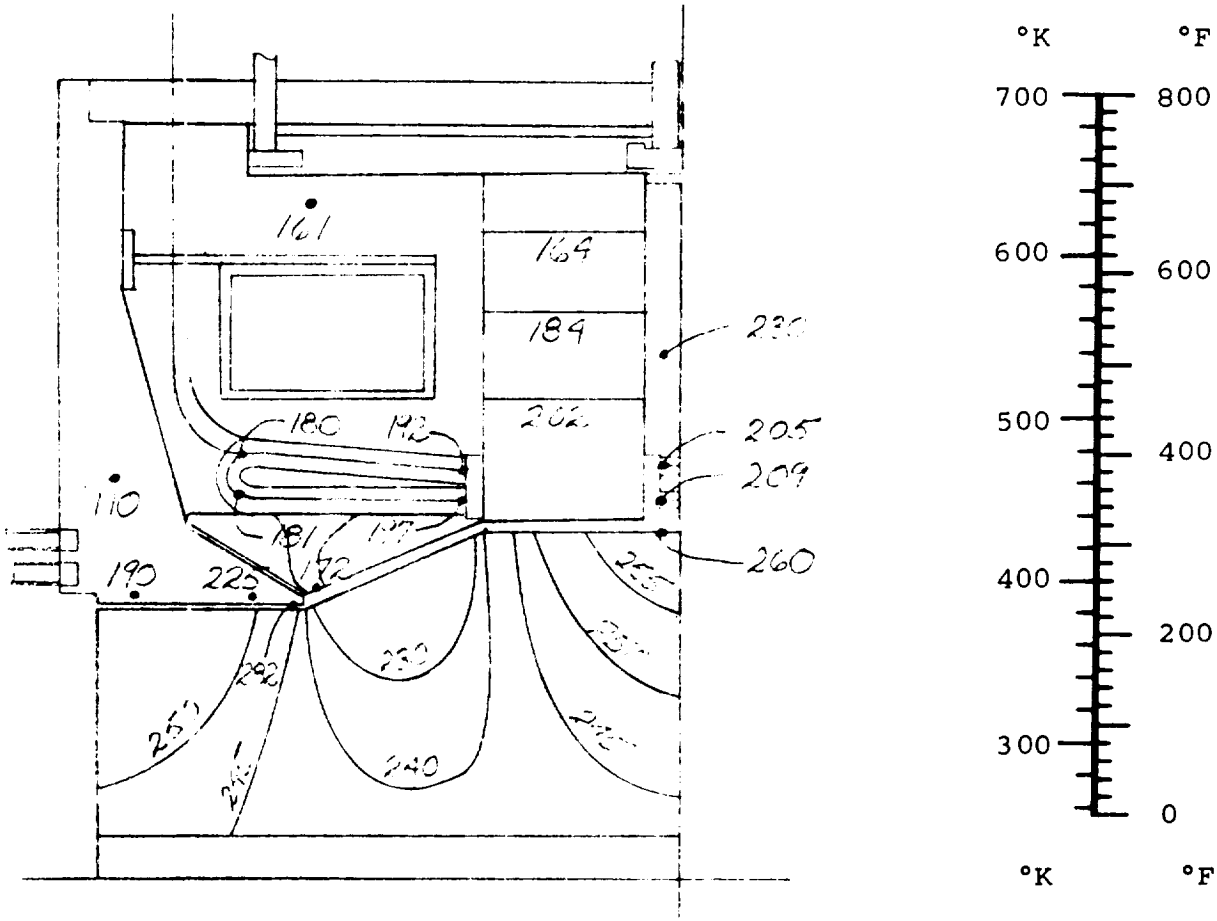
Avg. Pole Face Temperature: 257°F (398°K)
Avg. Winding Temperature: 192°F (363°K)

Windage	Avg. Gas Temp., °F	Windage Loss Watts (HeXe)
Main Air Gap	218 (377°K)	4,550
Cone Gap	185 (358°K)	2,940
Aux. Air Gap	261 (401°K)	2,710
Total Windage		10,200

Gas Circulation Rate: 2200 lbm/hr per side (0.277 kg/sec)
Aux. Gap Gas Flow Rate

Aux. Gap Gas Flow Inlet Temperature

FIGURE 125



107°F (315°K) COOLANT
86 PSIA (593 kN/m^2 abs) CAVITY PRESSURE

Special Conditions: None

Avg. Pole Face Temperature, 253°F (397°K)

Avg. Winding Temperature, 194°F (363°K)

Windage	Avg. Gas Temp. °F	Windage Loss watts (HeXe)
Main Air Gap	219 (377°K)	5,140
Cone Gap	186 (359°K)	3,310
Aux. Air Gap	268 (409°K)	3,100
Total Windage		11,550

Gas Circulation Rate: 2710 lbm/hr per side (0.341 kg/sec)

Aux. Gap Gas Flow Rate

Aux. Gap Gas Flow Inlet Temperature

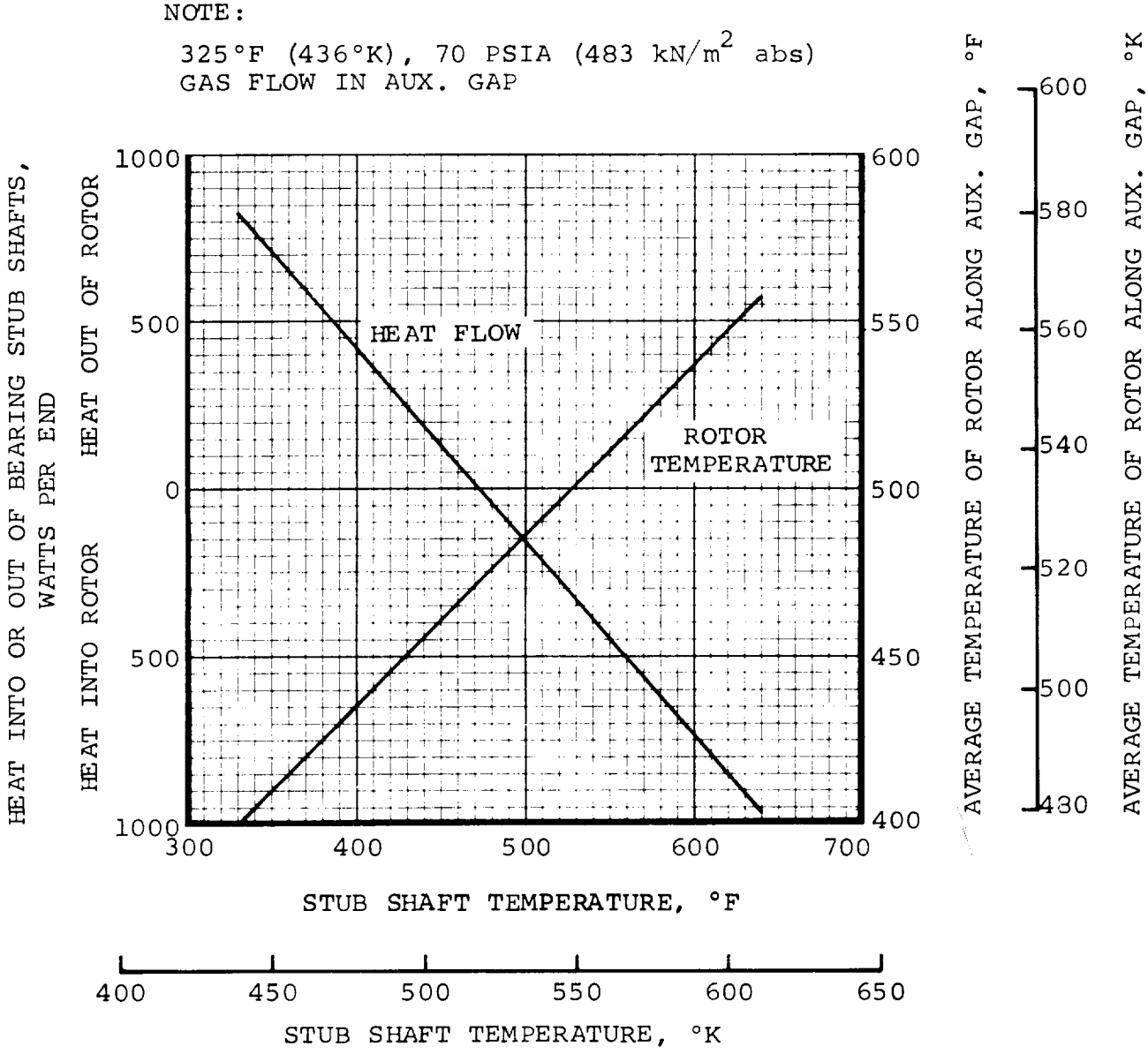
FIGURE 126

rate initially assumed. In general, it appears that either the addition of coolant in the end bell, the addition of forced circulation through the auxiliary gap, or a combination of both can be used to obtain desired interface temperatures between the rotor and stub shaft.

Design No. 3 of Table 48 is a slight variation of Design No. 2. For this design, the forced convection mode of heat-transfer from the end extensions to the gas was reduced by decreasing the heat-transfer coefficient by a factor of four. The maximum temperature of the windings increased from 593° to 610°F (585° to 593°K). This means the flow pattern over the conductors will not be critical to the thermal state of the windings. Furthermore, the likelihood of damage to the ANADUR insulation on the conductors when subject to a high velocity gas stream precludes the use of a cooling scheme which requires a high convection mode of heat-transfer from the end extensions.

Design No. 6 through 9 of Table 48 are cases investigated for a coolant supply temperature of 325°F (436°K). Heat flow in and out of the stub shaft interface was considered for Designs No. 7 and No. 8. For these cases, a copper heat shunt was added to the end of rotor and under the stub shaft extension in order to conduct heat from the bearing with a small temperature gradient. The copper heat shunt shoulders against the rotor end and extends downward to the bore to provide necessary additional interface surface contact area. Figure 127 gives the heat flow rate as a function of the stub shaft interface temperature which can be used for thermal integration of the turbine, compressor, and bearing components with the rotor.

A comparison of Design No. 9 with Design No. 6 and a comparison of Design No. 10 with Design No. 11 shows the influence of cavity pressure upon the temperatures. In general, increasing the cavity pressure from 70 to 86 psia (483 to 593 kN/m^2 abs) did not have a significant effect upon the thermal state of the alternator. Windage losses increased;



STUB SHAFT THERMAL INTEGRATION

FIGURE 127

the gas flow rate and the forced convection mode of heat-transfer increased also. However, the net change in the thermal maps was slight.

With the low temperature windings and coolant supply temperature, there appears to be a significant temperature difference between the rotor and bearing system based upon an adiabatic interface with coolant in the end bells. A cooling scheme without coolant in the end bell would probably offer an advantage over Design No. 9 and 10 since the adiabatic interface temperature of the rotor would approach that of the possibly hotter stub shaft.

In summary, the thermal analysis of the 2-pole alternator at rated load for 70 and 86 psia (483 and 593 kN/m^2 abs) and for coolant supply temperatures of 107,325 and 466°F (315, 436 and 514°K) indicate the gas recirculation cooling scheme is both feasible and practical. A considerable portion of the internal losses within the generator are transported by the gas to the heat sink within the frame. Typical values for the heat transport mode are:

Cavity pressure, psia (kN/m^2 abs)	70 (483)	86 (593)
ΔT of gas, °F (°K)	90 (50)	70 (39)
Gas flow rate, lb/hr (kg/hr)	2800 (0.353)	4000 (0.505)
Specific heat of gas, Btu/lb °F (Cal/gm °C)	0.1243	0.1243
Heat transport, kw	9.2	10.2

The temperature of the interface between the rotor and stub shaft can be varied to be compatible with the thermal state of the bearing by alterations of the cooling scheme with the auxiliary gaps and within the end bells.

6.3.4 Mechanical Design Considerations

6.3.4.1 Rotor Stress and Bonding

The maximum stress intensity (92,000 psi, 638,000 kN/m^2) will occur around the central hole in the 8.0 in. (20.4 cm) cylinder at 20 percent overspeed. Tensile properties of the rotor materials are:

Material	Hardness	Temperature	0.2% Yield Strength	Tensile Strength
SAE 4340	RC32	700°F (643°K)	110,000 psi (760,000 kN/m^2)	130,000 psi (897,000 kN/m^2)
Inconel 718	RC38	700°F (643°K)	125,000 psi (863,000 kN/m^2)	150,000 psi (1,034,000 kN/m^2)

A comparison of the maximum stress and the stress at design speed (24,000 rpm) with the tensile properties of the materials given:

$$\frac{\text{Stress @ 24,000 rpm}}{\text{Y.S. of SAE 4340}} = \frac{64,200}{110,000} = 59.4\%$$

$$\frac{\text{Overspeed stress}}{\text{T.S. of SAE 4340}} = \frac{92,500}{130,000} = 71.1\%$$

% creep strain at bore in 5 years $<$ 0.01%

Three methods of rotor bonding are available; brazing, casting the 718 in place and diffusion welding which is the preferred approach.

The rotor design was reviewed to determine if design requirements could be satisfied in an Inconel 718-4340 Lundell rotor fabricated by hot isostatic pressure welding (high temperature gas pressure diffusion bonding). Analysis shows that this technique will be suitable for the application with minimum development. Feasibility of this approach is currently being demonstrated at the Westinghouse Astronuclear Laboratory under Contract NAS 3-11837, "Development of a Gas Pressure Bonded Four-Pole Alternator Rotor." Current results in this program have indicated joint strengths of 55,000 psi (379,000 kN/m^2) are readily achieved using nonoptimized welding schedules. Actual joint strengths of 136,000 psi bending (937,000 kN/m^2) have been achieved. Welding schedules for the 92,500 psi (638,000 kN/m^2) joint strength at 700°F (644°K) required for 20 percent overspeed appear entirely realistic.

Similarly, 92,500 psi (638,000 kN/m^2) yield strength at 700°F (644°K) is achievable in both base metals since the metallurgical heat treatment and welding thermal cycles are compatible. Strength will be achieved in the 718 by selecting welding temperatures and times compatible with solution annealing and/or aging temperatures. The 4340 strength will then be developed, as the assembly cools in the autoclave, through transformation of the austenitic structure to a mixture of martensite, ferrite and bainite. With controlled autoclave cooling, this structure has given a hardness of R_c30. Slightly higher cooling rates can provide higher hardness.

In addition, this process for fabrication of the rotor can be utilized to attach pole inserts of improved magnetic properties to reduce pole face losses. Typically, these would be a mild steel such as AlSl, 1010. Rotor fabrication would still be accomplished in one operation by welding the 718, 4340, and 1010 in one autoclave run.

Satisfactory joints between 718 and 4340 have been obtained by holding for four hours at 1650°F (1172°K) and 30,000 psi (206,500 kN/m^2) These joints, in fact, appear to be overdeveloped and it is anticipated that shorter times at temperature or lower temperatures will give higher strength joints.

The ideal bonding temperature from the standpoint of metallurgical structure will be in the range of 1325° to 1400°F (992° to 1033°K) since this is the first aging temperature of 718 and will be above the Ae3 temperature of 4340. If this temperature range proves suitable for rotor fabrication by hot isostatic pressure welding, then the 718 can be aged to the required strength during rotor welding. Similarly, this temperature will austenitize the 4340 permitting transformation on cooling to achieve the desired strength level. Interestingly, the deep hardening characteristics of 4340 are sufficient to achieve R_C30 at a controlled furnace cooling rate of 240°F/hr (133°K/hr). Since this rate can be increased, even higher strengths may be realized. In this process 718 would not have to be double aged. The second aging treatment at 1200°F (922°K) would result in a higher strength of 718 than desired while causing simultaneous transformation of the 4340 to an undesirable low strength spherodized carbide structure.

The hot isostatic pressure welding process provides increased flexibility if alternate approaches are required to develop adequate joint strength simultaneous with the required base metal structure. As an example, joining could be accomplished by holding for a short time at 1750°F (1228°K). This provides solution annealing of the 718. The 718 can then be strengthened by aging at 1350°F (1005°K) while strengthening of the 4340 is again achieved upon cooling to room temperature at a controlled rate. In this approach, however, the aging reaction in 718 will be less effective as a result of slow cooling from the solution annealing temperature [400°F/min (222°K/min) is usually specified]. This problem is typical of large section sizes in 718 and would require special definition should a higher bonding temperature be required.

The ability of a fabricated rotor to withstand the thermal strains associated with the austenite transformation is not entirely resolved at this time. Current results appear encouraging in this respect and a full clarification will be available with the conclusions of Contract NAS 3-11837. The primary concern is that the joint strength must be sufficient to permit accommodation of the expansion of 4340 due to austenite transformation during cooldown of the rotor assembly. A net strain across the interface as high as 1.4 percent may have to be accommodated. Accommodation will occur by straining of the 4340 since it is the weaker of the two alloys. It should be emphasized that this problem is common to all the alternate rotor fabrication techniques, all of which require heating above the Ae3 temperature during rotor fabrication.

As cooldown from the rotor joining temperature progresses, straining will increase as the austenite transformation proceeds. At the higher temperatures, above 900°F (755°K), the transformation strain will be accommodated at relatively low stress by creep of the 4340. At this point, the 4340 is weakest both because of high temperature and because the transformation product contributes little strength. As the temperature decreases further, and transformation continues, the 4340 strength will eventually increase to such an extent that thermal stresses of the order of the yield strength are required for accommodation of the thermal strain (by plastic deformation). Typically, locked in residual stresses will be near the final yield strength of the 4340. These stresses will probably be highest precisely at the joint interface. Further, straining can be considerably magnified in the vicinity of joint defects.

Although this problem is not fully defined at this time, hot isostatic pressure welding has two distinct advantages individually or in combination over other assembly processes. These are: first, the strain is more readily accommodated by high temperature transformation

achieved by cooling at a minimum rate consistent with final strength requirements, and; second, compressive loading can be maintained durin cooling in an autoclave. In the practice of metal forming compressive loading is frequently beneficial in minimizing failures during deforma tion.

As described above two primary objectives must be satisfied by the rotor fabrication process:

(a) A metallurgical structure of satisfactory strength must be developed in both alloys

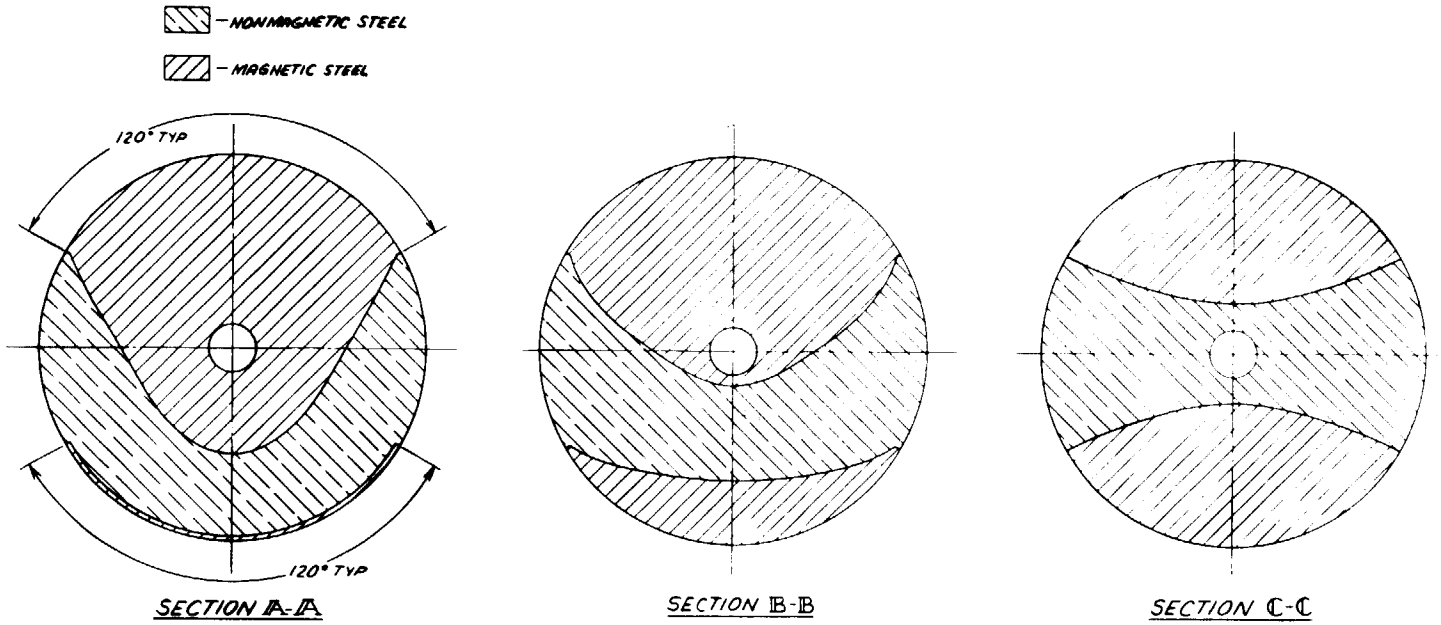
(b) Stresses associated with the austenite transormation strain must be carried by the bi-metal joint to permit accommodatior of the strain by plastic deformation, primarily in the 4340 steel.

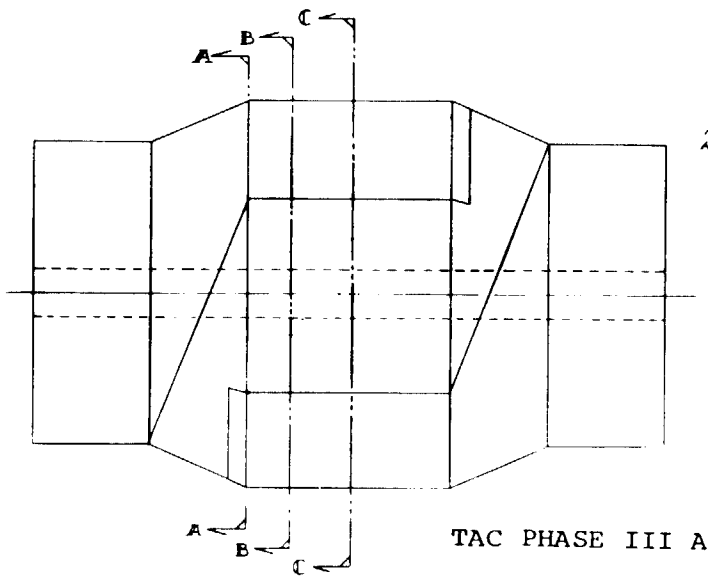
3.4.2 Mass Unbalance

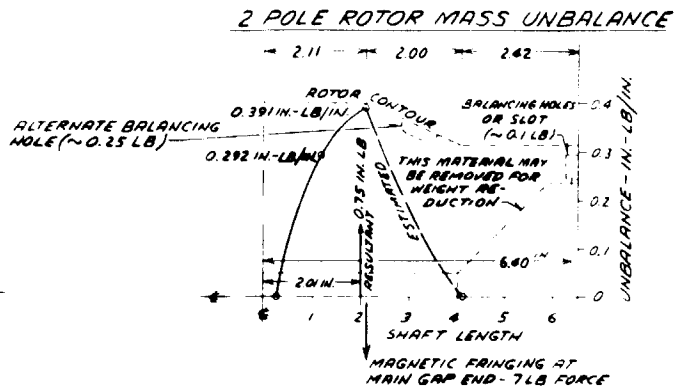
The rotor detail, including significant cross-sections to illus-
ate the nonsymmetric distribution of magnetic and nonmagnetic steels,
d a plot of the mass unbalance are shown in Figure 128. The density
the nonmagnetic steel (Inconel 718) is 5 percent greater than the
nsity of the magnetic steel (AISI 4340). This density difference
sults in the center of mass of sections between the small end of the
nical section and the (axial) center of the shaft being shifted
ward the predominantly nonmagnetic side of the shaft center line.
cause the pattern shown for the left end of the rotor is reversed on
e right end, a couple will exist. The magnitude of the mass unbal-
ce was calculated for sections AA and BB on Figure 128 and then
lotted, with the points of zero unbalance, to determine the unbalance
r unit axial length. This plot (shown on Figure 128) was integrated
determine a resultant unbalance of 0.75 in.-lb (0.864 kg-cm) with a
ment arm of 2.01 in. (5.11 cm) from the shaft center for each end of
e shaft.

The preferred balancing procedure would remove about 0.25 pounds
0.1134 kg) from the nonmagnetic steel at, or near, the conical sur-
aces. This corresponds to about 0.84 cubic in. (13.8 cubic centi-
eters) of steel.

This mass unbalance can also be balanced by means of holes or
eights at the rotor planes at the outboard ends of the auxiliary gaps.
sing holes, several 0.5 in. (1.27 cm) diameter holes are required at
ach plane. These would be located in line with the center of the non-
agnetic steel at the corresponding end of the rotor, and would remove
bout 0.1 pounds (0.0045 kg) of magnetic iron. To prevent a reduction
f the auxiliary gap magnetic flux path, and a resultant decrease in
lternator capacity, these holes would be located at a diameter of







TAC PHASE III ALTERNATOR ROTOR DETAILS

FIGURE 120

bout 5.875 in. (0.1492 m), with a depth of 0.25 in. (0.064 cm). hese counterbalancing holes would be part of the basic rotor design nd would be drilled prior to final balancing. The same planes would e available for final balancing purposes after manufacture of the otor.

Either of the above balancing procedures, or a combination of hem, may be used for the initial balancing to overcome the severe nbalance of the nonsymmetrical 2-pole rotor. The preferred method ay prove desirable to reduce the difference in the moment arms between he removed material and the unbalanced mass plane.

A potential complication to the task arises when the effects of hermal expansion and creep are considered. Specifically, the nonmag- etic alloy 718 will expand about 0.03 percent more than the magnetic AISI 4340 from room temperature to the average estimated operating emperature with 466°F (514°K) coolant. This effect, plus the effects f creep, may result in warpage of the rotor and a consequent unbalanced oment.

Experimental development will be required to obtain an acceptable alancing technique for the unsymmetric 2-pole rotor, and to determine he short and long term effects of thermal expansion and creep.

The 6-pole rotor, with its symmetrical magnetic and nonmagnetic aterials (each cross section is balanced), is inherently balanced. In ddition, it should not be subject to warping due to differential therm- l expansion or material creep. Thus, little development should be re- uired in this area for the 6-pole alternator.

6.3.4.3 Magnetic Unbalance

A magnetic moment is created by the unequal leakage flux passing from the stack ends to the rotor at each end of a 2-pole Lundell alternator. The magnitude of this force for the TAC alternator was calculated by making flux plots of the leakage flux passing through the conical sections of the rotor at each end to determine the flux density and magnetic force distribution along the conical rotor section. Integration of the force distribution resulted in a radial unbalance force of 58.4 pounds (26.5 kg) acting in opposite directions at each end of the rotor. Since these forces were considered excessive, the tips of the rotor poles were extended a small distance beyond the armature stack to reduce the forces to 7 pounds (3.2 kg) at each end. The extensions increased rotor leakage flux a small amount. While this unbalanced force will oppose the mass unbalance, the force will vary with excitation and therefore cannot be used as a balancing force.

When the auxiliary gap varies circumferentially, as when the shaft is eccentric to the end bell, a nonuniform flux density occurs and an unbalanced magnetic force acts on the shaft. The magnitude of this force can be estimated by the following method.

The radial gap (g), as a function of angular position, is expressed as:

$$g = c - e \cos \theta$$

where

g = radial gap at θ, in.

c = average radial gap, in.

e = radial eccentricity, in.

ϑ = angular position on the shaft, $\vartheta = 0$ at the position where $g = c-e$

The local radial flux density may be expressed as:

$$B = \frac{3.19\ NI}{g} \times 10^{-3} = B_{avg}\ (1 - \frac{e}{c} \cos \vartheta)^{-1}$$

where

B = magnetic flux density, kilolines/in.^{2}

NI = ampere turns across the gap, amperes

B_{avg} = average magnetic flux density, kilolines/in.^{2}

The force acting upon the shaft in the direction of the radial eccentricity is given by:

$$F_e = \frac{LR}{72.13} \int_0^{2\pi} B^2 \cos \vartheta \, d\, \theta$$

where

F_e = force acting on the shaft in the direction of the eccentricity, pounds

R = radius of shaft, in.

L = length of air gap, in.

Evaluation of this definite integral gives the force per unit of eccentricity:

$$\frac{F_e}{e} = \frac{2\pi RL}{72.13c} B_{avg}^2 \left(1-\frac{e^2}{c^2}\right)^{-1.5}$$

The average gap (c) around the shaft is large compared with the radial eccentricity (e) of the shaft. Thus, e^2/c^2 is small compared to unity. Therefore, the spring constant due to magnetic attraction becomes:

$$\frac{F}{e} = \frac{\text{(Area of gap)}}{72.13} \times \frac{B_{avg}^2}{c}$$

The magnetic spring forces in the auxiliary gap at one end of the 2-pole alternator at standstill with full load and overload excitation are:

(a) Overload excitation

$$\frac{F}{e} = \frac{47.5 \text{ in.}^2 \ (68)^2 \text{ kilolines}^2 \text{ in.}^{-4}}{72.13 \ \frac{(\text{kilolines})^2}{\text{Lb}_f/\text{in.}^2} \ 0.05 \text{ in.}}$$

$$\frac{F}{e} = 6.08 \times 10^4 \text{ lb/in. } (10.65 \times 10^4 \text{ N/cm})$$

(b) Full load excitation

$$\frac{F}{e} = \frac{47.5 \times (58)^2}{72.13 \times .05} = 4.43 \times 10^4 \text{ lb/in. } (7.75 \times 10^4 \text{ N/cm})$$

The use of the standstill magnetic spring force, as calculated above, will produce a conservative design of the bearing system.

6.3.5 Alternator Conclusions and Recommendations

Results of the design study revealed no significant circumstances which would preclude recommending the 2-pole, 400 Hz alternator, even the conservative design shown. However, because the 6-pole, 1200 Hz alternator will have better weight, efficiency and performance characteristics, Westinghouse must maintain the recommendation of the 6-pole over the 2-pole.

Other pertinent conclusions associated with the Phase III studies are as follows:

(a) The likelihood of the high temperature Anadur wire insulation eventually entering the gas circuit as an abrasive dust precludes the use of Anadur in the TAC alternator. A recommended high temperature alternative is a bare wire with mica and alumina in the slots and with the end turns either (1) uninsulated and physically supported (separated) or (2) insulated with plasma sprayed alumina. Alternately a Ceramic-Eze insulation could be applied to the bare wire. These will require materials development to reduce laboratory techniques to practical hardware. The other alternative is the organic insulation system which is suitable for the TAC application, assuming the use of low temperature 107°F (315°K) coolant.

(b) It appears it is technically feasible to cope with the unbalances and non-uniform deformations of the 2-pole rotor. However, these introduce problems which are unique to the unsymmetrical 2-pole configuration. The severity of these new problems must be clarified by experiments before one can conclude that the performance of the TAC over its five to potential-ten year life will not be plagued with problems which could have been obviated with a symmetrical 6-pole alternator.

(c) The present design having the 8-inch (20.4 cm) rotor O.D. is conservative. Future designs should result in a slightly smaller diameter, typically 7.5 inches (19.1 cm). This should also reduce the weight to slightly less than twice the 6-pole alternator weight.

(d) The part-load efficiency is noticeably lower than that for the 6-pole alternator (1 to 3 points electromagnetic) and there appears to be little that can be done to further improve it significantly.

(e) Reconnectability from 240 to 480 volts is physically possible. In addition, if corona precludes the use of even 240 volts, it will be possible to obtain a 120 volt design by substituting a different stack and winding into the same frame and rotor configuration. The use of the same rotor is based upon adaptation of a third material into the pole faces as discussed below.

(f) Corona considerations limit the minimum cavity pressure to 14 psia (9.7 kN/m^2) at 240 volts (possibly half that if absolutely required). At 480 volts, the limiting pressure is 53 psia (370 kN/m^2). Substitution of an organic insulation for a 107°F (315°K) coolant system is entirely feasible and would possibly permit the use of output voltages up to 480 volts depending on the quality of the impregnation.

(g) Addition of a third material to the rotor pole faces apparently does not significantly increase the complexity of gas pressure bonding the rotor, and is therefore recommended. Its use also significantly enhances the likelihood of achieving a 7.5 inch (19.1 cm) rotor O.D. and of achieving a single, basic alternator configuration capable of being built with outputs of either 120, 240, or 480 volts.

(h) Several cooling configurations can be designed into the alternator to adequately cool it. Any one of the acceptable configurations can handle the multitude of different pressures, temperatures, gases and boundary conditions anticipated. The latter includes relatively widely divergent rotor stub shaft boundary conditions.

6.4 Rotor Dynamics

A dynamic analysis of the TAC rotor system was conducted to evaluate the affect of magnetic unbalance. The calculated mass, and the estimated bearing stiffness are listed below:

M = 225 lb (102 kg)
K = 150,000 lb/in. (262,500 N/cm)

The magnetic attracting force is assumed to be 50,000 lb/in (87,500 N/cm) of shaft deflection. The calculated critical speeds and bearing loads at rotor operating speed, with and without magnetic affect, are summarized below:

Magnetic Affect	Critical Speed, rpm			Bearing Load at 100% Speed, lb (N)	
	N_1	N_2	N_3	Compressor End	Turbine End
Without	6,740	8,520	36,200	19.2 (85.4)	15.1 (67.2)
With	5,530	8,110	36,100	18.9 (84.1)	15.0 (66.7)

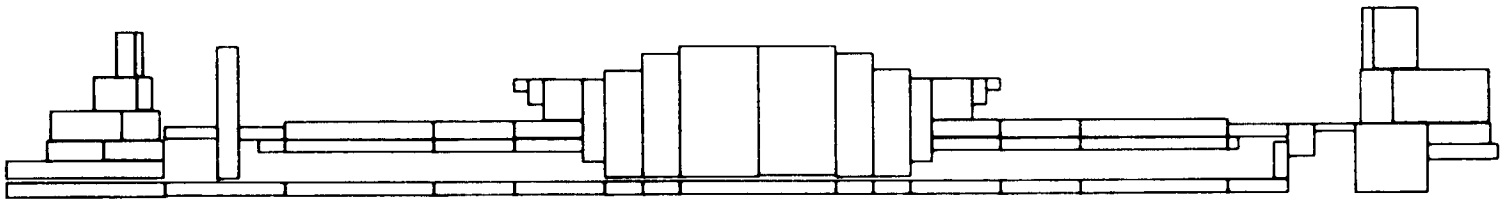
The mathematical mass and stiffness models for the rotor system are presented in Figure 129. The mode shapes at criticals and the calculated bearing loads versus shaft speed without magnetic affect are given in Figures 130 and 131, respectively.

The following conclusions are the result of the present analysis:

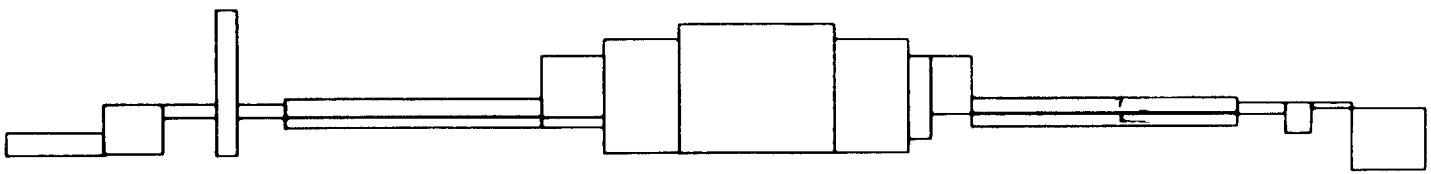
(a) The relation between magnetic force and the air gap is nonlinear. The present assumption of linear force and air gap is satisfactory, since the shaft deflections at these locations are very small.

(b) The magnetic unbalance between the stator and rotor has reduced the first two rigid body criticals; however, it has no effect on the bending criticals.

(c) At engine operating speed, the magnetic effect on the bearing loads is negligible.



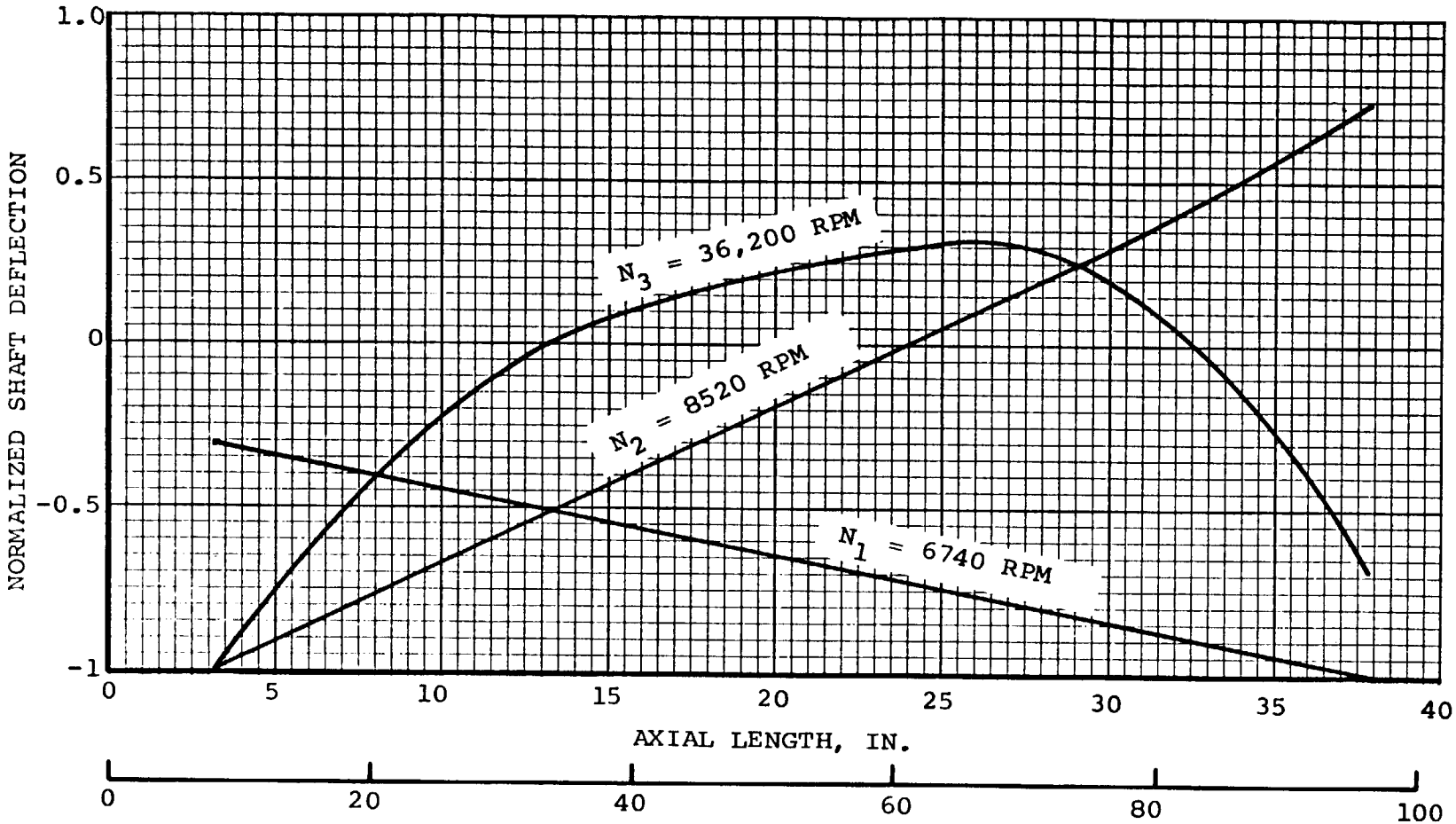
MASS ELEMENTS OF ROTATING GROUP



STIFFNESS ELEMENTS OF ROTATING GROUP

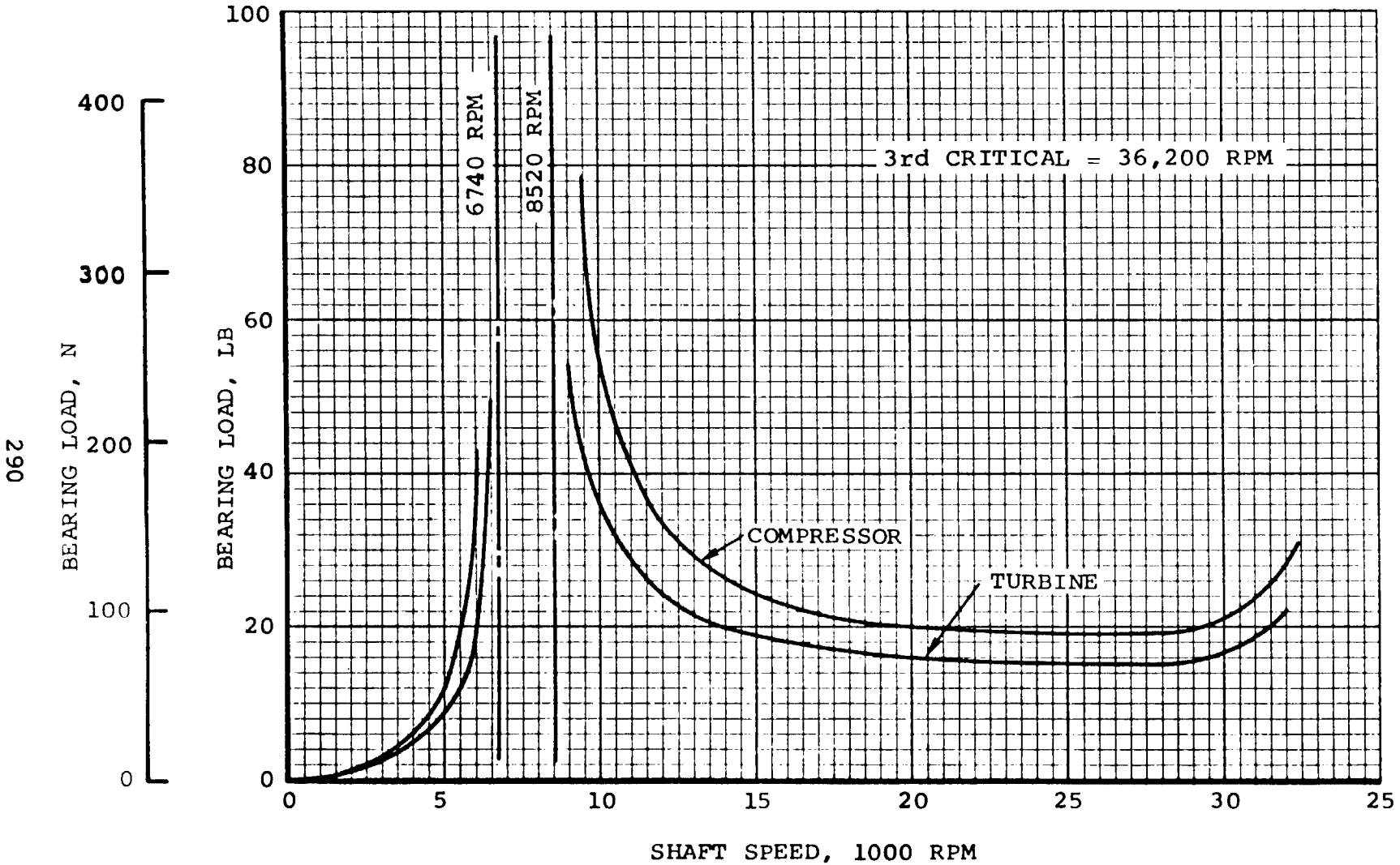
MASS AND STIFFNESS MODEL

FIGURE 129



SHAFT MODE SHAPE AT CRITICAL SPEEDS

FIGURE 130



BEARING LOAD AND CRITICAL SPEED ANALYSIS

FIGURE 131

6.5 Bearing Design

6.5.1 Journal Bearing Design

6.5.1.1 Required Load Capacity

The 400 Hz TAC rotating group mass is 225 lb (102 kg). Design practice dictates that each journal bearing should, as a minimum, support one-half of the rotor mass during horizontal self-acting operation in a 1 g field.

Additional requirements of the Phase III study defined the space maneuvering loads as 1.5 g (to be sustained for a duration of 5 minutes). Thus, the TAC journal bearings must be capable of sustaining a load of 169 lb (752 N) at a reasonable minimum film thickness.

6.6.1.2 Minimum Film Thickness

The ambient bearing cavity pressure was set at 92 percent of the compressor discharge pressure at both the 40 and 160 kw_e power level conditions. The 8 percent pressure loss was assumed to account for line and filtration losses. The resulting cavity pressures are shown below:

Power Output, kw_e	Cavity Pressure psia	Cavity Pressure kN/m^2
40	27.6	190.4
160	122.4	844.5

Preliminary thermal analyses of the TAC indicated that the journal bearings would run at approximately 960°R (533°K) if the alternator coolant temperatures were 785°R (436°K).

The journal bearing minimum lubricant film thickness (h_m) at "worst case" conditions of low cavity pressure and overload was arbitrarily selected to be no less than 0.0003 in. (0.00762 mm).

6.5.1.3 Size and Clearance Ratio Selection

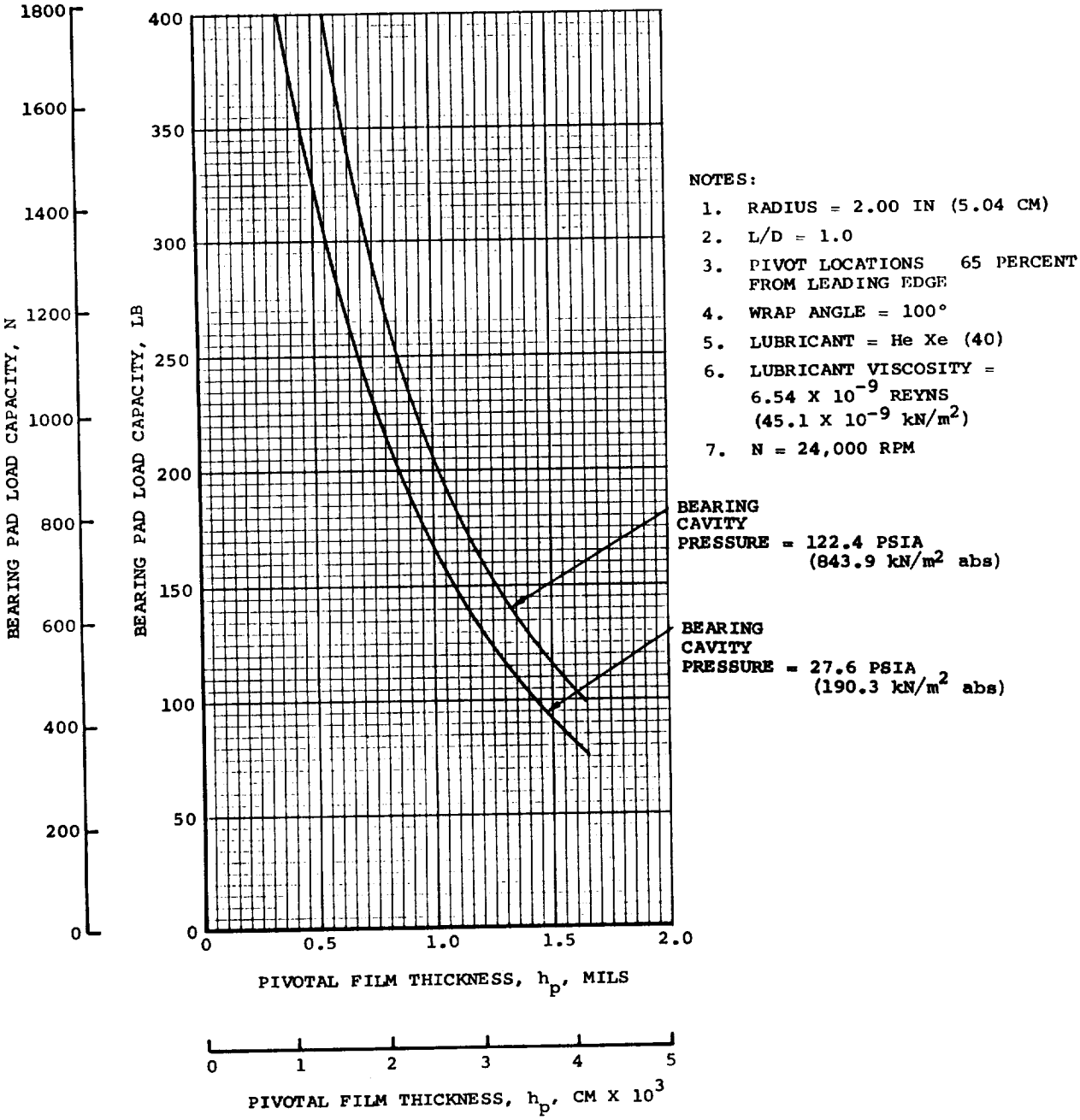
A clearance ratio (C/R) of 0.0018 was initially selected and single pad performance generated for a journal bearing diameter range of 3.5 to 4.1 in. (9.89 to 10.4 cm). The stability data shown in Figure 89 was used as a guide to establish journal pad operating loads. Results of this analysis showed that a 4.0 in. diameter journal bearing (10.16 cm) would adequately fulfill the arbitrary decision to limi h_m to 0.0003 in. (0.00762 mm) under "worst case" conditions.

Single pad performance was then generated for a range of clearanc ratios (0.0012 to 0.0022) with the bearing diameter held constant at 4.0 in. (10.16 cm).

In general, the larger clearance ratios will provide the lowest bearing power loss and the lowest bearing stiffness. A clearance ratio value of 0.0016 was selected for moderate power loss as well as bearing stiffness.

6.5.1.4 Journal Bearing Performance

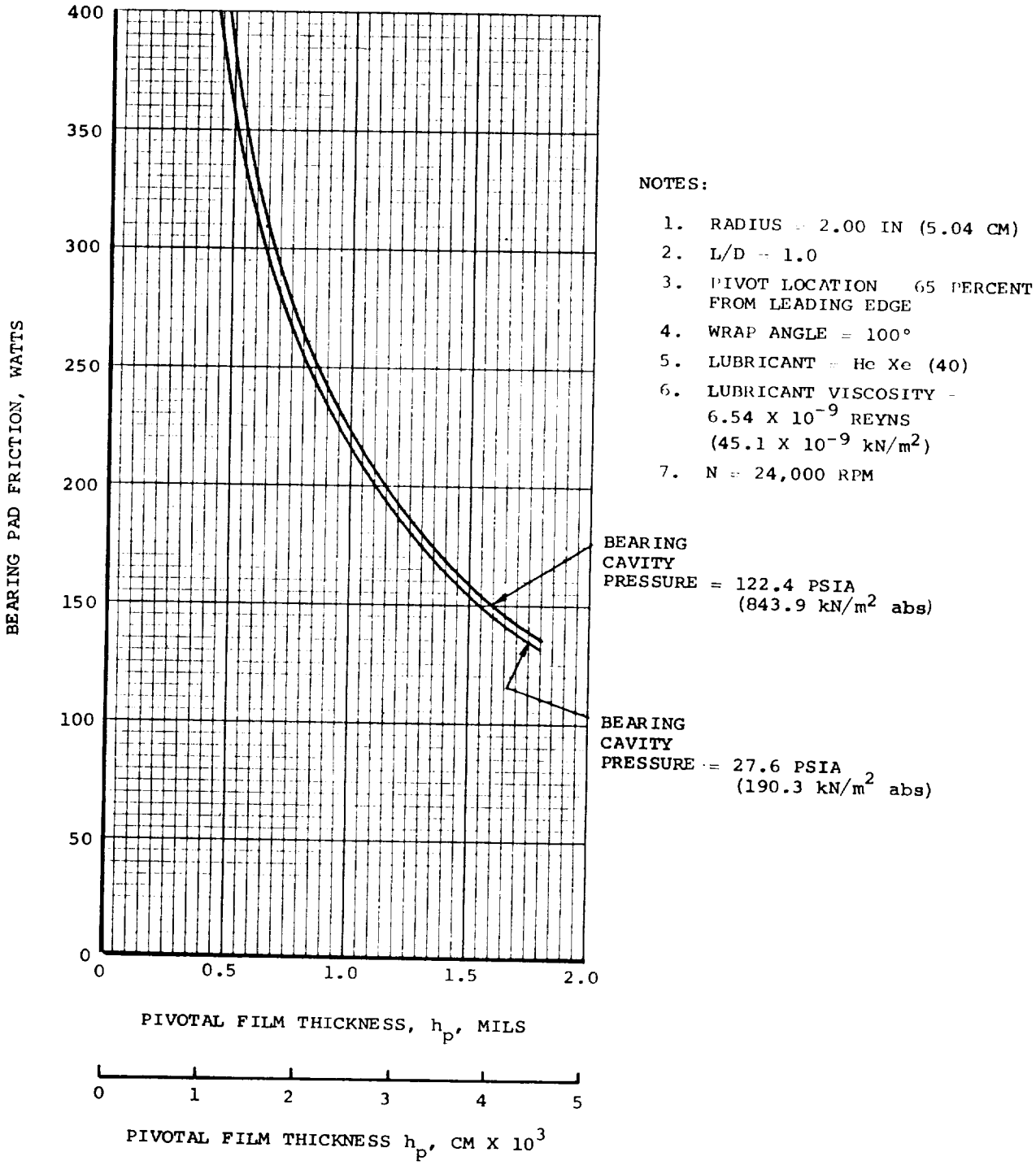
Predicted single pad performance for the selected bearing is shown in Figures 132 and 133. Figures 134 and 135 present complete journal bearing performance for a typical 3-pad journal, in which two pads are solidly mounted and the third pad is resiliently mounted as shown on the following page.



TAC GAS JOURNAL BEARING PAD LOAD CAPACITY

VS PIVOTAL FILM THICKNESS

FIGURE 132

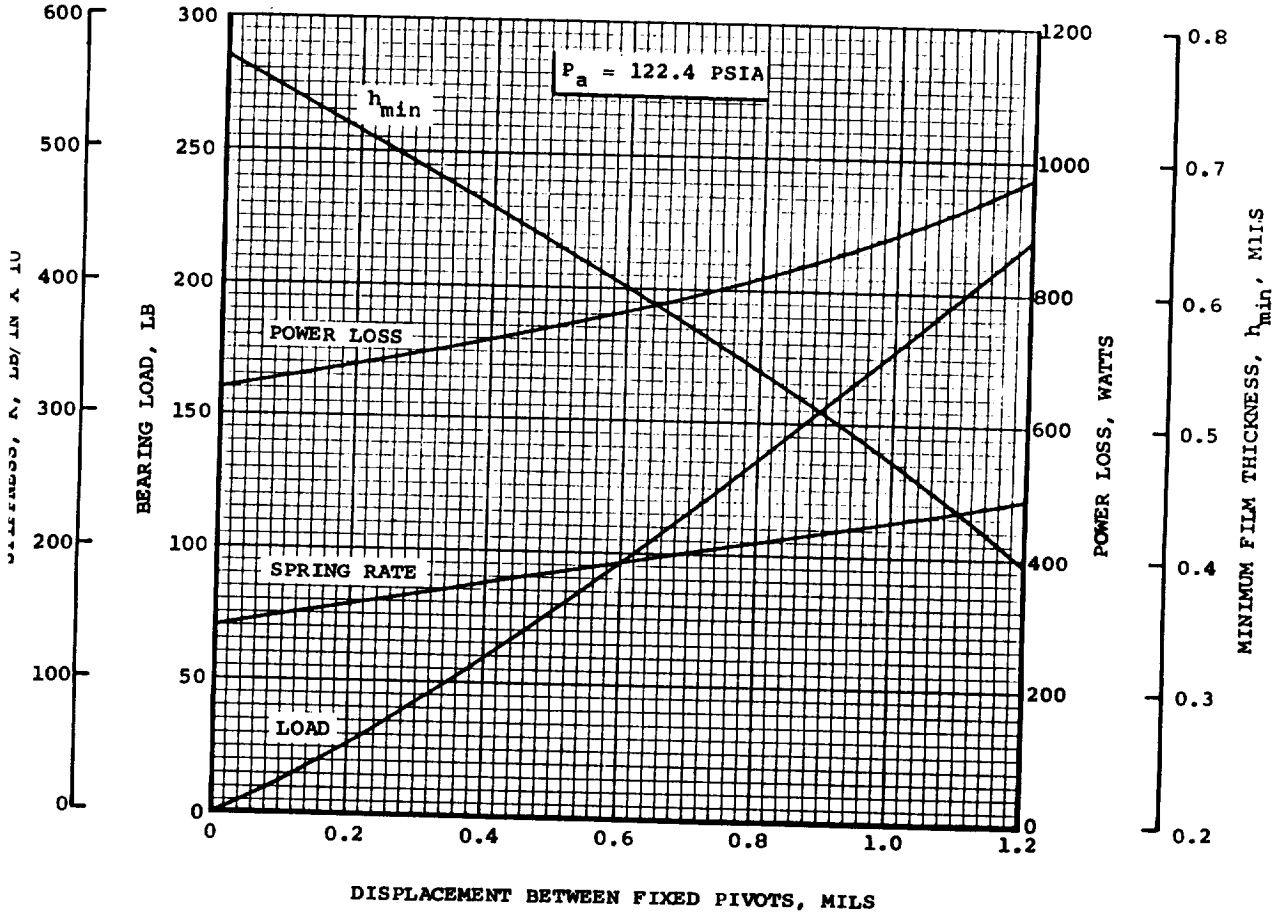


TAC GAS JOURNAL BEARING PAD FRICTION
VS PIVOTAL FILM THICKNESS

FIGURE 133

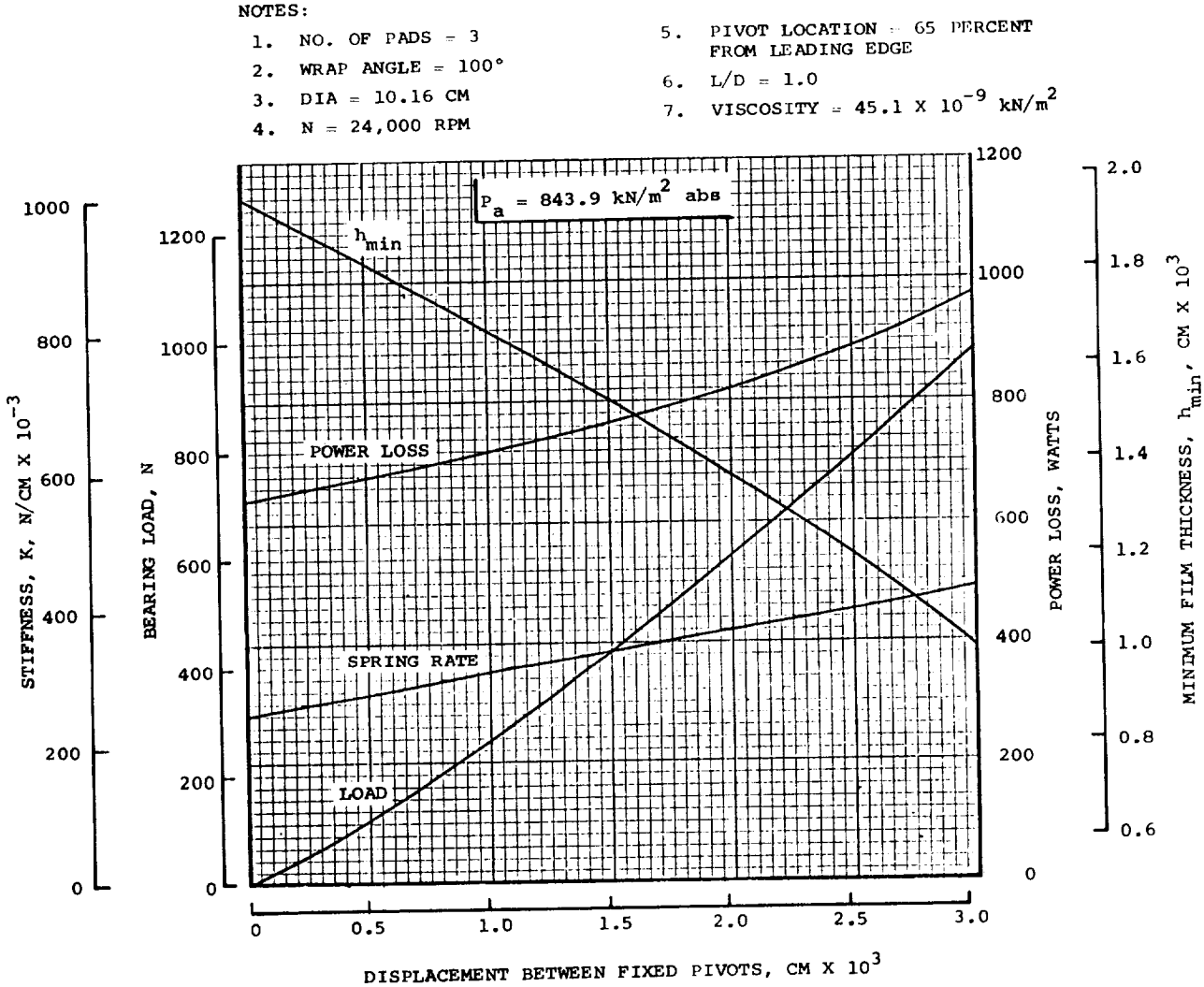
NOTES:

1. NO. OF PADS = 3
2. WRAP ANGLE = 100°
3. DIA = 4.00 IN.
4. N = 24,000 RPM
5. PIVOT LOCATION = 65 PERCENT FROM LEADING EDGE
6. L/D = 1.0
7. VISCOSITY = 6.54 X 10^{-9} REYNS



TILTING PAD GAS JOURNAL BEARING PERFORMANCE
He Xe LUBRICANT (MW = 39.94)

FIGURE 134



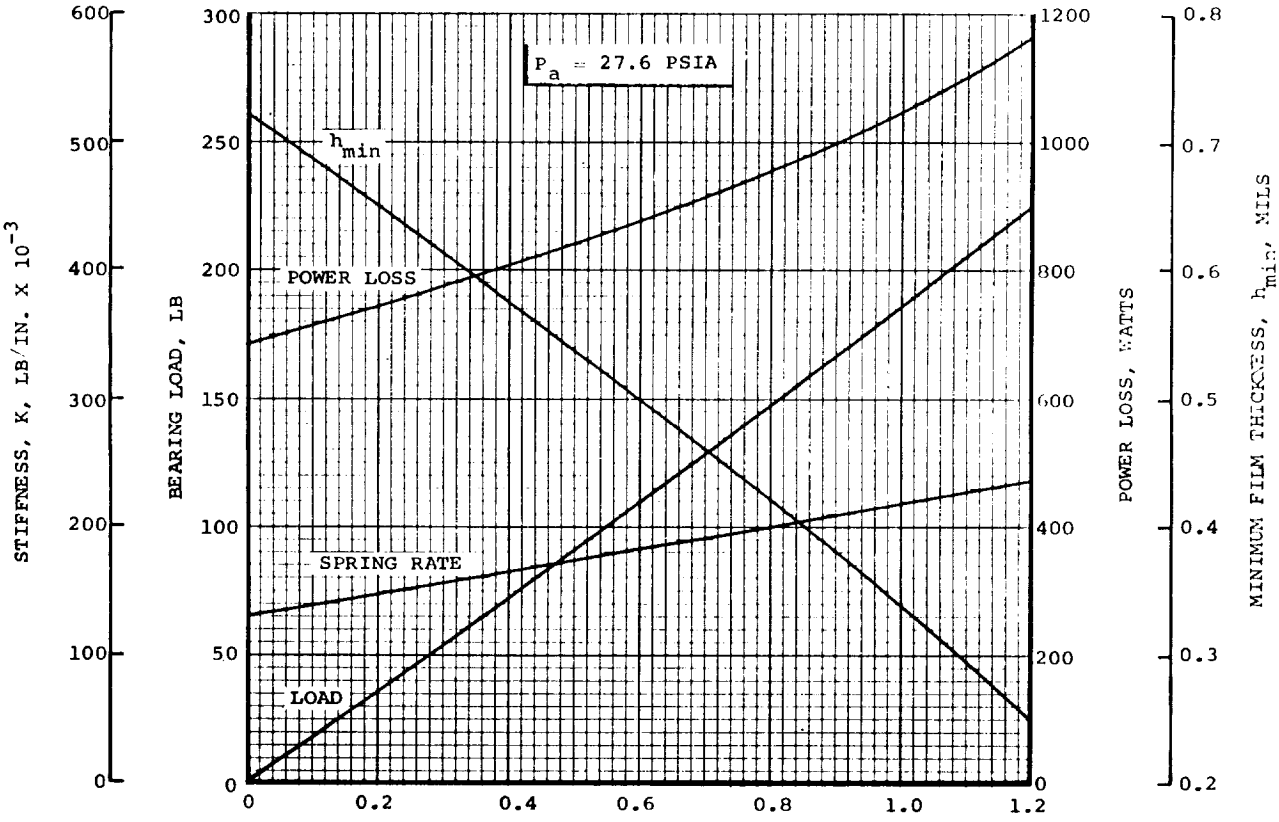
TILTING PAD GAS JOURNAL BEARING PERFORMANCE

He Xe LUBRICANT (MW = 39.94)

FIGURE 134 (Contd)

NOTES:

1. NO. OF PADS = 3
2. WRAP ANGLE = 100°
3. DIA 4.00 IN
4. N = 24,000 RPM
5. PIVOT LOCATION = 65 PERCENT FROM LEADING EDGE
6. L/D = 1.0
7. VISCOSITY 6.54 X 10^{-9} REYNS



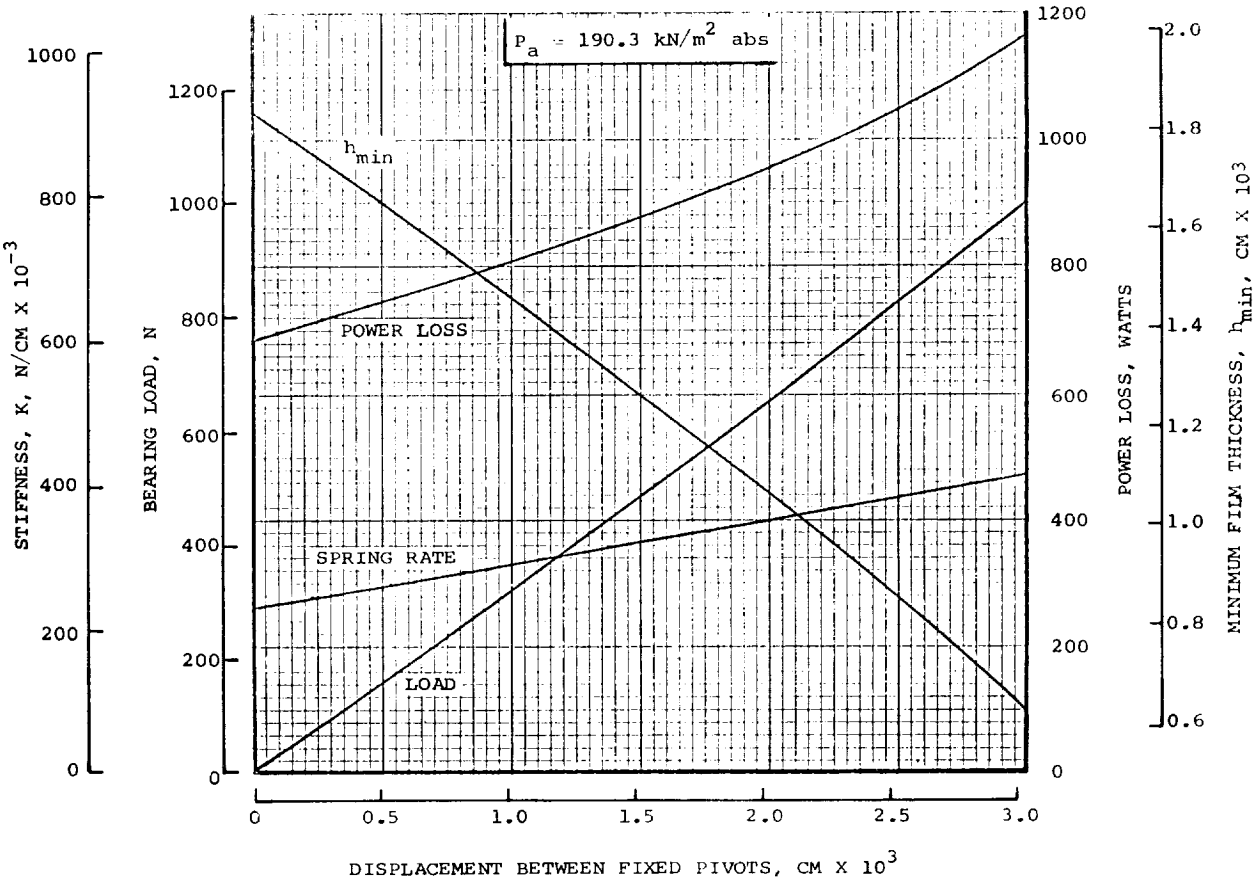
TILTING PAD GAS JOURNAL BEARING PERFORMANCE

He Xe LUBRICANT (MW = 39.94)

FIGURE 135

NOTES:

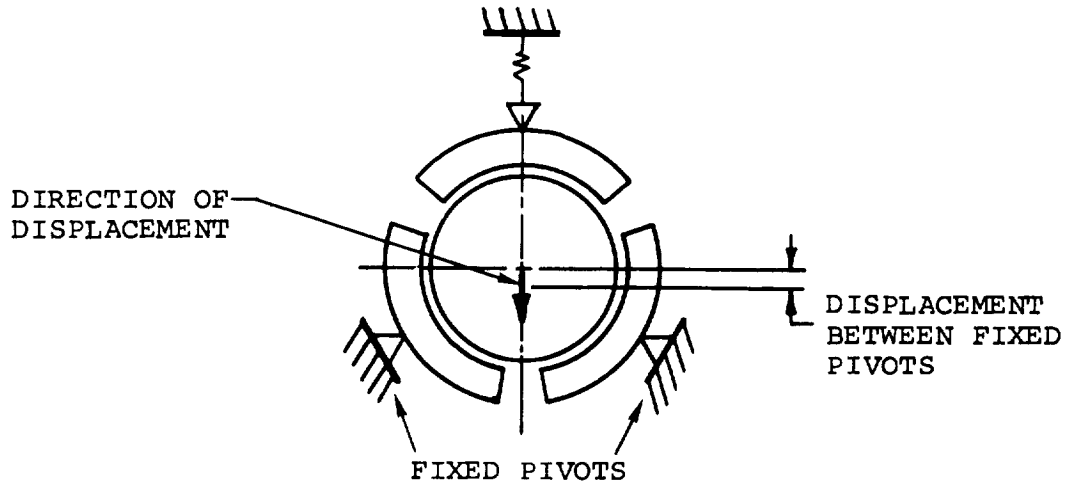
1. NO. OF PADS = 3
2. WRAP ANGLE = 100°
3. DIA 10.16 CM
4. N 24,000 RPM
5. PIVOT LOCATION = 65 PERCENT FROM LEADING EDGE
6. L/D 1.0
7. VISCOSITY 45.1×10^{-9} kN/m^2



TILTING PAD GAS JOURNAL BEARING PERFORMANCE

He Xe LUBRICANT (MW = 39.94)

FIGURE 135 (Contd)



The absissia on Figures 134 and 135 is the physical shaft displacement away from the bearing center toward the fixed pivots as shown above.

Zero journal bearing load represents the case of a vertically oriented rotor on earth or a zero g environment. A journal bearing load of 169 lb (752 N) on Figure 134 represents the "worst case" 1.5 g acceleration perpendicular to the TAC rotor and directed between the fixed pivots. Table 49 presents hydrodynamic performance of the selected TAC journal bearings under three operating regimes.

6.5.2 Thrust Bearing

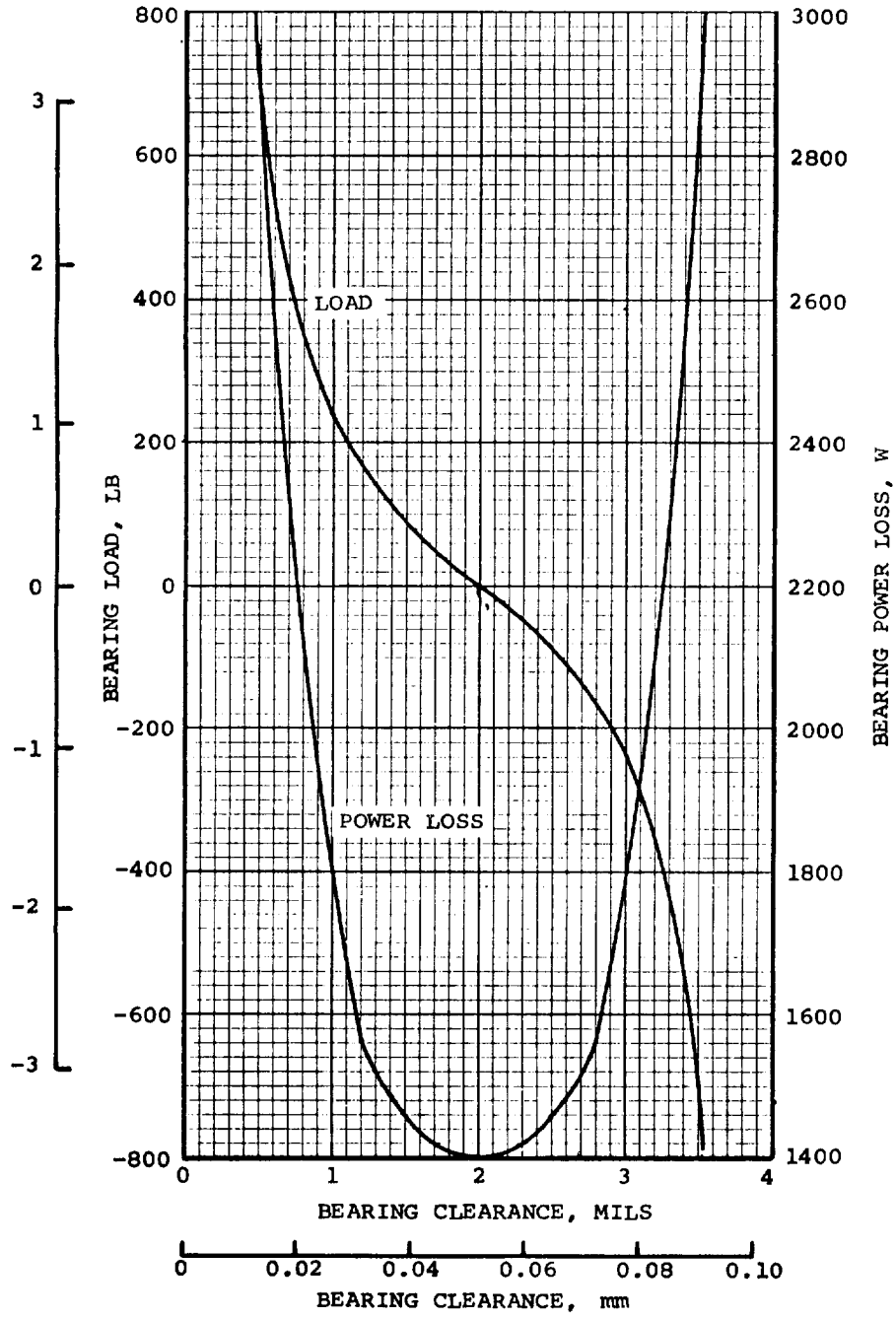
The thrust bearing selected for the Phase III TAC is a preloaded pair of identical stator plates of the Reyleigh step-sector type. Figure 136 presents the predicted steady state performance of the 8 inch O.D. (2.16 cm) thrust bearing system as a function of the axial displacement of the thrust runner.

Anticipated thrust bearing performance for three orientations are shown in Table 49.

TABLE 49

JOURNAL AND THRUST BEARING PERFORMANCE

	Bearing Load, lb	Bearing Load, N	Minimum Film Thickness, mil	Minimum Film Thickness, mm	Power Loss, w	Stiffness, lb/in.	Stiffness, N/cm
Journal Bearing							
Output power = 40 kw_e							
Vertical or zero g	0	0	0.722	0.01834	684	130,000	227,650
Horizontal terrestrial	113	502.6	0.497	0.01262	885	185,000	323,970
1.5 g acceleration	169	751.7	0.372	0.00946	1005	212,000	371,250
Journal Bearing							
Output Power = 160 kw_e							
Vertical or zero g	0	0	0.770	0.01956	639	140,000	245,160
Horizontal terrestrial	113	502.6	0.570	0.01448	795	198,000	346,730
1.5 g acceleration	169	751.7	0.484	0.01229	885	222,000	388,760
Thrust Bearing							
Output power = 160 kw_e							
Vertical terrestrial	325	1448	0.84	0.02136	2090		
Horizontal or zero g	100	445	1.46	0.0371	1470		
1.5 g acceleration	437.5	1946	0.65	0.0165	2420		



D_o = 8 IN. (20.32 cm)
D_i = 4.4 IN. (11.16 cm)
P_a = 123 PSIA
- 848 kN/m^2 abs)
N = 24,000 RPM
NINE PADS

THRUST BEARING HYDRODYNAMIC PERFORMANCE

FIGURE 136

6.5.3 Combined Bearing System Losses

Comparison of the journal and thrust bearing losses at the vario operating conditions and design output power are shown below. The lo ses corresponding to zero g operation were used in the final TAC defi ition discussed in Section 4.

Operating Condition	Combined Losses, Watts		
	Journal Bearings	Thrust Bearings	Total
Zero g	1278	1440	2748
Terrestrial Horizontal	1590	1470	3060
Terrestrial Vertical	1278	2090	3368
1.5 g Acceleration Parallel with Shaft	1278	2420	3698
1.5 g Acceleration perpendicular to Shaft	1770	1470	3240

.6 Labyrinth Seal Leakage

Leakages were calculated with the methods described in Reference 1 or labyrinth seals with the following conditions:

Upstream temperature 960°R (533°K)

Upstream pressure 122 psia (841.1 kN/m^2 abs)

Discharge coefficient related to pressure ratio as shown in Figure 137 with $\Delta/\delta = 1.58$

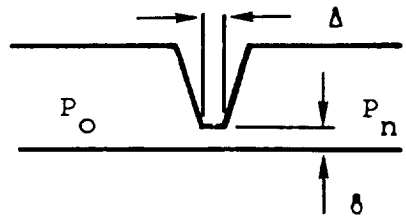
he upstream pressure was set at the compressor discharge pressure inus an 8 percent pressure loss to allow for line and filter losses. eakages were determined for staggered and straight-through seal esigns over a range of number of teeth with a total seal length of .0 in. (2.54 cm). Downstream seal pressure and diameter varied as ollows:

	Pressure psia	Pressure kN/M^2	Diameter inch	Diameter cm
Compressor end seal	86.5	596	3.8	9.65
Turbine end seal	84.5	582.5	3.8	9.65
Alternator isolation seal	70.0	482.5	4.0	10.16

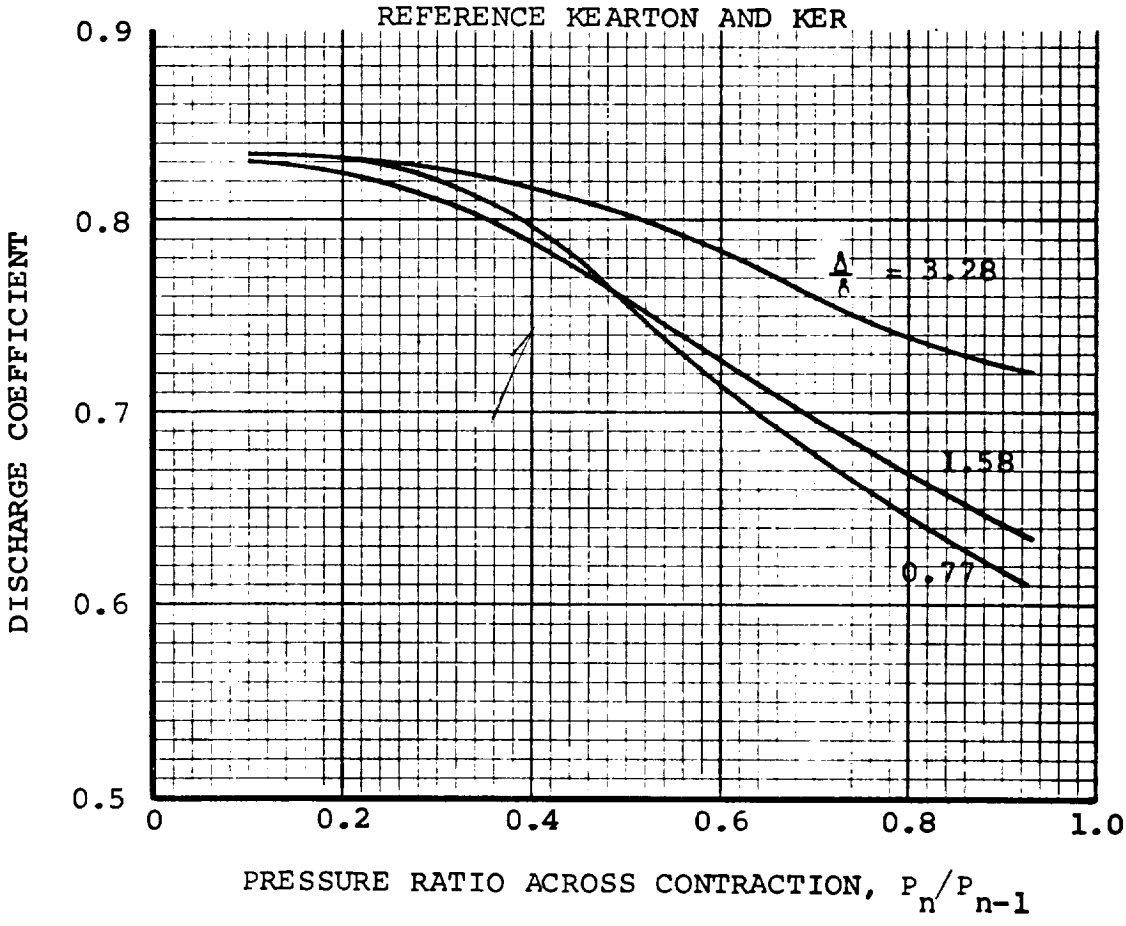
he compressor and turbine end seals have downstream pressures typical of the rotor back face. The alternator rotor cavity is vented to the compressor inlet.

Figures 138 and 139 show the leakages for the alternator and turbine seals for their radial clearances. The compressor seal leakage data is similar to the turbine data and is not presented for brevity.

[1]Potassium Turboalternator (KTA) Preliminary Design Study, Vol. 1 and Vol. 2. Prepared by AiResearch. NASA CR 1498 and 1499.

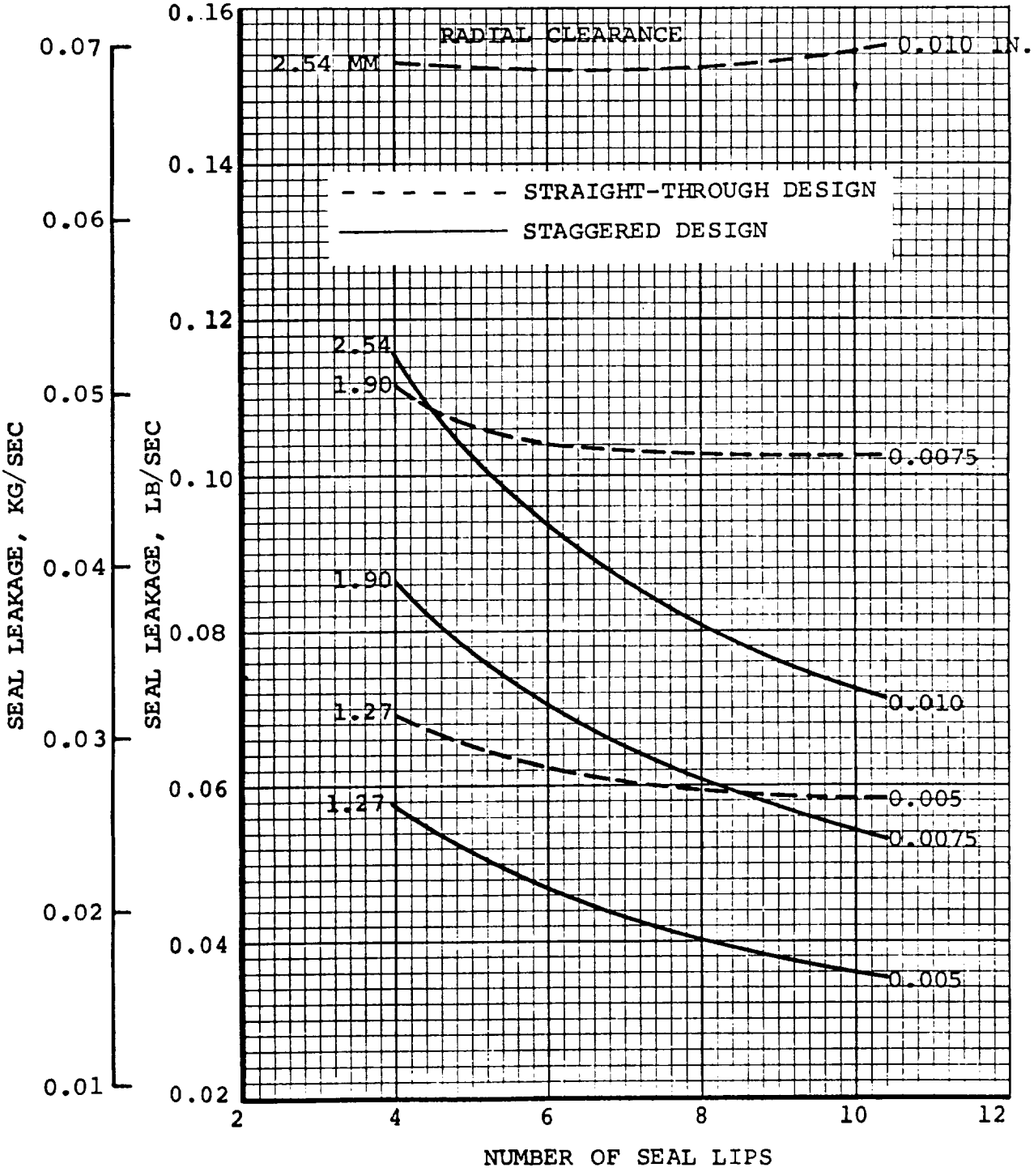


Δ = THICKNESS OF LABYRINTH LIP
δ = RADIAL CLEARANCE
P_n = STATIC PRESSURE
P_o = TOTAL PRESSURE



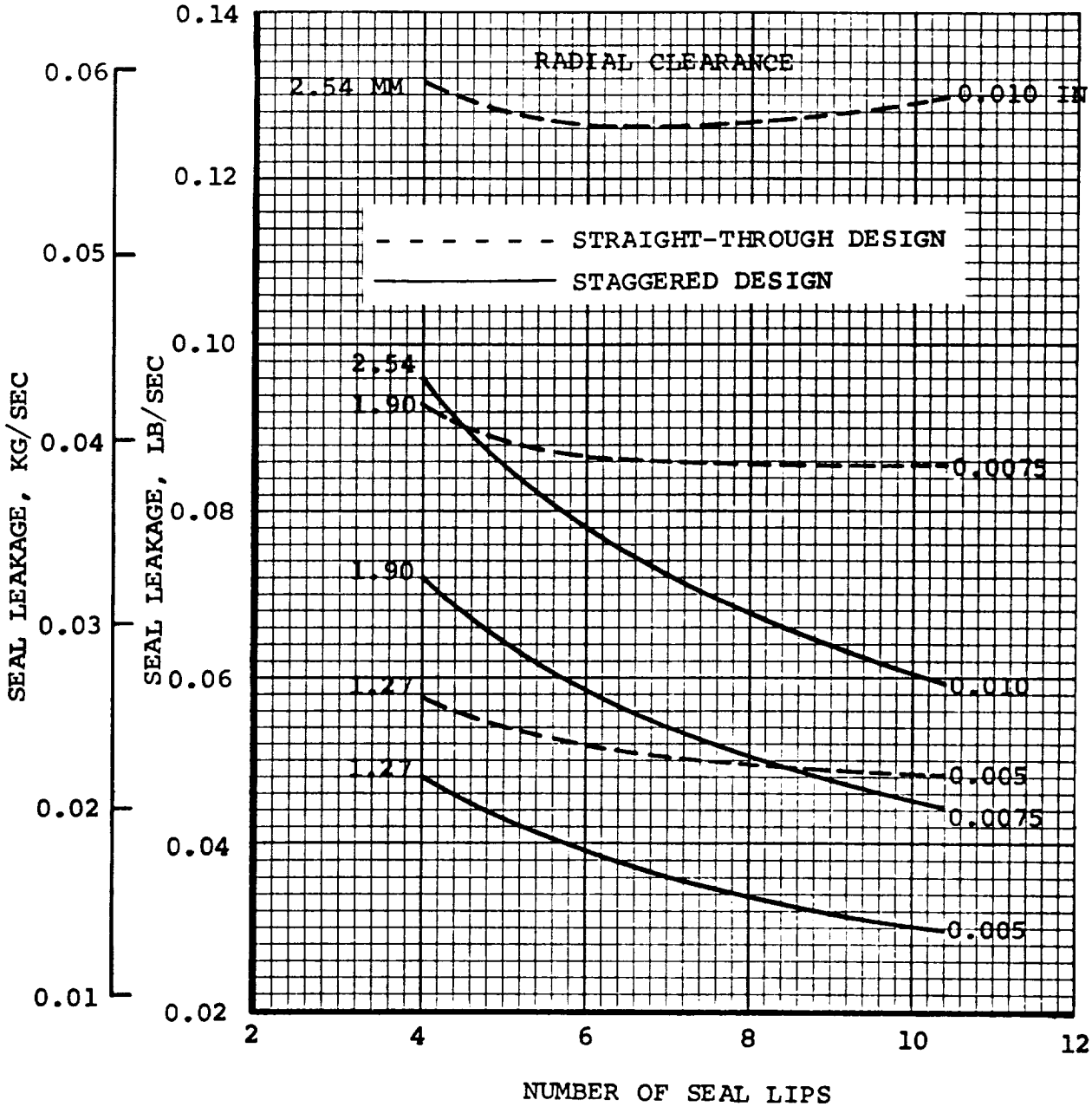
COEFFICIENT OF DISCHARGE FOR CONTRACTIONS

FIGURE 137



ALTERNATOR SEAL LEAKAGE

FIGURE 138



TURBINE SEAL LEAKAGE

FIGURE 139

Seal clearance must be determined in conjunction with a complete differential thermal expansion analysis. A clearance of 0.0075 inch (1.9 mm) was selected for the example seal leakage evaluation. A summary of the seal leakage is shown below:

	No. of Lips	Design Type	Leakage lb/sec	Leakage kg/sec
Compressor end	8	Straight	0.083	0.0374
Turbine end	8	Straight	0.085	0.0386
Alternator cavity (2 required)	6	Staggered	0.0140	0.0635
TOTAL leakage			0.308	0.1395

This seal leakage represents approximately 2.24 percent of the compressor inlet mass flow rate. Selection of 8 lips for both the compressor and turbine seals result in near minimum leakage for the straight-through design. Staggered lip seal designs were not considered for these requirements due to manufacturing and assembly requirements. A staggered seal lip design was selected for the alternator seals at the expense of reducing the number of lips. If a straight-through alternator seal lip design is necessary the seal leakage would increase to about 2.9 percent, a significant performance penalty.

7. TAC FAILURE MODE AND EFFECTS ANALYSIS

A failure mode and effects analysis has been conducted for the TAC unit. The purpose of this analysis is to identify the potentially critical failure areas so that efforts can be made to reduce the probability of these failures to an absolute minimum. This analysis was conducted separately by the aerodynamic and bearing designers at AiResearch and the electrical designers at Westinghouse. Table 50 shows the results of these analyses.

TABLE 50

TAC FAILURE MODE ANALYSIS

COMPONENT	FAILURE MODE	FAILURE EFFECT	REMARKS
Turbine wheel	Excessive or non-uniform creep due to non-uniform properties	Unbalance, bearing failure	Accelerated by over-temperature
	Burst due to overspeed	Immediate, zero power	
	Rim cracking due to low cycle fatigue	Variable, no effect to serious rim loss	Due only to hundreds of rapid start cycles, not expected for this application
	Blade loss due to fatigue	Increased unbalance	
Compressor wheel	Blade loss due to fatigue	Increased unbalance	
Journal bearings	Pivot wear	Increased clearance, may induce whirl instability	Highly wear resistant pivot material is used
	Wear due to foreign particles	Increased clearance, reduced load capacity	Bearing supply gas is filtered. Clean bearing compartments during assembly
	Overload	Bearing seizure	Operation at critical speeds or high shock loads cause failure
Thrust bearing	Wear due to foreign particles	Alters geometry, reduced load capacity	Bearing supply gas is filtered
	Slider distortion due to overspeed and over-temperature	Loss of load capacity, possible bearing rub	Support equipment failure
	Overload	Bearing seizure	Caused by shock or acceleration
Labyrinth seals	Rub	Increased leakage	Will tolerate minor rubs
Alternator rotor	Non-uniform creep or yield due to non-uniform properties	Increased vibration, possible bearing overload	
	Bore crack propagation due to high stresses	Rotor failure, loss of power system	Due to overspeed or flaw in material
	Creep due to high temperatures	Rotor failure	
Alternator stator	Excessive losses due to loosened stack fits	Accelerated deterioration or increased vibration. Reduced life	Caused by overtemperature
	Heat exchanger separates from frame or stack	Excessive temperature and losses. Reduced life	Due to bond or contact pressure loss
	Lamination fatigue due to mechanical or electrical vibration	Laminations break, flux unbalance. Decreased output.	

TABLE 50 (Contd)

COMPONENT	FAILURE MODE	FAILURE EFFECT	REMARKS
Alternator windings and insulation	Extended short circuit operation	Armature conductors open	Due to user system malfunction or long end turns touching
	Slot cell insulation fatigue due to vibration	Loss of slot liner or wedges. Stator shorts	
	Cladding breaks	Silver migrates out of wire. Insulation shorts or wire opens	Due to handling abuse, electrical stresses, poor manufacturing
	Anadur frets away due to vibration	Loosening of windings, plug heat exchanger. Reduced life	
	Armature conductor opens	Output reduction, phase unbalance	
	Field conductor opens	Loss of output, overspeeds	
	Field turns open due to insulation wear	Increased excitation to maintain voltage	
	Excessive losses, wire sagging due to excessive coolant temperature	Accelerated deterioration, possible short	
Alternator coolant	Excessive temperature	Alternator stator and/or bearing failure	
	Reduced flow	Increased temperature. higher losses, shorten life	Due to plugging or support equipment failure

NASA-Langley, 1971 —— 22